Functional Cellulosic Porous Materials

Structure Design, Surface Engineering, and Applications

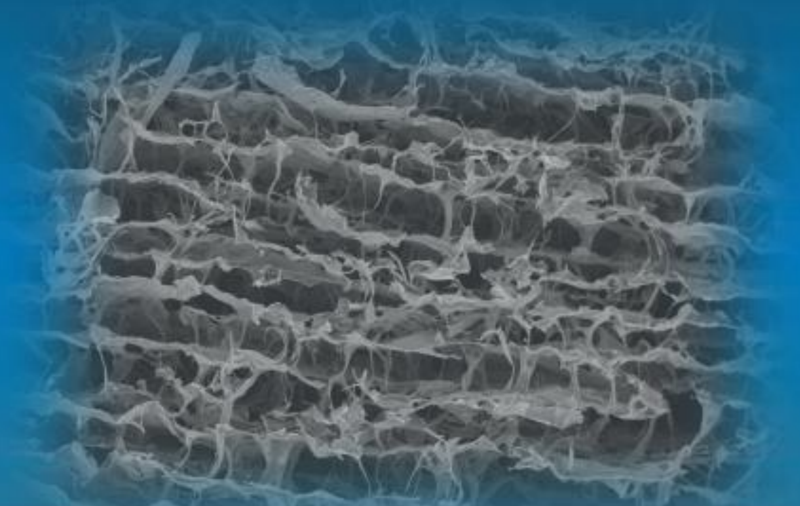

Huan Cheng

FUNCTIONAL CELLULOSIC POROUS MATERIALS: STRUCTURE DESIGN, SURFACE ENGINEERING, AND APPLICATIONS

Huan Cheng

Graduation Committee:

Chairman:	**Prof. dr. J. L. Herek**	**University of Twente**
Promotors:	**Prof. dr. G. J. Vancso**	**University of Twente**
	Prof. dr. X. Sui	**Donghua University**
Assistant-promotor:	**Dr. M. A. Hempenius**	**University of Twente**
Members:	**Prof. dr. ir. W. M. de Vos**	**University of Twente**
	Prof. dr. D. Stamatialis	**University of Twente**
	Prof. dr. S. Zapotoczny	**Jagiellonian University**
	Dr. L. Xu	**Sappi Europe | Sappi Biotech**
	Prof. dr. C. Nardin	**Université de Pau et des Pays de l'Adour**

The research described in this Thesis was carried out in the groups of Materials Science and Technology, and Sustainable Polymer Chemistry, MESA+ Institute for Nanotechnology, Faculty of Science and Technology, University of Twente, the Netherlands and in the Key Lab of Science and Technology of Eco-Textile, Ministry of Education, College of Chemistry, Chemical Engineering and Biotechnology, Donghua University, China.

This research was financially supported by the MESA+ Institute for Nanotechnology, University of Twente, by Donghua University, China, and by the China Scholarship Council.

Cover design: Huan Cheng
Printed by: Ipskamp Printing, Enschede, the Netherlands
ISBN: 978-90-365-5266-0
DOI: 10.3990/1.9789036552660

FUNCTIONAL CELLULOSIC POROUS MATERIALS: STRUCTURE DESIGN, SURFACE ENGINEERING, AND APPLICATIONS

DISSERTATION

to obtain
the degree of doctor at the Universiteit Twente,
on the authority of the rector magnificus,
prof. dr. ir. A. Veldkamp,
on account of the decision of the Doctorate Board
to be publicly defended
on Wednesday 3 November 2021 at 12.45 hours

by

Huan Cheng

born on the 26th of December, 1992
in Shandong, China

This dissertation has been approved by:

Promotors:	
Prof. dr. G. J. Vancso	University of Twente
Prof. dr. X. Sui	Donghua University
Assistant-promotor:	
Dr. M. A. Hempenius	University of Twente

Contents

Chapter 1

General Introduction

1.1 Introduction

The application of functional porous materials for tackling challenges in the areas of environment, energy, and healthcare has attracted distinguished interest [1-2]. Cellulose within this class of materials, which is one of the most abundant and renewable polymers, provides attractive alternatives to synthetic plastics for numerous applications. The inherent properties of hydrophilicity, biodegradability and the rich chemistry enabled by its hydroxyl groups make cellulose easy to modify and functionalize [3-6]. When cellulosic materials are endowed with controlled (micro)porous structures, a range of applications becomes feasible due to the combined advantages of controlled porosity, high specific surface area, and the intrinsic materials' properties of cellulose. For example, porous cellulosic materials with precise surface modification and engineered pore structure have been employed in molecular delivery, catalyst support, absorption, separation, and thermal insulation [7-11].

The performance of cellulosic porous materials, however, is critically dependent on their mechanical properties, which are determined by the material's inner structure, and surface chemistry [12]. Therefore, the structure design, the selection of chemical or physical crosslinking methods, other materials engineering operations, and post-synthesis modifications are decisive factors to optimize structure, and thus performance and function. Organosilanes are commonly used for enhancing the mechanical properties of porous cellulosic materials. In my previous work, multiple chemical crosslinking systems composed of γ-glycidoxypropyltrimethoxysilane and amine-containing polymers (polyethyleneimine, chitosan) were developed to significantly enhance the mechanical properties of cellulosic porous materials. The resulting polymers were used in heavy metal ion adsorption, sensors, energy harvesting, and wound dressings [13-15]. However, in this work, structural characteristics of the cellulosic materials were not specifically engineered, which leaves room for performance improvement of these porous materials.

1.2 Concept of this Thesis

Based on my previous work on cellulosic porous materials, improving their application performance is the focus of this thesis. Structure design and surface modification are promising ways to endow cellulosic porous materials with excellent functionalities and improved performance.

In this thesis, cellulosic porous materials with unique structures, or surface properties, were readily prepared by adjusting freeze-drying conditions and mixing with, or post-modification of, functional materials. Aiming at diversified functionalities that give rise to improving the performance of cellulosic porous materials, a variety of structures and functional systems are introduced in this thesis, including Janus structures, chitosan, polyvinyl alcohol (PVA), carbon nanotubes (CNTs), polyurethanes (PU), polypyrroles (PPy), and polyferrocenylsilanes (PFS). The introduction of these chemistries and the resulting functional materials provide cellulosic porous systems with novel characteristics, allowing these to address a broad range of applications such as wound dressing, evaporators for efficient solar desalination, thermal management, wearable heaters, and catalyst support. The following topics will be presented and discussed in detail in this thesis.

In **chapter 2**, we review recent advances in cellulosic porous materials that are used in different applications. Following an introduction providing details about the importance of cellulose porous materials, their preparation is briefly reviewed. Subsequently, the focus is laid on their environmental applications, including pollutant adsorption, oil/water separation, use as eco-friendly catalyst support, electromagnetic shielding, and CO_2 capture. Then energy applications as supercapacitors, ion-infused batteries, and thermal insulation materials are surveyed. Utilization in healthcare applications as wound dressing, cell culture scaffolds, drug delivery, and pressure sensors are also discussed. Finally, the challenges related to cellulosic porous materials are discussed.

In **chapter 3**, we describe the production of cellulose sponges with Janus character, using cellulose nanofibers (CNFs) and different organosilanes, by heterogeneous mixing and freeze-drying. The as-prepared sponges exhibit different wettability characteristics. The comprehensive advantages of the unique Janus structure with different wettability on both sides, and the hemostatic property of chitosan, endowed the sponges with a superior blood clotting performance compared with a hydrophilic control sample and with common gauze.

In **chapter 4**, the Janus structure presented in **Chapter 3** is further discussed, following design and preparation in a cylindrical shape. A floatable and robust monolithic integrated cellulose aerogel-based evaporator (MiCAE) is fabricated by carefully controlling and integrating three functional components, including hydrophilic cellulose-PVA aerogel (CPA), hydrophobic silylated cellulose aerogel (SCA), and a multi-walled carbon nanotube (MCNT) coating layer (CPA@CNT), through the heterogeneous mixing and freeze-drying method. Inspired by the wood and mushrooms in nature, this evaporator provides a facile solution for seawater desalination in a salt-resistant and efficient manner.

In **chapter 5**, based on our previous work on amine-modified cellulosic porous materials, wearable heaters using waterproof and breathable composite aerogels are described, which were made by additional coating with PPy, a fluorinated finishing agent, and polyurethane. The combined properties resulting from the porous aerogel structure and outstanding Joule heating performance from PPy make this composite aerogel highly promising for wearable devices and personal thermal management systems.

In **chapter 6**, a symbiotic sponge containing natural and synthetic polymers are discussed by co-dissolving cellulose and poly(ferrocenylsilane) (PFS)-based poly(ionic liquid) in ionic liquid environment, regeneration in water, and freeze-drying. By taking advantage of the redox property of PFS, palladium (Pd) nanoparticles were prepared in situ and immobilized in the composite sponge without using an external reducing agent. The as-prepared Pd nanoparticles-loaded sponge exhibited excellent performance in the reduction of 4-nitrophenol to 4-aminophenol.

In **chapter 7**, Some PFS-based poly(ionic liquid)s, zwitterionic poly(ionic liquid)s and hydrogels were synthesized by introducing different substituents. This outlook chapter is expected to inspire a new strategy for designing stimuli-responsive PFS modified cellulosic porous materials and to explore new applications.

1.3 References

(1) Jiang, S.; Agarwal, S.; Greiner, A. Low-density open cellular sponges as functional materials. *Angewandte Chemie International Edition* **2017,** *56* (49), 15520-15538.

(2) Gesser, H.; Goswami, P. Aerogels and related porous materials. *Chemical Reviews* **1989,** *89* (4), 765-788.

(3) Chen, W.; Yu, H.; Lee, S.-Y.; Wei, T.; Li, J.; Fan, Z. Nanocellulose: A promising nanomaterial for advanced electrochemical energy storage. *Chemical Society Reviews* **2018,** *47* (8), 2837-2872.

(4) Klemm, D.; Heublein, B.; Fink, H. P.; Bohn, A. Cellulose: Fascinating biopolymer and sustainable raw material. *Angewandte Chemie International Edition* **2005,** *44* (22), 3358-3393.

(5) Klemm, D.; Cranston, E. D.; Fischer, D.; Gama, M.; Kedzior, S. A.; Kralisch, D.; Kramer, F.; Kondo, T.; Lindström, T.; Nietzsche, S. Nanocellulose as a natural source for groundbreaking applications in materials science: Today’s state. *Materials Today* **2018,** *21* (7), 720-748.

(6) Li, T.; Chen, C.; Brozena, A. H.; Zhu, J.; Xu, L.; Driemeier, C.; Dai, J.; Rojas, O. J.; Isogai, A.; Wågberg, L. Developing fibrillated cellulose as a sustainable technological material. *Nature* **2021,** *590* (7844), 47-56.

(7) Cheng, H.; Li, L.; Wang, B.; Feng, X.; Mao, Z.; Vancso, G. J.; Sui, X. Multifaceted applications of cellulosic porous materials in environment, energy, and health. *Progress in Polymer Science* **2020,** *106*, 101253.

(8) Kontturi, E.; Laaksonen, P.; Linder, M. B.; Gröschel, A. H.; Rojas, O. J.; Ikkala, O. Advanced materials through assembly of nanocelluloses. *Advanced Materials* **2018,** *30* (24), 1703779.

(9) De France, K. J.; Hoare, T.; Cranston, E. D. Review of hydrogels and aerogels containing nanocellulose. *Chemistry of Materials* **2017,** *29* (11), 4609-4631.

(10) Zhao, S.; Malfait, W. J.; Guerrero-Alburquerque, N.; Koebel, M. M.; Nyström, G. Biopolymer aerogels and foams: Chemistry, properties, and applications. *Angewandte Chemie International Edition* **2018,** *57* (26), 7580-7608.

(11) Kargarzadeh, H.; Huang, J.; Lin, N.; Ahmad, I.; Mariano, M.; Dufresne, A.; Thomas, S.; Gałęski, A. Recent developments in nanocellulose-based biodegradable polymers, thermoplastic polymers, and porous nanocomposites. *Progress in Polymer Science* **2018,** *87*, 197-227.

(12) Ferreira, E. S.; Rezende, C. A.; Cranston, E. D. Fundamentals of cellulose lightweight materials: bio-based assemblies with tailored properties. *Green Chemistry* **2021,** *23*, 3542-3568.

(13) Cheng, H.; Li, Y.; Wang, B.; Mao, Z.; Xu, H.; Zhang, L.; Zhong, Y.; Sui, X. Chemical crosslinking reinforced flexible cellulose nanofiber-supported cryogel. *Cellulose* **2018,** *25* (1), 573-582.

(14) Cheng, H.; Li, C.; Jiang, Y.; Wang, B.; Wang, F.; Mao, Z.; Xu, H.; Wang, L.; Sui, X. Facile preparation of polysaccharide-based sponges and their potential application in wound dressing. *Journal of Materials Chemistry B* **2018,** *6* (4), 634-640.

(15) Cheng, H.; Du, Y.; Wang, B.; Mao, Z.; Xu, H.; Zhang, L.; Zhong, Y.; Jiang, W.; Wang, L.; Sui, X. Flexible cellulose-based thermoelectric sponge towards wearable pressure sensor and energy harvesting. *Chemical Engineering Journal* **2018,** *338*, 1-7.

Chapter 2

Multifaceted Applications of Cellulosic Porous Materials in Environment, Energy, and Health

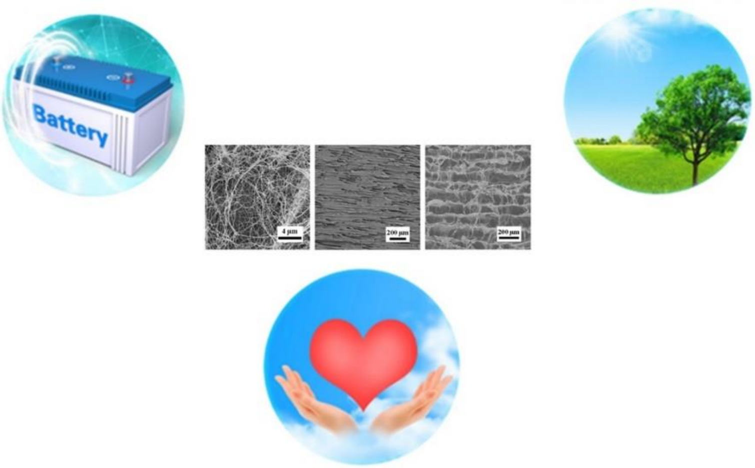

Macromolecular materials of natural origin, like cellulose, provide attractive alternatives to synthetic polymers for numerous applications. These advantages are related to the renewable and bio-based resources that are used to obtain cellulosic materials. Additionally, their intrinsic hydrophilicity, biodegradability, chemical similarity to soft matter in living organisms, and the rich chemistry one can employ to modify their structure, and thus properties, provide other benefits. When cellulosic materials are endowed with controlled (micro)porous structures, a range of hitherto unattainable applications become feasible due to the combined advantages of controlled porosity, high surface-to-volume ratio, and intrinsic materials properties of cellulose and its derivatives such as the high density of hydroxyl groups available for chemical modifications. This chapter provides an update of cellulosic porous materials with a focus on the selected application areas, related to the environment, energy and health.

The contents of this chapter have been published as: Huan Cheng, Lijie Li, Bijia Wang, Xueling Feng, Zhiping Mao, G. Julius Vancso, and Xiaofeng Sui, Multifaceted Applications of Cellulosic Porous Materials in Environment, Energy, and Health. *Progress in Polymer Science*, **2020**, *106*, 101253.

2.1 Introduction

Cellulosic porous materials combine the advantages of cellulose and porous materials. Generally, the low density, the high specific surface area, the readiness for chemical modifications, and the interconnected porous structure of cellulosic porous materials are very favorable for loading and releasing molecular guests. These properties endow porous cellulosic materials with technological importance in energy storage and conversion, catalyst support, adsorption, separation, and biomaterials [1-14]. Owing to the structural and functional variety, easy access, and renewable nature, functional cellulosic porous materials have attracted considerable attention in recent years [15-18].

Numerous terms, including aerogel [15], cryogel [19], sponge [20], scaffold [21], and foam [16] have been used to identify cellulosic porous materials in the literature. All these terms are used in this chapter when discussing the corresponding original articles. Otherwise, we use the general term “cellulosic porous materials” (CPM).

Most of the current review literature on CPM focuses on their preparation and characterization. While the importance of such materials and their applications have become increasingly prominent, their utilization in catalysis, molecular imprinting, gas storage and adsorption, and as biomedical platforms have only been individually reviewed, *i.e.* no single comprehensive report exists focusing on all these major fields of use [1-3, 9, 15-16].

In recent years, we have been active in exploring the multifaceted applications of CPM. We reported on the design, preparation, characterization and applications of these materials in oil/water separation [22], heavy metal adsorption [19, 23], thermal insulation [24], catalyst support [25-27], electro-magnetic interference (EMI) shielding [28], thermoelectric materials [29], antibacterial materials [30], and wound healing [20]. Here we present the recent progress with focus on three main application areas including the environment, energy, and health. Current challenges hampering the use of functional CPM, possible solutions, and future prospective are also discussed.

Following an introduction providing details about the importance of CPM, their preparation is first briefly overviewed. Subsequently, focus is laid on their environmental applications including pollutant adsorption, oil/water separation, use as eco-friendly catalyst support, EMI shielding and CO_2 capture. Then energy applications as supercapacitors, as ion-infused batteries, and as thermal insulation materials are surveyed. Non-toxicity is essential for biomaterials, and is also an inherent advantage of cellulose. Hence utilization in health-care as wound dressing, cell culture scaffolds, drug delivery and pressure sensors are also considered.

2.2 Preparation of functional cellulosic porous materials

Precursors to CPM include raw substances that exhibit different morphologies across the length scales [10, 31], varying from cellulose nanofibers, or cellulose nanofibrils, or nanofibrillated cellulose (CNFs or NFC) [32], cellulose nanocrystals (CNCs) [33-34], to regenerated cellulose (RC) [35]. One option to obtain these materials includes the generation of a cellulose solution by dissolving the raw material in a solvent (e.g., *N*-methylmorpholine-*N*-oxide (NMMO), in NaOH aqueous solution, or in ionic liquids). Subsequently, following solvent exchange to derive regenerated cellulose, removal the solvent by supercritical drying, freeze drying, or ambient drying should be performed. Other routes to obtain (micro)porous cellulose include preparation from cellulose suspension *via* mechanical disintegration or enzymatic treatment, and removal of the solvent by supercritical drying, freeze drying, or ambient drying [36-37]. CPM can also be prepared directly, from delignified natural wood and bacterial cellulose (BC) hydrogels, using a facile top-down approach [38-40]. Functionality can be introduced prior to the formation of the CPM. This step can include modifications by functional polymers, nanoparticles, or small molecular modifiers.

2.3 Environmental applications

With the growing awareness concerning the rising concerns of environmental pollution and fossil fuel consumption, different functional CPM are continuously developed for environmental utilization [41-48]. This is facilitated by the earlier mentioned excellent properties of cellulosic materials. The surface wettability of these materials, for example, is conveniently tunable, enabling applications in separation of oil/water mixture and oil/water emulsions. Chelating moieties, such as amino or thiol groups, and metal organic frameworks (MOFs) could be added to prepare cellulosic porous adsorbents for effective removal of heavy metal ions or dyes. CPM are also great eco-friendly catalyst supports for improved catalytic efficiency and a lower environmental footprint. CPM can further be tuned to capture particles from the air, coated with electrically conductive materials for EMI shielding, or modified with amino groups to capture CO_2. Although these routes encompass attractive environmentally friendly approaches, the corresponding preparation processes are still too complex to be widely employed. Post-modification is often necessary for enhanced utilization efficiency, which inevitably increases the environmental burden and calls for reuse of the modified cellulose porous material. Practically, the mechanical properties of these systems still need to be improved to match with those of petroleum-based materials in practical applications.

2.3.1 Oil/water separation

Oil spillages and discharge of organic solvents can cause severe damage to the environment. Materials that can effectively remove and absorb organic solvents and oils from water are needed to solve these pollution problems [49-52]. The porous structures are superior for enhanced adsorption capacities and promoting liquid diffusion. Additionally, tuning the hydrophobicity of the CPM further boost the removal of oils and organic solvents from water [53-57]. Numerous studies reported on the use of hydrophobic CPM in oil/water separation, and we provide an overview of relevant references in **Table 2.1**. Here we add a brief narrative section discussing some relevant examples.

Table 2.1. Functional cellulosic porous materials used in oil/water separation.

Materials	**Functionalization**	***WCA (°)**	***A.C. (in g g^{-1}) Ref.**
CNFs	*n*-Dodecyltriethoxysilane	150	80-197 [58]
CNFs	Methyltrichlorosilane	138	60-136 [59]
CNFs	Styrene-acrylic	144	30-47 [60]
CNFs	Methyltrimethoxysilane and hexadecyltrimethoxysilane	159	65-205 [61]
CNFs	Methyltrichlorosilane	/	54-140 [62]
CNFs	Hexadecyltrimethoxysilane	139	56-162 [63]
CNFs	Methylene diphenyl diisocyanate	/	128-181 [64]
CNFs	Triethoxyl(octyl) silane	/	139-356 [65]
Cellulose fibers	Methyltrimethoxysilane	155	58-101 [66]
Natural bamboo fibers	Pyrolysis	151	23-51 [67]
Microfibrillated cellulose	Methyltriethoxysilane	152	116-260 [68]
Nanocellulose	Stearoyl chloride	160	25-55 [69]

aqueous suspension			
Bacterial cellulose	Trimethylchlorosilane	147	86-185 [70]
Ethyl cellulose	Nanosilica and hexadecyltrimethoxysilane	158	30-65 [71]
Ethyl cellulose	Hexadecyltrimethoxysilane	> 150	37-51 [72]
Ethyl cellulose	Silver nanoparticles and *n*-dodecyl mercaptan	161	36-48 [73]
Balsa wood	Epoxy	140	6-20 [74]
Balsa wood	Methyltrimethoxysilane	151	16-41 [75]
Cellulose in ionic liquid	Trimethylchlorosilane	136	12-22 [76]
Cellulose in NaOH/urea	Trimethylchlorosilane	153	14-28 [77]

* A.C. (in g g^{-1}): adsorption capacity of oils and organic solvents (g g^{-1}); WCA: static water contact angle

Hydrophobic organosilanes are the most common reagents used to prepare hydrophobic CPM as the alkoxy group on the organosilane is susceptible to hydrolysis and reacts with the hydroxyl groups on the cellulose. Zhang et al., for example, described a hydrophobic nanocellulose sponge prepared by modifying suspended nanocellulose, using pre-hydrolyzed methyltrimethoxysilane (MTMS) followed by freeze-drying (**Figure 2.1A**) [78]. The hydrophobic and oleophilic properties of this sponge made it efficient for removing chloroform from water with adsorption capacities up to 100 times of the materials' weight. The material also showed selectivity for removing dodecane, spilled at the surface of water, and additionally, it was also recyclable (**Figure 2.1B**).

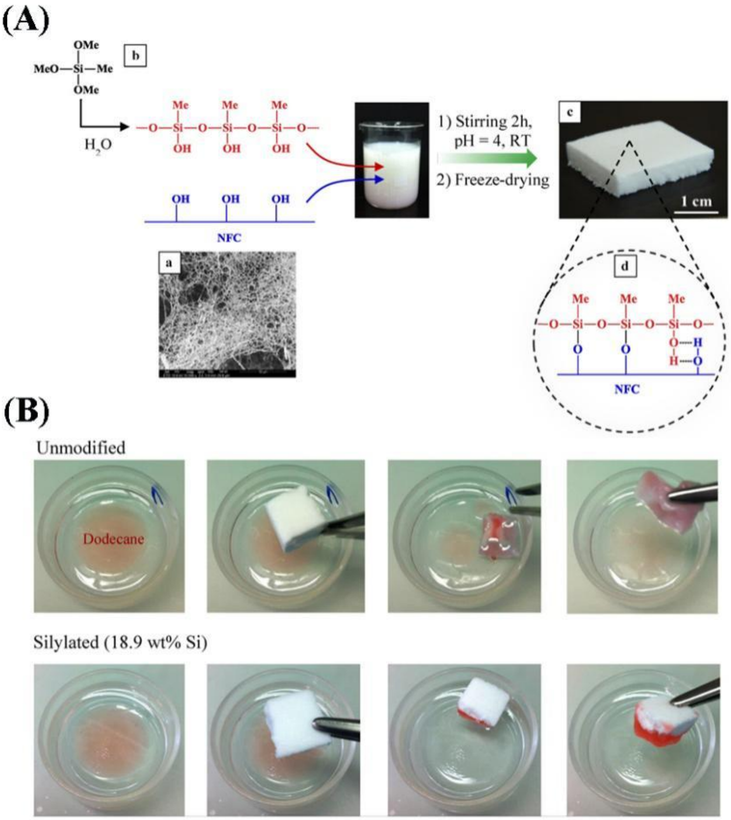

Figure 2.1 (A) General scheme for the synthesis of silylated NFC sponges. (B) Adsorption of a red-colored dodecane spill using unmodified NFC sponge and silylated NFC sponge [78].

Oil-water emulsions stabilized by surfactants are difficult to separate[79]. CPM can be used as platforms in efficient oil-water emulsion separation of surfactant stabilized systems. Wang and co-authors designed a double-layer-structured regenerated cellulosic sponge with excellent under-water superoleophobicity that allows the water phase to quickly permeate while the oil phase would be retained by the top-layer with a pore size of less than 1 μm (**Figure 2.2A**). The sponge showed >99.4% separation efficiency for an oil/water emulsion without any applied pressure (**Figure 2.2B**). It also showed excellent antifouling properties [80].

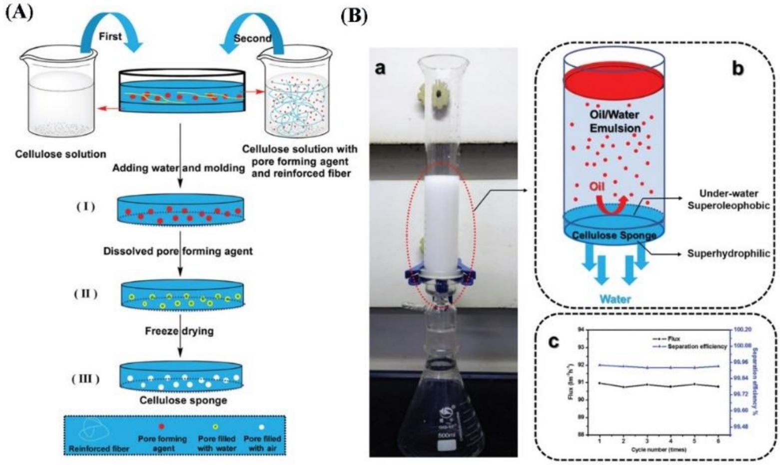

Figure 2.2 (A) Fabrication process of double layer structured cellulose sponges. (B) The oil/water emulsion separation process (a, b) and cycling performance (c) of the sponge [80].

Our group prepared a hydrophilic cellulose sponge for oil/water separation by post-modification utilizing thiol-ene reactions [22]. The reactive vinyl groups were introduced by treating a cellulose sponge with vinyltrimethoxysilane (VTMS) followed by subsequent functionalization with 3-mercaptopropionic acid. The separation experiments showed high stability and high separation efficiency for a *n*-hexane/water mixture (100% after 10 cycles) and a *n*-hexane-in-water emulsion (95% after 6 cycles).

Modification using stimulus responsive polymers is beneficial to achieve separation control. For example, poly(*N,N*-dimethylamino-2-ethyl methacrylate) (PDMAEMA) polymer brushes were grafted from CNFs aerogels to prepare a CO_2-responsive oil/water separation system in our group. The CO_2-responsive aerogel showed high separation efficiency for an oil/water mixture and for surfactant-stabilized emulsions [81]. For separation of oil-water mixtures and emulsions, the separation efficiency is determined by the pore dimensions and by the surface wettability of the cellulose porous material. Grafting of stimuli-responsive polymers not only changes the wettability of the material, but also endows the material with changeable pore size due to collapse and stretching of the polymer chains. This dual effect is worthy of further exploration.

2.3.2 Adsorption of heavy metal ions

Heavy metal ions can affect the normal physiological functions of organisms due to their high toxicity and bioaccumulation [82], hence they have been considered as a serious environmental threat. Thus, their removal from water is attracting swiftly growing attention. CPM have become a very promising platform to tackle this problem [83]. Chemical modification is an efficient way to improve their adsorption properties and make them particularly useful for the treatment of heavy metal pollution. Although research of functional CPM in the field of heavy metal ion adsorption is extensive, the reusability of the materials is still a significant problem. Adsorbed heavy metal ions need to be removed from the cellulosic matrix using a stronger chelating agent or acid solution.

A CNF aerogel, grafted with the dendrimer poly(amidoamine) (PAMAM) by repeating two reactions (Michael addition of methyl acrylate to amine groups on the surface, and amidation of terminal ester groups with ethylenediamine), was synthesized by the group of Lu (**Figure 2.3A**) [84]. The PAMAM-*g*-CNFs obtained were transformed into aerogels *via* the freeze-drying method. The resulting aerogels contained abundant functional groups for removing Cr(VI) with a maximum removal capacity up to 380 mg g^{-1} (**Figure 2.3B**). Importantly, part of the Cr(VI) ions was reduced to Cr(III) during the adsorption process, contributing to further decrease of the toxicity [84].

In our group, we have developed a chemical crosslinking method for preparing CNF-supported cryogels joined up using γ-glycidoxypropyltrimethoxysilane (GPTMS) and branched polyethyleneimine (PEI) [19]. The cryogels proved to be efficient for removing Cu (II) from aqueous solutions with a maximum uptake of 138 mg g^{-1}. The cryogels remained stable in water and retained up to 75% adsorption capacity after four adsorption-desorption cycles.

Thiol containing groups are also capable of efficiently holding/grasping heavy metal ions. Thiol-functionalized cellulose sponges can be conveniently synthesized by reacting 2,2,6,6-tetramethylpiperidine-1-oxyl (TEMPO) oxidized cellulose nanofibrils (TO-CNF) with (3-mercaptopropyl)-trimethoxysilane [23]. The sponges were used to selectively adsorb Hg(II) with an excellent adsorption capacity of up to 700 mg g^{-1}.

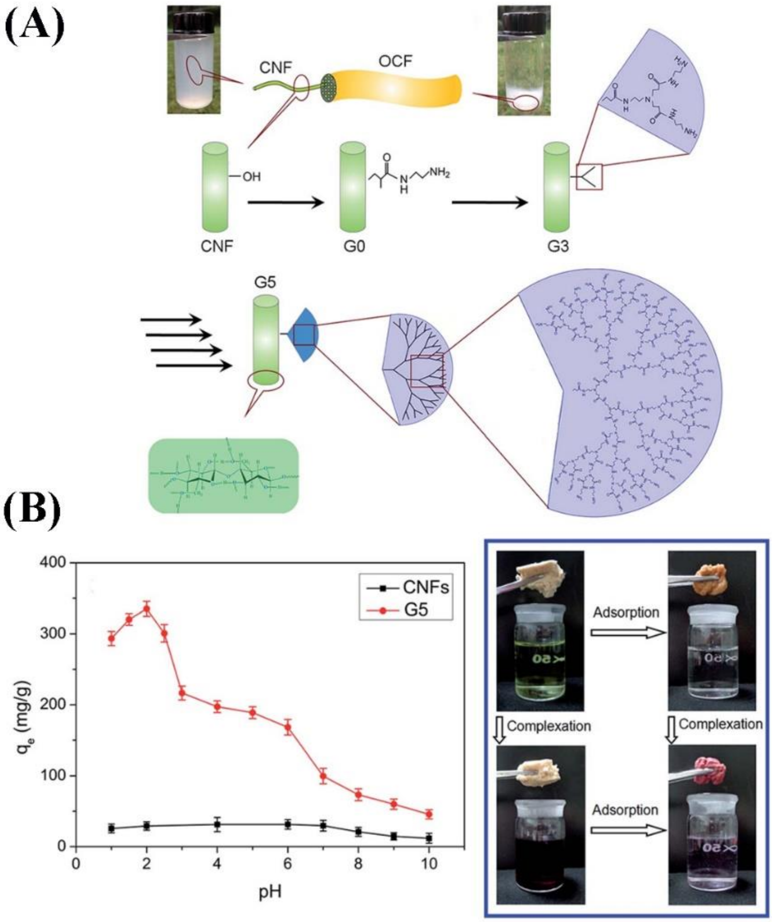

Figure 2.3 (A) The schematic of the synthesis of PAMAM-g-CNFs, G5 was the modified CNF prepared by repeating two reactions (Michael addition of methyl acrylate to amine groups on the surface, and amidation of terminal ester groups with ethylenediamine) for 5 times. (B) Effect of pH on Cr(VI) adsorption (q_e, expressed in mg/g) of pure CNFs and G5, and photographs of the Cr(VI) solution before and after adsorption using G5 [84].

Another study aiming at removing heavy metals and other contaminants uses a robust bulk aerogel, prepared from the carboxylated CNF. These aerogels had strong coagulation-flocculation ability (87.1%), high adsorption capacity for MB removal (up to approximately130 mg g^{-1}), and a moderate Cu^{2+} adsorption capacity (45 mg g^{-1}). These high adsorption capacity values were due to a combined mechanism of charge neutralization, a network capture effect, and chain bridging of the high aspect ratio carboxylated CNF [85].

Table 2.2 Functional cellulosic porous materials for adsorption of metal ions.

Materials	**Functionalization**	**Ion species** $^{\text{Ref.}}$
CNFs	Poly (amidoamine)	Cr(VI) [84]
CNFs	Polyvinyl alcohol and acrylic acid	Cu(II) and Pb(II) [86]
CNFs	Polyvinyl alcohol	Pb(II) and Hg(II) [87]
CNFs	PEI	Cu(II) and Pb(II) [88]
CNFs	PEI	Cu(II) [19]
CNFs	PEI and polydopamine	Cu(II) [89]
CNFs	Poly (methacrylic acid-*co*-maleic acid)	Pb(II), Cd(II), Zn(II) and Ni(II) [90]
Carboxymethylated CNFs	Polyurethane	Cu(II), Cd(II), and Pb(II) [91]
TEMPO oxidized CNFs	3-Mercaptopropyltrimethoxysilane	Hg(II) [92]
TEMPO-oxidized cellulose	Branched PEI	Cu(II), Co(II), Ni(II), Cd(II) [93]
Waste ginger fibers	Carboxylated CNF	Cu(II) [85]
CNCs	ZIF-8, UiO-66 and MIL-100(Fe))	Cr(VI) [94]
CNCs	Reduced graphene oxide	Cu(II) and Cd(II) [95]
BC	ZIF-8 and UiO-66	Pb(II) [96]
Microcrystalline cellulose	Mesoporous carbon	Cr(VI) [97]
Cellulose in NaOH/urea	ZIF-8	Cr(IV) [98]
Cellulose in NaOH/urea	Chitosan	Cu(II) [99]
Cellulose in NaOH/urea	UiO-66 and UiO-66-NH_2	Pb(II) and Cu(II) [100]
Cellulose in ionic liquid	Chitosan	Cu(II) [101]

* MIL-100(Fe): Material Institute de Lavoisier-100(Fe); UiO-66: University of Oslo-66; ZIF-8: zeolitic imidazolate framework-8

Table 2.2 summarizes recent studies on functional cellulosic porous absorbents, illustrating the widespread applicability of MOFs as modifiers. As a representative example, a hybrid aerogel was reported, obtained by a facile sol-gel process [94]. Three MOF types, namely the ZIF-8, UiO-66, and MIL-100 (Fe) systems, were synthesized and incorporated into cellulosic aerogels (**Figure 2.4A**). Loading of 50 wt.% UiO-66 enables the aerogel to adsorb 85% of the Cr(VI) after 24 h. Moreover, the aerogel showed a good underwater shape recovery property (**Figure 2.4B**). Hybrid aerogels with ZIF-8 and MIL-100 also showed a high adsorption capacity for hazardous organics including benzotriazole and Rhodamine B. It is important to note that no MOF particles were discharged during the adsorption processes.

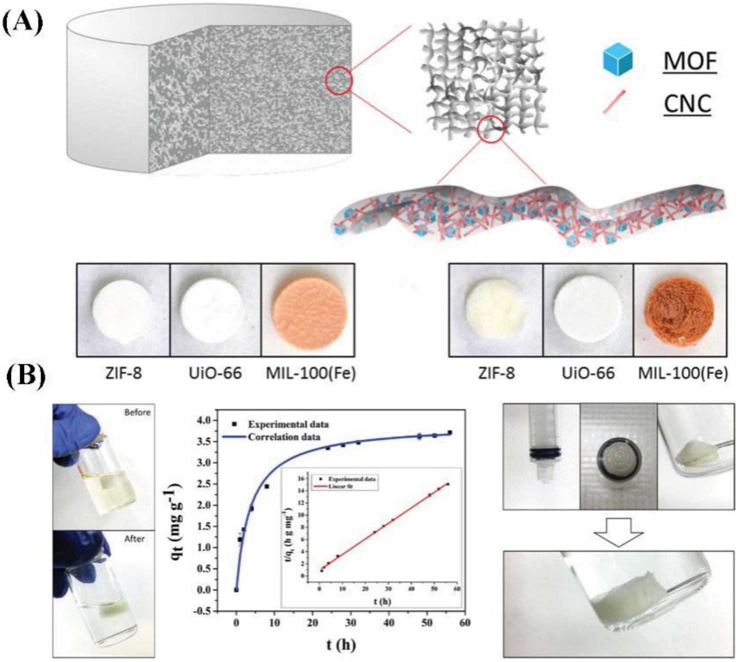

Figure 2.4 (A) Schematic of MOF-cellulose hybrid aerogel and photographs of the hybrid aerogels. (B) Photographs of the contaminated aqueous solution before and after adsorbing Cr(VI) by the aerogel. In the middle, adsorption as a function of time is captured (inset shows a pseudo-second-order fit of adsorption as a function of time, X axis is t (h), Y axis is t/q_t ($h \cdot g \cdot mg^{-1}$)). Photographs on the right show that a wet hybrid aerogel (50 wt.% UiO-66) can be incorporated into a syringe and compressed fully by the piston [94].

2.3.3 Catalyst supports

Adequate support for metallic nanoparticles is very important for maximizing catalytic efficiency and recyclability. One approach to facilitate this includes the use of porous materials as a reaction medium. While applications of CPM in this area have high promise, their use has also significant challenges. The facile preparation and modification, the open-cell structure and large surface area, the superior environmental friendliness, the broad availability, and the good stability of CPM are properties that make these systems useful as catalyst supports [102]. However, CPM as catalyst supports have limitations under strong acidic or basic conditions. Also, the catalyst-loaded cellulosic porous material can only be used under mild agitation conditions, because its skeleton strength is insufficient to satisfy the conditions of strong agitation.

We have, for example, described an *in situ* strategy to firmly immobilize Pd nanoparticles on cellulose sponges (Pd NPs@CS) [25]. The resulting sponges were used in catalyzing Suzuki and Heck cross-coupling reactions. Excellent yields were obtained for all the reactants examined. The porous Pd NPs@CS produced could be easily taken out and reused. The activity and the chemical contents of the catalyst could be maintained up to seven reaction cycles.

In a recent study, a thermo-responsive catalyst support was prepared by grafting poly(*N*-isopropylacrylamide)-*co*-poly(glycidyl methacrylate) (PNIPAM-*co*-PGM) to a cellulose sponge [27]. Au nanoparticles (Au NPs) were immobilized *via in situ* reduction of $HAuCl_4$ with polydopamine (PDA). A controllable reaction could be achieved due to a decreased reaction rate at temperatures above the lower critical solution temperature (LCST) of the polymer. The sponge could be easily separated and reused up to 22 cycles.

A thiol-functionalized cellulose sponge was used as a support to immobilize copper cations *via in situ* Cu(II) to Cu(I) reduction and complexation [26]. Excellent conversion and regioselectivity were achieved in catalyzing hydroboration of alkynes. The sponge-supported catalysts had a broad scope for different substrates, and retained 93% activity after six catalytic cycles.

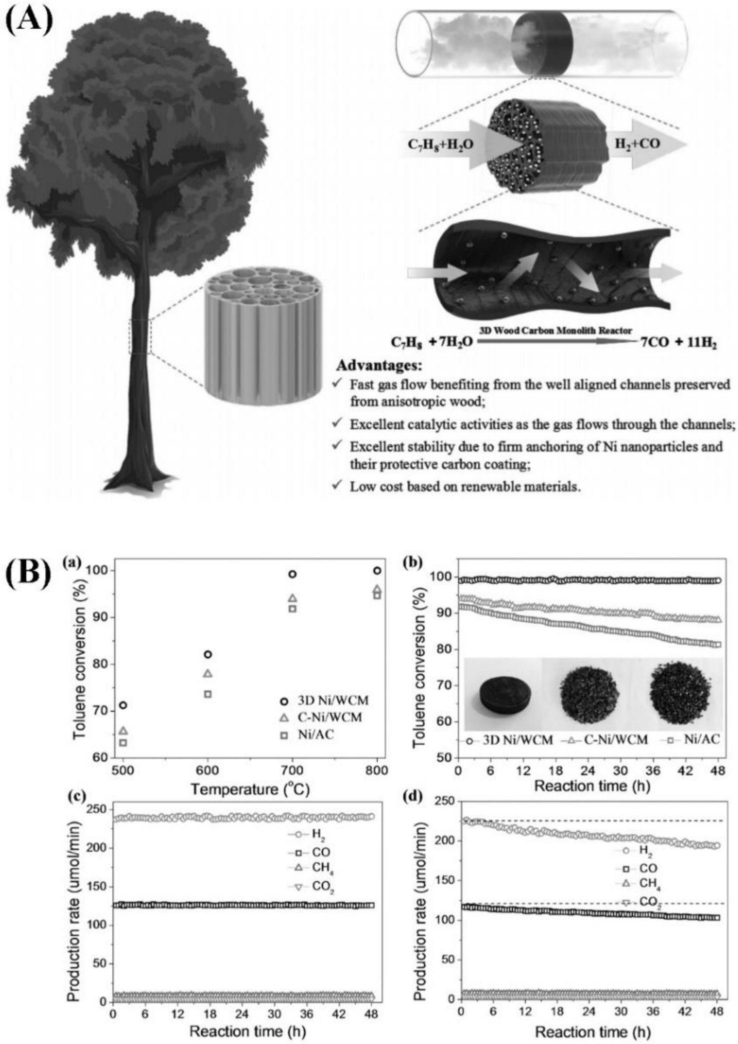

Figure 2.5 (A) Wood has a microstructure exhibiting channels in the growth direction, which are preserved after carbonization. Ni nanoparticle decorated 3D wood carbon can function effectively as a high-temperature reactor due to its aligned channels. (B) Effect of reaction temperature on toluene conversion (a) and catalytic stability (b) of Ni nanoparticle decorated 3D wood carbon monolith (3D Bi/WCM), crushed Ni/wood carbon monolith (C–Ni/WCM) and Ni/activated carbon (Ni/AC); production rates of H_2, CO, CH_4, and CO_2 versus time for the 3D Ni/WCM (c) and Ni/AC (d) [104].

Using cost effective 3D carbon monoliths as support for metallic nanoparticles is a convenient and promising way to reach highly efficient catalysis [103]. As a representative example, we mention that Ni nanoparticle decorated 3D wood-derived carbon was synthesized and reported by Hu and co-workers (**Figure 2.5A**) [104]. The 3D wood-derived carbon inherited the mesoporous structures with continuous channels that allow effective gas flow while maintaining high reactivity for the Ni catalyst anchored to the walls. The 3D catalyst-decorated wood carbon system was significantly better performing than its crushed counterpart and traditional Ni/activated carbon catalysts (**Figure 2.5B**).

2.3.4 Air filtration

Air pollution is a significant environmental concern nowadays resulting from human activities, such as industrial production and transportation [105-106]. The components of the pollutants include noxious chemicals and particulate matter (PM), of which particles with sizes less than 2.5 μm ($PM_{2.5}$), are particularly harmful. These particles can stay in the atmosphere for a prolonged time, readily triggering allergy, respiratory disease, and even cancer [107]. Many studies have focused on employing CPM to filter out such PM particles.

Combatting air pollution is elucidated in a representative study utilizing porous air filters based on CPM. In this work, high efficiency filters were prepared using high fibrillation surface wood pulps by freeze drying [108]. The influence of pulp type, beating time, and the freezing process on the structure and filtration performance of cellulose porous air filters were then investigated. The results showed that a high-density layer would form on the side farthest from the cold plate during the freezing process leading to reduced permeability. A filter satisfying the N95 standard was produced using anionic polyacrylamide addition and a softwood Kraft pulp.

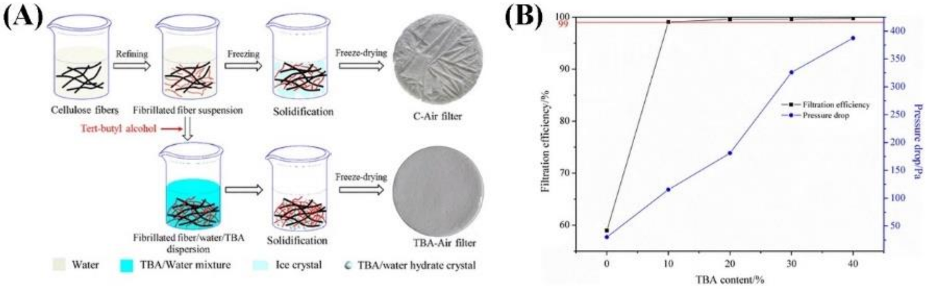

Figure 2.6 (A) Schematic diagram of the preparation procedure of cellulose-based air filters. (B) Filtration efficiency and pressure drop of produced air filters as a function of TBA content [109].

A porous air filter made from CPM with a spider-web-like structure based on fibrillated cellulose fibers by adding *tert*-butyl alcohol (TBA) was reported by Zhang et al (**Figure 2.6A**). The spider-web-like structures not only increased the specific surface area but also enhanced the physical interception capacity between PM matter and fibrillated structures. The filtration efficiency for removing $PM_{0.3}$ particles (of which particles were also included with sizes less than 0.3 μm) could, as a result, exceed 99% with pressure drop values of about 120 Pa (**Figure 2.6B**) [109]. These authors also prepared cellulosic porous air filters by combining fibrillated cellulose fibers with several different MOFs. The results revealed that these materials had a sufficient efficiency for removing $PM_{0.3}$ particles due to the incorporation of MOFs, which increased the specific surface area, strengthened the interactions, and provided abundant cavities and gas adsorption sites for filtering [110-112].

2.3.5 EMI shielding

Electromagnetic pollution is a rising public concern due to the extensive use of electronic devices, which interfere with instruments and can even affect human health [113-115]. CPM are regarded as a matrix to produce EMI shielding materials. This application has been elucidated in numerous articles, as described below.

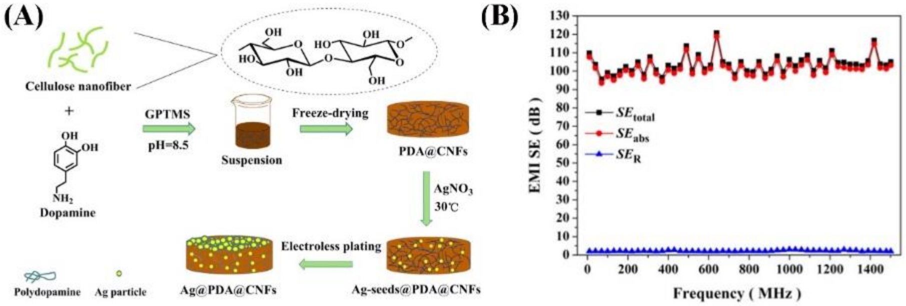

Figure 2.7 (A) Schematic illustration of the synthetic procedures of polydopamine/Ag-modified cellulose composite sponges (Ag@PDA@CNFs). (B) SE_{total}, SE_{R}, SE_{A} curves of Ag@PDA@CNFs with electroless plating time 120 min as a function of frequency [28].

In the Sui group, polydopamine/Ag-modified cellulose composite sponges were prepared (**Figure 2.7A**). The firm and uniform Ag coating was introduced *via* the electroless plating method. The resulting sponge showed high conductivity without breaking up the porous structure. In addition, the obtained composite cellulosic sponge exhibited the highest SE_{total} value of 120.85 dB at 639 MHz and thus showed great potential in effective EMI shielding (**Figure 2.7B**) [28].

We draw attention to another study, which reported on a series of cellulose-derived carbon aerogels that were obtained by Li et al. Their materials featured multi-walled carbon nanotubes (MWCNTs) [116], graphene oxide (GO) [117], and goethite (α-FeOOH) nanoneedles and nanoflowers [118], all of which showed good electrical conductivity and absorption-dominant EMI shielding effects. Among them, GO decorated cellulose aerogels had the best total EMI shielding ability SE_{total} having the value of 58.4 dB at 8.2-12.4 GHz.

2.3.6 Carbon dioxide (CO_2) capture

Porous adsorbents that can capture CO_2 from a flue gas mixture or from the environment to treat anthropogenic CO_2 emissions, are attracting more and more attention in human efforts to reduce global warming [119-123]. CPM with positively charged surfaces show high selectivity toward CO_2 [124-125].

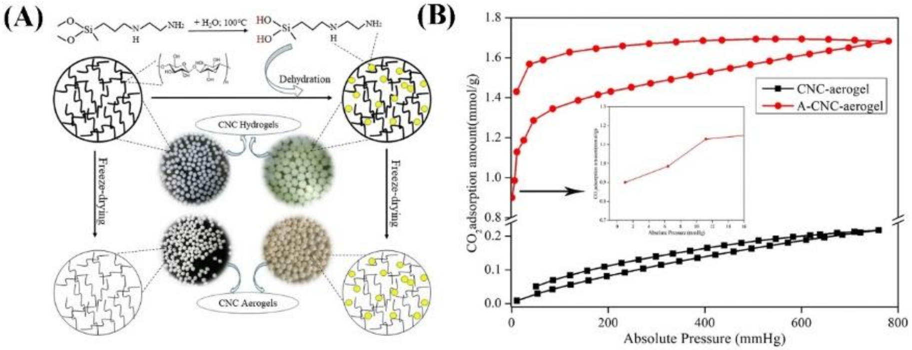

Figure 2.8 (A) Description of the reaction mechanism and the display of the CNC aerogels. (B) The CO_2 absorption and desorption curves of CNC-aerogel and AEAPMDS modified CNC aerogel (ACNC-aerogel) (inset shows the CO_2 absorption curve of ACNC-aerogel in low absolute pressure) [126].

Amino groups are common functionalities to modify CPM for CO_2 capture. Aminosilanes react readily with CPM, resulting in both enhanced mechanical properties and abundant incorporation of amino groups. CNC-based aerogels with high concentration of amine functionalities were successfully introduced *via* reactions with *N*-(2-aminoethyl)(3-aminopropyl) methyldimethoxysilane (AEAPMDS) (**Figure 2.8A**). Due to the presence of chemisorption, the amount of CO_2 adsorbed by the modified aerogel at a pressure of 3 bar (2.63 mmol g^{-1}) was greatly improved compared with the unmodified aerogel (0.26 mmol g^{-1}) (**Figure 2.8B**) [126-127].

In another study, Steinfeld et al. prepared a CO_2 adsorbent through freeze-drying of an aqueous suspension of NFC and AEAPDMS. The adsorption capacity was up to 1.39 mmol CO_2 g^{-1} at 12 h, at a CO_2 concentration of 506 ppm in air and a relative humidity of 40% at 25°C. Stability was examined for up to 20 consecutive 2-h-adsorption/1-h-desorption cycles, keeping a cyclic capacity of 0.695 mmol CO_2 g^{-1} [128]. The difference between this study and previously mentioned examples is that while using the same silane compound, these authors utilized CNF as opposed to CNC.

The effects of amine loading on the CO_2 adsorption capacity of the functional CNF/aminosilane aerogels were also discussed[129]. The high amine loading resulted in a rough aerogel surface, a relatively large average pore size and a high adsorption capacity. The highest adsorption capacity could reach 1.91 mmol g^{-1} (25°C, 1 bar), and could be easily regenerated by heating at 80 °C [130].

Zimmermann et al. employed PEI as alternative to aminosilanes for the functionalization of CNF derived sorbents [131]. The influence of PEI content and relative humidity (RH) on capture capacity and sorbent stability under atmospheric conditions (moist air with ~400 ppm of CO_2) were further explored. The optimum CO_2 capacity was 2.22 mmol g^{-1} with a PEI content of 44 wt.% at 80% RH. We mention that it is difficult to compare the values of CO_2 adsorption capacity reported by the different authors, as the conditions used to determine these were different. For a concerted approach, agreements to obtain adsorption data under the same conditions would be desirable.

2.4 Energy applications

The rapid worldwide growth of energy consumption stimulates researchers to develop advanced, low-cost, and environmentally friendly energy storage materials and thermal insulation materials [132]. Major challenges in this regard include (a) cost reduction of production and devices used, (b) the flexibility of the devices, (c) the utilization of green and abundantly available raw materials, and (d) the environmentally friendly processing and recyclability [133-134]. Among the numerous materials, cellulose-based materials have gained great attention as components of energy storage systems and thermal insulation systems [135-148]. In this section, CPM for supercapacitors, ion-infused batteries, and thermal insulation materials will be reviewed.

2.4.1 Supercapacitors (SCs)

Supercapacitors are electrical energy storage devices that are gaining in popularity due to the cycle efficiency, high capacitance, high power density, and good cyclability [149-

[154]. CPM are very promising substrates for fabricating SCs due to their flexibility and usability. When CPM is combined with a conductive material, the abundant pore structure would facilitate the transport of ions or electrolytes.

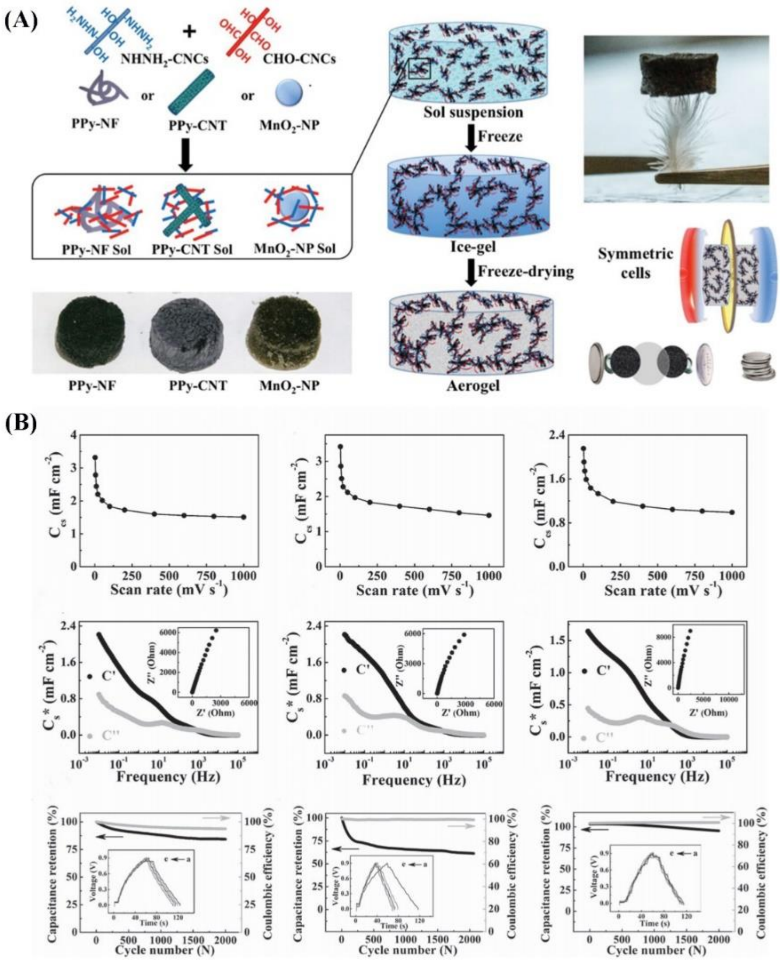

Figure 2.9 (A) Schematic representation of the aerogel components, including functionalized CNCs and capacitive nanoparticles which form the initial suspension of cross-linked clusters in supercapacitors. (B) Capacitive performance *vs* scan rate and frequency (insets show Nyquist plots of complex impedance, X axis is Z’ (Ohm), Y axis is Z” (Ohm)), as well as retention of the capacitive performance (insets show charge-discharge curves for 1st, 500th, 1000th, 1500th, and 2000th cycle from a to e, X axis is Time (s), Y axis is Voltage (V)), for symmetric supercapacitor cells containing hybrid CNC aerogels with PPy-NF (left), PPy-CNT (mid), and MnO_2-NP (right) [155].

Capacitive nanomaterials, such as polypyrrole nanofibers (PPy-NFs), polypyrrole-coated carbon nanotubes (PPy-CNTs), and spherical manganese dioxide nanoparticles (MnO_2-NPs) could be incorporated into cellulose aerogel structures (**Figure 2.9A**). The resulting capacitive hybrid materials have a large accessible surface area for optimum charge storage [155]. Excellent capacitance retention at high charge-discharge rates could be achieved due to the high mass ratio of the active component with respect to the total electrode mass. Multiple channels provide numerous paths for diffusion of charge carriers, resulting in lower internal resistance. The operational data is shown in **Figure 2.9B**, as presented in ref.[155].

In another study, PPy was *in situ* polymerized in an aerogel composed of crosslinked CNCs and MWCNTs [156]. With a mass loading of 17.8 mg cm^{-2} and PPy to current collector mass ratio of 0.57, a single-electrode areal capacitance of 2.1 F cm^{-2} was obtained. Large area electrodes and devices reported in this study showed flexibility, compression stability, and electrochemical cyclic stability. Meanwhile, good retention of capacitive properties was achieved at high charge-discharge rates and during compression cycling.

As a noteworthy development, Yu and co-workers reported the supramolecular self-assembly of 3D lightweight nanocellulose aerogels prepared from carboxylated ginger CNFs and polyaniline (PANI). The supercapacitors prepared from the flexible supramolecular aerogel exhibited a high normalized capacitance (C_m) of around 200 F g^{-1} [157].

Layer-by-Layer (LbL) assembly of charged polyions is a generic technique used for surface coating to obtain functional materials [158-161]. The simplicity of repeatedly immersing substrates into the receptacle containing solutions, and easy incorporation of functional groups within the multilayers, are among the chief advantages of this technology [162]. LbL assembly was also employed in combination with CPM. For example, LbL of conductive polymers and nanoparticles was used to obtain conductive thin films on negatively charged carboxymethylated CNF aerogels [163]. LbL coatings of poly (3,4-ethylenedioxythiophene): poly(styrene sulfonate) (PEDOT: PSS) and single-wall carbon nanotubes (SWCNT) onto the CNF aerogels yielded an electrical conductivity value of 1.4×10^{-5} S cm^{-1} with 10 bilayers. These SWCNT/CNF aerogels were used as electrodes in a supercapacitor with a capacitance estimated to have values up to 420 F g^{-1}.

Another strategy of exploiting CPM in SCs is based on carbonization of cellulose [164-166]. Due to the good conductivity and stability, porous carbon materials have a great potential to fabricate SCs electrodes [167-171]. Porous carbon scaffolds used as electrodes showed improved mechanical and thermal conductivity properties, in particular when combined with graphene flakes. The specific capacitance of the hierarchical porous graphene carbon-based supercapacitors was at the level of 300 F g^{-1} in 6 M KOH solution with an energy density of 67 W h kg^{-1} [172]. BC could be used as both template and precursor for the synthesis of nitrogen-doped carbon networks through carbonization of PANI that was employed as coating. The as-assembled asymmetric supercapacitor exhibits a considerably high energy density of 63 W h kg^{-1} in a 1.0 M Na_2SO_4 aqueous solution. More importantly, this asymmetric supercapacitor possesses good cycling performance with 92% specific capacitance retention after 5000 cycles [173].

Yu's group further developed 3D P-doped, N, P-co-doped, and B, P-co-doped carbon nanofiber networks, which were fabricated by pyrolysis of BC immersed in H_3PO_4, $NH_4H_2PO_4$, and H_3BO_3/H_3PO_4 aqueous solution, respectively. The as-prepared N, P-co-doped carbon nanofiber was used as electrode material for high-performance supercapacitors with a maximum specific supercapacitance of 204.9 F g^{-1} in a 2.0 M H_2SO_4 aqueous electrolyte [174].

2.4.2 Ion infused batteries

Rechargeable batteries are favored energy storage systems for the integration of renewable energy power sources [175-176]. The flexibility originating from the entangled networks of CPM strongly promotes their use in wearable devices. Capacity and longevity, the important parameters of batteries and supercapacitors, have been and will continue to be the focus of works in the field.

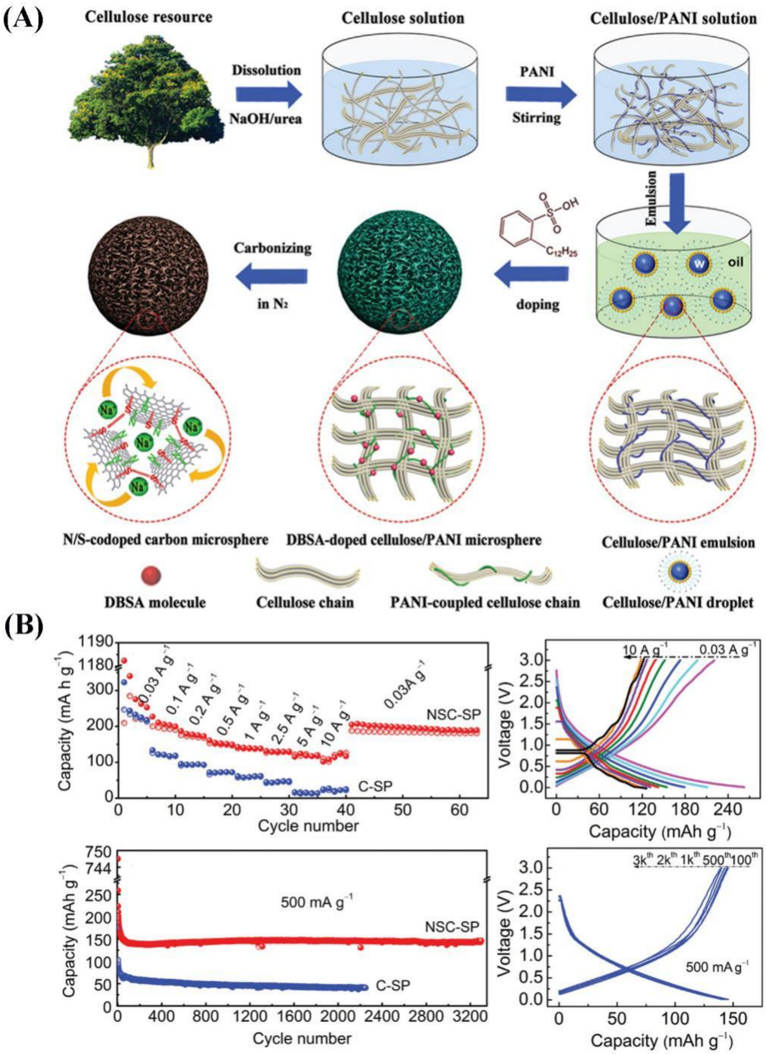

Figure 2.10 Preparation and performance of ion-infused batteries. (A) Schematic of the formation process of N/S co-doped carbon microspheres. (B) Electrochemical sodium storage performance for undoped carbon microsphere (C-SP) and N/S co-doped carbon microspheres (NSC-SP) electrodes [177].

As a first example for a high-performance battery, we draw attention to a study describing a N/S-co-doped carbon anode containing device. The anode material used was fabricated from regenerated cellulose/polyaniline microspheres (**Figure 2.10A**), which exhibited a hierarchical structure [177]. The co-dopant nitrogen and sulfur heteroatoms donated by PANI and dodecyl benzene sulfonic acid, respectively, induced defects and expanded the interlayers and hierarchical micro- and nanostructure of the carbon framework. The anode exhibited a capacity of around 280 mA h g^{-1} at 30 mA g^{-1} and a cycle life of more than 3000 cycles. Due to dual action diffusion and capacitively controlled Na-storage mechanisms, the discharge curves of NSC-SP showed only gently-sloping lines with variable tilt (**Figure 2.10B**).

BC was exploited as a template to construct a hybrid electrolyte from $Li_7La_3Zr_2O_{12}$ (LLZO) and poly(ethylene oxide). The well-organized LLZO network employed in this cited study significantly enhances the ionic conductivity to 1.12×10^{-4} S cm^{-1} by extending the transport pathways for the Li ions [178]. A N-CNF aerogel by direct pyrolysis of BC followed by NH_3 activation was further developed by Yu and co-workers. The resultant aerogel was used as a cathode catalyst for constructing the air electrode of Zn-air battery, it exhibited high voltages of 1.34 and 1.25 V at the discharge current densities of 1.0 and 10 mA cm^{-2}, respectively. These values are comparable to the state-of-the art Pt/C catalyst indicating great application potential and room for further development [179].

BC derived carbon nanofiber aerogels decorated with nano-Fe_3O_4 were used for high-performance flexible and binder-free lithium-ion battery anodes [180]. The BC aerogel was immersed in an aqueous solution of $Fe(NO_3)_3 \cdot 9H_2O$ to allow incorporation of Fe ions onto the BC nanofibers *via* chemisorption and electroadsorption. The Fe_2O_3-BC obtained in this study was carbonized to form Fe_3O_4-BC-nanofibers. The so obtained nanofiber electrodes can reach a reversible capacity of approximately 750 mA h g^{-1} (after 100 cycles at 100 mA g^{-1}). This excellent electrochemical performance is ascribed to the highly dispersed Fe_3O_4 nanoparticles, the large surface area and the interconnected porous structure.

Sulfur exhibits significantly higher theoretical specific capacity and energy density than traditional Li batteries [181]. Thus flexible cathodes with high sulfur content (up to 81 wt.%) and multifunctional interlayers based on carbonized BC were developed for advanced Li-S batteries [182]. The carbonized BC interlayer provided an extra conductive framework and adsorbed migrating polysulfides to a certain degree, thus preventing the over-aggregation of sulfur on the cathode surface by acting as an additional collector for sulfur. Thus, a high-capacity of 1134 mA h g^{-1} at 200 mA g^{-1} current density and long-term cycle stability (700 mA h per g_{Sul} at 400 mA g^{-1} over 400 cycles) were achieved.

Until this point, we discussed active energy supply applications. We note that some related issues have been included in the review by Wu et al. describing 3D networks of cellulose-based energy storage devices and emerging new areas for use [135]. We add that our review has a clear focus on CPM while Wu et al. discuss cellulose in general. Next, we turn our attention to passive energy saving areas, as well as thermal insulation and fire-resistant materials.

2.4.3 Thermal insulation and fire-resistance

An effective way to control the energy efficiency of buildings and reduce conductive heat loss can be achieved by decreased thermal conductivity (λ) using porous materials. Most porous materials currently employed to this purpose, such as expanded polystyrene and polyurethane, are prepared from petrochemicals. Efficient thermally insulating materials based on renewable resources are needed to meet the market demand in an environmentally friendly way [183].

A key parameter to enhance thermal insulation is the cell size of the porous materials employed. Smaller pore size and higher specific surface area would facilitate the inclusion of more air in the porous matrix, leading to lower thermal conductivity. Additionally, when the pore size becomes smaller than the collision mean free path of gas molecules captured within them, further reduction of thermal conductivity can be achieved due to the so-called Knudsen effect [183].

As a milestone on the road of achieving low thermal conductivity and maintaining mechanical performance, nanocellulose and other nanomaterials, such as graphene oxide (GO) and sepiolite nanorods (SEP), were combined to prepare lightweight (7.5 kg m^{-3}) and highly porous foams (**Figure 2.11A**) [184]. These cellular materials could be obtained with an average pore size of 3 nm according to the analysis of nitrogen gas adsorption isotherms. In comparison, for petroleum-based polymer foams, cell sizes in the sub-micron domain are only rarely reported [183]. Overall, in this passive energy material application area, cellulose-based hybrid nanomaterials showed excellent mechanical performance and combustion resistance (**Figure 2.11B and C**) and exhibited a thermal conductivity of 18 mW m^{-1} K^{-1} in the radial orientation, which a value less than those of the currently used, petroleum-based insulation materials. Furthermore, a thermal conductivity of 15 mW m^{-1} K^{-1} was measured for the nanocomposite foam with 10 wt.% GO and 10 wt.% SEP. The nanosized components contribute to enhance interfacial thermal resistance.

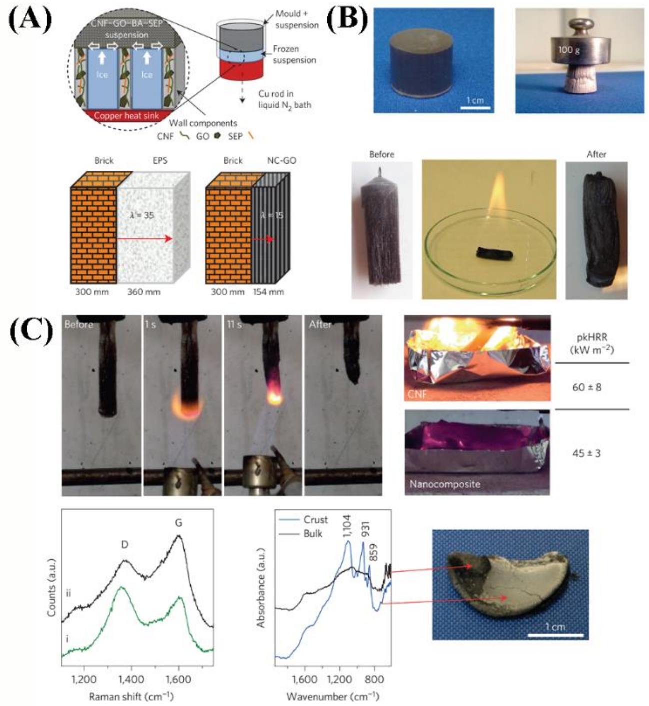

Figure 2.11 (A) Illustration of the freeze-casting process, highlighting the growth of anisotropic ice crystals surrounded by walls of the dispersed nanoparticles, and schematic illustration of the thickness of expanded polystyrene (EPS) and an optimized nanocomposite foam needed for house insulation. (B) Photograph and overview of the mechanical, thermal and fire-retardant properties of nanocomposite foams. (C) Flame resistance of nanocomposite foams [184].

Silica aerogels are well-known thermal insulation materials. In spite of their desirable properties, unfortunately their brittleness and lack of processability hamper their widespread application. Using cellulose nanofibers and organic silica to prepare composite aerogels is considered as a promising way to replace silica-based aerogels. In this area, Hayase and coworkers recently developed a polymethylsilsesquioxane-cellulose nanofiber (PMSQ-CNFs) composite aerogel with low thermal conductivity (15 mW m^{-1} K^{-1}) and good bending flexibility [145]. The nanoporous structure (pore size values around 100 nm) of these aerogels was the key to reducing the thermal conductivity [145]. In addition, due to the Knudsen effect related to the small pore size, heat transfer by gas molecule collisions would be essentially eliminated [183]. BC nanofibrillar networks were also used to mitigate the brittleness of silica aerogels. Such reported composite aerogels were flexible and had excellent thermal insulation performance with a low thermal conductivity of 15.3 mW m^{-1} K^{-1} [185].

Highly stable Pickering emulsions using TEMPO-oxidized cellulose nanofibrils (NFC) are also used as template to form super-insulating aerogels. A hierarchical porous morphology of three levels exists in the aerogel: an alveolar organization of larger macro-pores formed *via* ice-crystal templating, smaller spherical macro-pores induced by emulsion templating, and mesoporous domains localized at the pore-wall level. Low thermal conductivities were obtained for these NFC aerogels, namely 18 mW $m^{-1}{\cdot}K^{-1}$ [186].

We have reported on the preparation of cellulose composite sponges with good mechanical, heat-insulating and flame-retardant properties [24]. Simultaneous polymerization of dopamine and hydrolysis of organosilicon in a suspension of microfibrillated cellulose provided good flame retardancy of these composite sponges. The sponges were composed of a 3D cellulosic network and had a thermal conductivity of 46 mW m^{-1} K^{-1}. The limiting oxygen index (LOI) of the sponge was 29.5 with 15 wt.% polydopamine and could self-extinguish immediately when removed from torch.

2.5 Health applications

As a material of biological origin, and due to biocompatibility and non-toxicity, cellulose-based materials have been extensively used in health-care applications [187-192]. Their structure is highly advantageous for promoting wound exudate adsorption and liquid permeability that are required for wound dressing use. The high specific surface area is beneficial for higher drug loading capacity, when used as drug delivery material. As an example, we mention BC, which has been extensively used as a scaffold for cell adhesion and proliferation in regenerative medicine [193]. Pressure sensors are also being developed for health monitoring [194]. The utilization of CPM in the most recently developed self-powered pressure sensor is further discussed in this section.

2.5.1 Wound dressings

Wound dressing greatly reduces the continuous deterioration of body damage and promotes skin restoration. Biocompatibility is a primary and necessary requirement for wound dressing applications. High fluid absorption capacity is also needed so that wound exudates can be absorbed fast to reduce the risk of infection. Proper moist environment, provided by the wound dressing, is needed to facilitate healing. Wound dressing needs to be able to block the invasion of bacteria, or should have antimicrobial activity to suppress microbial growth. Non-stickiness is also a specific requirement to avoid secondary damage to the wound when the dressing is removed [191, 195].

As the first example, we mention a study of basic fibroblast growth factor immobilized in a cellulose/gelatin sponge, which has excellent skin repairing ability [196]. In particular, the complete wound healing time treated with the sponges was faster than those treated with gauze for the full-thickness wound model. The thin-walled pores in the sponges played an important role and successfully met the requirements for oxygen permeability, controlled water vapor evaporation and wound exudate adsorption. Recently, the same group reported CNFs/quaternized chitin/organic rectorite (BACNF/QCR) composite sponges prepared for wound dressing. In a rat tail amputation test, the BACNF/QCR sponges rapidly induced hemostasis and could substantially promote collagen synthesis and neovascularization, thereby shortened the wound healing by 3 days compared to gauze [197].

A TEMPO-oxidized cellulose nanofiber (TOCN)-silk fibroin scaffold reported by Lee and co-workers, was shown to facilitate growth of L929 primary fibroblast cells in *in vitro* studies. *In vivo* evaluation using a critical sized rat skin excisional model revealed that the silk fibroin therein was critical for promoting wound healing [198].

The Sui group reported on the preparation of cellulose-chitosan hybrid sponges (CGC sponges) with controllable structure and morphologies using CNF, GPTMS and CS (**Figure 2.12A**) [20]. The CGC sponges with low blood clotting index were non-toxic and outperformed silicon in promoting blood coagulation according to the experiments, especially in high chitosan content (**Figure 2.12B**). The superior hemostatic property, shape recovery property, safety and non-cytotoxicity of the sponges make them ideal dressings for use in wounds with vascular diseases (**Figure 2.12C**). Cellulosic sponges with excellent antibacterial performance against *E. coli* and *S. aureus* were also prepared in our group, by initially multi-crosslinking of CNFs, cellulose acetoacetate and APTES, followed by surface modification with gentamicin [30]. Amoxicillin, as common antibacterial and anti-inflammatory drug, was also grafted onto BC sponge [199]. These constructs showed highly effective antibacterial activities against *E. coli, C. albicans*, and *S. aureus*, and were nontoxic. This sponge could also accelerate wound healing. Antibiotic-loaded CPM used in wound dressings greatly reduce the probability of antibiotics entering the body, thus preventing their abuse. However, if used on a wound for a long time, the bacteria will likely develop resistance, which may reduce the therapeutic effect.

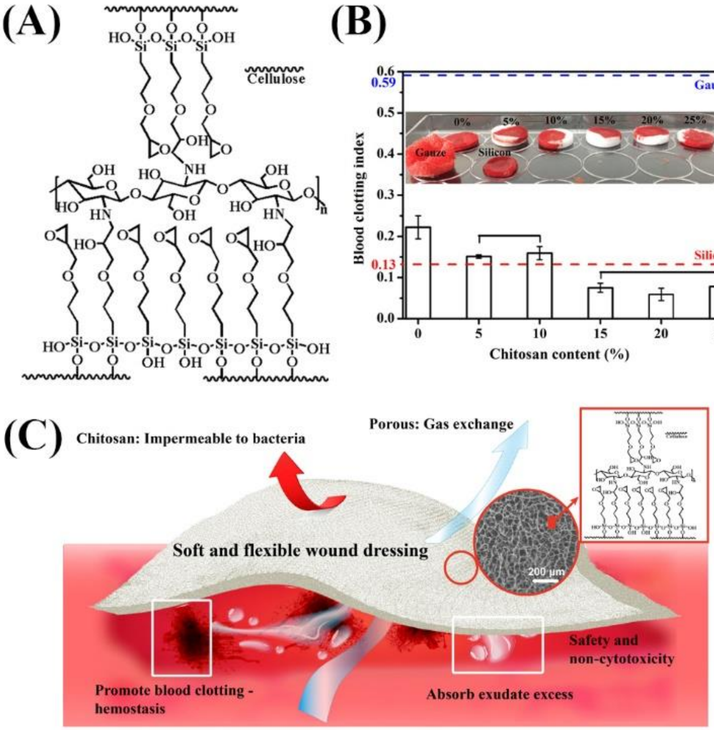

Figure 2.12 (A) Schematic of chemical crosslinking within the cellulose-GPTMS-chitosan (CGC) sponge. (B) Clotting formation capacity of CGC sponges. (C) Illustration showing the mechanism of CGC sponge [20].

2.5.2 Drug delivery

Controlling the release rate and the release profile of drugs, protecting them from physiological degradation, prolonging the action time, and achieving precisely targeted, local treatment have been central issues in biomedical sciences [200]. Porous materials are important encapsulating components for drug delivery vehicles. Cellulose and derivatives are candidates also for this application [201-202].

Chemical modification of CPM can strongly promote controlled delivery. For example, an aerogel prepared from PEI-grafted cellulose nanofibrils (CNFs-PEI) was developed for drug administration [203]. These CNFs-PEI aerogels exhibited a drug loading capability of nearly 300 mg g^{-1} for water-soluble sodium salicylate (NaSA). Drug release experiments demonstrated a sustained and controllable release behavior of these aerogels as a function of pH and temperature. In Melone's work, amoxicillin (AM) and ibuprofen

(IB) were considered as model drugs. The PEI modified TOCNFs aerogels showed good performance in adsorbing both AM and IB (ca. 200 mg g^{-1}) from methanol solution [204]. Sun and co-workers described the development of a PEI-grafted BC aerogel as an efficient drug delivery system. The aerogel exhibited a high loading capacity. Prolonged pH-dependent release of aspirin by the aerogel was also demonstrated [205].

Combination with traditional stimulus responsive materials, such as temperature-sensitive PNIPAm, is also a viable and promising strategy. Zhang et al used PNIPAm to modify cellulose nanofibril cryogel microspheres [206]. Pristine cryogel microspheres were first prepared using a spray-freeze drying method. Then, the cellulose cryogel microspheres were grafted with PNIPAm through *in situ* free radical polymerization. The results of swelling and releasing experiments (5-fluorouracil) indicated controlled release.

2.5.3 Cell culture scaffold

Bio-mimicking the cell microenvironment *in vivo* is a critical objective for successful fabrication of scaffolds in regenerative medicine. A key challenge herein is related to the design and fabrication of highly porous 3D platforms. CPM, possessing high mechanical strength, biocompatibility and a unique porous structure, has recently received distinguished attention as an excellent nanofibrous candidate scaffold for tissue regeneration. Refined 3D nanofibrillar network architectures were reported, which successfully mimicked the native extracellular matrix (ECM) [207-214].

In applications aiming at fabricating scaffolds for regenerative medicine, various surface modifications were carried out on the surface of BC to promote cell adhesion and proliferation [215-219]. As representative examples, we mention the study of Newby et al. that described BCs functionalized by organosilanes to improve the attachment and spreading of normal human dermal fibroblast (NHDF). The surfaces of those dried BCs were chemically modified by grafting APTES. NHDF cells exhibited improved attachment and spreading on the majority of APTES modified BCs with more rapid growth than on tissue culture polystyrene. In tissue engineering, cell adhesion and cell supply (oxygen, nutrients) must be enabled by designer scaffolds [220]. To this end, cell-derived adhesion proteins from fibroblasts were uniformly immobilized in 3D BC. These proteins activate integrin adhesion pathways that generate stronger cell adhesions. The cells that adhered on to modified BC exhibited higher mitochondrial activity and higher cell populations per cubic millimeter than the non-modified surfaces [221]. Sun et al. prepared electroactive and flexible 3D nanostructures based on BC nanofibers and PEDOT. The 3D BC/PEDOT nanostructures possess high specific surface area, excellent mechanical properties, electroactive stability, and low cell cytotoxicity [222].

A frequently employed strategy in regenerative medicine makes use of electrospun fibers to process scaffold materials. Electrospun substrates have high porosity, although this originates from the spinning process. While not strictly a subject of this review, we mention that 3D electrospun CA/pullulan (PULL) scaffolds were developed by Tezcaner et al [212]. Cell culture studies performed using mouse fibroblastic cell line (L929) showed that cells adhered, proliferated and populated CA/PULL (50/50) scaffolds *in vitro*, demonstrating their cytocompatibility.

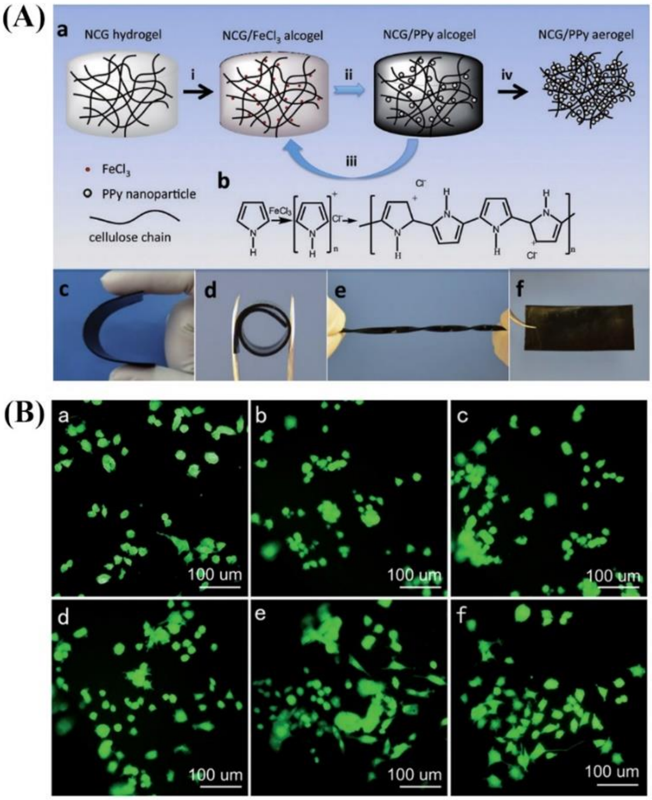

Figure 2.13 (A) Preparation of NCG/PPy composite aerogels. (B) Fluorescence micrographs of PC12 cells cultured on different composite gels after electrical stimulation (a: NCG, b: NCG/PPy-25%, c: NCG/PPy-37%, d:NCG/PPy-57%, e: NCG/PPy-57%-DBSA1, and f: NCG/PPy-57%-DBSA2, DBSA: dodecylbenzenesulfonic acid, DBSA2: doping with DBSA during the final polymerization cycles, DBSA1: doping during each polymerization cycle) [214].

Significant progress was reported by Cai et al. describing a robust, conductive cellulose/polypyrrole (NCG/PPy) composite aerogel. The authors revealed their potential application in nerve regeneration (**Figure 2.13A**) [214]. PC12 cells cultured on these NCG/PPy composites exhibited good adhesion and proliferation *in vitro* (**Figure 2.13B**). Furthermore, the cellular morphologies of PC12 showed a remarkable neuronal phenotype upon doping with dodecylbenzene sulfonic acid under electrical stimulation.

We wish to stress that while there are numerous *in vitro* studies described in the literature, the use of CPM *in vivo* has been hampered by their limited biodegradability.

2.5.4 Medical pressure sensors

Flexible and low-cost pressure sensors are highly desirable in electronic skin, health and sport performance monitoring [223-227]. The performance of pressure sensors is largely influenced by their flexibility and electrical conductivity. Different forms of pressure sensor have been prepared to meet the requirements of ideal sensor devices [228-229].

Carbon nanotubes (CNTs) were the common conductive materials to enhance the electrical conductivity and sensitivity of porous sensors. Qi et al. fabricated a CNT/cellulose composite aerogel by the flash freezing/lyophilization process using wet-gel precursors prepared from homogeneous dispersions of CNTs and cellulose in alkaline–urea aqueous solution [230]. These cellulose/CNT composite systems showed good sensitivity to pressure variations under ambient conditions.

BC fiber was used as a nanobinder to join MXene (Ti_3C_2) nanosheets into continuous and wave-shaped lamellae. The lamellae are highly flexible and elastic, and a carbon aerogel with super compressibility and elasticity could be prepared by alignment. The aerogel could withstand an extremely high strain of 99% for more than 100 cycles and long-term compression at 50% strain for at least 10^6 cycles. Furthermore, the aerogel had a high sensitivity [231].

Electroactive polymers in combination with CPM can be utilized also as pressure sensors. To this end, Wei and co-workers reported compressible and conductive aerogels prepared by incorporating polyaniline (PANI) into BC/chitosan (BC/CH) composites. The PANI/BC/CH aerogel displayed a high resistance response and showed extremely high sensitivity (1.41 kPa^{-1}), low pressure detection (32 Pa), wide range of pressure deformation, and extraordinary stability as a piezoresistive sensor [232].

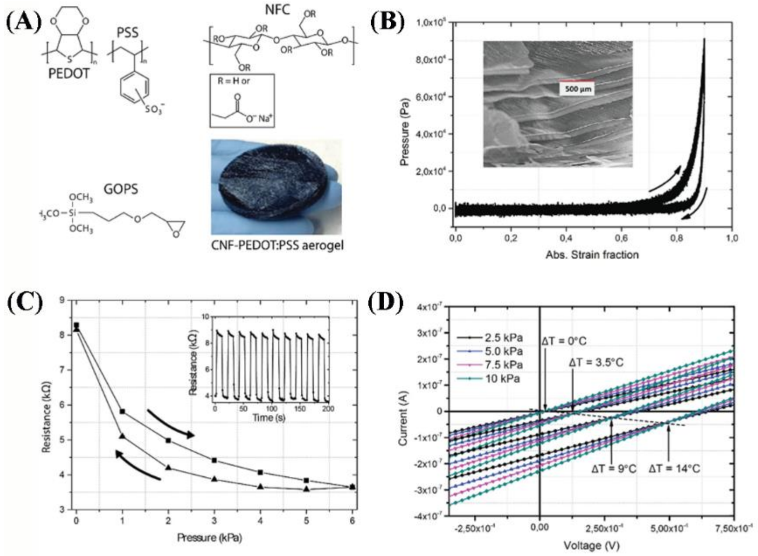

Figure 2.14 (A) The components and photograph, (B) stress-strain curve and morphology, and (C) press-release curve (resistivity *vs* pressure) of CNF aerogels. (D) The I-V curves for the aerogel under various levels of pressures and temperature differences [233].

Thermoelectric (TE) materials can utilize temperature differences to produce electric energy, which could be used in self-powered electronic sensors and devices, and be applied in health monitoring and information collection. CPM with intrinsic low thermal conductivity are considered as desirable and eco-friendly substrates for the fabrication of flexible TE materials [29]. We discuss here a flexible and compressible thermoelectric polymer aerogel as reported by Khan et al [233]. Their material exhibited a thin sheet morphology, prepared from the CNF, glycidoxypropyl trimethoxysilane (GOPS), and employing the conducting polymer PEDOT:PSS (**Figure 2.14A and B**) [233]. The resulting CNF-PEDOT-PSS aerogel had an electrical conductivity of ≈1 mS cm^{-1} and a Seebeck coefficient of around 37 µV K^{-1}. The resistance had a large drop when a small pressure of < 1 kPa was applied (**Figure 2.14C**). Hence, this thermoelectric aerogel can be used as a temperature-pressure dual sensor (**Figure 2.14D**). The same group also reported on a dimethylsulfoxide (DMSO)-treated PEDOT-coated CNF aerogel for independent pressure and temperature sensing [234]. The pressure sensitivity was increased by almost two orders of magnitude after 5 min exposure to DMSO vapor. This enhanced sensitivity provided more accurate pressure monitoring. This is a significant result, as for medical pressure sensors, sensitivity is critical. High sensitivities enable the CPM to detect minute pressure fluctuations, thereby reflecting the state of the subject more accurately.

2.6 Conclusions

Cellulose is abundant, environmentally friendly and biodegradable. This in part justifies the swiftly growing current interest in CPM, propelling this class of materials to the forefront of biopolymer research and related technology transformations. However, the complex preparation process of obtaining functionalized CPM is a large practical burden on high volume applications. Currently, the most efficient strategy to prepare CPM is by freeze-drying and supercritical fluid drying. Owing to methodological limitations (time and energy consumption, high pressure, low temperature), CPM *via* this route cannot be prepared on a large-scale, which restricts their current industrialization and hampers technology development [235]. Efforts to establish drying methods under ambient temperature and pressure are needed to realize large-scale. Further efforts are also required to increase the durability and reduce the cost for the nanoscale fibrillated cellulose based CPM [236]. The field is undergoing swift development and with the growing demand for bio-based materials and environmentally friendly technologies it will likely remain so for the next decades to come.

Although the mechanical properties of bio-based microporous cellulose in some cases are sufficiently high, they are still not comparable with the performance of their synthetic commercial counterparts. Environmental applications of CPM have distinct and clear advantages, but they are still underutilized due to high costs in comparison with synthetic platforms for the same function. CPM have been widely studied in the field of biomaterials *in vitro*, but research on CPM used *in vivo* has been hampered by their limited biodegradability. New approaches in chemical modifications, or physical hybridization bring up novel opportunities for developing unique functional CPM based biomaterials. The chemical modification of CPM has greatly promoted the development of CPM in various fields. However, the novel structural design can still make this material radiate new vitality.

Overall, by designing novel structures and using different functional materials, combining inherent advantages of cellulosic materials and porous structure, the development of functional cellulosic porous materials has a bright prospect in the future development of natural polymers.

2.7 References

(1) Chen, W.; Yu, H.; Lee, S. Y.; Wei, T.; Li, J.; Fan, Z. Nanocellulose: A promising nanomaterial for advanced electrochemical energy storage. *Chemical Society Reviews* **2018,** *47* (8), 2837-2872.
(2) Jiang, S.; Agarwal, S.; Greiner, A. Low-density open cellular sponges as functional materials. *Angewandte Chemie International Edition* **2017,** *56* (49), 15520-15538.
(3) Lavoine, N.; Bergström, L. Nanocellulose-based foams and aerogels: Processing, properties, and applications. *Journal of Materials Chemistry A* **2017,** *5* (31), 16105-16117.
(4) Klemm, D.; Kramer, F.; Moritz, S.; Lindstrom, T.; Ankerfors, M.; Gray, D.; Dorris, A. Nanocelluloses: A new family of nature-based materials. *Angewandte Chemie International Edition* **2011,** *50* (24), 5438-5466.
(5) Klemm, D.; Heublein, B.; Fink, H. P.; Bohn, A. Cellulose: Fascinating biopolymer and sustainable raw material. *Angewandte Chemie International Edition* **2005,** *44* (22), 3358-3393.
(6) Maleki, H. Recent advances in aerogels for environmental remediation applications: A review. *Chemical Engineering Journal* **2016,** *300*, 98-118.
(7) Xue, Y.; Mou, Z.; Xiao, H. Nanocellulose as a sustainable biomass material: Structure, properties, present status and future prospects in biomedical applications. *Nanoscale* **2017,** *9* (39), 14758-14781.
(8) Klemm, D.; Cranston, E. D.; Fischer, D.; Gama, M.; Kedzior, S. A.; Kralisch, D.; Kramer, F.; Kondo, T.; Lindström, T.; Nietzsche, S.; Petzold-Welcke, K.; Rauchfuß, F. Nanocellulose as a natural source for groundbreaking applications in materials science: Today's state. *Materials Today* **2018,** *21* (7), 720-748.
(9) Kontturi, E.; Laaksonen, P.; Linder, M. B.; Nonappa; Groschel, A. H.; Rojas, O. J.; Ikkala, O. Advanced materials through assembly of nanocelluloses. *Advanced Materials* **2018,** *30* (24), 1703779.
(10) Moon, R. J.; Martini, A.; Nairn, J.; Simonsen, J.; Youngblood, J. Cellulose nanomaterials review: Structure, properties and nanocomposites. *Chemical Society Reviews* **2011,** *40* (7), 3941-3994.
(11) Gesser, H. D.; Goswami, P. C. Aerogels and related porous materials. *Chemical Reviews* **1989,** *89*, 765-788.
(12) Ling, S.; Chen, W.; Fan, Y.; Zheng, K.; Jin, K.; Yu, H.; Buehler, M. J.; Kaplan, D. L. Biopolymer nanofibrils: Structure, modeling, preparation, and applications. *Progress in Polymer Science* **2018,** *85*, 1-56.
(13) Kargarzadeh, H.; Huang, J.; Lin, N.; Ahmad, I.; Mariano, M.; Dufresne, A.; Thomas, S.; Gałeski, A. Recent developments in nanocellulose-based biodegradable polymers, thermoplastic polymers, and porous nanocomposites. *Progress in Polymer Science* **2018,** *87*, 197-227.
(14) Wan, C.; Jiao, Y.; Wei, S.; Zhang, L.; Wu, Y.; Li, J. Functional nanocomposites from sustainable regenerated cellulose aerogels: A review. *Chemical Engineering Journal* **2019,** *359*, 459-475.
(15) De France, K. J.; Hoare, T.; Cranston, E. D. Review of hydrogels and aerogels

containing nanocellulose. *Chemistry of Materials* **2017,** *29* (11), 4609-4631.

(16) Zhao, S.; Malfait, W. J.; Guerrero-Alburquerque, N.; Koebel, M. M.; Nystrom, G. Biopolymer aerogels and foams: Chemistry, properties, and applications. *Angewandte Chemie International Edition* **2018,** *57* (26), 7580-7608.

(17) Wang, H.; Chen, Q.; Zhou, S. Carbon-based hybrid nanogels: A synergistic nanoplatform for combined biosensing, bioimaging, and responsive drug delivery. *Chemical Society Reviews* **2018,** *47* (11), 4198-4232.

(18) Olsson, R. T.; Azizi Samir, M. A.; Salazar-Alvarez, G.; Belova, L.; Strom, V.; Berglund, L. A.; Ikkala, O.; Nogues, J.; Gedde, U. W. Making flexible magnetic aerogels and stiff magnetic nanopaper using cellulose nanofibrils as templates. *Nature Nanotechnology* **2010,** *5* (8), 584-588.

(19) Cheng, H.; Li, Y.; Wang, B.; Mao, Z.; Xu, H.; Zhang, L.; Zhong, Y.; Sui, X. Chemical crosslinking reinforced flexible cellulose nanofiber-supported cryogel. *Cellulose* **2017,** *25* (1), 573-582.

(20) Cheng, H.; Li, C.; Jiang, Y.; Wang, B.; Wang, F.; Mao, Z.; Xu, H.; Wang, L.; Sui, X. Facile preparation of polysaccharide-based sponges and their potential application in wound dressing. *Journal of Materials Chemistry B* **2018,** *6* (4), 634-640.

(21) Nge, T. T.; Nogi, M.; Yano, H.; Sugiyama, J. Microstructure and mechanical properties of bacterial cellulose/chitosan porous scaffold. *Cellulose* **2010,** *17* (2), 349-363.

(22) Wu, Z.; Li, Y.; Zhang, L.; Zhong, Y.; Xu, H.; Mao, Z.; Wang, B.; Sui, X. Thiol–ene click reaction on cellulose sponge and its application for oil/water separation. *RSC Advances* **2017,** *7* (33), 20147-20151.

(23) Rong, L.; Zhu, Z.; Wang, B.; Mao, Z.; Xu, H.; Zhang, L.; Zhong, Y.; Sui, X. Facile fabrication of thiol-modified cellulose sponges for adsorption of hg^{2+} from aqueous solutions. *Cellulose* **2018,** *25* (5), 3025-3035.

(24) Li, Y.; Wang, B.; Sui, X.; Xu, H.; Zhang, L.; Zhong, Y.; Mao, Z. Facile synthesis of microfibrillated cellulose/organosilicon/polydopamine composite sponges with flame retardant properties. *Cellulose* **2017,** *24* (9), 3815-3823.

(25) Li, Y.; Xu, L.; Xu, B.; Mao, Z.; Xu, H.; Zhong, Y.; Zhang, L.; Wang, B.; Sui, X. Cellulose sponge supported palladium nanoparticles as recyclable cross-coupling catalysts. *ACS Applied Materials & Interfaces* **2017,** *9* (20), 17155-17162.

(26) Zhang, C.; Zhou, M.; Liu, S.; Wang, B.; Mao, Z.; Xu, H.; Zhong, Y.; Zhang, L.; Xu, B.; Sui, X. Copper-loaded nanocellulose sponge as a sustainable catalyst for regioselective hydroboration of alkynes. *Carbohydrate Polymers* **2018,** *191*, 17-24.

(27) Li, Y.; Zhu, L.; Wang, B.; Mao, Z.; Xu, H.; Zhong, Y.; Zhang, L.; Sui, X. Fabrication of thermoresponsive polymer-functionalized cellulose sponges: Flexible porous materials for stimuli-responsive catalytic systems. *ACS Applied Materials & Interfaces* **2018,** *10* (33), 27831-27839.

(28) Wu, L.-P.; Li, Y.-Z.; Wang, B.-J.; Mao, Z.-P.; Xu, H.; Zhong, Y.; Zhang, L.-P.; Sui, X.-F. Electroless ag-plated sponges by tunable deposition onto cellulose-derived templates for ultra-high electromagnetic interference shielding. *Materials and Design* **2018,** *159*, 47-56.

(29) Cheng, H.; Du, Y.; Wang, B.; Mao, Z.; Xu, H.; Zhang, L.; Zhong, Y.; Jiang, W.; Wang, L.; Sui, X. Flexible cellulose-based thermoelectric sponge towards wearable pressure sensor and energy harvesting. *Chemical Engineering Journal* **2018,** *338*, 1-7.

(30) Xiao, Y.; Rong, L.; Wang, B.; Mao, Z.; Xu, H.; Zhong, Y.; Zhang, L.; Sui, X. A light-

weight and high-efficacy antibacterial nanocellulose-based sponge via covalent immobilization of gentamicin. *Carbohydrate Polymers* **2018,** *200*, 595-601.

(31) Rajinipriya, M.; Nagalakshmaiah, M.; Robert, M.; Elkoun, S. Importance of agricultural and industrial waste in the field of nanocellulose and recent industrial developments of wood based nanocellulose: A review. *ACS Sustainable Chemistry & Engineering* **2018,** *6* (3), 2807-2828.

(32) Sharma, P. R.; Joshi, R.; Sharma, S. K.; Hsiao, B. S. A simple approach to prepare carboxycellulose nanofibers from untreated biomass. *Biomacromolecules* **2017,** *18* (8), 2333-2342.

(33) Trache, D.; Hussin, M. H.; Haafiz, M. K.; Thakur, V. K. Recent progress in cellulose nanocrystals: Sources and production. *Nanoscale* **2017,** *9* (5), 1763-1786.

(34) Du, L.; Wang, J.; Zhang, Y.; Qi, C.; Wolcott, M. P.; Yu, Z. Preparation and characterization of cellulose nanocrystals from the bio-ethanol residuals. *Nanomaterials* **2017,** *7* (3), 51.

(35) Jia, X.; Chen, Y.; Shi, C.; Ye, Y.; Wang, P.; Zeng, X.; Wu, T. Preparation and characterization of cellulose regenerated from phosphoric acid. *Journal of Agricultural and Food Chemistry* **2013,** *61* (50), 12405-12414.

(36) Wang, S.; Lu, A.; Zhang, L. Recent advances in regenerated cellulose materials. *Progress in Polymer Science* **2016,** *53*, 169-206.

(37) Long, L.-Y.; Weng, Y.-X.; Wang, Y.-Z. Cellulose aerogels: Synthesis, applications, and prospects. *Polymers* **2018,** *10* (6), 623.

(38) Song, J.; Chen, C.; Yang, Z.; Kuang, Y.; Li, T.; Li, Y.; Huang, H.; Kierzewski, I.; Liu, B.; He, S.; Gao, T.; Yuruker, S. U.; Gong, A.; Yang, B.; Hu, L. Highly compressible, anisotropic aerogel with aligned cellulose nanofibers. *ACS Nano* **2018,** *12* (1), 140-147.

(39) Li, T.; Song, J.; Zhao, X.; Yang, Z.; Pastel, G.; Xu, S.; Jia, C.; Dai, J.; Chen, C.; Gong, A.; Jiang, F.; Yao, Y.; Fan, T.; Yang, B.; Wågberg, L.; Yang, R.; Hu, L. Anisotropic, lightweight, strong, and super thermally insulating nanowood with naturally aligned nanocellulose. *RSC Advances* **2018,** *4*, eaar3724.

(40) Liebner, F.; Haimer, E.; Wendland, M.; Neouze, M. A.; Schlufter, K.; Miethe, P.; Heinze, T.; Potthast, A.; Rosenau, T. Aerogels from unaltered bacterial cellulose: Application of $scco_2$ drying for the preparation of shaped, ultra-lightweight cellulosic aerogels. *Macromolecular Bioscience* **2010,** *10* (4), 349-352.

(41) Carpenter, A. W.; de Lannoy, C. F.; Wiesner, M. R. Cellulose nanomaterials in water treatment technologies. *Environmental Science & Technology* **2015,** *49* (9), 5277-5287.

(42) Olivera, S.; Muralidhara, H. B.; Venkatesh, K.; Guna, V. K.; Gopalakrishna, K.; Kumar, K. Y. Potential applications of cellulose and chitosan nanoparticles/composites in wastewater treatment: A review. *Carbohydrate Polymers* **2016,** *153*, 600-618.

(43) Doshi, B.; Sillanpaa, M.; Kalliola, S. A review of bio-based materials for oil spill treatment. *Water Research* **2018,** *135*, 262-277.

(44) Rahman, N. S. A.; Yhaya, M. F.; Azahari, B.; Ismail, W. R. Utilisation of natural cellulose fibres in wastewater treatment. *Cellulose* **2018,** *25*, 4887-4903.

(45) Wang, Z.; Song, L.; Wang, Y.; Zhang, X.-F.; Hao, D.; Feng, Y.; Yao, J. Lightweight uio-66/cellulose aerogels constructed through self-crosslinking strategy for adsorption applications. *Chemical Engineering Journal* **2019,** *371*, 138-144.

(46) Hokkanen, S.; Bhatnagar, A.; Sillanpää, M. A review on modification methods to cellulose-based adsorbents to improve adsorption capacity. *Water Research* **2016,** *91*,

156-173.

(47) Ifelebuegu, A. O.; Johnson, A. Nonconventional low-cost cellulose- and keratin-based biopolymeric sorbents for oil/water separation and spill cleanup: A review. *Critical Reviews in Environmental Science and Technology* **2017,** *47* (11), 964-1001.

(48) Jiang, F.; Dinh, D. M.; Hsieh, Y. L. Adsorption and desorption of cationic malachite green dye on cellulose nanofibril aerogels. *Carbohydrate Polymers* **2017,** *173*, 286-294.

(49) Chai, W.; Liu, X.; Zou, J.; Zhang, X.; Li, B.; Yin, T. Pomelo peel modified with acetic anhydride and styrene as new sorbents for removal of oil pollution. *Carbohydrate Polymers* **2015,** *132*, 245-251.

(50) Li, J.; Li, D.; Yang, Y.; Li, J.; Zha, F.; Lei, Z. A prewetting induced underwater superoleophobic or underoil (super) hydrophobic waste potato residue-coated mesh for selective efficient oil/water separation. *Green Chemistry* **2016,** *18* (2), 541-549.

(51) Ma, Q.; Cheng, H.; Fane, A. G.; Wang, R.; Zhang, H. Recent development of advanced materials with special wettability for selective oil/water separation. *Small* **2016,** *12* (16), 2186-2202.

(52) Wang, B.; Liang, W.; Guo, Z.; Liu, W. Biomimetic super-lyophobic and super-lyophilic materials applied for oil/water separation: A new strategy beyond nature. *Chemical Society Reviews* **2015,** *44* (1), 336-361.

(53) Su, C.; Xu, Y.; Zhang, W.; Liu, Y.; Li, J. Porous ceramic membrane with superhydrophobic and superoleophilic surface for reclaiming oil from oily water. *Applied Surface Science* **2012,** *258* (7), 2319-2323.

(54) Dudchenko, A. V.; Rolf, J.; Shi, L.; Olivas, L.; Duan, W.; Jassby, D. Coupling underwater superoleophobic membranes with magnetic pickering emulsions for fouling-free separation of crude oil/water mixtures: An experimental and theoretical study. *ACS Nano* **2015,** *9* (10), 9930-9941.

(55) Arslan, O.; Aytac, Z.; Uyar, T. Superhydrophobic, hybrid, electrospun cellulose acetate nanofibrous mats for oil/water separation by tailored surface modification. *ACS Applied Materials & Interfaces* **2016,** *8* (30), 19747-19754.

(56) Li, L.; Li, B.; Wu, L.; Zhao, X.; Zhang, J. Magnetic, superhydrophobic and durable silicone sponges and their applications in removal of organic pollutants from water. *Chemical Communications* **2014,** *50* (58), 7831-7833.

(57) Turco, A.; Malitesta, C.; Barillaro, G.; Greco, A.; Maffezzoli, A.; Mazzotta, E. A magnetic and highly reusable macroporous superhydrophobic/superoleophilic pdms/mwnt nanocomposite for oil sorption from water. *Journal of Materials Chemistry A* **2015,** *3* (34), 17685-17696.

(58) Mi, H.-Y.; Jing, X.; Politowicz, A. L.; Chen, E.; Huang, H.-X.; Turng, L.-S. Highly compressible ultra-light anisotropic cellulose-graphene aerogel fabricated by bidirectional freeze drying for selective oil absorption. *Carbon* **2018,** *132*, 199-209.

(59) Xu, Z.; Jiang, X.; Zhou, H.; Li, J. Preparation of magnetic hydrophobic polyvinyl alcohol (pva)–cellulose nanofiber (cnf) aerogels as effective oil absorbents. *Cellulose* **2018,** *25*, 1217-1227.

(60) Mulyadi, A.; Zhang, Z.; Deng, Y. Fluorine-free oil absorbents made from cellulose nanofibril aerogels. *ACS Applied Materials & Interfaces* **2016,** *8* (4), 2732-2740.

(61) Laitinen, O.; Suopajarvi, T.; Osterberg, M.; Liimatainen, H. Hydrophobic, superabsorbing aerogels from choline chloride-based deep eutectic solvent pretreated and silylated cellulose nanofibrils for selective oil removal. *ACS Applied Materials &*

Interfaces **2017,** *9* (29), 25029-25037.

(62) Zhai, T.; Zheng, Q.; Cai, Z.; Xia, H.; Gong, S. Synthesis of polyvinyl alcohol/cellulose nanofibril hybrid aerogel microspheres and their use as oil/solvent superabsorbents. *Carbohydrate Polymers* **2016,** *148*, 300-308.

(63) Rafieian, F.; Hosseini, M.; Jonoobi, M.; Yu, Q. Development of hydrophobic nanocellulose-based aerogel via chemical vapor deposition for oil separation for water treatment. *Cellulose* **2018,** *25*, 4695-4710.

(64) Jiang, F.; Hsieh, Y. L. Cellulose nanofibril aerogels: Synergistic improvement of hydrophobicity, strength, and thermal stability via cross-linking with diisocyanate. *ACS Applied Materials & Interfaces* **2017,** *9* (3), 2825-2834.

(65) Jiang, F.; Hsieh, Y. L. Amphiphilic superabsorbent cellulose nanofibril aerogels. *Journal of Materials Chemistry A* **2014,** *2* (18), 6337-6342.

(66) Yin, T.; Zhang, X.; Liu, X.; Li, B.; Wang, C. Cellulose-based aerogel from eichhornia crassipes as an oil superabsorbent. *RSC Advances* **2016,** *6*, 98563-98570.

(67) Jiao, Y.; Wan, C.; Li, J. Synthesis of carbon fiber aerogel from natural bamboo fiber and its application as a green high-efficiency and recyclable adsorbent. *Materials and Design* **2016,** *107*, 26-32.

(68) Zhou, S.; Liu, P.; Wang, M.; Zhao, H.; Yang, J.; Xu, F. Sustainable, reusable, and superhydrophobic aerogels from microfibrillated cellulose for highly effective oil/water separation. *ACS Sustainable Chemistry & Engineering* **2016,** *4*, 6409-6416.

(69) Phanthong, P.; Reubroycharoen, P.; Kongparakul, S.; Samart, C.; Wang, Z.; Hao, X.; Abudula, A.; Guan, G. Fabrication and evaluation of nanocellulose sponge for oil/water separation. *Carbohydrate Polymers* **2018,** *190*, 184-189.

(70) Sai, H.; Fu, R.; Xing, L.; Xiang, J.; Li, Z.; Li, F.; Zhang, T. Surface modification of bacterial cellulose aerogels' web-like skeleton for oil/water separation. *ACS Applied Materials & Interfaces* **2015,** *7* (13), 7373-7381.

(71) Lu, Y.; Yuan, W. Superhydrophobic/superoleophilic and reinforced ethyl cellulose sponges for oil/water separation: Synergistic strategies of cross-linking, carbon nanotube composite, and nanosilica modification. *ACS Applied Materials & Interfaces* **2017,** *9* (34), 29167-29176.

(72) Lu, Y.; Wang, Y.; Liu, L.; Yuan, W. Environmental-friendly and magnetic/silanized ethyl cellulose sponges as effective and recyclable oil-absorption materials. *Carbohydrate Polymers* **2017,** *173*, 422-430.

(73) Lu, Y.; Yuan, W. Superhydrophobic three-dimensional porous ethyl cellulose absorbent with micro/nano-scale hierarchical structures for highly efficient removal of oily contaminants from water. *Carbohydrate Polymers* **2018,** *191*, 86-94.

(74) Fu, Q.; Ansari, F.; Zhou, Q.; Berglund, L. A. Wood nanotechnology for strong, mesoporous, and hydrophobic biocomposites for selective separation of oil/water mixtures. *ACS Nano* **2018,** *12* (3), 2222-2230.

(75) Guan, H.; Cheng, Z.; Wang, X. Highly compressible wood sponges with a spring-like lamellar structure as effective and reusable oil absorbents. *ACS Nano* **2018,** *12* (10), 10365-10373.

(76) Jin, C.; Han, S.; Li, J.; Sun, Q. Fabrication of cellulose-based aerogels from waste newspaper without any pretreatment and their use for absorbents. *Carbohydrate Polymers* **2015,** *123*, 150-156.

(77) Li, Z.; Shao, L.; Hu, W.; Zheng, T.; Lu, L.; Cao, Y.; Chen, Y. Excellent reusable

chitosan/cellulose aerogel as an oil and organic solvent absorbent. *Carbohydrate Polymers* **2018,** *191*, 183-190.

(78) Zhang, Z.; Sèbe, G.; Rentsch, D.; Zimmermann, T.; Tingaut, P. Ultralightweight and flexible silylated nanocellulose sponges for the selective removal of oil from water. *Chemistry of Materials* **2014,** *26* (8), 2659-2668.

(79) Chaudhary, J. P.; Nataraj, S. K.; Gogda, A.; Meena, R. Bio-based superhydrophilic foam membranes for sustainable oil–water separation. *Green Chemistry* **2014,** *16* (10), 4552-4558.

(80) Wang, G.; He, Y.; Wang, H.; Zhang, L.; Yu, Q.; Peng, S.; Wu, X.; Ren, T.; Zeng, Z.; Xue, Q. A cellulose sponge with robust superhydrophilicity and under-water superoleophobicity for highly effective oil/water separation. *Green Chemistry* **2015,** *17* (5), 3093-3099.

(81) Li, Y.; Zhu, L.; Grishkewich, N.; Tam, K. C.; Yuan, J.; Mao, Z.; Sui, X. Co_2-responsive cellulose nanofibers aerogels for switchable oil-water separation. *ACS Applied Materials & Interfaces* **2019,** *11* (9), 9367–9373.

(82) Gotoh, T.; Matsushima, K.; Kikuchi, K.-I. Adsorption of cu and mn on covalently cross-linked alginate gel beads. *Chemosphere* **2004,** *55* (1), 57-64.

(83) Wang, J.; Chen, C. Biosorbents for heavy metals removal and their future. *Biotechnology Advances* **2009,** *27* (2), 195-226.

(84) Zhao, J.; Zhang, X.; He, X.; Xiao, M.; Zhang, W.; Lu, C. A super biosorbent from dendrimer poly(amidoamine)-grafted cellulose nanofibril aerogels for effective removal of cr(vi). *Journal of Materials Chemistry A* **2015,** *3* (28), 14703-11471.

(85) Wang, D.; Yu, H.; Fan, X.; Gu, J.; Ye, S.; Yao, J.; Ni, Q. High aspect ratio carboxylated cellulose nanofibers cross-linked to robust aerogels for superabsorption-flocculants: Paving way from nanoscale to macroscale. *ACS Applied Materials & Interfaces* **2018,** *10* (24), 20755-20766.

(86) She, J.; Tian, C.; Wu, Y.; Li, X.; Luo, S.; Qing, Y.; Jiang, Z. Cellulose nanofibrils aerogel cross-linked by poly(vinyl alcohol) and acrylic acid for efficient and recycled adsorption with heavy metal ions. *Journal of Nanoscience and Nanotechnology* **2018,** *18* (6), 4167-4175.

(87) Zheng, Q.; Cai, Z.; Gong, S. Green synthesis of polyvinyl alcohol (pva)–cellulose nanofibril (cnf) hybrid aerogels and their use as superabsorbents. *Journal of Materials Chemistry A* **2014,** *2* (9), 3110-3118.

(88) Li, J.; Zuo, K.; Wu, W.; Xu, Z.; Yi, Y.; Jing, Y.; Dai, H.; Fang, G. Shape memory aerogels from nanocellulose and polyethyleneimine as a novel adsorbent for removal of cu(ii) and pb(ii). *Carbohydrate Polymers* **2018,** *196*, 376-384.

(89) Tang, J.; Song, Y.; Zhao, F.; Spinney, S.; da Silva Bernardes, J.; Tam, K. C. Compressible cellulose nanofibril (cnf) based aerogels produced via a bio-inspired strategy for heavy metal ion and dye removal. *Carbohydrate Polymers* **2019,** *208*, 404-412.

(90) Maatar, W.; Boufi, S. Poly(methacylic acid-co-maleic acid) grafted nanofibrillated cellulose as a reusable novel heavy metal ions adsorbent. *Carbohydrate Polymers* **2015,** *126*, 199-207.

(91) Hong, H. J.; Lim, J. S.; Hwang, J. Y.; Kim, M.; Jeong, H. S.; Park, M. S. Carboxymethlyated cellulose nanofibrils (cmcnfs) embedded in polyurethane foam as a modular adsorbent of heavy metal ions. *Carbohydrate Polymers* **2018,** *195*, 136-142.

(92) Geng, B.; Wang, H.; Wu, S.; Ru, J.; Tong, C.; Chen, Y.; Liu, H.; Wu, S.; Liu, X. Surface-tailored nanocellulose aerogels with thiol-functional moieties for highly efficient and selective removal of hg(ii) ions from water. *ACS Sustainable Chemistry & Engineering* **2017,** *5*, 11715-11726.

(93) Melone, L.; Rossi, B.; Pastori, N.; Panzeri, W.; Mele, A.; Punta, C. Tempo-oxidized cellulose cross-linked with branched polyethyleneimine: Nanostructured adsorbent sponges for water remediation. *ChemPlusChem* **2015,** *80*, 1408-1415.

(94) Zhu, H.; Yang, X.; Cranston, E. D.; Zhu, S. Flexible and porous nanocellulose aerogels with high loadings of metal-organic-framework particles for separations applications. *Advanced Materials* **2016,** *28* (35), 7652-7657.

(95) Yousefi, N.; Wong, K. K. W.; Hosseinidoust, Z.; Sorensen, H. O.; Bruns, S.; Zheng, Y.; Tufenkji, N. Hierarchically porous, ultra-strong reduced graphene oxide-cellulose nanocrystal sponges for exceptional adsorption of water contaminants. *Nanoscale* **2018,** *10* (15), 7171-7184.

(96) Ma, X.; Lou, Y.; Chen, X.-B.; Shi, Z.; Xu, Y. Multifunctional flexible composite aerogels constructed through in-situ growth of metal-organic framework nanoparticles on bacterial cellulose. *Chemical Engineering Journal* **2019,** *356*, 227-235.

(97) Liu, Y.-J.; Liu, S.; Li, Z.-W.; Ma, M.-G.; Wang, B. A microwave synthesized mesoporous carbon sponge as an efficient adsorbent for Cr(VI) removal. *RSC Advances* **2018,** *8*, 7892-7898.

(98) Bo, S.; Ren, W.; Lei, C.; Xie, Y.; Cai, Y.; Wang, S.; Gao, J.; Ni, Q.; Yao, J. Flexible and porous cellulose aerogels/zeolitic imidazolate framework (ZIF-8) hybrids for adsorption removal of cr(iv) from water. *Journal of Solid State Chemistry* **2018,** *262*, 135-141.

(99) Li, Z.; Shao, L.; Ruan, Z.; Hu, W.; Lu, L.; Chen, Y. Converting untreated waste office paper and chitosan into aerogel adsorbent for the removal of heavy metal ions. *Carbohydrate Polymers* **2018,** *193*, 221-227.

(100) Lei, C.; Gao, J.; Ren, W.; Xie, Y.; Abdalkarim, S. Y. H.; Wang, S.; Ni, Q.; Yao, J. Fabrication of metal-organic frameworks@cellulose aerogels composite materials for removal of heavy metal ions in water. *Carbohydrate Polymers* **2019,** *205*, 35-41.

(101) Peng, S.; Meng, H.; Ouyang, Y.; Chang, J. Nanoporous magnetic cellulose–chitosan composite microspheres: Preparation, characterization, and application for cu(ii) adsorption. *Industrial & Engineering Chemistry Research* **2014,** *53*, 2106-2113.

(102) Cai, J.; Kimura, S.; Wada, M.; Kuga, S. Nanoporous cellulose as metal nanoparticles support. *Biomacromolecules* **2009,** *10*, 87-94.

(103) Lam, E.; Luong, J. H. T. Carbon materials as catalyst supports and catalysts in the transformation of biomass to fuels and chemicals. *ACS Catalysis* **2014,** *4*, 3393-3410.

(104) Wang, Y.; Sun, G.; Dai, J.; Chen, G.; Morgenstern, J.; Wang, Y.; Kang, S.; Zhu, M.; Das, S.; Cui, L.; Hu, L. A high-performance, low-tortuosity wood-carbon monolith reactor. *Advanced Materials* **2017,** *29* (2), 1604257.

(105) Zhang, R.; Liu, C.; Hsu, P. C.; Zhang, C.; Liu, N.; Zhang, J.; Lee, H. R.; Lu, Y.; Qiu, Y.; Chu, S.; Cui, Y. Nanofiber air filters with high-temperature stability for efficient $pm_{2.5}$ removal from the pollution sources. *Nano Letters* **2016,** *16* (6), 3642-3649.

(106) Nemoto, J.; Saito, T.; Isogai, A. Simple freeze-drying procedure for producing nanocellulose aerogel-containing, high-performance air filters. *ACS Applied Materials & Interfaces* **2015,** *7* (35), 19809-19815.

(107) He, M.; Ichinose, T.; Kobayashi, M.; Arashidani, K.; Yoshida, S.; Nishikawa, M.; Takano, H.; Sun, G.; Shibamoto, T. Differences in allergic inflammatory responses between urban $pm_{2.5}$ and fine particle derived from desert-dust in murine lungs. *Toxicology and Applied Pharmacology* **2016,** *297*, 41-55.

(108) Macfarlane, A. L.; Kadla, J. F.; Kerekes, R. J. High performance air filters produced from freeze-dried fibrillated wood pulp: Fiber network compression due to the freezing process. *Industrial & Engineering Chemistry Research* **2012,** *51* (32), 10702-10711.

(109) Lu, Z.; Su, Z.; Song, S.; Zhao, Y.; Ma, S.; Zhang, M. Toward high-performance fibrillated cellulose-based air filter via constructing spider-web-like structure with the aid of tba during freeze-drying process. *Cellulose* **2017,** *25* (1), 619-629.

(110) Ma, S.; Zhang, M.; Nie, J.; Yang, B.; Song, S.; Lu, P. Multifunctional cellulose-based air filters with high loadings of metal–organic frameworks prepared by in situ growth method for gas adsorption and antibacterial applications. *Cellulose* **2018,** *25* (10), 5999-6010.

(111) Su, Z.; Zhang, M.; Lu, Z.; Song, S.; Zhao, Y.; Hao, Y. Functionalization of cellulose fiber by in situ growth of zeolitic imidazolate framework-8 (ZIF-8) nanocrystals for preparing a cellulose-based air filter with gas adsorption ability. *Cellulose* **2018,** *25* (3), 1997-2008.

(112) Ma, S.; Zhang, M.; Nie, J.; Tan, J.; Yang, B.; Song, S. Design of double-component metal-organic framework air filters with $PM_{2.5}$ capture, gas adsorption and antibacterial capacities. *Carbohydrate Polymers* **2019,** *203*, 415-422.

(113) Kheifets, L.; Afifi, A. A.; Shimkhada, R. Public health impact of extremely low-frequency electromagnetic fields. *Environmental Health Perspectives* **2006,** *114* (10), 1532-1537.

(114) Shen, B.; Zhai, W.; Zheng, W. Ultrathin flexible graphene film: An excellent thermal conducting material with efficient emi shielding. *Advanced Functional Materials* **2014,** *24* (28), 4542-4548.

(115) Wan, Y.-J.; Zhu, P.-L.; Yu, S.-H.; Sun, R.; Wong, C.-P.; Liao, W.-H. Ultralight, super-elastic and volume-preserving cellulose fiber/graphene aerogel for high-performance electromagnetic interference shielding. *Carbon* **2017,** *115*, 629-639.

(116) Li, J.; Wan, C. Cellulose aerogels decorated with multi-walled carbon nanotubes: Preparation, characterization, and application for electromagnetic interference shielding. *Frontiers of Agricultural Science and Engineering* **2015,** *2* (4), 341-346.

(117) Wan, C.; Li, J. Graphene oxide/cellulose aerogels nanocomposite: Preparation, pyrolysis, and application for electromagnetic interference shielding. *Carbohydrate Polymers* **2016,** *150*, 172-179.

(118) Wan, C.; Jiao, Y.; Qiang, T.; Li, J. Cellulose-derived carbon aerogels supported goethite (alpha-feooh) nanoneedles and nanoflowers for electromagnetic interference shielding. *Carbohydrate Polymers* **2017,** *156*, 427-434.

(119) Gong, J.; Antonietti, M.; Yuan, J. Poly(ionic liquid)-derived carbon with site-specific n-doping and biphasic heterojunction for enhanced co_2 capture and sensing. *Angewandte Chemie International Edition* **2017,** *56* (26), 7557-7563.

(120) Dani, A.; Crocellà, V.; Magistris, C.; Santoro, V.; Yuan, J.; Bordiga, S. Click-based porous cationic polymers for enhanced carbon dioxide capture. *Journal of Materials Chemistry A* **2017,** *5* (1), 372-383.

(121) Sun, J. K.; Antonietti, M.; Yuan, J. Nanoporous ionic organic networks: From

synthesis to materials applications. *Chemical Society Reviews* **2016,** *45* (23), 6627-6656.

(122) Gong, J.; Lin, H.; Antonietti, M.; Yuan, J. Nitrogen-doped porous carbon nanosheets derived from poly(ionic liquid)s: Hierarchical pore structures for efficient co_2 capture and dye removal. *Journal of Materials Chemistry A* **2016,** *4* (19), 7313-7321.

(123) Goeppert, A.; Czaun, M.; Surya Prakash, G. K.; Olah, G. A. Air as the renewable carbon source of the future: An overview of co_2 capture from the atmosphere. *Energy & Environmental Science* **2012,** *5* (7), 7833-7853.

(124) Janakiram, S.; Ahmadi, M.; Dai, Z.; Ansaloni, L.; Deng, L. Performance of nanocomposite membranes containing 0d to 2d nanofillers for CO_2 separation: A review. *Membranes* **2018,** *8* (2), 24.

(125) Mahfoudhi, N.; Boufi, S. Nanocellulose as a novel nanostructured adsorbent for environmental remediation: A review. *Cellulose* **2017,** *24* (3), 1171-1197.

(126) Wang, X.; Zhang, Y.; Wang, S.; Jiang, H.; Liu, S.; Yao, Y.; Zhang, T.; Li, Q. Synthesis and characterization of amine-modified spherical nanocellulose aerogels. *Journal of Materials Science* **2018,** *53* (18), 13304-13315.

(127) Zhang, T.; Zhang, Y.; Jiang, H.; Wang, X. Aminosilane-grafted spherical cellulose nanocrystal aerogel with high CO_2 adsorption capacity. *Environmental Science and Pollution Research International* **2019,** *26* (16), 16716-16726.

(128) Gebald, C.; Wurzbacher, J. A.; Tingaut, P.; Zimmermann, T.; Steinfeld, A. Amine-based nanofibrillated cellulose as adsorbent for CO_2 capture from air. *Environmental Science & Technology* **2011,** *45* (20), 9101-9108.

(129) Wu, Y.; Zhang, Y.; Chen, N.; Dai, S.; Jiang, H.; Wang, S. Effects of amine loading on the properties of cellulose nanofibrils aerogel and its CO_2 capturing performance. *Carbohydrate Polymers* **2018,** *194*, 252-259.

(130) Jiang, F.; Hu, S.; Hsieh, Y.-l. Aqueous synthesis of compressible and thermally stable cellulose nanofibril–silica aerogel for CO_2 adsorption. *ACS Applied Nano Materials* **2018,** *1* (12), 6701-6710.

(131) Sehaqui, H.; Galvez, M. E.; Becatinni, V.; cheng Ng, Y.; Steinfeld, A.; Zimmermann, T.; Tingaut, P. Fast and reversible direct co_2 capture from air onto all-polymer nanofibrillated cellulose-polyethylenimine foams. *Environmental Science & Technology* **2015,** *49* (5), 3167-3174.

(132) Chu, S.; Majumdar, A. Opportunities and challenges for a sustainable energy future. *Nature* **2012,** *488* (7411), 294-303.

(133) Larcher, D.; Tarascon, J. M. Towards greener and more sustainable batteries for electrical energy storage. *Nature Chemistry* **2015,** *7* (1), 19-29.

(134) Yang, Z.; Zhang, J.; Kintner-Meyer, M. C.; Lu, X.; Choi, D.; Lemmon, J. P.; Liu, J. Electrochemical energy storage for green grid. *Chemical Reviews* **2011,** *111* (5), 3577-3613.

(135) Dutta, S.; Kim, J.; Ide, Y.; Ho Kim, J.; Hossain, M. S. A.; Bando, Y.; Yamauchi, Y.; Wu, K. C. W. 3d network of cellulose-based energy storage devices and related emerging applications. *Materials Horizons* **2017,** *4* (4), 522-545.

(136) Hu, L.; Cui, Y. Energy and environmental nanotechnology in conductive paper and textiles. *Energy & Environmental Science* **2012,** *5* (4), 6423-6435.

(137) Jabbour, L.; Bongiovanni, R.; Chaussy, D.; Gerbaldi, C.; Beneventi, D. Cellulose-based li-ion batteries: A review. *Cellulose* **2013,** *20* (4), 1523-1545.

(138) Pérez-Madrigal, M. M.; Edo, M. G.; Alemán, C. Powering the future: Application

of cellulose-based materials for supercapacitors. *Green Chemistry* **2016,** *18* (22), 5930-5956.

(139) Sharifi, F.; Ghobadian, S.; Cavalcanti, F. R.; Hashemi, N. Paper-based devices for energy applications. *Renewable and Sustainable Energy Reviews* **2015,** *52*, 1453-1472.

(140) Ummartyotin, S.; Manuspiya, H. An overview of feasibilities and challenge of conductive cellulose for rechargeable lithium based battery. *Renewable and Sustainable Energy Reviews* **2015,** *50*, 204-213.

(141) Wang, Z.; Tammela, P.; Strømme, M.; Nyholm, L. Cellulose-based supercapacitors: Material and performance considerations. *Advanced Energy Materials* **2017,** *7* (18), 1700130.

(142) Yao, B.; Zhang, J.; Kou, T.; Song, Y.; Liu, T.; Li, Y. Paper-based electrodes for flexible energy storage devices. *Advanced Science* **2017,** *4* (7), 1700107.

(143) Zhang, Y. Z.; Wang, Y.; Cheng, T.; Lai, W. Y.; Pang, H.; Huang, W. Flexible supercapacitors based on paper substrates: A new paradigm for low-cost energy storage. *Chemical Society Reviews* **2015,** *44* (15), 5181-5199.

(144) Zheng, G.; Cui, Y.; Karabulut, E.; Wågberg, L.; Zhu, H.; Hu, L. Nanostructured paper for flexible energy and electronic devices. *MRS Bulletin* **2013,** *38* (4), 320-325.

(145) Hayase, G.; Kanamori, K.; Abe, K.; Yano, H.; Maeno, A.; Kaji, H.; Nakanishi, K. Polymethylsilsesquioxane-cellulose nanofiber biocomposite aerogels with high thermal insulation, bendability, and superhydrophobicity. *ACS Applied Materials & Interfaces* **2014,** *6* (12), 9466-9471.

(146) Nguyen, S. T.; Feng, J.; Ng, S. K.; Wong, J. P. W.; Tan, V. B. C.; Duong, H. M. Advanced thermal insulation and absorption properties of recycled cellulose aerogels. *Colloids and Surfaces A: Physicochemical and Engineering Aspects* **2014,** *445*, 128-134.

(147) Kim, J. H.; Lee, D.; Lee, Y. H.; Chen, W.; Lee, S. Y. Nanocellulose for energy storage systems: Beyond the limits of synthetic materials. *Advanced Materials* **2019,** *31* (20), 1804826.

(148) Pang, Q.; Tang, J.; Huang, H.; Liang, X.; Hart, C.; Tam, K. C.; Nazar, L. F. A nitrogen and sulfur dual-doped carbon derived from polyrhodanine@cellulose for advanced lithium-sulfur batteries. *Advanced Materials* **2015,** *27* (39), 6021-6028.

(149) Simon, P.; GoGotSi, Y. Materials for electrochemical capacitors. *Nature Materials* **2008,** *7*, 845-854.

(150) Winter, M.; Brodd., R. J. What are batteries, fuel cells, and supercapacitors? *Chemical Reviews* **2003,** *104*, 4245-4269.

(151) Wang, G.; Zhang, L.; Zhang, J. A review of electrode materials for electrochemical supercapacitors. *Chemical Society Reviews* **2012,** *41* (2), 797-828.

(152) Nyholm, L.; Nystrom, G.; Mihranyan, A.; Stromme, M. Toward flexible polymer and paper-based energy storage devices. *Advanced Materials* **2011,** *23* (33), 3751-3769.

(153) Liu, L.; Niu, Z.; Zhang, L.; Zhou, W.; Chen, X.; Xie, S. Nanostructured graphene composite papers for highly flexible and foldable supercapacitors. *Advanced Materials* **2014,** *26* (28), 4855-4862.

(154) Gui, Z.; Zhu, H.; Gillette, E.; Han, X.; Rubloff, G. W.; Hu, L.; Lee, S. B. Natural cellulose fiber as substrate for supercapacitor. *ACS Nano* **2013,** *7* (7), 6037-6046.

(155) Yang, X.; Shi, K.; Zhitomirsky, I.; Cranston, E. D. Cellulose nanocrystal aerogels as universal 3d lightweight substrates for supercapacitor materials. *Advanced Materials* **2015,** *27* (40), 6104-6109.

(156) Shi, K.; Yang, X.; Cranston, E. D.; Zhitomirsky, I. Efficient lightweight supercapacitor with compression stability. *Advanced Functional Materials* **2016,** *26* (35), 6437-6445.

(157) Wang, D. C.; Yu, H. Y.; Qi, D.; Ramasamy, M.; Yao, J.; Tang, F.; Tam, K. C.; Ni, Q.-Q. Supramolecular self-assembly of 3D conductive cellulose nanofiber aerogels for flexible supercapacitors and ultrasensitive sensors. *ACS Applied Materials & Interfaces* **2019,** *11*, 24435-24446.

(158) Decher, G. Fuzzy nanoassemblies: Toward layered polymeric multicomposites. *Science* **1997,** *277*, 1232-1237.

(159) Dubas, S. T.; Schlenoff, J. B. Factors controlling the growth of polyelectrolyte multilayers. *Macromolecules* **1999,** *32*, 8153-8160.

(160) Lee, D.; Rubner, M. F.; Cohen, R. E. All-nanoparticle thin-film coatings. *Nano Letters* **2006,** *6* (10), 2305-2312.

(161) Richardson, J. J.; Bjornmalm, M.; Caruso, F. Technology-driven layer-by-layer assembly of nanofilms. *Science* **2015,** *348* (6233), aaa2491.

(162) Xiao, F. X.; Pagliaro, M.; Xu, Y. J.; Liu, B. Layer-by-layer assembly of versatile nanoarchitectures with diverse dimensionality: A new perspective for rational construction of multilayer assemblies. *Chemical Society Reviews* **2016,** *45* (11), 3088-3121.

(163) Hamedi, M.; Karabulut, E.; Marais, A.; Herland, A.; Nystrom, G.; Wagberg, L. Nanocellulose aerogels functionalized by rapid layer-by-layer assembly for high charge storage and beyond. *Angewandte Chemie International Edition* **2013,** *52* (46), 12038-12042.

(164) Wu, Z. Y.; Liang, H. W.; Chen, L. F.; Hu, B. C.; Yu, S. H. Bacterial cellulose: A robust platform for design of three dimensional carbon-based functional nanomaterials. *Accounts of Chemical Research* **2016,** *49* (1), 96-105.

(165) Lu, H.; Zhao, X. S. Biomass-derived carbon electrode materials for supercapacitors. *Sustainable Energy & Fuels* **2017,** *1*, 1265-1281.

(166) Zheng, Q.; Kvit, A.; Cai, Z.; Ma, Z.; Gong, S. A freestanding cellulose nanofibril–reduced graphene oxide–molybdenum oxynitride aerogel film electrode for all-solid-state supercapacitors with ultrahigh energy density. *Journal of Materials Chemistry A* **2017,** *5*, 12528-12541.

(167) Cai, J.; Niu, H.; Li, Z.; Du, Y.; Cizek, P.; Xie, Z.; Xiong, H.; Lin, T. High-performance supercapacitor electrode materials from cellulose-derived carbon nanofibers. *ACS Applied Materials & Interfaces* **2015,** *7* (27), 14946-14953.

(168) Chen, L. F.; Zhang, X. D.; Liang, H. W.; Kong, M.; Guan, Q. F.; Chen, P.; Wu, Z. Y.; Yu, S. H. Synthesis of nitrogen-doped porous carbon nanofibers as an efficient electrode material for supercapacitors. *ACS Nano* **2012,** *6* (8), 7092-7102.

(169) Hao, P.; Zhao, Z.; Tian, J.; Li, H.; Sang, Y.; Yu, G.; Cai, H.; Liu, H.; Wong, C. P.; Umar, A. Hierarchical porous carbon aerogel derived from bagasse for high performance supercapacitor electrode. *Nanoscale* **2014,** *6* (20), 12120-12129.

(170) Dai, L.; Chang, D. W.; Baek, J. B.; Lu, W. Carbon nanomaterials for advanced energy conversion and storage. *Small* **2012,** *8* (8), 1130-1166.

(171) Xu, X.; Zhou, J.; Nagaraju, D. H.; Jiang, L.; Marinov, V. R.; Lubineau, G.; Alshareef, H. N.; Oh, M. Flexible, highly graphitized carbon aerogels based on bacterial cellulose/lignin: Catalyst-free synthesis and its application in energy storage devices.

Advanced Functional Materials **2015,** *25* (21), 3193-3202.
(172) Huang, J.; Wang, J.; Wang, C.; Zhang, H.; Lu, C.; Wang, J. Hierarchical porous graphene carbon-based supercapacitors. *Chemistry of Materials* **2015,** *27* (6), 2107-2113.
(173) Long, C.; Qi, D.; Wei, T.; Yan, J.; Jiang, L.; Fan, Z. Nitrogen-doped carbon networks for high energy density supercapacitors derived from polyaniline coated bacterial cellulose. *Advanced Functional Materials* **2014,** *24* (25), 3953-3961.
(174) Chen, L.-F.; Huang, Z.-H.; Liang, H.-W.; Gao, H.-L.; Yu, S.-H. Three-dimensional heteroatom-doped carbon nanofiber networks derived from bacterial cellulose for supercapacitors. *Advanced Functional Materials* **2014,** *24* (32), 5104-5111.
(175) Liu, J.; Zhang, J.-G.; Yang, Z.; Lemmon, J. P.; Imhoff, C.; Graff, G. L.; Li, L.; Hu, J.; Wang, C.; Xiao, J.; Xia, G.; Viswanathan, V. V.; Baskaran, S.; Sprenkle, V.; Li, X.; Shao, Y.; Schwenzer, B. Materials science and materials chemistry for large scale electrochemical energy storage: From transportation to electrical grid. *Advanced Functional Materials* **2013,** *23* (8), 929-946.
(176) Dunn, B.; Kamath, H.; Tarascon, J.-M. Electrical energy storage for the grid: A battery of choices. *Science* **2011,** *334*, 928-935.
(177) Xu, D.; Chen, C.; Xie, J.; Zhang, B.; Miao, L.; Cai, J.; Huang, Y.; Zhang, L. A hierarchical n/s-codoped carbon anode fabricated facilely from cellulose/polyaniline microspheres for high-performance sodium-ion batteries. *Advanced Energy Materials* **2016,** *6* (6), 1501929.
(178) Xie, H.; Yang, C.; Fu, K. K.; Yao, Y.; Jiang, F.; Hitz, E.; Liu, B.; Wang, S.; Hu, L. Flexible, scalable, and highly conductive garnet-polymer solid electrolyte templated by bacterial cellulose. *Advanced Energy Materials* **2018,** *8* (18), 1703474.
(179) Liang, H.-W.; Wu, Z.-Y.; Chen, L.-F.; Li, C.; Yu, S.-H. Bacterial cellulose derived nitrogen-doped carbon nanofiber aerogel: An efficient metal-free oxygen reduction electrocatalyst for zinc-air battery. *Nano Energy* **2015,** *11*, 366-376.
(180) Wan, Y.; Yang, Z.; Xiong, G.; Luo, H. A general strategy of decorating 3D carbon nanofiber aerogels derived from bacterial cellulose with nano-fe_3o_4 for high-performance flexible and binder-free lithium-ion battery anodes. *Journal of Materials Chemistry A* **2015,** *3* (30), 15386-15393.
(181) Bruce, P. G.; Freunberger, S. A.; Hardwick, L. J.; Tarascon, J. M. Li-O_2 and li-S batteries with high energy storage. *Nature Materials* **2011,** *11* (1), 19-29.
(182) Huang, Y.; Zheng, M.; Lin, Z.; Zhao, B.; Zhang, S.; Yang, J.; Zhu, C.; Zhang, H.; Sun, D.; Shi, Y. Flexible cathodes and multifunctional interlayers based on carbonized bacterial cellulose for high-performance lithium–sulfur batteries. *Journal of Materials Chemistry A* **2015,** *3* (20), 10910-10918.
(183) Liu, S.; Duvigneau, J.; Vancso, G. J. Nanocellular polymer foams as promising high performance thermal insulation materials. *European Polymer Journal* **2015,** *65*, 33-45.
(184) Wicklein, B.; Kocjan, A.; Salazar-Alvarez, G.; Carosio, F.; Camino, G.; Antonietti, M.; Bergstrom, L. Thermally insulating and fire-retardant lightweight anisotropic foams based on nanocellulose and graphene oxide. *Nature Nanotechnology* **2015,** *10* (3), 277-283.
(185) Zhang, J.; Cheng, Y.; Tebyetekerwa, M.; Meng, S.; Zhu, M.; Lu, Y. “Stiff–soft” binary aynergistic aerogels with superflexibility and high thermal insulation performance. *Advanced Functional Materials* **2019,** *29* (15), 1806407.
(186) Jimenez-Saelices, C.; Seantier, B.; Grohens, Y.; Capron, I. Thermal superinsulating

materials made from nanofibrillated cellulose-stabilized pickering emulsions. *ACS Applied Materials & Interfaces* **2018,** *10* (18), 16193-16202.

(187) Khoshnevisan, K.; Maleki, H.; Samadian, H.; Shahsavari, S.; Sarrafzadeh, M. H.; Larijani, B.; Dorkoosh, F. A.; Haghpanah, V.; Khorramizadeh, M. R. Cellulose acetate electrospun nanofibers for drug delivery systems: Applications and recent advances. *Carbohydrate Polymers* **2018,** *198*, 131-141.

(188) Sun, Q.; Qian, B.; Uto, K.; Chen, J.; Liu, X.; Minari, T. Functional biomaterials towards flexible electronics and sensors. *Biosensors and Bioelectronics* **2018,** *119*, 237-251.

(189) Svensson, A.; Nicklasson, E.; Harrah, T.; Panilaitis, B.; Kaplan, D. L.; Brittberg, M.; Gatenholm, P. Bacterial cellulose as a potential scaffold for tissue engineering of cartilage. *Biomaterials* **2005,** *26* (4), 419-431.

(190) Torgboa, S.; Sukyai, P. Bacterial cellulose-based scaffold materials for bone tissue engineering. *Applied Materials Today* **2018,** *11*, 34-49.

(191) Naseri-Nosar, M.; Ziora, Z. M. Wound dressings from naturally-occurring polymers: A review on homopolysaccharide-based composites. *Carbohydrate Polymers* **2018,** *189*, 379-398.

(192) Domingues, R. M.; Gomes, M. E.; Reis, R. L. The potential of cellulose nanocrystals in tissue engineering strategies. *Biomacromolecules* **2014,** *15* (7), 2327-2346.

(193) Kucin´ska-Lipka, J.; Gubanska, I.; Janik, H. Bacterial cellulose in the field of wound healing and regenerative medicine of skin: Recent trends and future prospectives. *Polymer Bulletin* **2015,** *72*, 2399-2419.

(194) Wang, L.; Wang, K.; Lou, Z.; Jiang, K.; Shen, G. Plant-based modular building blocks for “green” electronic skins. *Advanced Functional Materials* **2018,** *28* (51), 1804510.

(195) Naseri-Nosar, M.; Farzamfar, S.; Sahrapeyma, H.; Ghorbani, S.; Bastami, F.; Vaez, A.; Salehi, M. Cerium oxide nanoparticle-containing poly (epsilon-caprolactone)/gelatin electrospun film as a potential wound dressing material: In vitro and in vivo evaluation. *Materials Science and Engineering C* **2017,** *81*, 366-372.

(196) Pei, Y.; Ye, D.; Zhao, Q.; Wang, X.; Zhang, C.; Huang, W.; Zhang, N.; Liu, S.; Zhang, L. Effectively promoting wound healing with cellulose/gelatin sponges constructed directly from a cellulose solution. *Journal of Materials Chemistry B* **2015,** *3* (38), 7518-7528.

(197) Gao, H.; Zhong, Z.; Xia, H.; Hu, Q.; Ye, Q.; Wang, Y.; Chen, L.; Du, Y.; Shi, X.; Zhang, L. Construction of cellulose nanofibers/quaternized chitin/organic rectorite composites and their application as wound dressing materials. *Biomaterials Science* **2019,** *7* (6), 2571-2581.

(198) Shefa, A. A.; Amirian, J.; Kang, H. J.; Bae, S. H.; Jung, H. I.; Choi, H. J.; Lee, S. Y.; Lee, B. T. In vitro and in vivo evaluation of effectiveness of a novel tempo-oxidized cellulose nanofiber-silk fibroin scaffold in wound healing. *Carbohydrate Polymers* **2017,** *177*, 284-296.

(199) Ye, S.; Jiang, L.; Wu, J.; Su, C.; Huang, C.; Liu, X.; Shao, W. Flexible amoxicillin-grafted bacterial cellulose sponges for wound dressing: In vitro and in vivo evaluation. *ACS Applied Materials & Interfaces* **2018,** *10* (6), 5862-5870.

(200) Uhrich, K. E.; Cannizzaro, S. M.; Langer, R. S.; Shakesheff, K. M. Polymeric systems for controlled drug release. *Chemical Reviews* **1999,** *99*, 3181-3198.

(201) Shelke, N. B.; James, R.; Laurencin, C. T.; Kumbar, S. G. Polysaccharide biomaterials for drug delivery and regenerative engineering. *Polymers for Advanced Technologies* **2014,** *25*, 448-460.

(202) García-González, C. A.; Alnaief, M.; Smirnova, I. Polysaccharide-based aerogels-promising biodegradable carriers for drug delivery systems. *Carbohydrate Polymers* **2011,** *86* (4), 1425-1438.

(203) Zhao, J.; Lu, C.; He, X.; Zhang, X.; Zhang, W.; Zhang, X. Polyethylenimine-grafted cellulose nanofibril aerogels as versatile vehicles for drug delivery. *ACS Applied Materials & Interfaces* **2015,** *7* (4), 2607-2615.

(204) Fiorati, A.; Turco, G.; Travan, A.; Caneva, E.; Pastori, N.; Cametti, M.; Punta, C.; Melone, L. Mechanical and drug release properties of sponges from cross-linked cellulose nanofibers. *ChemPlusChem* **2017,** *82* (6), 848-858.

(205) Chen, X.; Xu, X.; Li, W.; Sun, B.; Yan, J.; Chen, C.; Liu, J.; Qian, J.; Sun, D. Effective drug carrier based on polyethylenimine-functionalized bacterial cellulose with controllable release properties. *ACS Applied Bio Materials* **2018,** *1* (1), 42-50.

(206) Zhang, F.; Wu, W.; Zhang, X.; Meng, X.; Tong, G.; Deng, Y. Temperature-sensitive poly-nipam modified cellulose nanofibril cryogel microspheres for controlled drug release. *Cellulose* **2015,** *23* (1), 415-425.

(207) Bodin, A.; Bharadwaj, S.; Wu, S.; Gatenholm, P.; Atala, A.; Zhang, Y. Tissue-engineered conduit using urine-derived stem cells seeded bacterial cellulose polymer in urinary reconstruction and diversion. *Biomaterials* **2010,** *31* (34), 8889-8901.

(208) Huang, J. W.; Lv, X. G.; Li, Z.; Song, L. J.; Feng, C.; Xie, M. K.; Li, C.; Li, H. B.; Wang, J. H.; Zhu, W. D.; Chen, S. Y.; Wang, H. P.; Xu, Y. M. Urethral reconstruction with a 3d porous bacterial cellulose scaffold seeded with lingual keratinocytes in a rabbit model. *Biomedical Materials* **2015,** *10* (5), 055005.

(209) Martinez Avila, H.; Feldmann, E. M.; Pleumeekers, M. M.; Nimeskern, L.; Kuo, W.; de Jong, W. C.; Schwarz, S.; Muller, R.; Hendriks, J.; Rotter, N.; van Osch, G. J.; Stok, K. S.; Gatenholm, P. Novel bilayer bacterial nanocellulose scaffold supports neocartilage formation in vitro and in vivo. *Biomaterials* **2015,** *44*, 122-133.

(210) Osorio, D. A.; Lee, B. E. J.; Kwiecien, J. M.; Wang, X.; Shahid, I.; Hurley, A. L.; Cranston, E. D.; Grandfield, K. Cross-linked cellulose nanocrystal aerogels as viable bone tissue scaffolds. *Acta Biomaterialia* **2019,** *87*, 152-165.

(211) Atila, D.; Keskin, D.; Tezcaner, A. Crosslinked pullulan/cellulose acetate fibrous scaffolds for bone tissue engineering. *Materials Science and Engineering C* **2016,** *69*, 1103-1115.

(212) Atila, D.; Keskin, D.; Tezcaner, A. Cellulose acetate based 3-dimensional electrospun scaffolds for skin tissue engineering applications. *Carbohydrate Polymers* **2015,** *133*, 251-261.

(213) Lukanina, K. I.; Grigoriev, T. E.; Krasheninnikov, S. V.; Mamagulashvilli, V. G.; Kamyshinsky, R. A.; Chvalun, S. N. Multi-hierarchical tissue-engineering ecm-like scaffolds based on cellulose acetate with collagen and chitosan fillers. *Carbohydrate Polymers* **2018,** *191*, 119-126.

(214) Shi, Z.; Gao, H.; Feng, J.; Ding, B.; Cao, X.; Kuga, S.; Wang, Y.; Zhang, L.; Cai, J. In situ synthesis of robust conductive cellulose/polypyrrole composite aerogels and their potential application in nerve regeneration. *Angewandte Chemie International Edition* **2014,** *53* (21), 5380-5384.

(215) Kirdponpattara, S.; Khamkeaw, A.; Sanchavanakit, N.; Pavasant, P.; Phisalaphong, M. Structural modification and characterization of bacterial cellulose–alginate composite scaffolds for tissue engineering. *Carbohydrate Polymers* **2015,** *132*, 146-155.

(216) Wang, B.; Lv, X.; Chen, S.; Li, Z.; Yao, J.; Peng, X.; Feng, C.; Xu, Y.; Wang, H. Use of heparinized bacterial cellulose based scaffold for improving angiogenesis in tissue regeneration. *Carbohydrate Polymers* **2018,** *181*, 948-956.

(217) Noh, Y. K.; Dos Santos Da Costa, A.; Park, Y. S.; Du, P.; Kim, I. H.; Park, K. Fabrication of bacterial cellulose-collagen composite scaffolds and their osteogenic effect on human mesenchymal stem cells. *Carbohydrate Polymers* **2019,** *219*, 210-218.

(218) Wan, Y.; Cui, T.; Zhang, Q.; Yang, Z.; Yao, F.; Luo, H. Submicrofiber-incorporated 3d bacterial cellulose nanofibrous scaffolds with enhanced cell performance. *Macromolecular Materials and Engineering* **2018,** *303* (11), 1800316.

(219) Chen, C.; Zhang, T.; Zhang, Q.; Feng, Z.; Zhu, C.; Yu, Y.; Li, K.; Zhao, M.; Yang, J.; Liu, J.; Sun, D. Three-dimensional bc/pedot composite nanofibers with high performance for electrode–cell interface. *ACS Applied Materials & Interfaces* **2015,** *7* (51), 28244-28253.

(220) Taokaew, S.; Phisalaphong, M.; Newby, B. Z. Modification of bacterial cellulose with organosilanes to improve attachment and spreading of human fibroblasts. *Cellulose* **2015,** *22* (4), 2311-2324.

(221) Osorio, M.; Ortiz, I.; Ganan, P.; Naranjo, T.; Zuluaga, R.; van Kooten, T. G.; Castro, C. Novel surface modification of three-dimensional bacterial nanocellulose with cell-derived adhesion proteins for soft tissue engineering. *Materials Science and Engineering C* **2019,** *100*, 697-705.

(222) Chen, C.; Yu, Y.; Li, K.; Zhao, M.; Liu, L.; Yang, J.; Liu, J.; Sun, D. Facile approach to the fabrication of 3d electroconductive nanofibers with controlled size and conductivity templated by bacterial cellulose. *Cellulose* **2015,** *22* (6), 3929-3939.

(223) Amjadi, M.; Pichitpajongkit, A.; Lee, S.; Ryu, S.; Park, I. Highly stretchable and sensitive strain sensor based on silver nanowire-elastomer nanocomposite. *ACS Nano* **2014,** *8* (5), 5154-5163.

(224) Trung, T. Q.; Tien, N. T.; Kim, D.; Jang, M.; Yoon, O. J.; Lee, N.-E. A flexible reduced graphene oxide field-effect transistor for ultrasensitive strain sensing. *Advanced Functional Materials* **2014,** *24* (1), 117-124.

(225) Yao, H. B.; Ge, J.; Wang, C. F.; Wang, X.; Hu, W.; Zheng, Z. J.; Ni, Y.; Yu, S. H. A flexible and highly pressure-sensitive graphene-polyurethane sponge based on fractured microstructure design. *Advanced Materials* **2013,** *25* (46), 6692-6698.

(226) Chen, C.; Song, J.; Zhu, S.; Li, Y.; Kuang, Y.; Wan, J.; Kirsch, D.; Xu, L.; Wang, Y.; Gao, T.; Wang, Y.; Huang, H.; Gan, W.; Gong, A.; Li, T.; Xie, J.; Hu, L. Scalable and sustainable approach toward highly compressible, anisotropic, lamellar carbon sponge. *Chem* **2018,** *4* (3), 544-554.

(227) Toivonen, M. S.; Kaskela, A.; Rojas, O. J.; Kauppinen, E. I.; Ikkala, O. Ambient-dried cellulose nanofibril aerogel membranes with high tensile strength and their use for aerosol collection and templates for transparent, flexible devices. *Advanced Functional Materials* **2015,** *25* (42), 6618-6626.

(228) Si, Y.; Wang, X.; Yan, C.; Yang, L.; Yu, J.; Ding, B. Ultralight biomass-derived carbonaceous nanofibrous aerogels with superelasticity and high pressure-sensitivity. *Advanced Materials* **2016,** *28* (43), 9512-9518.

(229) Sun, J.; Zhang, X.; Lang, Y.; Bian, J.; Gao, R.; Li, P.; Wang, Y.; Li, C. Piezo-phototronic effect improved performance of n -ZnO nano-arrays/ p -Cu_2O film based pressure sensor synthesized on flexible cu foil. *Nano Energy* **2017,** *32*, 96-104.

(230) Qi, H.; Mäder, E.; Liu, J. Electrically conductive aerogels composed of cellulose and carbon nanotubes. *Journal of Materials Chemistry A* **2013,** *1* (34), 9714-9720.

(231) Chen, Z.; Hu, Y.; Zhuo, H.; Liu, L.; Jing, S.; Zhong, L.; Peng, X.; Sun, R.-c. Compressible, elastic, and pressure-sensitive carbon aerogels derived from 2D titanium carbide nanosheets and bacterial cellulose for wearable sensors. *Chemistry of Materials* **2019,** *31* (9), 3301-3312.

(232) Huang, J.; Li, D.; Zhao, M.; Ke, H.; Mensah, A.; Lv, P.; Tian, X.; Wei, Q. Flexible electrically conductive biomass-based aerogels for piezoresistive pressure/strain sensors. *Chemical Engineering Journal* **2019,** *373*, 1357-1366.

(233) Khan, Z. U.; Edberg, J.; Hamedi, M. M.; Gabrielsson, R.; Granberg, H.; Wagberg, L.; Engquist, I.; Berggren, M.; Crispin, X. Thermoelectric polymers and their elastic aerogels. *Advanced Materials* **2016,** *28* (22), 4556-4562.

(234) Han, S.; Jiao, F.; Khan, Z. U.; Edberg, J.; Fabiano, S.; Crispin, X. Thermoelectric polymer aerogels for pressure-temperature sensing applications. *Advanced Functional Materials* **2017,** *27* (44), 1703549.

(235) Chen, Y.; Zhang, L.; Yang, Y.; Pang, B.; Xu, W.; Duan G.; Jiang, S.; Zhang, K. Recent progress on nanocellulose aerogels: Preparation, modifcation, composite fabrication, applications. *Advanced Materials* **2021**, *33*, 2005569.

(236) Li, T.; Chen, C.; Brozena, A. H.; Zhu, J. Y.; Xu, L.; Driemeier, C.; Dai, J.; Rojas, O. J.; Isogai, A.; Wagberg, L.; Hu, L. Developing fibrillated cellulose as a sustainable technological material. *Naure* **2021**, *590*, 47-56.

Chapter 3

Sponges with Janus Character: Preparation and Applications in the Treatment of Hemorrhagic Wounds

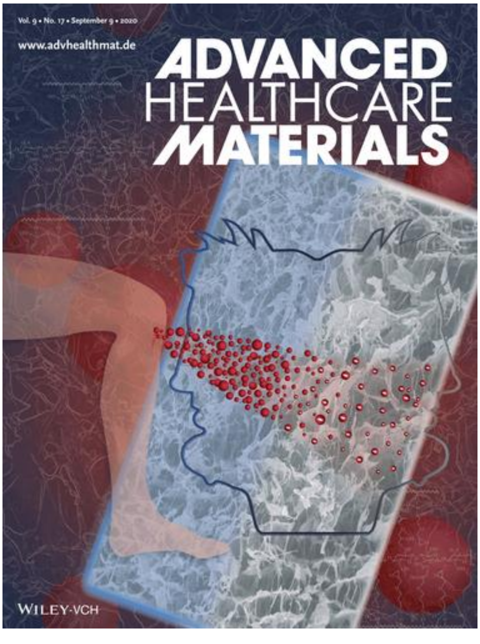

The development of a rapid and effective hemostatic dressing is highly desired in the treatment of hemorrhagic wounds. In this chapter, we describe sponges with Janus character using cellulose nanofibers (CNFs) that exhibit materials facets of different wettability characters using heterogeneous mixing and freeze-drying. The bonding of the interface between the hydrophilic and hydrophobic facets has been achieved by using interpenetrating chemical crosslinking between CNFs and organosilanes. The hydrophilic layer absorbs water from blood and works synergistically with the inherent hemostatic chitosan-rich complementary layer to accelerate blood clotting, displaying both active and passive hemostatic mechanisms. The hydrophobic layer prevents blood penetration into the construct and exerts proper pressure on the wound. Compared with the hydrophilic control samples and commercial gauzes, the Janus sponges can achieve effective bleeding control with nearly 50% less blood loss in the femoral artery injury model and prolong the survival time in the carotid artery injury model. Compared with the only hydrophilic layer, the time to hemostasis of Janus sponge was reduced from 165 ± 20 s to 131 ± 26 s in femoral artery injury model and from 102 ± 21 s to 83 ± 15 s in liver femoral artery injury model.

The contents of this chapter have been published as: Huan Cheng, Dongdong Xiao, Yujing Tang, Bijia Wang, Xueling Feng, Mujun Lu, G. Julius Vancso, and Xiaofeng Sui, Sponges with Janus Character from Nanocellulose: Preparation and Applications in the Treatment of Hemorrhagic Wounds. *Advanced Healthcare Materials*, **2020**, *9*, 1901796.

3.1 Introduction

Bionanotechnology harvests materials of natural origin and uses them in a broad range of applications. The field is based on the interface of nanotechnology, bio(medical) technology and biology [1]. Nanomaterials of biological origin, including nanocellulose, have gained a prominent place in bionanotechnology. Various forms of nanocellulose have become highly promising nanomaterials also in relation to the high concentration of chemical functional groups utilizing various substitution and modification chemistries [2-6]. In the field of biomaterials, especially in wound dressings, nanocellulose is very popular because of its unique advantages and easy processability. The effect of nanocellulose based composite materials on wound healing, preventing wound infection and hemostatic properties were studied widely in recent years [7-14].

In trauma, uncontrolled bleeding is a severe problem that can have detrimental consequences [15-16]. Therefore, it is necessary to control bleeding quickly and effectively [17]. For bleeding wounds, an urgent and effective treatment is to use a hemostatic dressing to cover the wound and to exert adequate pressure on the wound [18-19]. To induce clotting, hemostatic dressings either initiate platelet activation and clotting factors, or concentrate platelets, erythrocytes, and clotting factors *via* adsorbing water in blood [19].

Hemostatic materials are classified as being active and passive according to their mechanism of action. Active hemostatic materials activate platelets and the physiological coagulation cascade *in vivo,* such as human plasma components like thrombin and fibrin. Passive materials, such as gelatin and natural polysaccharide, promote blood absorption, and create pressure on wounds upon being swollen [20-21]. In order to achieve better hemostatic performance, many recent studies focused on the rational of combining active and passive hemostatic materials. Some examples include gelatin/thrombin loaded electrospun membranes [22], plant derived oxidized nanocellulose/silk fibroin/thrombin scaffolds [23], microporous starch with assembled thrombin [24], and thrombin-graphene sponge [25]. A variety of hemostatic dressings have been developed to meet the above hemostatic mechanisms. For example, Fan et al. employed a method to tightly bind mesoporous single-crystal chabazite zeolites onto the surface of cotton fibers. The as-prepared hemostatic materials have superior performance when compared with most other clay or zeolite-based inorganic hemostats, in terms of higher procoagulant activity, minimized loss of active components and better scalability for practical applications [26]. Hammond et al. coated active clotting proteins, such as thrombin, onto a water-sorbing gelatin sponge. These sponges promoted rapid hemostasis in a porcine spleen bleeding model [27]. A series of graphene based composite sponges were also reported for safe and effective hemostasis [28-32].

Functional materials with specific wettability [33] play an important role in hemostasis. For instance, Xu et al. described a gauze dressing exhibiting Janus character by integrating superhydrophobically modified gauzes with traditional superhydrophilic ones. Effective bleeding control and reduced blood loss were achieved with these materials [17]. However, most of these systems rely only on concentrating blood to cause hemostasis.

Among the reported hemostatic dressings, natural polysaccharide-based materials have received distinguished attention due to their unparalleled inherent advantages. In our previous work, cellulose nanofiber-chitosan hybrid sponges with controllable structure and morphology were prepared by a facile pathway [34]. Cellulose nanofibers (CNF), which are fundamental building components for these sponges, are eco-friendly materials with excellent mechanical properties and biodegradability in nature [35]. Although there are still questions about the cytotoxicity and/or biocompatibility caused by its nano-features, numerous studies proved that it can be applied to the field of biomaterials [36]. The cellulose nanofibers formed a skeleton support in our sponges, and the functional chitosan was coated onto the surface of the skeleton by crosslinking with γ-glycidoxypropyltrimethoxysilane (GPTMS). The hybrid sponges were non-toxic and outperformed silicon and gauze in promoting blood coagulation [34]. Encouraged by these promising studies we continue with the design and development of hemostatic sponges that combine the inherent hemostatic property of chitosan and the physical barrier of Janus structures.

Herein, we demonstrate a facile method to fabricate sponges of Janus character, based on cellulose nanofibers, by integrating heterogeneous mixing and freeze-drying. Attributed to the unique cellular composite framework composed of flexible cellulose nanofibers and organosilanes, the Janus structures we report on here present integrated features of low bulk density, contrasting wettability of hydrophobic and hydrophilic facets, and excellent underwater mechanical properties. More importantly, the sponges exhibit an outstanding blood clotting performance of up to 50% reduction in bleeding. Additionally, the sponges can also prolong the survival time in the carotid artery injury model. We anticipate that these Janus sponges would provide a new and promising alternative for developing novel, high performance hemostatic wound dressings.

3.2 Results and discussion

3.2.1. Fabrication and FT-IR characterization

To satisfy the requirements of wound dressing, we designed a sponge exhibiting a Janus structure using the following five design considerations: 1) the building blocks of flexible CNFs, the functional organosilane binders and chitosan should be assembled into a 3D framework with well-interconnected open structure to guarantee the absorption of blood; 2) the sponge must be partly or overall hydrophilic to ensure rapid liquid absorption; 3) the sponge should be non-cytotoxic to ensure safe contact with blood cells and body tissues; 4) the sponge should be able to stop bleeding quickly to minimize the risk of blood loss; and 5) the sponge may be able to block water and bacteria. A versatile freeze-drying technique was used to provide the porous framework. To satisfy the other design criteria, flexible cellulose nanofibers with good biocompatibility and biodegradability were chosen as building blocks and different organosilanes were used to change the wettability. Finally, chitosan with excellent hemostatic property was selected as a functional modifier.

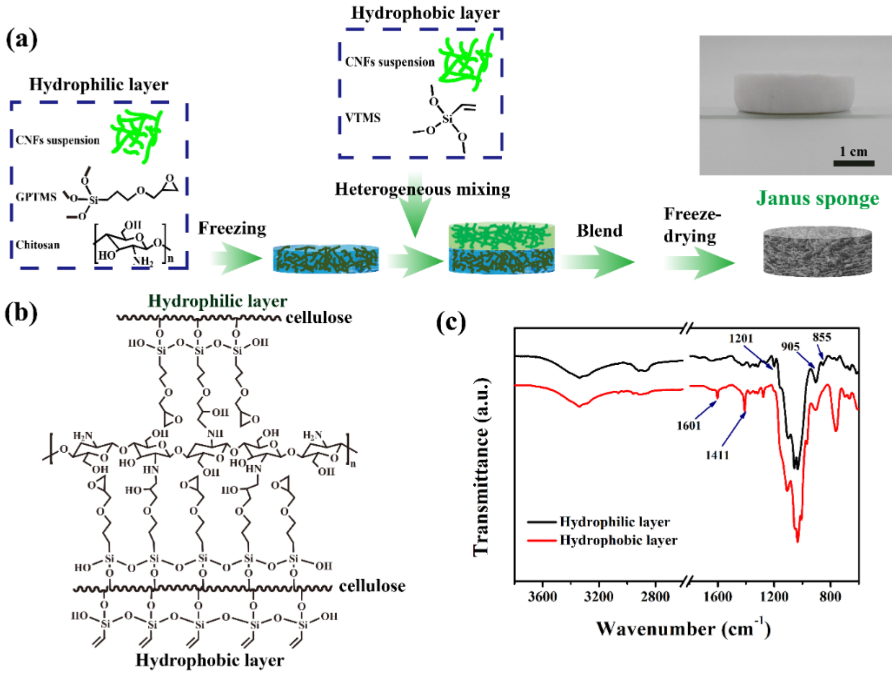

Figure 3.1 Fabrication and chemical characterization of sponges with Janus character. (a) illustration of fabricating Janus sponges, (b) proposed molecular structure of crosslinking within Janus sponges, and (c) FT-IR spectrum of the hydrophilic and hydrophobic layers in the Janus sponge.

The fabrication process of the sponges with Janus character is illustrated in **Figure 3.1a**, which involves five main components: CNFs, γ-glycidoxypropyltrimethoxysilane (GPTMS), chitosan, vinyltrimethoxysilane (VTMS) and deionized water. Generally, a CNFs/GPTMS/chitosan suspension and a CNFs/VTMS suspension were stirred at room temperature for 4 hours to hydrolyze the GPTMS and VTMS and allow crosslinking to take place. Subsequently, the hydrophilic layer suspension obtained was frozen into an ice gel, followed by pouring the hydrophobic layer suspension onto the upper portion of the ice gel. The mixture was allowed to stand at room temperature for 30 minutes so that the interface melted and the constituents mutually fixed. The final mixture was freeze-dried to obtain the Janus structure. To further synchronously build up stable bonding points among CFNs and organosilanes, the as-prepared sponge was heated (take 110°C for 30 min) to realize crosslinking.

To enhance the bonding between the two constituents at the relatively weak interface between the hydrophilic and the hydrophobic layers, we used two organosilanes of GPTMS and VTMS as crosslinkers. In the hydrophilic layer, GPTMS underwent hydrolysis and auto-condensation to form oligomers that hydrogen-bonded and reacted with cellulose and chitosan to form Si-O-C bonds [37-38]. In addition, the epoxy groups on GPTMS would also react with the amino groups on chitosan, forming stable chemical crosslinkings [39-40]. Meanwhile, in the hydrophobic layer, VTMS underwent hydrolysis and auto-condensation to form oligomers that hydrogen-bonded and reacted with the cellulose. Importantly, GPTMS and VTMS can then react with each other to form Si-O-Si bonds at the interface. The proposed chemical crosslinking within the Janus structured sponge is shown in **Figure 3.11b**. The auto-condensation of GPTMS and VTMS enhanced the mechanical properties of the Janus structured sponges and avoided the dissolution of GPTMS and VTMS during applications.

Figure 3.1c shows the FTIR spectra of the hydrophilic and the hydrophobic layers of the Janus structures. The absorption peaks at 1201, 905 and 855 cm^{-1} in the spectrum of the hydrophilic layer are attributed to the epoxy groups in the GPTMS [41-42], while the absorption peaks at 1601 and 1411 cm^{-1} present in the spectrum of the hydrophobic layer demonstrate the presence of the vinyl groups in the VTMS [43-44].

3.2.2 Wettability and morphology characterization

The two sides of this Janus structured wound dressing exhibit different wettability due to their inherently different affinity for water. The abundant presence of vinyl groups in the hydrophobic layer causes it to exhibit a large contact angle of 137°, promoting water droplets to be completely seated on its surface (**Figure 3.2a** and **b**). On the other hand, the hydrophilic layer with abundant amino and hydroxyl groups can quickly absorb the water droplets. However, the absorbed water does not further penetrate into the hydrophobic layer beyond the interface between the two phases with different wettability, as shown in **Figure 3.2b** and **c**. The interface is slightly stained by the blue dye in water, indicating the crosslinking of GPTMS and VTMS causing changes in the wettability of the layers.

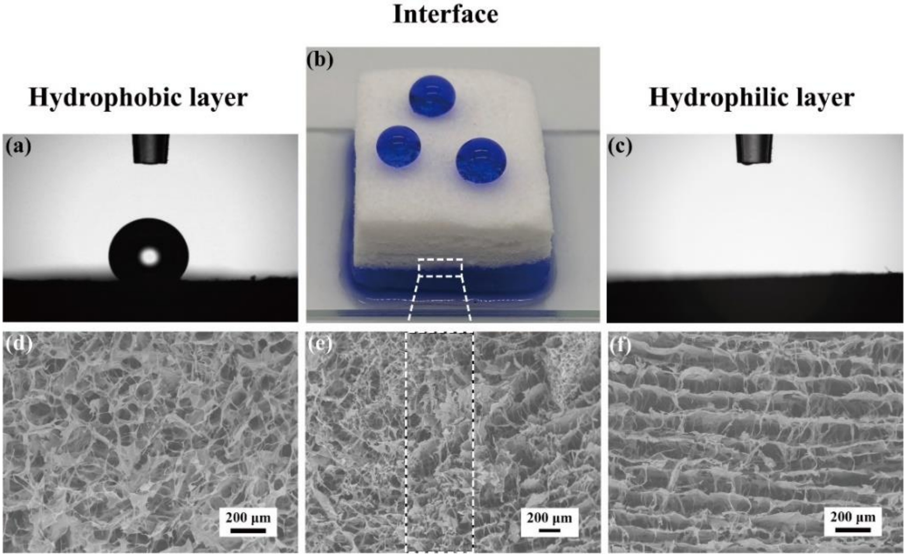

Figure 3.2 Wettability (a-c) and SEM images (d-f) of hydrophobic layer, hydrophilic layer and interface of the sponges with Janus character, respectively.

The micro structures of the sponges were observed by SEM. As can be seen from **Figure 3.2d-f**, the Janus sponge exhibited a disordered morphology in the hydrophobic layer, a regular structure in the hydrophilic layer and a transitional “interphase” structure at the interior interphase boundary. The porous structures facilitate the clotting components to enter the sponge and concentrate and accumulate in the pores [45]. Due to the aggregation of the nanofibers and the crosslinking of the organosilanes and nanofibers, there is no obvious secondary pore structure and nanoscale features on the thin sheets of the hydrophilic layer (**Figure S3.2**).

The formation mechanism of the unique hybrid structure is ascribed to the synergistic effects of the templating ice crystals utilized during freeze-drying and the phase separation and aggregation of chitosan molecular chains. In the hydrophilic layer, during the freeze-casting process, the gradual growth and fusion of the ice crystals render the dissolved chitosan to concentrate and aggregate among the ice crystals. The aggregated chitosan would then drive the cellulose nanofibers to move and settle down between the ice crystals [46]. Finally, chitosan and GPTMS would be bonded on the surface of the cellular walls together with the chemically crosslinked cellulose. However, the hydrophobic layer exhibits a disordered state since there is no soluble substance to drive the arrangement of the cellulose. The following lyophilization treatment allows the sponge layers to maintain their original 3D framework structures by removing the ice crystal template [47].

3.2.3 Mechanical characteristics and flexibility

Due to the interconnected cellular structure and the robust bonding interaction among nanofibers, sponges have a very low bulk density and excellent mechanical properties. The excellent mechanical properties of the hydrophilic layer have been confirmed in our previous work [34]. After compounding with the hydrophobic layer, the mechanical properties of the sponge only slightly changed.

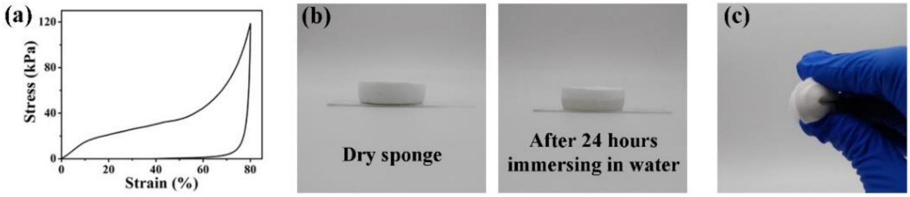

Figure 3.3 (a) Compressive stress-strain curve, (b) stability in water, and (c) flexibility of the Janus sponges.

The compressive stress-strain curve of the Janus structure at a deformation of 80% is presented in **Figure 3.3a**. It is noteworthy to mention that the sponge displayed a typical three-region stress-strain curve characteristic of traditional honeycomb-structured foam materials in the loading process, including an elastic region ($\varepsilon<10\%$) with a Young’s modulus of 47.0 kPa, a yield zone ($10\%<\varepsilon<60\%$) with mildly increasing stress, and a densification region (ε>60%) with rapidly increasing stress [48-51]. The Janus sponge exhibited 50% deformation when compressed with a load of 120 kPa. As hemostatic dressings are commonly used in aqueous environments and under pressure, therefore, it is more critical to evaluate the underwater mechanical properties of the Janus type sponges under these conditions. As shown in **Figure 3.3b-c**, the Janus type sponges displayed superior stability and flexibility after being immersed in water for 24 hours. More importantly, the squeezed sponge could quickly return to its original state once it is placed in water (**Figure S3.3**).

3.2.4 Cytocompatibility and hemostatic performance

Good cytocompatibility is an essential requirement for wound dressing materials. Materials with nano-features are considered to have potentially harmful risks to cells [52]. Since cellulose nanofibers have nano-level characteristics, its cytocompatibility needs to be studied. However, in this sponge, due to the extrusion of ice crystals and the crosslinking of organosilanes, cellulose nanofibers have basically lost their nano-features. This greatly reduces the potential toxicity due to the nano-features of the material.

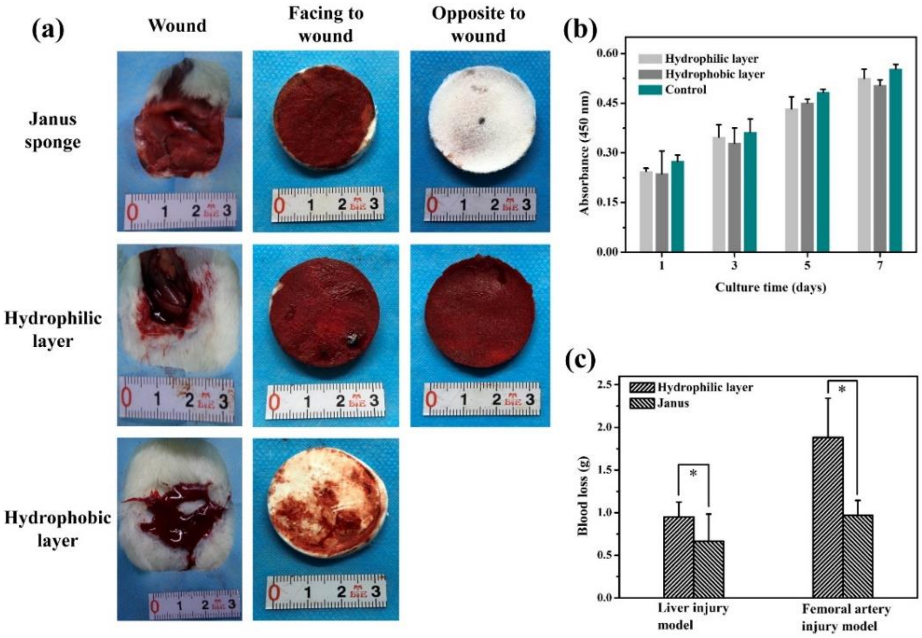

Figure 3.4 Cytocompatibility and hemostatic performance. (a) Representative photos of the rats with the injured femoral artery wrapped with Janus type sponge, hydrophilic layer,

and hydrophobic layer, respectively. (b) Biocompatibility of each component of Janus type sponge measured by their effects on human fibroblast proliferation. (c) Comparison of total blood loss absorbed by hydrophilic layer or Janus type sponges in the liver injury model and the femoral artery injury model. Significant differences are marked by (*) for $p < 0.05$.

The cytocompatibility of the components of the Janus sponges described here with human skin fibroblasts was evaluated. Results of *in vitro* cytotoxicity shown in **Figure 3.4b** illustrated that none of the two components exhibits toxicity and does not harm cell growth, making the sponge a promising candidate for wound dressing with good cytocompatibility. Importantly, this Janus sponge is a hemostatic dressing for external use and will not apply to the wound for a long time to cause cell adhesion and tissue growth, which is essential for removal from the wound without secondary injury. The Janus sponge is a potentially non-absorbable dressing for external use, the degradability and swelling properties are not key features and will not be evaluated.

To evaluate the hemostatic performance, a pure hydrophobic layer, a pure hydrophilic layer and a Janus sponge were used, respectively. Liver injury and femoral artery injury models were employed to measure total blood loss. Taking the femoral artery injury model as example (**Figure 3.4a**), the hydrophilic layer and the Janus sponge absorb blood quickly and completely. However, the blood passes through the hydrophilic layer due to the absence of a hydrophobic barrier. For the Janus sponge, only the inner hydrophilic layer is wetted by blood whereas the outer hydrophobic layer remains essentially clean.

The total blood loss decreased by 29%, and by 49% in liver, and femoral artery injury model, respectively, when the Janus sponge was used (**Figure 3.4c**). Compared with the only hydrophilic layer, the time to hemostasis of Janus sponge was reduced from 165 ± 20 s to 131 ± 26 s in the femoral artery injury model and from 102 ± 21 s to 83 ± 15 s in the liver femoral artery injury model. The effective hemostasis and the remarkable decrease of blood loss are due to the fact that the hydrophilic layer absorbs water in the blood and accelerates the clotting with a synergistic effect supported by the inherent hemostatic properties of chitosan, while the hydrophobic layer prevents further blood permeating and exerts proper pressure. Chitosan can facilitate the interaction and aggregation of platelets, improve the release of serotonin and thromboxane A2, and promote the rapid formation of platelet thrombus. The abundant amino and hydroxyl groups within the sponge can also affect the complement system, allowing platelets to exert better hemostasis [53]. Platelets can adhere well to the pore walls of the hydrophilic layer, which has a good promoting effect on hemostasis (**Figure S3.4**). For the Janus sponges, the second hydrophobic layer is only marginally wetted by blood due to its hydrophobicity.

Although the hemostatic effect of only the hydrophilic control sample is superior to that of the conventional gauze of the same mass (total blood loss of 3.38 ± 0.54 g for common gauze, **Figure S3.5**), the hemostatic performance of the Janus sponge is further improved compared to the hydrophilic sponge used alone. For the carotid artery injury model with a higher bleeding flow, although there is no remarkable decrease in total blood loss using the Janus sponges, the survival time prolongs from 99 ± 36 s for the hydrophilic layer to 170 ± 60 s for the Janus type sponges, corresponding to an increase of 73%. The prolonged survival time could be ascribed to the blood repellence of the hydrophobic layer as it competes against the suction of blood by the hydrophilic layer, slowing down the bleeding. Accordingly, the use of Janus sponges might provide more rescue time for prehospital patients or for the wounded in the battlefield. The morphology of the Janus type sponge after use is shown in **Figure S6**. The pores of the hydrophilic layer are filled with dried blood clots.

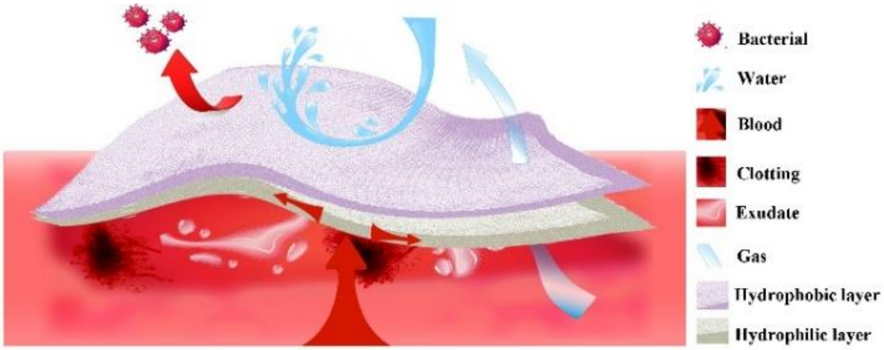

Figure 3.5 Illustration showing wound repair assisted by the sponges described here with Janus character.

In view of the results mentioned above, a scheme describing the proposed wound repair mechanism is shown in **Figure 3.5**. We further note that the material of these Janus sponges as a whole is safe and non-toxic. The hydrophobic layer not only prevents blood from penetrating, but also provides a waterproof layer and may block the penetration of bacteria (**Figure S3.7**), reducing the possibility of infection during use. The Janus sponge has a proper moisture permeability of 2530 ± 196 g/m^2·day, which is beneficial to maintenance of a breathable and moist wound environment.

3.3 Conclusions

In summary, we report on the successful development of a new hemostatic wound dressing construct sponge obtained by the integration of heterogenous, microporous materials with different wettability. Benefitting from the 3D fibrous cellular network that consists of flexible cellulose nanofibers and organosilanes, the sponges showed Janus character that exhibited excellent underwater flexibility and shape-memory behavior. The comprehensive advantages of the unique Janus structure with different wettability on both sides, supported by the hemostatic property of chitosan, endowed the sponges with a 49% reduction of blood loss compared with only a hydrophilic control sample and common gauze. We anticipate that such Janus sponges have a great potential in emergency hemostatic wound dressing applications.

3.4 Experimental Section

3.4.1 Materials

Cellulose nanofiber suspension (solid content: 1.3 wt.%, raw material: spruce wood pulp, carboxyl and aldehydes content: 0%, cellulose content: 86.08%, hemicellulose content: 13.68%, lignin content: 0.24%; homogenized 12 times with the pressure 100 MPa) was provided by Tianjin Haojia Cellulose Co., Ltd. (China) and was subjected to high pressure homogenization (APV-2000 Homogenizer, Germany) before use (homogenized once with the pressure 500 bar). A TEM image of the CNFs after high pressure homogenization is provided as supporting information (**Figure S1**). Cellulose nanofibers with diameters under 100 nm and lengths in the micrometer range were dominant in the suspension. Chitosan (CS, degree of deacetylation ≥ 95%, viscosity > 400 mPa s^{-1}) was obtained from Shanghai Macklin Biochemical Co., Ltd (China). γ-Glycidoxypropyltrimethoxysilane (GPTMS), vinyltrimethoxysilan (VTMS), and acetic acid (AcOH) were purchased from Sinopharm Chemical Reagent Co., Ltd (China). All reagents were analytical grade and used without further purification. Deionized water was used in sample preparation.

3.4.2 Preparation

3.4.2.1 Hydrophilic layer suspension. Chitosan (0.13 g) was dissolved in 9.87 g of acetic acid aqueous solution (1.0 wt.%) to prepare the chitosan solution (1.3 wt.%). 0.13 g of GPTMS was added dropwise into 10 g of mixed suspension of CNF (1.3 wt.%) and chitosan (1.3 wt.%), and the mixture was magnetically stirred for 4 h at ambient temperature.

3.4.2.2 Hydrophobic layer suspension. 0.13 g of VTMS was added dropwise into 10 g suspension of CNF (1.3 wt.%), and the mixture was magnetically stirred for 4 h at ambient temperature.

3.4.2.3 Preparation of the sponges. The hydrophilic layer suspension was first frozen into an ice gel at -80°C. The same amount of hydrophobic layer suspension was then poured onto the ice gel and allowed to stand at room temperature (20°C) for 30 minutes to allow the interface to melt and mutually permeate. The resulting mixture was then frozen and freeze-dried at -50°C for 36 h by a freeze-drier (Labconco FD5-3, USA) to yield a sponge which was heated to and maintained at 110°C for 30 min to promote crosslinking among cellulose, chitosan and GPTMS. The cured sponges were washed with deionized water and acetone to remove physically-adsorbed GPTMS followed by vacuum drying at 30°C for 24 h.

3.4.3 Characterization

3.4.3.1 Scanning electron microscopy (SEM). Morphologies of the hydrophobic and the hydrophilic layer and the Janus sponges were observed by a Hitachi TM-3030 scanning electron microscope (Japan). Samples for SEM were prepared by ion sputtering with an Au target by using an ion sputtering system (SBC-12, KYKY Technology Development Ltd, China) in vacuum. The acceleration voltage was 15 kV. The supplement SEM images of pore wall of the sponge were explored by field emission scanning electron microscopy (FESEM) (SU8010, Hitachi, Japan) at 15 kV after sputtering with an Au target by using an ion sputtering system (SBC-12, KYKY Technology Development Ltd, China) in vacuum.

3.4.3.2 Fourier transform infrared spectroscopy (FT-IR). FT-IR was carried out on a Perkin Elmer Spectrum Two in the wavenumber range of 3800-600 cm^{-1} at a resolution of 4 cm^{-1}.

3.4.3.3 Mechanical properties. The mechanical properties of the sponge samples (diameter 37 mm, scale distance 9 mm) were evaluated using a Youhong universal testing machine (China) at a compression speed of 2 mm min^{-1}. The thickness recovery S was defined as the percentage of the original thickness according to equation (1):

$$S\ (\%) = 100 - \varepsilon_{\mathrm{final}} \tag{1}$$

where $\varepsilon_{\mathrm{final}}$ is the strain when the force detected reached 0 N.

3.4.3.4 Wettability.

Water contact angle was measured by an optical contact angle analyzer (Attension theta, Biolin scientific, Finland), and liquid drops (5.0 μL) on the surface of the sponge substrate were recorded after 30 s. At least three points were chosen on each sample to calculate the average contact angle value.

3.4.3.5 Cytocompatibility.

The cytocompatibility of each component of the Janus sponges was evaluated by extraction using human skin fibroblast (Shanghai Cell Library of Chinese Academy of Science, Shanghai, China) proliferation using a Cell Counting Kit-8 (CCK-8) (Dojindo Molecular Technologies, Inc., Kumamoto, Japan) according to the manufacturer's protocol. In brief, fourth passage human fibroblasts were counted and pre-seeded into 96-well plates (BD Falcon, Corning Inc., NY, USA) with a density of 1,000 cells per well in Dulbecco's Modified Eagle Medium (DMEM) supplemented with 10% fetal bovine serum and cultured at 37°C in 5% humidified carbon dioxide (CO_2) overnight. Then, the culture medium was replaced by conditioned medium of each component of the Janus sponge, which was prepared by immersing hemostatic materials (0.8 g) in the aforementioned complete DMEM culture medium (50 mL) under constant stirring at 37°C for 48 hours in advance. Cells incubated with fresh complete DMEM medium were set as the positive control group. Complete DMEM medium without cells is regarded as the blank control. At 1, 3, 5, and 7 days, the culture media were aspirated, replaced by fresh DMEM, and 10 μL of CCK-8 per well was added. After 2 hours of incubation at 37°C in 5% humidified CO_2, the absorbance at 450 nm was measured using a microplate reader (Varioskan, Thermo Fisher Scientific Inc., MA, USA).

3.4.3.6 Animal model

We guarantee that all operations in experimental animals included in this study are in accordance with the national legislations on animal welfare and were supervised in this study by the Institutional Animal Care and Use Committee of Shanghai Ninth People's Hospital (Licence number: HKDL [2016]149). Eight-week-old male Sprague-Dawley (SD) rats (150-200 g, Shanghai Sippr-BK Laboratory Animals Ltd., Shanghai, China were used for hemostatic in vivo studies. The sample size and group allocation are described below accordingly. They were housed in a pathogen-free environment at temperatures of 20-22°C, humidity of 40-70% and day/night cycle of 12/12 h with free access to food and water.

In general, the sponge was tailored into a round shape (diameter: 3 cm; thickness: 0.8 cm; weight: 0.8 g). The hemostatic efficacy of the Janus sponges was evaluated in three representative models of liver injury model, femoral artery injury model, and carotid artery injury model. Six SD rats were randomly assigned for each sample in the respective animal model. Anaesthesia before animal experiments was induced by inhalation of isoflurane. After experiments, SD rats received euthanasia by inhalation of CO_2.

Liver injury model: After disinfected by iodine, SD rats' upper abdominal region was incised longitudinally along the linear alba for approximately 3 cm. The right lobe of the liver was extruded out of the abdominal cavity and a T-shape incision was created in the central area by scalpel (longitudinal length: 1 cm, transverse length: 1 cm, depth: 0.2 cm). Then round-shaped Janus sponges (hydrophilic side towards liver), and single hydrophilic and hydrophobic layers of sponges were applied to cover the liver incision immediately with a pressure.

Femoral artery animal model: After disinfection and hair shaving, a 3 cm incision was created along the right groin to expose the right femoral neurovascular bundle. The right femoral artery was isolated from the femoral neurovascular bundle and cut at the junction with inguinal ligament. The sponges were applied to the injury immediately.

Carotid artery animal model: After disinfection and hair shaving, a 2 cm longitudal incision was created in the middle of the neck, and underlying muscle layer to expose the trachea. The right carotid artery was isolated and cut at the level of cricoid cartilage. The sponges were applied to the injury immediately.

The hemostatic materials were weighed before and after hemostatic application to measure the total blood loss, which was not performed for sponges with a single hydrophobic layer because of its inability to absorb blood. The bleeding site was observed every 20 s to determine whether bleeding had been stanched. The period from the moment when the wound was wrapped by hemostatic materials to the moment when bleeding was stanched (no rebleeding within 10 s) was recorded as the hemostasis time. The heartbeat of rats was monitored in carotid artery animal model. The survival time was defined as the time from the injury creation to the heartbeat termination. All hemostatic *in vivo* experiments were performed by a professional surgeon who was blind to hemostatic materials group allocation.

3.4.3.7 Statistical analysis.

The data presented in this paper are expressed as mean ± standard error. Six adult rats as a group were assigned randomly for each sample in each animal model (n=6). Origin 8.0 (OriginLab Corporation, USA) was used to perform the statistical analyses and draw corresponding statistical graphs. Two-tailed Student's t-test or one-way analysis of variance with Tukey's *post hoc* test was selected according to different data sets. A P value of <0.05 was regarded as statistical significance.

3.5 References

(1) Goodsell, D. S. *Bionanotechnology: Lessons from nature*, Wiley-Liss: Hoboken, N.J., 2004.

(2) Klemm, D.; Kramer, F.; Moritz, S.; Lindstrom, T.; Ankerfors, M.; Gray, D.; Dorris, A. Nanocelluloses: A new family of nature-based materials. *Angewandte Chemie International Edition* **2011,** *50* (24), 5438-5466.

(3) Dufresne, A. Nanocellulose: A new ageless bionanomaterial. *Materials Today* **2013,** *16* (6), 220-227.

(4) Habibi, Y. Key advances in the chemical modification of nanocelluloses. *Chemical Society Reviews* **2014,** *43* (5), 1519-42.

(5) De France, K. J.; Hoare, T.; Cranston, E. D. Review of hydrogels and aerogels containing nanocellulose. *Chemistry of Materials* **2017,** *29* (11), 4609-4631.

(6) Mohammed, N.; Grishkewich, N.; Tam, K. C. Cellulose nanomaterials: Promising sustainable nanomaterials for application in water/wastewater treatment processes. *Environmental Science: Nano* **2018,** *5* (3), 623-658.

(7) Nordli, H. R.; Pukstad, B.; Chinga-Carrasco, G.; Rokstad, A. M. Ultrapure wood nanocellulose-assessments of coagulation and initial inflammation potential. *ACS Applied Bio Materials* **2019,** *2* (3), 1107-1118.

(8) Ahn, S.; Chantre, C. O.; Gannon, A. R.; Lind, J. U.; Campbell, P. H.; Grevesse, T.; O'Connor, B. B.; Parker, K. K. Soy protein/cellulose nanofiber scaffolds mimicking skin extracellular matrix for enhanced wound healing. *Advanced Healthcare Materials* **2018,** *7* (9), e1701175.

(9) Cheng, F.; Liu, C.; Wei, X.; Yan, T.; Li, H.; He, J.; Huang, Y. Preparation and characterization of 2,2,6,6-tetramethylpiperidine-1-oxyl (tempo)-oxidized cellulose nanocrystal/alginate biodegradable composite dressing for hemostasis applications. *ACS Sustainable Chemistry & Engineering* **2017,** *5* (5), 3819-3828.

(10) Li, J.; Cha, R.; Mou, K.; Zhao, X.; Long, K.; Luo, H.; Zhou, F.; Jiang, X. Nanocellulose-based antibacterial materials. *Advanced Healthcare Materials* **2018,** *7* (20), e1800334.

(11) Yuan, H.; Chen, L.; Hong, F. F. A biodegradable antibacterial nanocomposite based on oxidized bacterial nanocellulose for rapid hemostasis and wound healing. *ACS Applied Materials & Interfaces* **2020,** *12* (3), 3382-3392.

(12) Xu, C.; Zhang Molino, B.; Wang, X.; Cheng, F.; Xu, W.; Molino, P.; Bacher, M.; Su, D.; Rosenau, T.; Willfor, S.; Wallace, G. 3d printing of nanocellulose hydrogel scaffolds with tunable mechanical strength towards wound healing application. *Journal of Materials Chemistry B* **2018,** *6* (43), 7066-7075.

(13) Gao, H.; Zhong, Z.; Xia, H.; Hu, Q.; Ye, Q.; Wang, Y.; Chen, L.; Du, Y.; Shi, X.; Zhang, L. Construction of cellulose nanofibers/quaternized chitin/organic rectorite composites and their application as wound dressing materials. *Biomaterials Science* **2019,** *7* (6), 2571-2581.

(14) Ye, S.; Jiang, L.; Wu, J.; Su, C.; Huang, C.; Liu, X.; Shao, W. Flexible amoxicillin-

grafted bacterial cellulose sponges for wound dressing: In vitro and in vivo evaluation. *ACS Applied Materials & Interfaces* **2018,** *10* (6), 5862-5870.

(15) Katzenell, M. U.; Ash, B. G. N.; Tapia, C. A. L.; Campino, M. G. A.; Glassberg, L. C. E. Analysis of the causes of death of casualties in field military setting. *Military Medicine* **2012,** *117* (9), 1065-1068.

(16) Bu, Y.; Zhang, L.; Liu, J.; Zhang, L.; Li, T.; Shen, H.; Wang, X.; Yang, F.; Tang, P.; Wu, D. Synthesis and properties of hemostatic and bacteria-responsive in situ hydrogels for emergency treatment in critical situations. *ACS Applied Materials & Interfaces* **2016,** *8* (20), 12674-12683.

(17) Zhu, T.; Wu, J.; Zhao, N.; Cai, C.; Qian, Z.; Si, F.; Luo, H.; Guo, J.; Lai, X.; Shao, L.; Xu, J. Superhydrophobic/superhydrophilic janus fabrics reducing blood loss. *Advanced Healthcare Materials* **2018,** *7* (7), e1701086.

(18) Arnaud, F.; Teranishi, K.; Tomori, T.; Carr, W.; McCarron, R. Comparison of 10 hemostatic dressings in a groin puncture model in swine. *Journal of Vascular Surgery* **2009,** *50* (3), 632-639.

(19) Jesty, J.; Wieland, M.; Niemiec, J. Assessment in vitro of the active hemostatic properties of wound dressings. *Journal of Biomedical Materials Research Part B: Applied Biomaterials* **2009,** *89* (2), 536-542.

(20) de Carvalho, M. V. H.; Marchi, E. Mechanism of action of topical hemostatic and adhesive tissue agents. *Rev Med Minas Gerais* **2013,** *23* (4), 488-493.

(21) Spotnitz, W. D.; Burks, S. Hemostats, sealants, and adhesives: Components of the surgical toolbox. *Transfusion* **2008,** *48* (7), 1502-1516.

(22) Cheng, H.; Xiong, J.; Xie, Z.; Zhu, Y.; Liu, Y.; Wu, Z.; Yu, J.; Guo, Z. Thrombin-loaded poly(butylene succinate)-based electrospun membranes for rapid hemostatic application. *Macromolecular Materials and Engineering* **2018,** *303* (2), 1700395.

(23) Shefa, A. A.; Taz, M.; Lee, S. Y.; Lee, B. T. Enhancement of hemostatic property of plant derived oxidized nanocellulose-silk fibroin based scaffolds by thrombin loading. *Carbohydrate Polymers* **2019,** *208*, 168-179.

(24) Li, Q.; Lu, F.; Shang, S.; Ye, H.; Yu, K.; Lu, B.; Xiao, Y.; Dai, F.; Lan, G. Biodegradable microporous starch with assembled thrombin for rapid induction of hemostasis. *ACS Sustainable Chemistry & Engineering* **2019,** *7* (10), 9121-9132.

(25) Li, G.; Quan, K.; Xu, C.; Deng, B.; Wang, X. Synergy in thrombin-graphene sponge for improved hemostatic efficacy and facile utilization. *Colloids and Surfaces B: Biointerfaces* **2018,** *161*, 27-34.

(26) Yu, L.; Shang, X.; Chen, H.; Xiao, L.; Zhu, Y.; Fan, J. A tightly-bonded and flexible mesoporous zeolite-cotton hybrid hemostat. *Nature Communications.* **2019,** *10* (1), 1932.

(27) Shukla, A.; Fang, J. C.; Puranam, S.; Jensen, F. R.; Hammond, P. T. Hemostatic multilayer coatings. *Advanced Materials* **2012,** *24* (4), 492-496.

(28) Li, G.; Quan, K.; Liang, Y.; Li, T.; Yuan, Q.; Tao, L.; Xie, Q.; Wang, X. Graphene-montmorillonite composite sponge for safe and effective hemostasis. *ACS Applied Materials & Interfaces* **2016,** *8* (51), 35071-35080.

(29) Quan, K.; Li, G.; Tao, L.; Xie, Q.; Yuan, Q.; Wang, X. Diaminopropionic acid reinforced graphene sponge and its use for hemostasis. *ACS Applied Materials & Interfaces* **2016,** *8* (12), 7666-7673.

(30) Li, G.; Quan, K.; Xu, C.; Deng, B.; Wang, X. Synergy in thrombin-graphene sponge for improved hemostatic efficacy and facile utilization. *Colloids Surf. B Biointerfaces*

2018, *161*, 27-34.

(31) Liang, Y.; Xu, C.; Li, G.; Liu, T.; Liang, J. F.; Wang, X. Graphene-kaolin composite sponge for rapid and riskless hemostasis. *Colloids and Surfaces B: Biointerfaces* **2018,** *169*, 168-175.

(32) Li, G.; Liang, Y.; Xu, C.; Sun, H.; Tao, L.; Wei, Y.; Wang, X. Polydopamine reinforced hemostasis of a graphene oxide sponge via enhanced platelet stimulation. *Colloids and Surfaces B: Biointerfaces* **2019,** *174*, 35-41.

(33) Sun, Y.; Guo, Z. Recent advances of bioinspired functional materials with specific wettability: From nature and beyond nature. *Nanoscale Horizons* **2019,** *4* (1), 52-76.

(34) Cheng, H.; Li, C.; Jiang, Y.; Wang, B.; Wang, F.; Mao, Z.; Xu, H.; Wang, L.; Sui, X. Facile preparation of polysaccharide-based sponges and their potential application in wound dressing. *Journal of Materials Chemistry B* **2018,** *6* (4), 634-640.

(35) Klemm, D.; Cranston, E. D.; Fischer, D.; Gama, M.; Kedzior, S. A.; Kralisch, D.; Kramer, F.; Kondo, T.; Lindström, T.; Nietzsche, S.; Petzold-Welcke, K.; Rauchfuß, F. Nanocellulose as a natural source for groundbreaking applications in materials science: Today's state. *Materials Today* **2018,** *21* (7), 720-748.

(36) Xue, Y.; Mou, Z.; Xiao, H. Nanocellulose as a sustainable biomass material: Structure, properties, present status and future prospects in biomedical applications. *Nanoscale* **2017,** *9* (39), 14758-14781.

(37) Zhang, Z.; Sèbe, G.; Rentsch, D.; Zimmermann, T.; Tingaut, P. Ultralightweight and flexible silylated nanocellulose sponges for the selective removal of oil from water. *Chemistry of Materials* **2014,** *26* (8), 2659-2668.

(38) Lu, J.; Askeland, P.; Drzal, L. T. Surface modification of microfibrillated cellulose for epoxy composite applications. *Polymer* **2008,** *49* (5), 1285-1296.

(39) Lv, L.; Zhang, J.; Yuan, S.; Huang, L.; Tang, S.; Liang, B.; Pehkonen, S. O. Enhanced adsorption of cu(ii) ions on chitosan microspheres functionalized with polyethylenimine-conjugated poly(glycidyl methacrylate) brushes. *RSC Advances* **2016,** *6* (81), 78136-78150.

(40) F. J. Xu; Q. J. Cai; Y. L. Li; E. T. Kang; Neoh, K. G. Covalent immobilization of glucose oxidase on well-defined poly(glycidyl methacrylate)–si(111) hybrids from surface-initiated atom-transfer radical polymerization. *Biomacromolecules* **2005,** *6*, 1012-1020.

(41) Dong, Z.; Zhao, J.; Du, J.; Li, C.; Zhao, L. Radiation synthesis of spherical cellulose-based adsorbent for efficient adsorption and detoxification of Cr(VI). *Radiation Physics and Chemistry* **2016,** *126*, 68-74.

(42) Cheng, H.; Li, Y.; Wang, B.; Mao, Z.; Xu, H.; Zhang, L.; Zhong, Y.; Sui, X. Chemical crosslinking reinforced flexible cellulose nanofiber-supported cryogel. *Cellulose* **2017,** *25* (1), 573-582.

(43) Smitha, S.; Shajesh, P.; Mukundan, P.; Warrier, K. G. K. Antiwetting silica–gelatin nanohybrid and transparent nano coatings synthesised through an aqueous sol–gel process. *Journal of Sol-Gel Science and Technology* **2007,** *42* (2), 157-163.

(44) Wu, Z.; Li, Y.; Zhang, L.; Zhong, Y.; Xu, H.; Mao, Z.; Wang, B.; Sui, X. Thiol–ene click reaction on cellulose sponge and its application for oil/water separation. *RSC Advances* **2017,** *7* (33), 20147-20151.

(45) Liu, C.; Liu, X.; Liu, C.; Wang, N.; Chen, H.; Yao, W.; Sun, G.; Song, Q.; Qiao, W. A highly efficient, in situ wet-adhesive dextran derivative sponge for rapid hemostasis.

Biomaterials **2019,** *205*, 23-37.

(46) Qian, F.; Lan, P. C.; Freyman, M. C.; Chen, W.; Kou, T.; Olson, T. Y.; Zhu, C.; Worsley, M. A.; Duoss, E. B.; Spadaccini, C. M.; Baumann, T.; Han, T. Y. Ultralight conductive silver nanowire aerogels. *Nano Letters* **2017,** *17* (12), 7171-7176.

(47) Zhu, L.; Zong, L.; Wu, X.; Li, M.; Wang, H.; You, J.; Li, C. Shapeable fibrous aerogels of metal-organic-frameworks templated with nanocellulose for rapid and large-capacity adsorption. *ACS Nano* **2018,** *12* (5), 4462-4468.

(48) Fu, Q.; Si, Y.; Duan, C.; Yan, Z.; Liu, L.; Yu, J.; Ding, B. Highly carboxylated, cellular structured, and underwater superelastic nanofibrous aerogels for efficient protein separation. *Advanced Functional Materials* **2019,** *29* (13), 1808234.

(49) Gao, H. L.; Zhu, Y. B.; Mao, L. B.; Wang, F. C.; Luo, X. S.; Liu, Y. Y.; Lu, Y.; Pan, Z.; Ge, J.; Shen, W.; Zheng, Y. R.; Xu, L.; Wang, L. J.; Xu, W. H.; Wu, H. A.; Yu, S. H. Super-elastic and fatigue resistant carbon material with lamellar multi-arch microstructure. *Nature Communications* **2016,** *7*, 12920.

(50) Kim, K. H.; Oh, Y.; Islam, M. F. Graphene coating makes carbon nanotube aerogels superelastic and resistant to fatigue. *Nature Nanotechnology* **2012,** *7* (9), 562-566.

(51) Qiu, L.; Liu, J. Z.; Chang, S. L.; Wu, Y.; Li, D. Biomimetic superelastic graphene-based cellular monoliths. *Nature Communications* **2012,** *3*, 1241.

(52) Andre, N.; Tian, X.; Lutz, M. D.; Ning, L. Toxic potential of materials at the nanolevel. *Science* **2006,** *311*, 622-627.

(53) Sagnella, S.; Mai-Ngam, K. Chitosan based surfactant polymers designed to improve blood compatibility on biomaterials. *Colloids and Surfaces B: Biointerfaces* **2005,** *42* (2), 147.

3.6 Supporting Information

3.6.1 Supporting experimental section

Platelet adhesion:

Whole blood (18.0 mL) from Sprague-Dawley rats and anticoagulant sodium citrate solution (38 mg/mL, 2.0 mL) were mixed under stirring, and the platelet solution was separated from the red blood cell portion by centrifuging for evaluating the platelet adhesion of samples.

The hydrophilic layer of the Janus sponge was rinsed 3 times with PBS buffer solution (6.7 mM, pH 7.4), then it was covered with platelet solution and incubated at 37°C under 5% CO_2 condition for 1 h. The sample was taken out and slightly rinsed 3 times with PBS to remove non-adherent platelets, and fixed in 2.5% glutaraldehyde fixative for 6 h at 4°C. Then it was freeze-dried for SEM observation.

The SEM images of platelets adhesion on the pore wall were tested by scanning electron microscopy (NeoScope, JCM-5100, JEOL, Japan) at 20-25 kV after sputter-coated with Au (NeoCaster, MP-1920NCTR, JEOL, Tokyo, Japan).

Water vapor transmission rate:

To determine the moisture permeability of the Janus cellulose sponge, the WVTR was measured according to the American Society for Testing and Materials (ASTM) standard. Briefly, a sample was cut into a disc and mounted on the mouth of a cylindrical cup containing distilled water. The sample and cup were sealed with Teflon tape across the edge and then placed into a 37°C incubator at 50% relative humidity. The loss weight of 1h was recorded. All measurements were repeated three times (n = 5).

$$WVTR\ (\mathrm{g}/m^2 \cdot \mathrm{day}) = \frac{m_0 - m}{A \bullet t} \times 24$$

Where m_0 is the initial weight of cup, m is the weight of cup after 1h in a 37°C incubator at 50% relative humidity, A is the area of the samples, t is 1h.

Antibacterial performance:

A qualitative assay- agar diffusion plate test was added to evaluate the antibacterial property of the hydrophilic layer (direct contact with skin and wounds) in comparison with gauze. This assay was carried out on round shaped sponges of 14 mm in diameter.

Pieces of samples were inoculated with approximately 1 mL of bacterial suspension (1 × 10^8 CFU/mL) per tryptic soya agar plate. The plates were incubated at 37°C for 24 h.

3.6.2 Supporting results and discussion

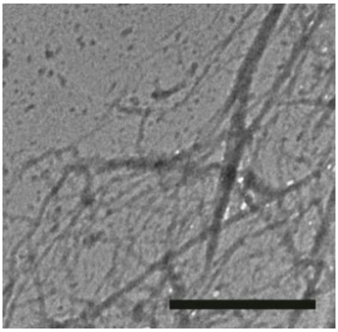

Figure S3.1 TEM image of cellulose nanofibers (scale bar: 500 nm).

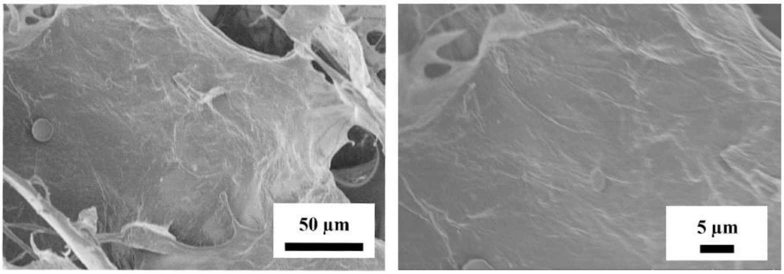

Figure S3.2 SEM images of pore wall of the hydrophilic layer of the sponge.

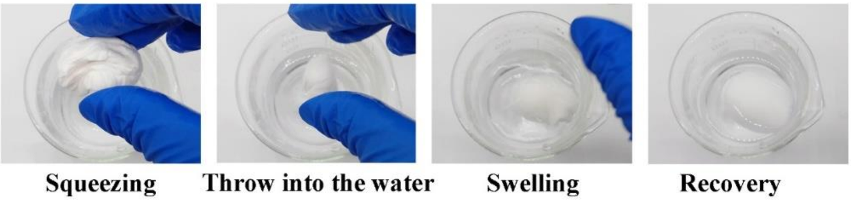

Figure S3.3 Underwater shape recovery of Janus sponge.

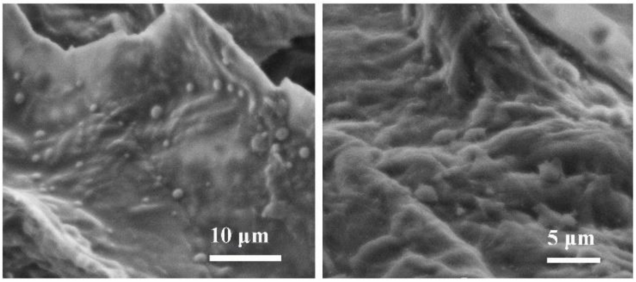

Figure S3.4 SEM images of the platelet adhesion on the pore wall.

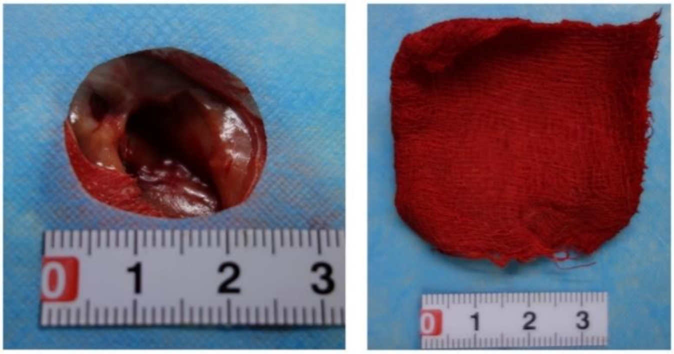

Figure S3.5 Clotting performance of common gauze in the femoral artery injury model.

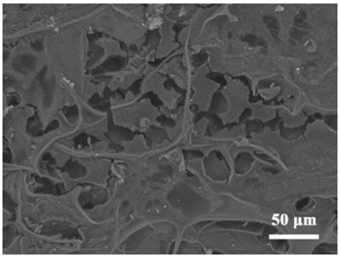

Figure S3.6 SEM image of the hydrophilic layer of a Janus sponge after use in femoral artery injury model.

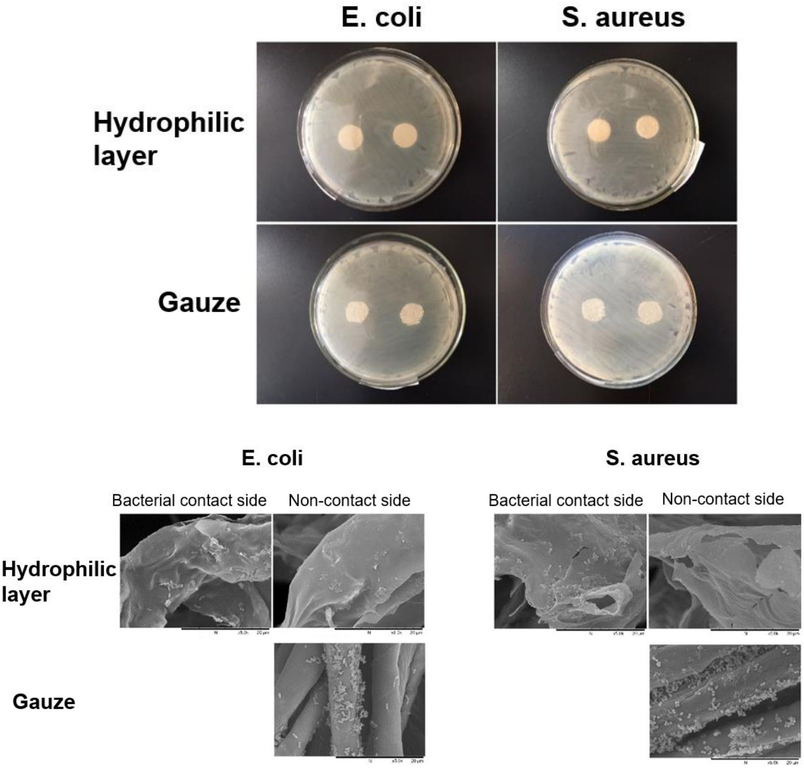

Figure S3.7 Antibacterial tests and SEM images of hydrophilic layer and gauze.

The sponges and gauze were observed using SEM. A barrier effect against *E. coli* (Gram-negative) and *S. aureus* (Gram-positive) can be seen, due to the chitosan component and the 3D structure of the sponge. On the hydrophilic layer (cellulose-chitosan sponge), the quantity of the bacteria was decreased, and the shape (growing states) of bacteria had an unhealthy appearance, compared to the gauze. This result demonstrated that our wound dressing was impermeable to bacteria.

The antibacterial activity of chitosan highly depends on various intrinsic and extrinsic factors, such as chitosan type, molecular weight, deacetylation degree, viscosity, solvent, concentration and the environmental conditions (Microb. Biotechnol. 2009, 2, 186). Considering these factors, we directly choose to “block the penetration of bacteria” rather than “antibacterial” to describe the function of the Janus sponge.

The application of the wound dressing in this study aimed at blood clotting rather than wound healing. There is limited time wound dressing contact with the tissue (a few minutes). In this case, the properties, such as promotes blood clotting, play a more critical role than antibacterial characteristics.

Chapter 4

A Nature-Inspired Monolithic Integrated Cellulose Aerogel-Based Evaporator for Efficient Solar Desalination

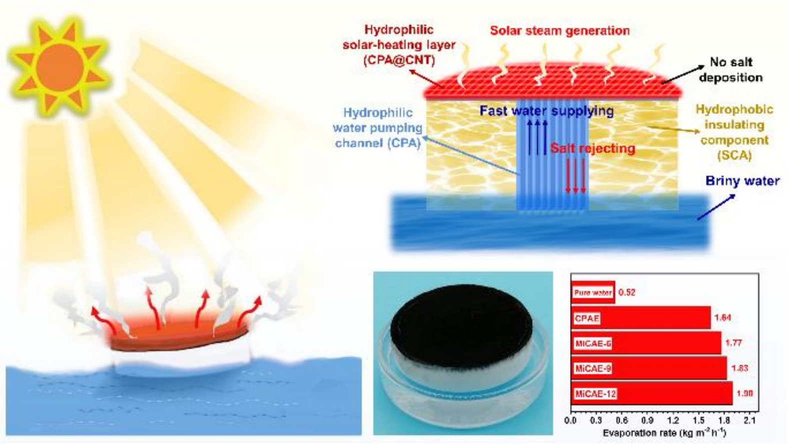

Solar-driven seawater desalination is a promising approach to tackle the problem of freshwater shortage. Establishing a robust, efficient solar-thermal water evaporator with great salt-resistance through a facile and scalable fabrication technique is still a challenge. Based on the Janus structure shown in **Chapter 3**, in this chapter, a floatable and robust monolithic integrated cellulose aerogel-based evaporator (MiCAE) with high performance is discussed. The material was obtained by carefully designing and integrating three functional components, including hydrophilic cellulose-PVA aerogel

(CPA), hydrophobic silylated cellulose aerogel (SCA), and a multiwalled carbon nanotube (MCNTs) coating layer (CPA@CNT), through heterogeneous mixing and freeze-drying of aerogel structures. Inspired by wood and mushrooms in nature, the incorporation of SCA with mushroom-shaped CPA possessing wood-like structures in MiCAE can realize heat localization and effectively suppress the irreversible heat dissipation. Meanwhile, CPA endows the evaporator with rapid water transportation and great salt excretion capability because of its porous structure exhibiting low tortuosity. Owing to the synergistic effects of the integrated functional structures, in the highly concentrated brine (17.5 wt.%), the MiCAE can still utilize the combination of high efficiency and obvious salt-resistance behavior. Results of this work offer a facile, efficient and salt-resistant solution for seawater desalination.

The contents of this chapter have been published as: Kuankuan Liu, Wenya Zhang, Huan Cheng, Liushan Luo, Bijia Wang, Zhiping Mao, Xiaofeng Sui, and Xueling Feng, A Nature-Inspired Monolithic Integrated Cellulose Aerogel-Based Evaporator for Efficient Solar Desalination. *ACS Applied Materials and Interfaces*, **2021**, *13*, 10612-10622.

4.1 Introduction

Water scarcity is an omnipresent and increasingly serious global issue that needs to be addressed urgently. As population grows, climate changes, and rampant pollution intensifies, hundreds of millions of people will face the challenges of inadequate freshwater accessibility [1-4]. As a vital component of the natural water cycle, solar-driven water evaporation is a promising and widely concerned approach to generate freshwater from solar steam, alleviating the shortage of freshwater with minimum environmental impact [5-7]. Over the past several years, a great amount of attention has been devoted to the development of highly efficient solar steam generators via designing smart devices with various advanced materials. In particular, interfacial evaporators were developed, exhibiting significantly improved solar-to-vapor conversion efficiency in comparison with that of the established bulk heating-based solar evaporators, as the former could localize the solar-heat at the air-liquid interface [8-10]. However, factors that limit the evaporation performance of the evaporators still exist, such as the transportation of water within steam generators, the inevitable heat loss at the evaporating interface, the serious accumulation of salt during the evaporation process, the cost and biodegradability of materials, and the ease of fabrication and utilization of the evaporators [6, 11-15].

Nature is the best teacher. To overcome the above-mentioned limitations, various nature-inspired solar vapor generators have been developed. Trees have the perfect system for the absorption and transportation of water and other nutrients during its natural growth [16]. Hu's group and Singamaneni's group reported tree-inspired solar vapor generators based on natural woods [17-18]. The high-performance of those generators was inherited from the wood, as it possessed natural hydrophilicity, plentiful vertically aligned microchannels and pits which were favorable for realizing a rapid water transportation (because of capillary effect) [19]. Moreover, the abundant low tortuosity porous structure in the wood could enable the salt to redissolve back into the water, decreasing the salt accumulation [20-21]. Besides natural wood, many other materials with analogous structure have also been used in evaporator fabrications, such as anodic aluminum oxide (AAO), vertically aligned carbon nanotube (VACNT) arrays, and vertically aligned graphene sheet membranes (VA-GSM) [22-25]. In this kind of evaporators, however, the evaporation occurred on the initial air-water interface and the filling of water in the open porous structure led to the increase of the thermal conductivity, causing more heat loss and weakening the heat localization effect. Some interesting works based on the Janus structure were recently reported, showing an improved heat localization effect and reformative evaporation performance [26-28]. Nonetheless, the steam generation efficiency of this type of evaporators is still relatively low and needs to be further improved.

Mushrooms possess a distinctive natural structure. The umbrella-shaped pileus, fibrous stipe and porous context of the mushrooms made themselves efficient solar steam generators [29]. The hydrophilic fibrous stipe, as a one-dimensional water supply channel, could pump up water by the capillary force. Moreover, a confined two-dimensional water pathway and three-dimensional hierarchically micro/nanoporous structures with high porosity were also constructed naturally for the water supplies [30-31]. The mushrooms' geometry is optimized naturally for reducing heat conduction losses as the interface between solar-absorber and water was reduced obviously. Based on the above advantages, a series of analogous materials have been employed to fabricate mushroom-like evaporators, such as fabric, lotus seedpods, natural cotton, aerogels, papers, and hydrogels [32-37]. In this type of evaporators, water could be uplifted to a higher interface for evaporating during the pumping process so that the downward heat transfer could be essentially avoided, enabling an ultrahigh vapor generation efficiency. Some interesting works based on structural transition from 2D to 3D was recently reported, showing an improved light absorption and greater evaporation performance [38-39]. In practical applications, however, these evaporators usually require the participation of commercial synthetic polymer foam as a floating layer and insulation layer. The structure separation and the lacking of a connection between the various parts would make the evaporators difficult to be employed in certain application scenarios. Only a few solar evaporating systems were built as integrated systems with controllable water transportation through electrospinning and 3D-printing methods [40-42]. The salt-resistance performance of this type of evaporators, however, needs to be considered and further improved [43-44].

Therefore, establishing a monolithic and robust solar-thermal water evaporation structure with high efficiency and great salt-resistance through a facile and scalable fabrication technique is still a challenge. Herein, we designed a floatable and robust monolithic integrated cellulose aerogel-based evaporator (MiCAE) based on cellulose nanofibers (CNFs) using a heterogeneous mixing and freeze-drying fabrication technique (**Figure 4.1**), which holds promise to become a powerful technique with the advantages of precise architectural control, easy scalability, versatility, and low cost. During the fabrication process, cellulose aerogels with different function were integrated together *in-situ*. Inspired by the internal structure of wood and the natural 3D structure of mushrooms, MiCAE can realize the combination of great water transportation, efficient salt-resistance performance and high efficiency. On account of the distinctive cellular framework of the flexible CNFs and versatile choices of organosilanes as binder, the MiCAE we report here presents integrated features of contrasting hydrophilicity and excellent stability. The hydrophobic hollow silylated cellulose aerogel (SCA) component on the bottom of the evaporator served as both a floating auxiliary layer and an effectual thermal barrier to enable the heat localization and hinder the irreversible heat dissipation to bulk water, enhancing the solar-energy conversion efficiency. The hydrophilic cellulose-PVA aerogel (CPA) component in the middle of the MiCAE possessed porous structures and vertically aligned channels analogous to wood which promoted the fast water transportation for continuous solar steam production by capillary action. Meanwhile, the salt accumulation caused by water evaporation was restricted at the evaporating interfaces, as the salt could be rapidly expelled through the low tortuosity channels. CPA was molded as a mushroom shape and integrated within the SCA through the heterogeneous mixing and freeze-drying aerogel fabrication step *in-situ*. The organosilanes were chosen as KH560 and VTMS, which contain reactive trimethoxysilane groups, and added into the CPA and SCA component, respectively. The trimethoxysilane groups would hydrolyze to form silanol groups, auto-condensed to form oligomers, and covalently cross-linked with the hydroxyl groups of cellulose, endowing the cellulose-based aerogels with specific functions while improving their mechanical properties by enhancing the bonding between the hydrophilic and hydrophobic components at the interfaces [45-47]. MCNTs were deposited onto the top of the obtained aerogel as solar-thermal conversion layer (CPA@CNT) to achieve highly efficient light absorption. Owing to the synergistic effect of integrated functional structure, the floatable and robust MiCAE possessed great solar-thermal conversion efficiency and thermal management abilities (an impressive evaporation rate of 1.90 kg m^{-2} h^{-1} and a favorable efficiency of 89% under one sun irradiation) with an obvious salt excretion capability in the highly concentrated brine (17.5 wt.%). This report may offer an efficient, salt-resistant and fascinating way to prepare a monolithic integrated evaporator for seawater desalination.

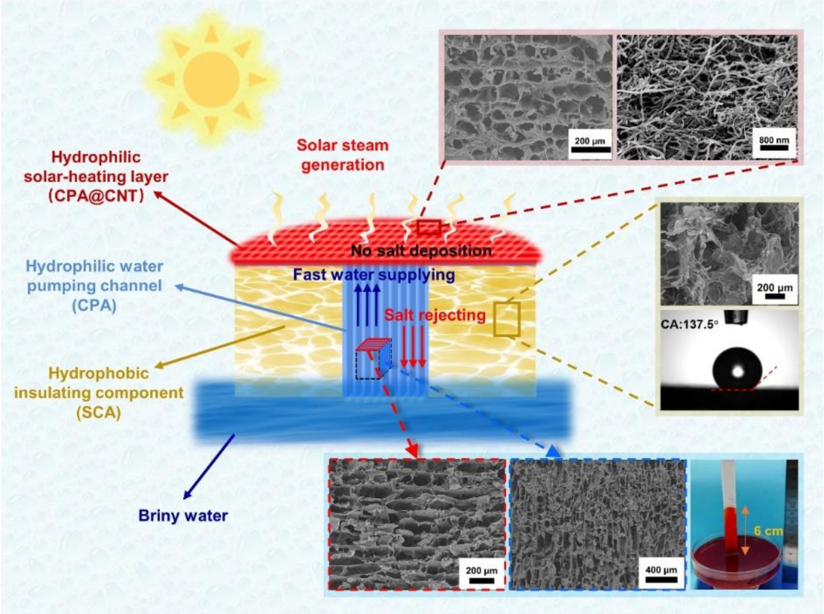

Figure 4.1 Schematic illustration of the monolithic integrated cellulose aerogel-based evaporator (MiCAE) for seawater desalination. The evaporator consists of the hydrophobic hollow silylated cellulose aerogel (SCA), hydrophilic cellulose-PVA aerogel (CPA) and MCNTs coating layer (CPA@CNT), interconnecting with each other.

4.2 Results and discussion

4.2.1 Preparation and characterization

The monolithic integrated cellulose aerogel-based evaporator (MiCAE) can be readily prepared by integrating three components with different functions through a facile heterogeneous mixing and freeze-drying process followed by a dip-coating method. **Figure 4.2a** schematically summarizes the fabrication route with several key steps: 1) pre-freezing of the precursor suspension of the hydrophobic hollow SCA; 2) freezing of the precursor suspension of the hydrophilic CPA within the hollow SCA in liquid nitrogen. The CPA was molded as a mushroom shape; 3) freeze-drying of SCA@CPA; 4) dip-coating a layer of MCNTs over the obtained aerogel. Briefly, the precursor suspension of CPA was directly frozen within the hollow pre-frozen precursor suspension of SCA in liquid nitrogen. During the freezing process, the ice crystals grew directionally along the temperature gradient, serving as a template for the final porous structure within the CPA aerogel (**Figure 4.2b**) [48]. The obtained CPA possessed the vertically aligned channels and low-tortuosity porous structures analogous to wood (**Figure 4.1** and **S4.2**), acting as the water transportation channel. In the meantime, an SEM image of the SCA cross-section demonstrates its disordered porous structure. It must be noted that CPA possesses a larger internal aperture compared with natural woods. The porous structure with low curvature and large channel width can significantly increase the aerogel's liquid absorption speed [49]. Thus, CPA showed excellent fluidic transport property in the wicking test as the water could rise up to 6 cm high in 10 min. In order to endow pristine cellulose aerogels with improved functions, organosilane coupling agents, KH560 and VTMS, were introduced into the system, respectively. **Figure 4.2c-d** display the FTIR spectra of the hydrophilic CPA and hydrophobic SCA. The absorption peaks at 1255, 907, and 845 cm^{-1} in the CPA spectrum are assigned to the epoxy groups of KH560. The introduction of slightly hydrophobic epoxy groups (compared to PVA) can provide a great floatability to pristine cellulose-PVA aerogel (CPA (CNFs: KH560: PVA=1:0:1 in weight ratio)) through slightly decreasing its water uptake ability. Meanwhile, by changing the different dosages of KH560, we found that CPA (1:1:1) retained excellent hydrophilicity and water absorption capacity (26.5 $g\ g^{-1}$) (**Figure S4.3**). Besides, CPA exhibited excellent mechanical strength and stability (**Figure S4.3a**) due to the formation of chemical crosslinking (between KH560 and CNF) and hydrogen bonding (between CNF and PVA). The absorption peaks at 3062, 3026, 2969, 1601, and 1408 cm^{-1} in the SCA spectrum are assigned to the vinyl groups of VTMS. The introduction of vinyl groups provided SCA a great hydrophobicity. By changing the different dosages of VTMS, we found that SCA (CNFs: VTMS=1:2 in weight ratio) exhibited excellent hydrophobicity (water contact angle: 137.5°). Before freeze-drying, the resulting mixture was standing still at 20°C for 30 min, allowing the interface to melt and mutually permeate. In the following facile freeze-drying process, two components with different wettability (**Figure S4.5b**) and morphologies (as shown in **Figure S4.4a,b**, the adsorption volume of SCA was much higher than that of CPA at $P/P_0 > 0.8$, indicating the presence of mesopores with the pore size ranging from 2 to 50 nm) were successfully integrated as a monolithic cellulose aerogel (SCA@CPA). **Figure 4.2f** and **S4.5c** show the SEM images of the aerogel SCA@CPA cross-section, which confirms the existence of an obvious interface (a transitional “interphase” structure) and different morphologies on both sides of the interface. Importantly, KH560 and VTMS in the system could undergo hydrolysis and react with themselves and cellulose at the interface to form Si-O-Si bonds and Si-O-C bonds (1276, 1180-690 cm^{-1}), enhancing the stability of the interface (**Figure S4.6a**). **Figure 4.2f** also indicates that the obtained SCA@CPA possessed great flexibility and interfacial stability. Finally, MCNTs infused into the top of the obtained aerogel, forming a network on the CNFs skeleton as the solar-thermal conversion layer (CPA@CNT) by dip-coating while maintaining the wood-like structure of CPA. Both the introduction of MCNTs with a high specific surface area and the formation of MCNTs network on the pileus CPA (~thickness of 3 mm) not only greatly improves the specific surface area of CPA, but also enhances it thermal stability (**Figure 4.2e** and **S4.4c**, **S4.6b-e**).

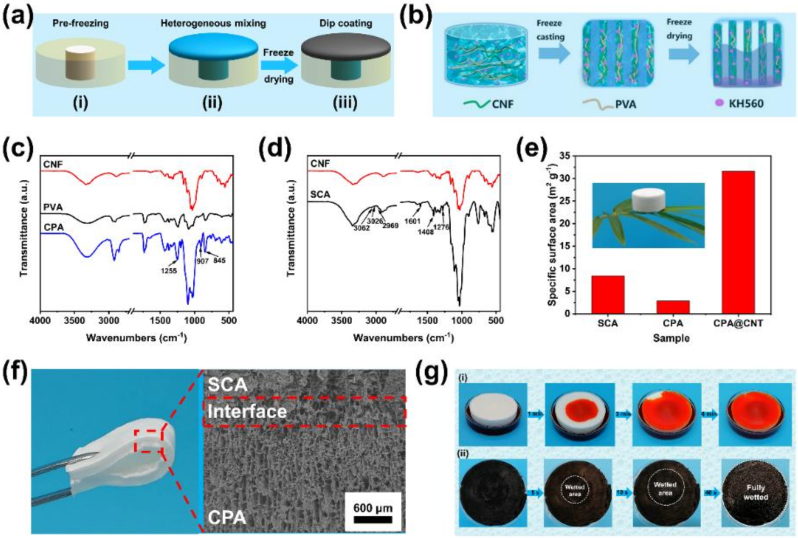

Figure 4.2 (a) Schematic illustration of the construction steps of the MiCAE. (b) Mechanism scheme for the preparation of wood-like CPA. FTIR spectra of (c) the hydrophilic CPA and (d) the hydrophobic SCA. (e) Specific surface area of SCA, CPA and CPA@CNT. The inset illustrates that cellulose aerogel has a relatively low density, which can be placed on the bamboo leaves. (f) Digital picture of SCA@CPA and the corresponding SEM image of the interface of SCA and CPA. (g) Snapshots of the water-uptake behavior of (i) SCA@CPA and (ii) MiCAE-12 in water. For clarity, SCA@CPA was tested with the red ink.

In order to evaluate the robustness and stability of MiCAE, various severe conditions such as ultrasonication (400 W, 2 h) and high temperature (80°C, 1 h) were applied to the evaporator continuously (**Figure S4.7a-b**). After these harsh tests, no obvious changes in the appearances of MiCAE were observed and the integrity of evaporators remained. In addition, MiCAE kept floating on the water during the tests. The requisite robustness and stability of the evaporator are essential for long-term usability in solar desalination. Besides, the water transportation property of the evaporator is another key factor affecting the functioning of the solar evaporation. In order to comprehensively measure the water transport performance, surface wettability and water extraction behavior of MiCAE were investigated, respectively. The time for the water droplet to completely penetrate the top surface of MiCAE is shortened to 0.3 s from 3 s required by SCA@CPA (**Figure S4.7c**). To assess water-uptake performance, the evaporator was put in water to visualize the water movement. As shown in **Figure 4.2g**, the wood-like CPA component acts as the liquid transport channel, delivering adequate water to the CPA@CNT layer and then spreads the water from the center to the surroundings via capillary action. It only takes 40 s for the MiCAE (effective upper surface area of ~22.90 cm^2) to be fully wetted by water, indicating the excellent water transport performance. Without the networks of MCNTs, it would take 6 min for SCA@CPA to be fully wetted. These phenomena demonstrate the synergistic effect generated by the nanomaterials and wood-like structure: the nano-structure produced by MCNTs networks can generate high capillary pressure while the micro-structure (wood-like structure) can provide low resistant pathways [50].

4.2.2 Solar-thermal and heat localization properties

The solar evaporation efficiency is highly dependent on the light absorption ability of the evaporator, thus the evaporator with high absorbance is preferred. The MiCAE shows greater absorbance (93.7%) compared with that of the blank SCA (9.6%) and CPA (6.1%) (**Figure 4.3a**). When light beats down on the evaporator, the incident light would be directed into the aligned channels because of the porous structure. Most of the light is absorbed by the rough MCNTs networks, and the scattered light would strike on channel walls recurrently until being fully absorbed (**Figure S4.8a**). Owing to the great solar absorption, the evaporator's surface temperature increased from 20°C to over 65°C within 250 s by putting the evaporator under one-sun irradiation in dry state (**Figure S4.8b**), indicating a rapid light-thermal response and extraordinary solar-to-thermal conversion competence.

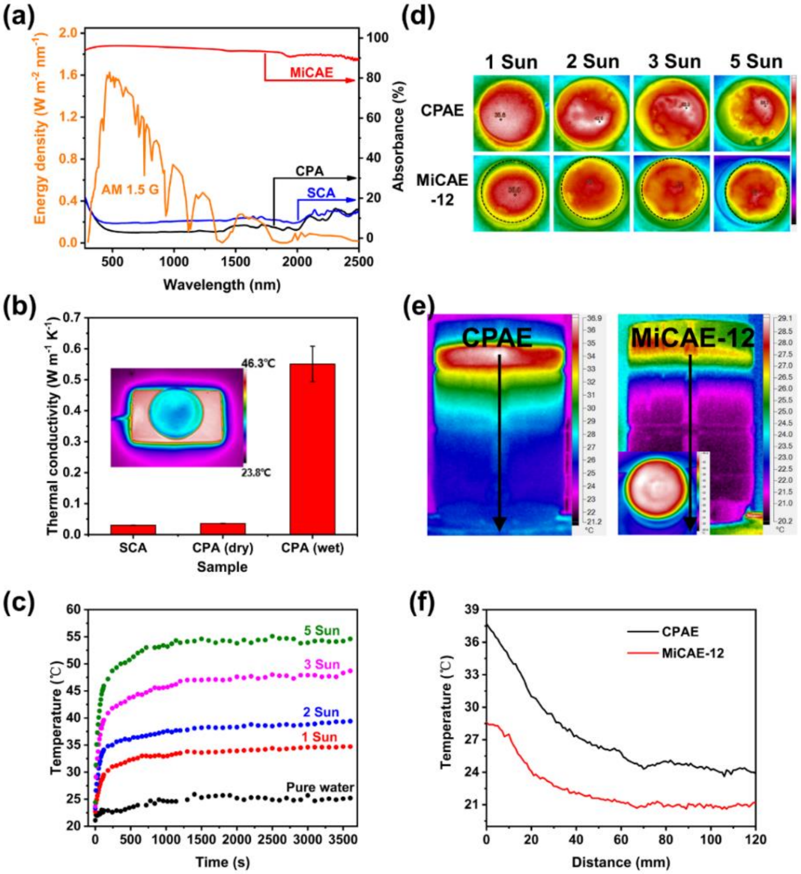

Figure 4.3 Solar-thermal and heat localization properties of MiCAE. (a) Absorption spectra of SCA, CPA and MiCAE (wavelength range: 280 to 2500 nm). The normalized spectrum of air mass 1.5 global (AM 1.5 G) is displayed by an orange line. (b) Thermal conductivities of SCA and CPA in dry and wet conditions. IR images in the inset showed that SCA still remained at a relatively low temperature when placed on the hot disk (45℃), illustrating that SCA has a low thermal conductivity. (c) Surface temperature variation over heating time of MiCAE-12 in water under different sunlight intensities. The temperature for pure water under one-sun irradiation served as the control (black dot). (d) Infrared images of the CPAE and MiCAE-12 under different concentrated sunlight at 60 min. (e) IR images of CPAE and MiCAE-12 under 5-sun intensity in water for 10 min. (f) Surface temperature vs. distance plot along the black arrow in (e).

Admirable heat-localization is another key trait to ensure highly efficient utilization of thermal energy for solar desalination[10]. In our design, the hydrophobic SCA with an intrinsic low thermal conductivity (0.030 W m^{-1} K^{-1}) (**Figure 4.3b**) is employed to solve two limitations in realization the heat-localization: 1) the contradiction between better water transportation ability and low thermal conductivity required for the evaporators. (For example, CPA displays a low thermal conductivity of 0.036 W m^{-1} K^{-1} in dry conditions, inherited from its highly porous structure. In the wet state, the thermal conductivity of the CPA significantly enhances to 0.551 W m^{-1} K^{-1}, which would harm the heat-localization.); 2) the level of evaporating interface that influences heat loss to the bulk water. To illustrate the design concept more clearly, CPAE were prepared as the control (**Figure S4.8c**). The surface temperature of MiCAE increased from 20°C to over 35°C within 250 s by placing the MiCAE on the water surface under one-sun irradiation (**Figure 4.3c**). At the same time, the corresponding temperature profiles of the evaporators after 60 min at different irradiation intensity were measured by an IR camera (**Figure 4.3d**). It is clearly found that there is a clear temperature boundary between the evaporating interface and the surrounding water interface in MiCAE, while the temperature boundary is fuzzy and even no longer exists in the CPAE. With the increase of irradiation intensity, this phenomenon would become more obvious. The temperature distributions of the CPAE and MiCAE-12 in water under 5 sun irradiation for 10 min are also displayed in the IR thermographs (**Figure 4.3e-f**). Most of the heat is confined at the irradiating surface of MiCAE-12, leading to a less pronounced increase of temperature with depth compared to that of CPAE. These phenomena all demonstrate the great heat localization capability of MiCAE. While providing the wetted integrated aerogel with a low thermal conductivity, the incorporation of the SCA with the mushroom-shaped CPA in MiCAE also effectively results in a smaller contact area between solar absorber and water, restraining the heat conduction to the bulk water. Besides, the hydrophobic SCA serves as a floating auxiliary layer to maintain the evaporating interface above the water surface (**Figure S4.8d**), which is beneficial for realizing heat localization and hindering heat loss to the bulk water.

4.2.3 Solar steam performance

To quantitatively characterize the solar vapor generation performance, the weight loss of brine (3.5 wt.%, average salinity of seawater) was evaluated using an electrical balance under the different irradiation intensities (one-sun, two-sun, three-sun, and five-sun) during the solar light illumination (**Figure 4.4a**). Considering the evaporation process, there is a balance between fast water transportation, effective water evaporation at the upper interface and rapid salt excretion due to the concentration gradient. The MiCAEs with different thicknesses of thermal barriers (6, 9, and 12 mm) were selected for testing (**Figure 4.4b** and **S4.9a-b**). The steam generation performance of CPAE having the same thickness with MiCAE-12 serves as the control (**Figure S4.9c**). As a control, the pure water exhibited an evaporation rate of ~0.52 kg m^{-2} h^{-1} and efficiency of 18.2% under one-sun irradiation). When a CPAE was put on the water, the evaporation rate of ~1.64 kg m^{-2} h^{-1} and efficiency of 76.44% under same irradiation were then observed (**Figure 4.4c-d**). When MiCAE was irradiated by one-sun on the top of water, the cumulative mass change of brine increased with the increase of the thickness of the thermal barrier in the evaporator, exhibiting an evaporation rate of 1.77, 1.83, and 1.90 kg m^{-2} h^{-1} under one-sun irradiation, improving by 7.93%, 11.59%, and 16.04% compared with that of CPAE, respectively. From pure water, CPAE to MiCAE, the increases in evaporation rate are attributed to the heat localization effect mentioned above. The role of heat localization effect will become even more prominent as the incident solar irradiation power increased (**Figure 4.4e**). Under two-sun irradiation, the evaporation rate of MiCAE-12 with the highest evaporation performance increases by 33.0% compared with that of CPAE. Under three-sun irradiation, the evaporation rate of MiCAE-9 with the highest evaporation performance increased by 38.8% compared with that of CPAE. Under five-sun irradiation, however, the evaporation rate of MiCAE decreases with increase of the thickness of thermal barrier in the evaporator. Meanwhile, salt crystals appear on the MiCAE-9 and MiCAE-12 under five-sun irradiation of 90 minutes (**Figure S4.9d**). This may be due to the disruption of the balance between water transportation, water evaporation and salt excretion in the evaporators under high power solar irradiation. With the increase of thickness of the thermal barrier, the distance between the evaporating interface and the water level will increase and the water transport speed inside the evaporator will be slower. At the same time, the exchange of concentrated brine generated at the evaporating interface and bulk water will also slow down. When the liquid transport speed is lower than the water evaporation speed and the exchange rate between the concentrated brine and bulk water, salt crystals will appear and accumulate at the evaporating interface. The salt resistance ability of the evaporator will be discussed in detail below. The solar evaporation efficiency of MiCAE-12 under one-sun illumination was 89.2%, enhancing by 16.6% compared with that of CPAE (see the details in the **4.6.1**). Meanwhile, we have theoretically estimated the related energy loss of MiCAE-12 under one-sun irradiation (see the details in the **4.6.1**), from which we found that the total energy consumption by the water evaporator is about 86.8%. This number is close to the steam generation efficiency of 89.2%. We also summarized the properties of other photothermal materials or evaporators reported in recent years (**Table S4.1**). The values of steam evaporation rate and efficiency of the MiCAE are superior or comparable to those of other evaporators reported.

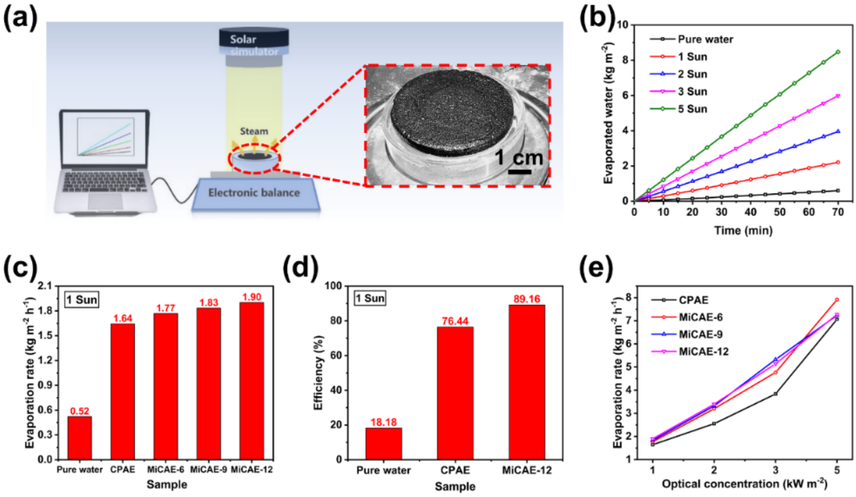

Figure 4.4 Solar steam performance of the MiCAE. (a) Illustration of the solar water evaporation setup. (b) Cumulative mass change versus time during water evaporation for the MiCAE-12 under different concentrated sunlight. The cumulative mass change vs. solar irradiation time for pure water under one-sun irradiation served as the control. (c) Comparison of the water evaporation rate obtained from various evaporators under one-sun irradiation. (d) Comparison of the energy conversion efficiency for water, CPAE and MiCAE-12 under one-sun irradiation. (e) Comparison of the water evaporation rate obtained from different evaporators under different concentrated sunlight.

4.2.4 Solar desalination performance

During the fast vapor generation, the salt nucleation and crystallization on the evaporator surface is unavoidable, which will reduce the solar-thermal conversion. The increase of solar reflection by the salt-deposited layer and the obstructing of the water supply channel will result in the remarkable decreases of evaporation efficiency. So, the salt resistance of the evaporator is a key property that must be considered in seawater desalination. To investigate the salt resistance behavior of the evaporators, actual East China seawater and the highly concentrated NaCl aqueous solution (17.5 wt.%, five times of average salinity of seawater) were used as the models in the continuous evaporation by MiCAE-12 (MiCAE-12 was selected because of its highest evaporation performance under one-sun irradiation) under one-sun irradiation. The experiment was conducted in a simulated natural environment with 8 hours illumination (to simulate day time). Digital pictures were taken every one hour to distinguish the salt particles precipitation on top of the evaporator. For the actual seawater (From the East China Sea), no salt crystals are observed during the process of continuous evaporation (**Figure 4.5a**). As shown in **Figure S4.10a**, the SEM image confirms no existence of salt crystals in the channels of water transportation in the evaporator. The corresponding evaporation rate remains above 1.7 kg m^{-2} h^{-1} during the process of continuous evaporation (**Figure 4.5b**). It must be noted that although the hydrophobic thermal barrier is designed to prevent heat loss, a portion of heat loss conducted to bulk water might occur via the inner hydrophilic water pumping channels during the seawater evaporation. Therefore, in the absence of salt deposition, the evaporation rate still slightly decreases with the irradiation time. For 17.5 wt.% NaCl solution, some lamellate solid salt particles can be found on the edge of the evaporating interface after 2 h of irradiation (**Figure 4.5c**). Increasing the irradiation time to 8 h, the number of salt crystals slightly increases. A salt ring is observed at certain distance from the center, showing a gradient of salt concentration in the direction from the center of evaporating interface to the edge. When the salt concentration finally exceeded its solubility limit, small seed crystals would form at the edge of the brine-wetted surface as a result of the slow water exchange during the wetting process [44]. Besides, these salt crystals are spatially isolated. When the continuous evaporation is over, salt particles of 1.38 g can be peeled off from the evaporating interface of the evaporator (**Figure S4.10b**), which may provide a way to collect salt crystals from a highly concentrated brine. From the SEM images (**Figure S4.10c**), it is obvious that the channels of water transportation inside the evaporator are not blocked during the continuous evaporation of NaCl aqueous solution (8h, 17.5 wt.%) although some salt particles were deposited on the evaporator's surface. With the deposition of salt particles, the evaporation rate of MiCAE also shows a downward trend, but it remains above 1.6 kg m^{-2} h^{-1} after 8 hours (**Figure 4.5d**). The great salt-resistance performance of the evaporator mentioned above may be derived from the design of the wood-like structure of the inner water transportation channels. To verify this viewpoint, MiCAE-12 with its high tortuosity structure (MiCAE-12-HT), prepared by directly putting the precursor suspension in cryogenic refrigerator for isotropic freezing to generate random porous structure [48-49], was selected to test on the NaCl solution (17.5 wt.%) under one-sun irradiation as the control. For the MiCAE-12-HT, some solid salt crystals can be observed at the edge of the brine-wetted surface after 2 h of irradiation. Moreover, when increasing the irradiation time (2h to 8h), the salt dimension and the coverage of salt became bigger rapidly from the edge to the center of the evaporating interface compared with those of MiCAE-12 with low tortuosity structure (**Figure S4.10d**). At 8 h, it is obvious that most of the surface is covered by salt crystals. Meanwhile, the evaporation rate decreased rapidly from ~1.9 kg m^{-2} h^{-1} to ~1.4 kg m^{-2} h^{-1} (**Figure S4.10e**). The SEM image shown in **Figure S4.10f** indicates that the channels of water transportation inside the MiCAE-12-HT are severely blocked by the salt crystals. To sum up, the abundant, large, and vertically aligned open micro-channels ensure the salt transportation from the high salt concentration evaporating surface to the bulk water along the shortest path by diffusion and convection (**Figure 4.5e**), endowing the MiCAE great salt-resistant performance [4, 17, 27]. To further examine intuitively the salt-resistance performance of the MiCAE-12 with low tortuosity structure, as shown in **Figure 4.5f**, 3 g salt can completely sink into the bulk water within 4 h at ambient conditions.

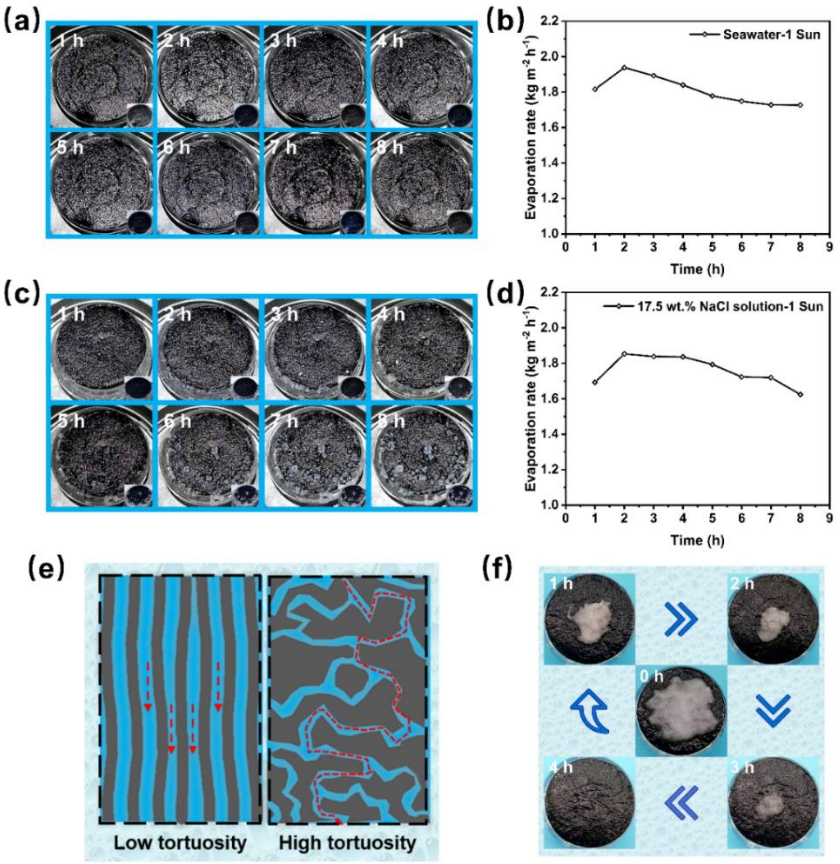

Figure 4.5 Solar desalination performance of the MiCAE. (a) Pictures and (b) corresponding evaporation rates of MiCAE-12 during continuous solar evaporation (8h) of the actual East China seawater under one-sun irradiation. (c) Pictures and (d) corresponding evaporation rates of MiCAE-12 during continuous solar evaporation NaCl solution (8 h, 17.5 wt.%) under one-sun irradiation. (e) Schematics illustration of the low-tortuosity porous structure and the high-tortuosity porous structure, the salt diffusion

paths are indicated by the red dashed lines with arrows in two kinds of porous structure. (f) Digital pictures of a salt rejection progression of the MiCAE-12 at ambient conditions.

4.2.5 Cycle stability, oil absorbing ability

Freshwater was gathered by the condensation of water steam (**Figure S4.11**) generated from the MiCAE-12 to systematically assess the desalination performance. An electron-coupled plasma atomic emission spectroscopy (ICP-AES) instrument was employed to detect the Na^+ concentration change by desalination in various simulated seawater (the Baltic Sea (0.8 wt.%), the North Sea (1.4 wt.%), the World Ocean (3.5 wt.%), the Red Sea (4 wt.%) and the Dead Sea (10 wt.%)). **Figure 4.6a** shows that the salt concentration in the condensed water is much lower than the salinity benchmark set by the World Health Organization (WHO) and the US Environmental Protection Agency (EPA) for drinking water (2-3 orders of magnitude). In addition, actual East China seawater was also used for desalination by the MiCAE-12. The concentration of four kinds of ion (Na^+, Mg^{2+}, Ca^{2+}, K^+) in real seawater and collected condensed water were evaluated (**Figure 4.6b**). After the process of desalination, the concentrations of four main ions in the condensed water are 2.53, 0.23, 0.01, and 0.35 mg L^{-1}, respectively, far less than the drinking water threshold specified by World Health Organization ($Na^+ < 200$ mg L^{-1}). Moreover, the concentrations of the main ions (Na^+, Mg^{2+}, Ca^{2+} and K^+) in condensed water generated by MiCAE were lower than that of water gained by membrane-based and distillation-based techniques (10-500 mg L^{-1} and 1-50 mg L^{-1}, respectively) [51-53].

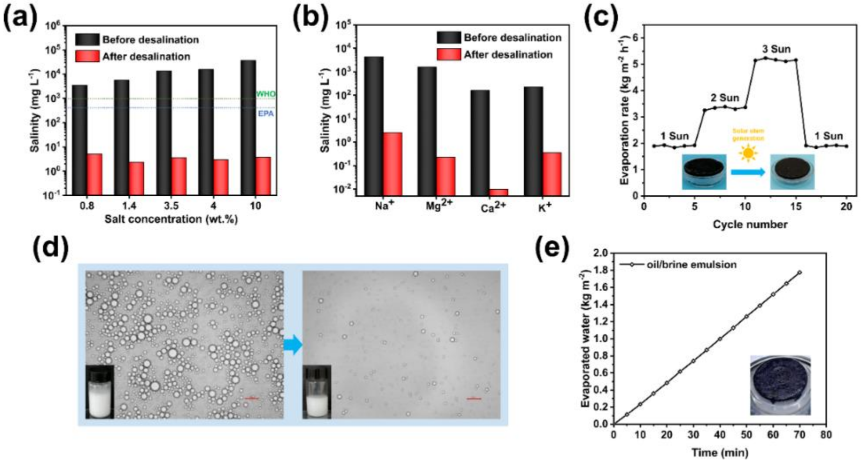

Figure 4.6 Ion concentrations in the desalinated water and cycle stability, oil absorbing ability of the MiCAE. (a) Na^+ concentration of five simulated seawater specimens before and after desalination by using the MiCAE-12. (b) The concentrations of main ions in the actual East China seawater sample before and after desalination. (c) Cycling tests for evaporation rates under different irradiation. Insets are the digital pictures of the evaporator before and after cycling tests. (d) Optical microscope images of oil/brine emulsion before and after desalination with MiCAE-12 under one-sun irradiation and (e) the corresponding evaporation-induced weight losses versus solar light irradiation time.

Stability is another important factor to determine the practical solar vapor production performance of the evaporator. The cycles of evaporation performance of MiCAE-12 under different solar irradiation intensity were tested as shown in **Figure 4.6c**. In each cycle, the irradiation was kept for 1 h while determining the evaporation rate, and then the evaporator was placed in deionized water for 15 min and recycled in the next trail (before each cycle test, it was made sure that the concentration of brine was 3.5 wt.%). The evaporation rate of the evaporator was stable in multiple cycles under the irradiation of same sunlight concentration. When the irradiation intensity goes back from three sun to one sun, the evaporation rate displayed a value similar to that of the initial under one-sun irradiation during the subsequent cycles. When the cycles were over, the evaporator maintained its original shape and integrated structure, indicating the great stability of the monolithic integrated cellulose aerogel-based evaporator.

Oil/petroleum pollution of seawater seriously harmed the environment and people's health [54]. Thus, it is necessary to adsorb and remove trace amounts of oil in brine in the process of seawater desalination. We used *n*-hexadecane as the representative of oil to form a stable oil-in-brine emulsion (w/w: 1/4) to test the performance of MiCAE. Because MiCAE has the hydrophobic heat-insulating layer, it shows a good oil droplets adsorption ability in brine. Under one-sun irradiation of 90 minutes, the number of oil droplets contained in the emulsion is greatly reduced (**Figure 4.6d**). Meanwhile, the evaporation rate has reduced from 1.90 kg m^{-2} h^{-1} in brine to 1.53 kg m^{-2} h^{-1} in the emulsion (**Figure 4.6e**). However, the evaporation rate is still appreciable. To investigate the stability and evaporation performance of the evaporators over longer periods of time, a continuous evaporation experiment by MiCAE-12 under one-sun irradiation was conducted. In the continuous evaporation process, the evaporation rate of MiCAE also shows a downward trend and no salt crystals are observed on the evaporator (**Figure S4.12a**). These phenomena mentioned above can further illustrate the important role played by the thermal barrier in the evaporator. When the air locked in the internal voids of thermal barrier is replaced by oil, the thermal conductivity of the SCA part would increase as the oil has higher thermal conductivity, lowering the heat localization effect of the evaporator.

Besides, the actual effect of oil treatment was evaluated by measuring the average total organic carbon (TOC) in the oil/brine emulsion and collected condensed water separately. The TOC contents of the emulsion and collected condensed water were 50.20 mg mL^{-1} and 0.30 mg mL^{-1} (**Figure S4.12b**), respectively, showing that the freshwater collected from the condensed vapor contained negligible oil. Hence, the monolithic integrated cellulose aerogel-based evaporator may become a prospective candidate for oil treatment during seawater desalination.

4.3 Conclusions

In summary, we reported a robust, nature-inspired and high-performance monolithic integrated cellulose aerogel-based evaporator (MiCAE) for seawater desalination using the facile and scalable heterogeneous mixing and freeze-drying technique. Inspired by wood and mushrooms, the incorporation of the hydrophobic SCA (possessing intrinsic low thermal conductivity) with mushroom-shaped CPA (having vertically aligned channels and porous structures analogous to wood) realized the heat localization and effectively suppressed the heat dissipation of the system, enhancing the solar-thermal conversion efficiency. The hydrophilic CPA component integrated in the SCA enabled fast water transportation by capillary action and great salt excretion because of the low tortuosity porous structure. By virtue of a synergistic effect of the integrated functional structures, the evaporator can realize the combination of great light absorption, efficient salt-resistance and impressive efficiency. As a result, the MiCAE exhibits a high irradiation absorption of 93.7%, a great evaporation rate of 1.90 kg m^{-2} h^{-1} and an impressive efficiency of 89.2% under one-sun irradiation. Moreover, the evaporator performs a stable vapor generation with almost no salt deposition on the actual East China seawater and exhibits an obvious salt-resistance performance in highly concentrated brine (17.5 wt.%) under one-sun irradiation for continuous evaporation of 8 hours. This work offers a new approach to achieve a monolithic integrated solar-thermal water evaporation structure with excellent efficiency and great salt-resistance for efficient seawater desalination and purification. However, as mentioned in the conclusions in Chapter 2, the complex preparation process of obtaining functionalized CPM is a large practical burden on high volume applications. But based on the excellent performance of the evaporator we designed, and the preparation technology has been gradually developed, we anticipate fertile opportunities for the scalability of this technology in seawater desalination and purification.

4.4 Experimental section

4.4.1 Preparation of hydrophobic SCA suspension

Vinyltrimethoxysilane (VTMS, 1.32 g) was dropwisely mixed with 55 g CNF suspension (1.2 wt.%). The mixture was mechanically stirred for 4 h at room temperature. The silylated cellulose aerogel obtained after freeze-drying was abbreviated as SCA. Similarly, by changing the different dosages of VTMS, we can prepare different types of SCA (CNFs: VTMS in weight ratio), such as SCA (1:1), SCA (1:2), SCA (1:3) and SCA (1:4).

4.4.2 Preparation of hydrophilic CPA suspension

PVA (5.0 g) was dissolved in deionized water (50 mL) and stirred at 95°C for 10 h. The PVA solution (10 wt.%) was then stored at room temperature. KH560 (0.38 g) was added dropwisely into a mixed suspension (35 g) of CNF (1.2 wt.%) and PVA solution. The mixture was mechanically stirred for 4 h. The cellulose aerogel obtained after freeze-drying was abbreviated as CPA. Similarly, by changing the different dosages of KH560, we can prepare different types of CPA (CNFs: KH560: PVA in weight ratio), such as CPA (1:0:1), CPA (1:1:1) and CPA (1:2:1). The CNF suspension (1.2 wt.%) was mechanically stirred for 4. The pristine cellulose aerogel obtained after freeze-drying was abbreviated as CA.

4.4.3 Preparation of the monolithic integrated cellulose aerogel-based evaporator (MiCAE)

The evaporator was prepared through the facile and scalable heterogeneous mixing and freeze-drying technique followed by a dip-coating method. Briefly, the precursor suspension of hydrophobic SCA (14, 18, and 22 g) was placed in the glass mold (with movable column mold (diameter of ~1.6 cm) in the middle), respectively. The precursor suspension was first frozen into an ice gel in liquid nitrogen (**Figure 4.2a(i)**). After removing the middle-column mold, the precursor suspension of hydrophilic CPA (9, 11, and 13 g) was poured into the hollow ice gel, respectively. The mixture was standing still at 20°C for 30 min, enabling the melting and mutual permeation at the interface. Then the mixture was frozen in liquid nitrogen and lyophilized at −50°C for 36 h by a Lyophilizor (Labconco FD5-3, USA) to yield a monolithic aerogel (**Figure 4.2a(ii)**), which was then kept at 110°C for 30 min to promote the crosslinking. The cured aerogels were put into deionized water and acetone to remove physically adsorbed silane coupling agents. The aerogels were then vacuum dried at 30°C for 24 h. Finally, the MCNTs suspension (10 wt.%) was prepared by dispersing MCNTs and CNTs dispersing agents (TNWDIS) in deionized water. The mixture was sonicated for 30 min. Then inverted aerogels were immersed into the MCNTs suspensions (9 g) and then lyophilized for more than 24 h (**Figure 4.2a(iii)**). These monolithic integrated evaporators obtained after freeze-drying were abbreviated as MiCAE-6, MiCAE-9 and MiCAE-12, respectively (6, 9, and 12 mm refer to the thickness of thermal barrier in the evaporators).

The CPA-based evaporator prepared by immersing the CPA into the MCNTs suspension directly was abbreviated as CPAE. The MiCAE-12 with the high tortuosity porous structure was fabricated through similar methods, except that all freezing was executed in the refrigerator (-80°C), was abbreviated as MiCAE-12-HT.

4.4.4 Preparation of oil/brine emulsions

Polyoxyethylene castor oil (3.2 g) was dissolved in 3.5 wt.% NaCl solution (32 mL) and *n*-hexadecane (8 g) was added to the brine. The oil/brine emulsion stabilized by polyoxyethylene castor oil, was prepared with homogenizer (IKA T18, Germany) at 12, 000 rpm for 3 min followed by 3 min ultrasonication (SCIENTZ, JY 92-IIDN, China).

4.5 References

(1) Chen, B.; Han, M.; Peng, K.; Zhou, S.; Shao, L.; Wu, X.; Wei, W.; Liu, S.; Li, Z.; Li, J. Global land-water nexus: Agricultural land and freshwater use embodied in worldwide supply chains. *Science of The Total Environment* **2018,** *613*, 931-943.
(2) Schewe, J.; Heinke, J.; Gerten, D.; Haddeland, I.; Arnell, N. W.; Clark, D. B.; Dankers, R.; Eisner, S.; Fekete, B. M.; Colón-González, F. J. Multimodel assessment of water scarcity under climate change. *Proceedings of the National Academy of Sciences* **2014,** *111* (9), 3245-3250.
(3) Alvarez, P. J.; Chan, C. K.; Elimelech, M.; Halas, N. J.; Villagrán, D. Emerging opportunities for nanotechnology to enhance water security. *Nature Nanotechnology* **2018,** *13* (8), 634.
(4) Dong, X.; Cao, L.; Si, Y.; Ding, B.; Deng, H. Cellular structured cnts@ SiO_2 nanofibrous aerogels with vertically aligned vessels for salt-resistant solar desalination. *Advanced Materials* **2020,** *32* (34), 1908269.
(5) Gao, M.; Zhu, L.; Peh, C. K.; Ho, G. W. Solar absorber material and system designs for photothermal water vaporization towards clean water and energy production. *Energy & Environmental Science* **2019,** *12* (3), 841-864.
(6) Chen, C.; Kuang, Y.; Hu, L. Challenges and opportunities for solar evaporation. *Joule* **2019,** *3* (3), 683-718.
(7) Zhang, P.; Liao, Q.; Yao, H.; Huang, Y.; Cheng, H.; Qu, L. Direct solar steam generation system for clean water production. *Energy Storage Materials* **2019,** *18*, 429-446.
(8) Tao, P.; Ni, G.; Song, C.; Shang, W.; Wu, J.; Zhu, J.; Chen, G.; Deng, T. Solar-driven interfacial evaporation. *Nature Energy* **2018,** *3* (12), 1031-1041.
(9) Zhou, J.; Gu, Y.; Liu, P.; Wang, P.; Miao, L.; Liu, J.; Wei, A.; Mu, X.; Li, J.; Zhu, J. Development and evolution of the system structure for highly efficient solar steam generation from zero to three dimensions. *Advanced Functional Materials* **2019,** *29* (50), 1903255.
(10) Ni, G.; Li, G.; Boriskina, S. V.; Li, H.; Yang, W.; Zhang, T.; Chen, G. Steam generation under one sun enabled by a floating structure with thermal concentration. *Nature Energy* **2016,** *1* (9), 1-7.
(11) Zhang, C.; Liang, H. Q.; Xu, Z. K.; Wang, Z. Harnessing solar-driven photothermal effect toward the water–energy nexus. *Advanced Science* **2019,** *6* (18), 1900883.
(12) Bai, H.; Zhao, T.; Cao, M. Interfacial solar evaporation for water production: From structure design to reliable performance. *Molecular Systems Design & Engineering* **2020,** *5* (2), 419-432.
(13) Dao, V.-D.; Vu, N. H.; Yun, S. Recent advances and challenges for solar-driven water evaporation system toward applications. *Nano Energy* **2020,** *68*, 104324.
(14) Zhu, L.; Gao, M.; Peh, C. K. N.; Ho, G. W. Recent progress in solar-driven interfacial water evaporation: Advanced designs and applications. *Nano Energy* **2019,** *57*, 507-518.
(15) Pang, Y.; Zhang, J.; Ma, R.; Qu, Z.; Lee, E.; Luo, T. Solar–thermal water evaporation: A review. *ACS Energy Letters* **2020,** *5* (2), 437-456.

(16) Zhu, M.; Li, Y.; Chen, G.; Jiang, F.; Yang, Z.; Luo, X.; Wang, Y.; Lacey, S. D.; Dai, J.; Wang, C. Tree - inspired design for high - efficiency water extraction. *Advanced Materials* **2017,** *29* (44), 1704107.

(17) Zhu, M.; Li, Y.; Chen, F.; Zhu, X.; Dai, J.; Li, Y.; Yang, Z.; Yan, X.; Song, J.; Wang, Y. Plasmonic wood for high - efficiency solar steam generation. *Advanced Energy Materials* **2018,** *8* (4), 1701028.

(18) Liu, K.-K.; Jiang, Q.; Tadepalli, S.; Raliya, R.; Biswas, P.; Naik, R. R.; Singamaneni, S. Wood–graphene oxide composite for highly efficient solar steam generation and desalination. *ACS Applied Materials & Interfaces* **2017,** *9* (8), 7675-7681.

(19) Chen, C.; Li, Y.; Song, J.; Yang, Z.; Kuang, Y.; Hitz, E.; Jia, C.; Gong, A.; Jiang, F.; Zhu, J. Highly flexible and efficient solar steam generation device. *Advanced Materials* **2017,** *29* (30), 1701756.

(20) He, S.; Chen, C.; Kuang, Y.; Mi, R.; Liu, Y.; Pei, Y.; Kong, W.; Gan, W.; Xie, H.; Hitz, E. Nature-inspired salt resistant bimodal porous solar evaporator for efficient and stable water desalination. *Energy & Environmental Science* **2019,** *12* (5), 1558-1567.

(21) Chen, F.; Gong, A. S.; Zhu, M.; Chen, G.; Lacey, S. D.; Jiang, F.; Li, Y.; Wang, Y.; Dai, J.; Yao, Y. Mesoporous, three-dimensional wood membrane decorated with nanoparticles for highly efficient water treatment. *ACS Nano* **2017,** *11* (4), 4275-4282.

(22) Zhou, L.; Tan, Y.; Wang, J.; Xu, W.; Yuan, Y.; Cai, W.; Zhu, S.; Zhu, J. 3d self-assembly of aluminium nanoparticles for plasmon-enhanced solar desalination. *Nature Photonics* **2016,** *10* (6), 393-398.

(23) Zhou, L.; Tan, Y.; Ji, D.; Zhu, B.; Zhang, P.; Xu, J.; Gan, Q.; Yu, Z.; Zhu, J. Self-assembly of highly efficient, broadband plasmonic absorbers for solar steam generation. *Science Advances* **2016,** *2* (4), e1501227.

(24) Yin, Z.; Wang, H.; Jian, M.; Li, Y.; Xia, K.; Zhang, M.; Wang, C.; Wang, Q.; Ma, M.; Zheng, Q.-s. Extremely black vertically aligned carbon nanotube arrays for solar steam generation. *ACS Applied Materials & Interfaces* **2017,** *9* (34), 28596-28603.

(25) Zhang, P.; Li, J.; Lv, L.; Zhao, Y.; Qu, L. Vertically aligned graphene sheets membrane for highly efficient solar thermal generation of clean water. *ACS Nano* **2017,** *11* (5), 5087-5093.

(26) Zhang, B.; Gu, Q.; Wang, C.; Gao, Q.; Guo, J.; Wong, P. W.; Liu, C. T.; An, A. K. Self-assembled hydrophobic/hydrophilic porphyrin-ti3c2tx mxene janus membrane for dual-functional enabled photothermal desalination. *ACS Applied Materials & Interfaces* **2021**.

(27) Hu, R.; Zhang, J.; Kuang, Y.; Wang, K.; Cai, X.; Fang, Z.; Huang, W.; Chen, G.; Wang, Z. A janus evaporator with low tortuosity for long-term solar desalination. *Journal of Materials Chemistry A* **2019,** *7* (25), 15333-15340.

(28) Chen, J.; Yin, J. L.; Li, B.; Ye, Z.; Liu, D.; Ding, D.; Qian, F.; Myung, N. V.; Zhang, Q.; Yin, Y. Janus evaporators with self-recovering hydrophobicity for salt-rejecting interfacial solar desalination. *ACS Nano* **2020,** *14* (12), 17419-17427.

(29) Xu, N.; Hu, X.; Xu, W.; Li, X.; Zhou, L.; Zhu, S.; Zhu, J. Mushrooms as efficient solar steam-generation devices. *Advanced Materials* **2017,** *29* (28), 1606762.

(30) Wu, X.; Robson, M. E.; Phelps, J. L.; Tan, J. S.; Shao, B.; Owens, G.; Xu, H. A flexible photothermal cotton-cus nanocage-agarose aerogel towards portable solar steam generation. *Nano Energy* **2019,** *56*, 708-715.

(31) Storer, D. P.; Phelps, J. L.; Wu, X.; Owens, G.; Khan, N. I.; Xu, H. Graphene and

rice-straw-fiber-based 3d photothermal aerogels for highly efficient solar evaporation. *ACS Applied Materials & Interfaces* **2020,** *12* (13), 15279-15287.

(32) Fang, J.; Liu, J.; Gu, J.; Liu, Q.; Zhang, W.; Su, H.; Zhang, D. Hierarchical porous carbonized lotus seedpods for highly efficient solar steam generation. *Chemistry of Materials* **2018,** *30* (18), 6217-6221.

(33) Xiao, P.; Gu, J.; Zhang, C.; Ni, F.; Liang, Y.; He, J.; Zhang, L.; Ouyang, J.; Kuo, S.-W.; Chen, T. A scalable, low-cost and robust photo-thermal fabric with tunable and programmable 2d/3d structures towards environmentally adaptable liquid/solid-medium water extraction. *Nano Energy* **2019,** *65*, 104002.

(34) Wu, X.; Wu, L.; Tan, J.; Chen, G. Y.; Owens, G.; Xu, H. Evaporation above a bulk water surface using an oil lamp inspired highly efficient solar-steam generation strategy. *Journal of Materials Chemistry A* **2018,** *6* (26), 12267-12274.

(35) Mu, P.; Zhang, Z.; Bai, W.; He, J.; Sun, H.; Zhu, Z.; Liang, W.; Li, A. Superwetting monolithic hollow-carbon-nanotubes aerogels with hierarchically nanoporous structure for efficient solar steam generation. *Advanced Energy Materials* **2019,** *9* (1), 1802158.

(36) Li, W.; Li, Z.; Bertelsmann, K.; Fan, D. E. Portable low-pressure solar steaming-collection unisystem with polypyrrole origamis. *Advanced Materials* **2019,** *31* (29), 1900720.

(37) Zhou, X.; Zhao, F.; Guo, Y.; Zhang, Y.; Yu, G. A hydrogel-based antifouling solar evaporator for highly efficient water desalination. *Energy & Environmental Science* **2018,** *11* (8), 1985-1992.

(38) Wang, Y.; Wu, X.; Shao, B.; Yang, X.; Owens, G.; Xu, H. Boosting solar steam generation by structure enhanced energy management. *Science Bulletin* **2020,** *65* (16), 1380-1388.

(39) Wang, Y.; Wu, X.; Gao, T.; Lu, Y.; Yang, X.; Chen, G. Y.; Owens, G.; Xu, H. Same materials, bigger output: A reversibly transformable 2d–3d photothermal evaporator for highly efficient solar steam generation. *Nano Energy* **2021,** *79*, 105477.

(40) Li, Y.; Gao, T.; Yang, Z.; Chen, C.; Luo, W.; Song, J.; Hitz, E.; Jia, C.; Zhou, Y.; Liu, B. 3d-printed, all-in-one evaporator for high-efficiency solar steam generation under 1 sun illumination. *Advanced Materials* **2017,** *29* (26), 1700981.

(41) Gao, T.; Li, Y.; Chen, C.; Yang, Z.; Kuang, Y.; Jia, C.; Song, J.; Hitz, E. M.; Liu, B.; Huang, H. Architecting a floatable, durable, and scalable steam generator: Hydrophobic/hydrophilic bifunctional structure for solar evaporation enhancement. *Small Methods* **2019,** *3* (2), 1800176.

(42) Li, Y.; Gao, T.; Yang, Z.; Chen, C.; Kuang, Y.; Song, J.; Jia, C.; Hitz, E. M.; Yang, B.; Hu, L. Graphene oxide-based evaporator with one-dimensional water transport enabling high-efficiency solar desalination. *Nano Energy* **2017,** *41*, 201-209.

(43) Ni, G.; Zandavi, S. H.; Javid, S. M.; Boriskina, S. V.; Cooper, T. A.; Chen, G. A salt-rejecting floating solar still for low-cost desalination. *Energy & Environmental Science* **2018,** *11* (6), 1510-1519.

(44) Xia, Y.; Hou, Q.; Jubaer, H.; Li, Y.; Kang, Y.; Yuan, S.; Liu, H.; Woo, M. W.; Zhang, L.; Gao, L. Spatially isolating salt crystallisation from water evaporation for continuous solar steam generation and salt harvesting. *Energy & Environmental Science* **2019,** *12* (6), 1840-1847.

(45) Cheng, H.; Xiao, D.; Tang, Y.; Wang, B.; Feng, X.; Lu, M.; Vancso, G. J.; Sui, X. Sponges with janus character from nanocellulose: Preparation and applications in the

treatment of hemorrhagic wounds. *Advanced Healthcare Materials* **2020,** *9* (17), 1901796.

(46) Zhang, Z.; Sèbe, G.; Rentsch, D.; Zimmermann, T.; Tingaut, P. Ultralightweight and flexible silylated nanocellulose sponges for the selective removal of oil from water. *Chemistry of Materials* **2014,** *26* (8), 2659-2668.

(47) Li, Y.; Xu, L.; Xu, B.; Mao, Z.; Xu, H.; Zhong, Y.; Zhang, L.; Wang, B.; Sui, X. Cellulose sponge supported palladium nanoparticles as recyclable cross-coupling catalysts. *ACS Applied Materials & Interfaces* **2017,** *9* (20), 17155-17162.

(48) Bai, H.; Chen, Y.; Delattre, B.; Tomsia, A. P.; Ritchie, R. O. Bioinspired large-scale aligned porous materials assembled with dual temperature gradients. *Science Advances* **2015,** *1* (11), e1500849.

(49) Cui, Y.; Wang, Y.; Shao, Z.; Mao, A.; Gao, W.; Bai, H. Smart sponge for fast liquid absorption and thermal responsive self-squeezing. *Advanced Materials* **2020,** *32* (14), 1908249.

(50) Li, J.; Zhang, M. Biporous nanocarbon foams and the effect of the structure on the capillary performance. *Progress in Natural Science: Materials International* **2020,** *30* (3), 360-365.

(51) Zhao, F.; Zhou, X.; Shi, Y.; Qian, X.; Alexander, M.; Zhao, X.; Mendez, S.; Yang, R.; Qu, L.; Yu, G. Highly efficient solar vapour generation via hierarchically nanostructured gels. *Nature Nanotechnology* **2018,** *13* (6), 489-495.

(52) Liu, Z.; Wu, B.; Zhu, B.; Chen, Z.; Zhu, M.; Liu, X. Continuously producing watersteam and concentrated brine from seawater by hanging photothermal fabrics under sunlight. *Advanced Functional Materials* **2019,** *29* (43), 1905485.

(53) Song, X.; Song, H.; Wang, S.; Liu, J.; Zhou, L.; Xu, J.; Chen, K. Enhancement of solar vapor generation by a 3d hierarchical heat trapping structure. *Journal of Materials Chemistry A* **2019,** *7* (46), 26496-26503.

(54) Shannon, M. A.; Bohn, P. W.; Elimelech, M.; Georgiadis, J. G.; Marinas, B. J.; Mayes, A. M. Science and technology for water purification in the coming decades. In *Nanoscience and technology: A collection of reviews from nature journals*; World Scientific: 2010; pp 337-346.

4.6 Supporting information

4.6.1 Supporting experimental section

Materials

CNF suspension (solid content: 1.2 wt.%, raw material: spruce wood pulp, carboxyl and aldehydes content: 0%, cellulose content: 86.08%, hemicellulose content: 13.68%, lignin content: 0.24%; homogenized 12 times with the pressure from 80 MPa to 100 MPa) was provided by Tianjin Woodelf biotechnology Co., Ltd. (China) and was subjected to high pressure homogenization (APV-2000 Homogenizer, Germany) before use (homogenized once with the pressure 500 bar). A transmission electron microscope image of the CNFs after ultrasonic dispersion by using an Ultrasonic cell grinder (SCIENTZ, JY92-IIDN, China) shows that uniform cellulose nanofibrils with diameters under 100 nm and lengths in the micrometer range are dominant in the suspension (**Figure S4.1a**). Poly(vinyl alcohol) 1788 (PVA, degree of alcoholysis: 87.0~89.0% (mol mol^{-1})) was purchased from Aladdin Chemical Reagent Co., Ltd (China). Polyoxyethylene castor oil was provided from MACKLIN Chemical Reagent Co., Ltd (China). Sodium chloride, γ-glycidoxypropyltrimethoxysilane (GPTMS, KH560), vinyltrimethoxysilane (VTMS) and *n*-hexadecane were obtained from Sinopharm Chemical Reagent Co., Ltd (China). Multiwalled carbon nanotubes (MCNTs) and CNTs dispersing agents were provided by Chengdu Organic Chemicals Co. Ltd., Chinese Academy of Sciences. A transmission electron microscope image of the MCNTs after ultrasonic dispersion by using an Ultrasonic cell grinder shows that MCNTs with diameters from 30 to 80 nm and lengths under 10 μm are dominant in the suspension and have a distinct hollow structure (**Figure S4.1b**). All reagents were analytical grade and used without further purification. The seawater was collected from the East China Sea, Shanghai. Deionized water was used in sample preparation.

Characterizations

The morphologies of CNFs and MCNTs (**Figure S4.1**) were observed using a transmission electron microscope (TEM, JEM-2100, JEOL, Japan). The morphologies and microstructure of samples (**Figure 4.1**, **4.2f**, and **S4.2**, **S4.5c, S4.10a,c,f)** were observed on a scanning electron microscopy (Hitachi TM-3030, Japan). The chemical structure of samples (**Figure 4.2c-d**) was characterized by Fourier transform infrared spectroscopy (PerkinElmer Spectrum Two, Germany) at a spectral range of 440 cm^{-1}-4000 cm^{-1}. The compressive properties (at ε = 50%) of samples (**Figure S4.3d,e,h** and **S4.6c**) were determined at a compression speed of 5 mm/min by a universal testing machine (UH6502, China). The porous structure and specific surface area of samples (**Figure 4.2e** and **S4.4**) were determined by using a surface area and porosimetry analyzer (V-Sorb 2800P, China). Water contact angle (**Figure 4.1** and **S4.5a**, **S4.7c**) measurements were performed on a DSA30 Contact Angle Analysis System (Kruss, Germany). The absorption spectra (**Figure 4.3a**) were calculated based on the reflectance and transmission spectra using a UV-VIS spectrometer equipped with an integrating sphere (UV3600, Shimadzu, Japan). Thermal gravimetric analysis (TGA) was carried out using a thermogravimetric analyzer (TG 209F1, Germany) from 30 to 700°C at a heating rate of 10 °C min^{-1} under a nitrogen atmosphere (**Figure S4.6d-e**). The thermal conductivity measurement (**Figure 4.3b**) was performed on a thermal constant analyzer (XIATECH-TC3000E, China) at room temperature. The obtained oil/brine emulsions before and after desalination were observed using an optical microscope (ECLIPSE 80i, NIKON Corporation, Japan) (**Figure 4.6d**). The average TOC (Total Organic Carbon) of the oil/brine emulsion and the corresponding collected freshwater were measured by TOC analyzer (Shimadzu, Japan) (**Figure S4.12b**).

Evaluation of solar-driven vaporization in laboratory

A solar simulator (PLS-SXE 300, Perfect light Ltd., China) was used for the solar desalination experiments (**Figure 4.4a-b**, **4.5b,d**, 4.**6e** and **S4.9a-c**, **S4.10e**, **S4.12a**). The evaporator was floated in a Petri dish of similar size to the evaporator (the radius of 3 cm) to furthest prevent weight loss arising from intrinsic water evaporation under solar irradiation. The whole device was then placed on an electronic balance (ME204E, Mettler Toledo Ltd., Switzerland) with an accuracy of 0.1 mg to record the weight loss of water during solar irradiation. Unless otherwise specified, the water used in the test is 3.5 wt.% NaCl solution (average salinity of seawater). The IR pictures of temperature distribution and temperature variations of evaporators in real-time during solar desalination were recorded by an IR thermal imager (Fluke TiX450, USA) (**Figure 4.3c-f**, and **S4.8b-c**). Each sample tested was balanced under a solar simulator for 20 minutes before counting began. The evaporation rate was obtained by calculating the linear slope of the evaporated water against time (**Figure 4.4e**). Evaporation performances of all the evaporators were measured at around room temperature (24.4 ~ 25.5°C) and humidity of 42 ~ 57 RH% in ambient environment. The setup (**Figure S4.11**) is designed to condense the steam for freshwater collection. Concentrations of metal ions in seawater and saline water samples after and before desalination were determined by an electron-coupled plasma atomic emission spectroscopy instrument (Prodigy-ICP, Leeman, USA) (**Figure 4.6a-b**).

Calculation of solar evaporation efficiency

The solar evaporation efficiency of pure water, CPAE and MiCAE-12 under the solar simulator is calculated by Equation 1: [1-2]

$$\eta = \frac{\dot{m} h_{lv}}{P_{in}} \tag{1}$$

where $\dot{m}$ is the net evaporation rate (kg m^{-2} h^{-1}), h_{lv} represents the latent enthalpy of the liquid-vapor phase change of water (kJ kg^{-1}), and P_{in} denotes the incident solar irradiation power (kW m^{-2}).

The net evaporation rate $\dot{m}$ is calculated by the following Equation 2: [3]

$$\dot{m} = \dot{m_{total}} - \dot{m_{dark}} - \frac{S_1 - S_2}{S_1} \dot{m_{water}} \tag{2}$$

Where $\dot{m_{total}}$ is the total evaporation rate of CPAE or MiCAE-12 under one-sun irradiation. $\dot{m_{total}}$ of CPAE and MiCAE-12 are 1.643 kg m^{-2} h^{-1} and 1.902 kg m^{-2} h^{-1} in **Figure 4.4c**, respectively. $\dot{m_{dark}}$ is the dark environment evaporation rate without sun irradiation. $\dot{m_{dark}}$ of pure water, CPAE and MiCAE-12 are 0.254 kg m^{-2} h^{-1}, 0.406 kg m^{-2} h^{-1} and 0.476 kg m^{-2} h^{-1}, respectively. $\dot{m_{water}}$ is the evaporation rate (0.521 kg m^{-2} h^{-1}) of brine under one sun irradiation. S_1 is the opening area of the Petri dish (28.27 cm^2), S_2 is the sample area (22.90 cm^2 in **Figure 4.4a**). The evaporation rate is calculated from the slope of the curve in **Figure 4.4b** and **S4.9a-c**.

h_{lv} changes under different temperature and their relationship can be described by Equation 3: [4]

$$h_{lv} = \alpha + \beta T + \gamma T^{1.5} + \delta T^{2.5} + \varepsilon T^3 \tag{3}$$

where α = 2500.304, β = -2.2521025, γ = -0.021465847, δ = 3.1750136×10^{-4}, ε = -2.8607959×10^{-5} are constants, and T is temperature (°C). Thus, the h_{lv} should be 2443.05 kJ kg^{-1} at 24.5°C (for pure water, **Figure 4.3c**), 2416.68 kJ kg^{-1} at 35.6°C (for CPAE, **Figure S4.8c**), 2418.11 kJ kg^{-1} at 35°C (for MiCAE-12, **Figure 4.3c**).

Finally, the solar evaporation efficiencies of pure water, CPAE and MiCAE-12 are calculated to be 18.2%, 76.4% and 89.2% under one-sun irradiation, respectively.

Estimation of heat loss

The energy losses of the monolithic integrated cellulose aerogel-based evaporator (MiCAE) with an exposed area of 22.90 cm^2 under one sun irradiation is calculated as an example. The MiCAE-12 is floating on the surface of brine to prevent the heat loss of the bulk solution from conduction and convection during test. The localized thermal energy at evaporator *via* photo-thermal conversion can be divided into five parts: energy consumption by water evaporator, loss of reflection on evaporator surface, heat radiation loss, heat conduction loss and heat convection loss. The detailed calculation of heat loss is analyzed below[5].

Evaporator surface reflection loss

Considering the optical absorption of MiCAE-12 is about 93.7%, the reflect heat loss should be about 6.3%.

Radiation loss

The radiation loss of the evaporator is calculated by the Stefan-Boltzmann equation, as below,

$$\Phi = \mathrm{A}\varepsilon\sigma(T_1^4 - T_2^4)$$

$$\text{Radiation loss} = \frac{\Phi}{AC_{opt}q_i} = \frac{\varepsilon\sigma(T_1^4 - T_2^4)}{C_{opt}q_i}$$

Where Φ is the heat flux, ε is the emissivity of the absorbing surface (0.95), A represents the exposed area, σ is the Stefan-Boltzmann constant which is 5.67×10^{-8} J m^{-2} s^{-1} K^{-4}, T_1 is the surface temperature of MiCAE-12 (32.73°C). T_2 is the adjacent environment temperature (28.40°C). The radiation heat loss is 2.61% for the evaporator under one-sun irradiation.

Conduction

Although the hydrophobic thermal barrier is set to prevent the heat loss to the bulk solution from conduction and convection, a portion heat loss conducted to bulk water might be occur via the hydrophilic water pumping layer. The conduction loss is calculated based on the bulk water absorption heat Q as follows,

$$Q = Cm\Delta T$$

$$\text{Conduction loss} = \frac{Q}{AC_{opt}q_i\Delta \mathrm{t}} = \frac{Cm\Delta \mathrm{T}}{AC_{opt}q_i\Delta \mathrm{t}}$$

Where Q represents the heat flux, C represents the specific heat capacity of water (4.2 kJ °C^{-1} kg^{-1}), m is the bulk water used in the experiment (~40 g), ΔT is the temperature change of the bulk water during the Δt (2.5°C after 90 min). The conduction heat loss is 3.3% in this experiment.

Convection

The convection loss is calculated based on Newton's Law of Cooling as below,

$$\Psi = \xi A\Delta T$$

Convection loss = $\dfrac{\Psi}{AC_{opt}q_i} = \dfrac{\xi\Delta T}{C_{opt}q_i}$

Where Ψ is the heat flux, ξ is the convection heat transfer coefficient (2.24 J m^{-2} s^{-1} K^{-1})[6], ΔT is the temperature difference between the surface temperature of the evaporator (32.73°C) and the adjacent environment temperature (28.40°C). The convective heat loss is 0.97% in this experiment.

In summary, the total heat loss for the MiCAE-12 under one-sun irradiation is about 13.2%. Therefore, the total energy consumption of the five parts is about 86.8%, which is in good agreement with the experimental photo-thermal conversion efficiency 89.2%.

4.6.2 Supporting results and discussion

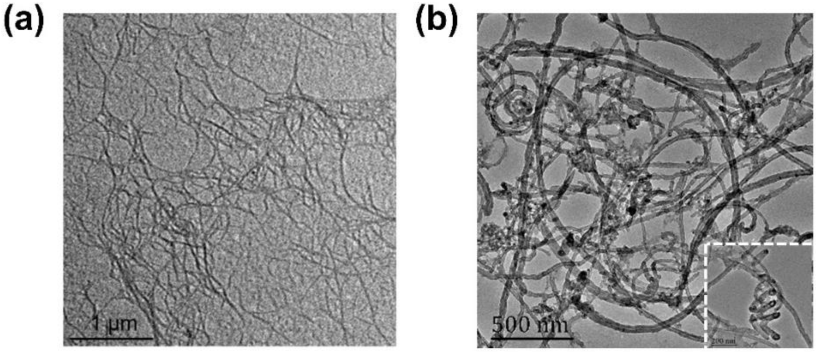

Figure S4.1 (a) TEM image of the CNFs, showing uniform cellulose nanofibrils used for assembly of cellulose aerogel. (b) TEM image of the MCNTs, showing the distinct hollow structure.

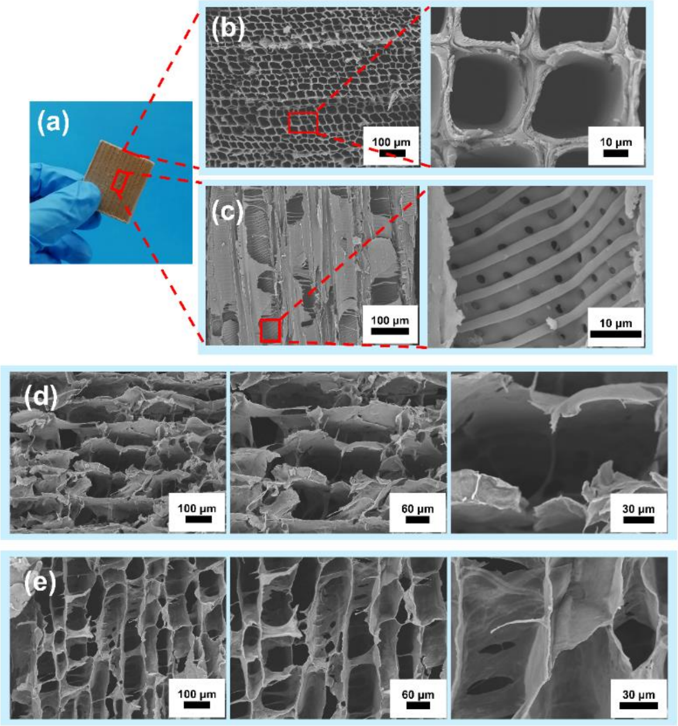

Figure S4.2 (a) Optical image and SEM images of (b) cross-section and (c) longitudinal section of pine wood at different magnifications, showing the horizontal hierarchical cellular networks, vertically aligned channels and porous structures. SEM images of (d) cross-section and (e) longitudinal section of CPA at different magnifications, showing the wood-like structures of CPA.

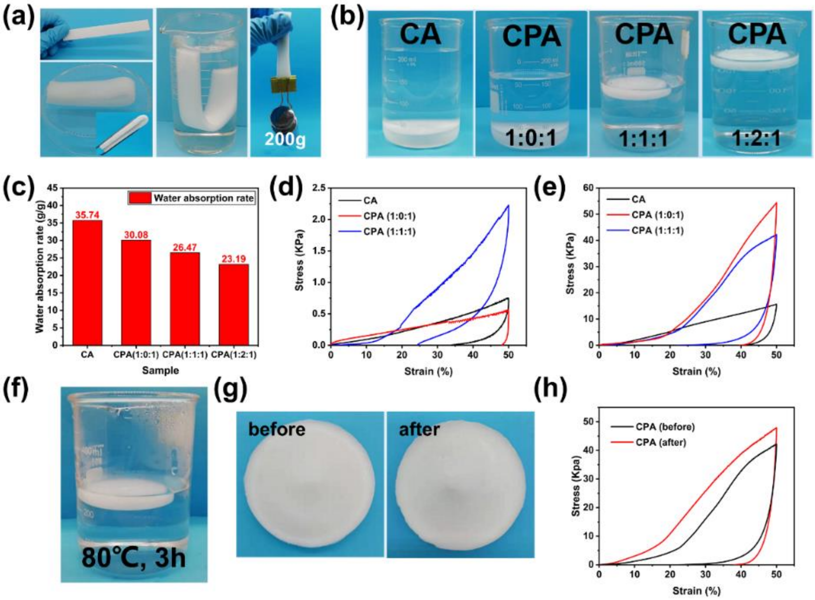

Figure S4.3 (a) Digital pictures of the CPA under both dry and wet conditions, showing the great flexibility and strength of the aerogel. (b) Digital pictures of the pristine cellulose aerogel (CA), CPA (CNFs: KH560: PVA in weight ratio) with different content of KH560 in water. (c) Water absorption capacity of CA, CPA with different content of KH560. Compressive stress-strain curves of CA, CPA (1:0:1), and CPA (1:1:1) both (d) in water-filled and (e) dry states (at ε = 50%). Digital pictures (f) showing the fine floating stability and (g) the great structural stability of the CPA in hot water. And (h) the corresponding compressive stress-strain curves of the CPA before and after the thermal treatment.

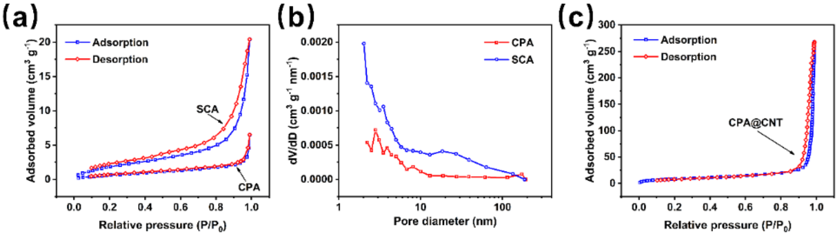

Figure S4.4 (a) Nitrogen adsorption and desorption isotherms and (b) BJH pore distribution for SCA and CPA. (c) Nitrogen adsorption and desorption isotherms for CPA@CNT.

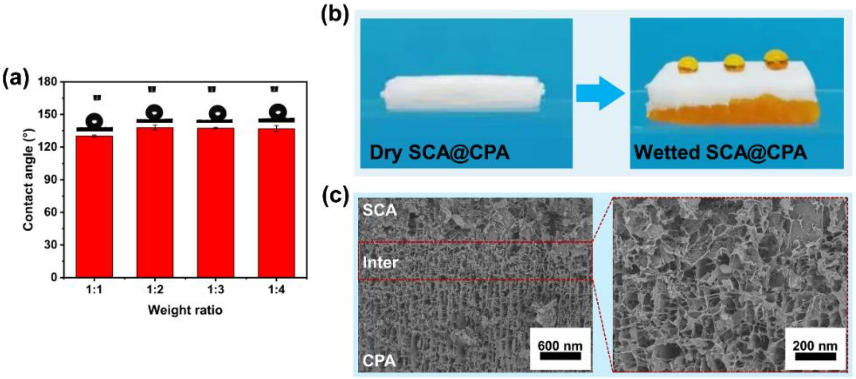

Figure S4.5 (a) The contact angle of SCA (CNFs: VTMS in weight ratio) with different content of VTMS. The maximum contact angle was observed on the SCA (1:2). Due to the certain number of reactive hydroxyl groups on the surface of cellulose aerogel, SCA prepared doesn't exhibit an increasing contact angle by further increasing the dosage of VTMS. (b) Wettability of SCA@CPA, showing an obvious different wettability. (c) SEM images of the interface of SCA and CPA at different magnifications, showing a transitional "interphase" structure at the interface.

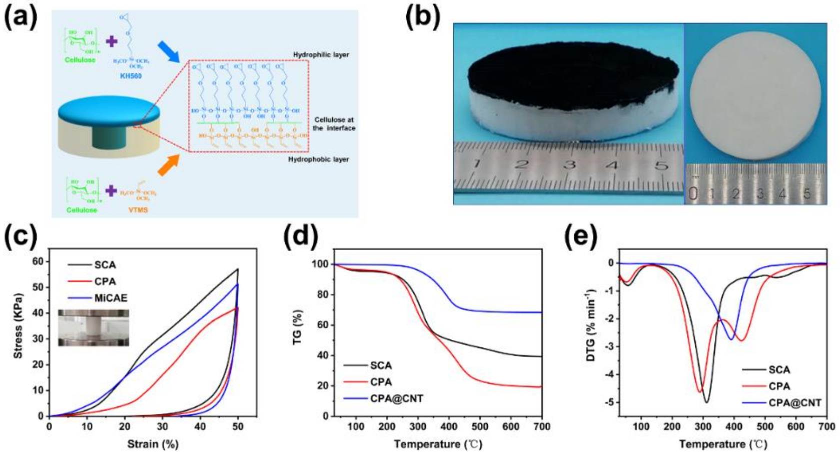

Figure S4.6 (a) Illustration of fabricating SCA@CPA aerogels, proposing molecular structure of cross-linking within the aerogels. (b) Digital pictures for the MiCAE: 5.4 cm in diameter, reflecting the ready scalability of the fabrication procedure. (c) Compressive stress-strain curves (at ε = 50%) and (d) and (e) thermogravimetric analysis of SCA, CPA and CPA@CNT.

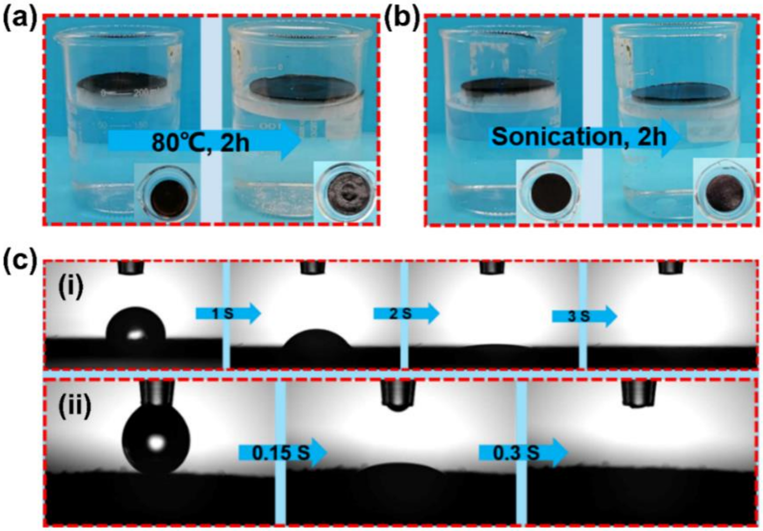

Figure S4.7 The robustness and stability of MiCAE under a series of continuous harsh tests: (a) high temperature (80°C, 2h) and (b) ultrasonic agitation (400 W, 2 h). (c) Snapshots of the water contact angle on the upper surface of (i) SCA@CPA and (ii) MiCAE-12 at different times.

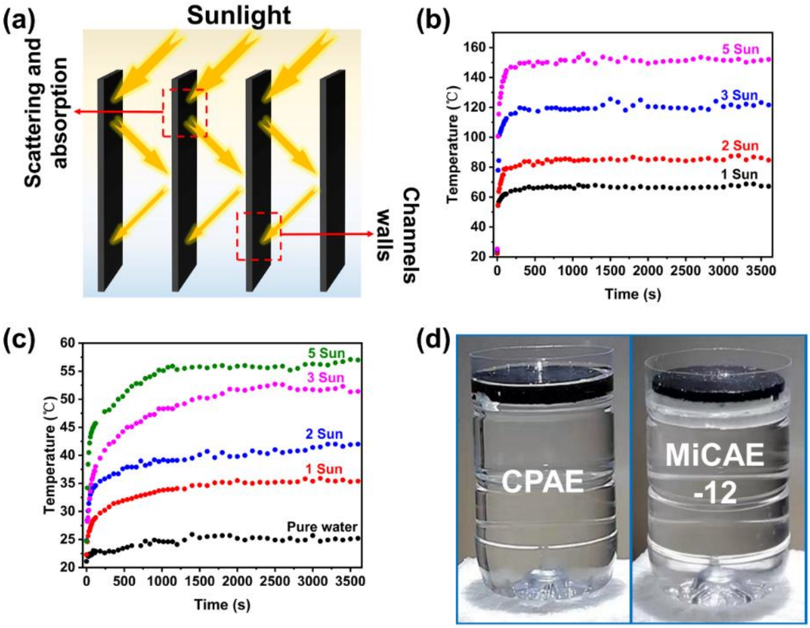

Figure S4.8 (a) Schematic demonstration of multiple scattering and absorption of light. (b) Temperature variation over time of MiCAE under dry conditions at different light intensity. (c) Temperature variation over time of CPAE under wet conditions at different light intensity. (d) Optical images of both the CPAE and the MiCAE-12 in water, showing the better heat localization property of MiCAE compared with the CPAE.

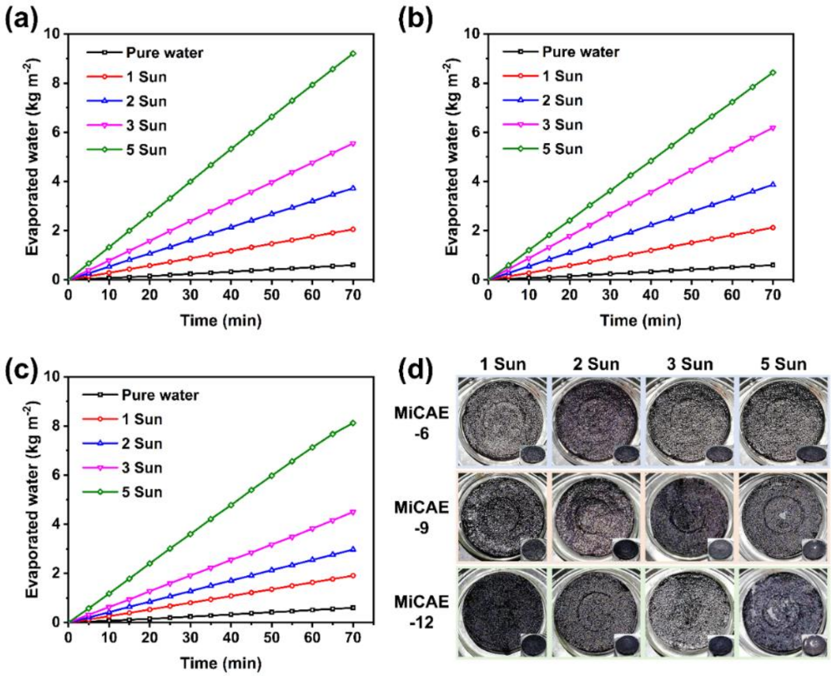

Figure S4.9 Cumulative mass change versus solar light irradiation time for (a) MiCAE-6, (b) MiCAE-9 and (c) CPAE under different concentrated sunlight. The cumulative mass change versus solar light irradiation time for pure water under one-sun irradiation served as the control. (d) Digital photos showing the salt deposition on the surfaces of different monolithic integrated cellulose aerogel-based evaporators under different concentrated sunlight after the irradiation of 90 min.

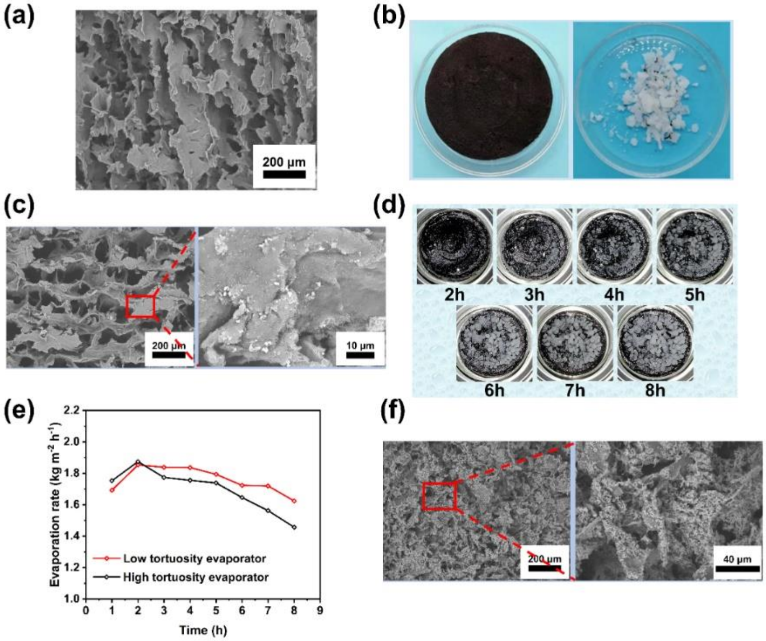

Figure S4.10 (a) SEM image of a longitudinal section of the MiCAE-12 with the low tortuosity porous structure after the continuous 8-hour solar evaporation of seawater under one-sun irradiation, showing no salt deposition both on the surface and in the internal of the evaporator. (b) Pictures of the MiCAE-12 with low tortuosity porous structure and salts collected from 17.5 wt.% NaCl solution after desalination, and (c) SEM images of the MiCAE-12 with low tortuosity porous structure at different magnifications after desalination, showing very little salt deposition on the surface of the evaporator. (d) Pictures and (e) the corresponding evaporation rates of the MiCAE-12-HT during the continuous 8-hour solar evaporation of 17.5 wt.% NaCl solution under one-sun irradiation. (f) SEM images of the MiCAE-12-HT at different magnifications after desalination, showing severe salt deposition in the channels of water transportation.

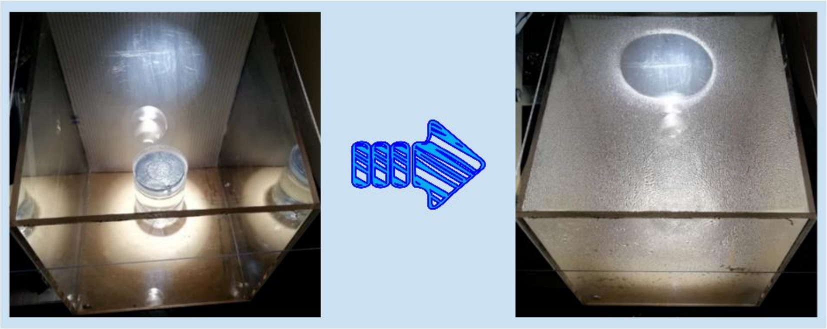

Figure S4.11 Solar thermal vapor generation device. Water vapor generation by using the solar vapor generation device with MiCAE-12 before and after one-sun irradiation.

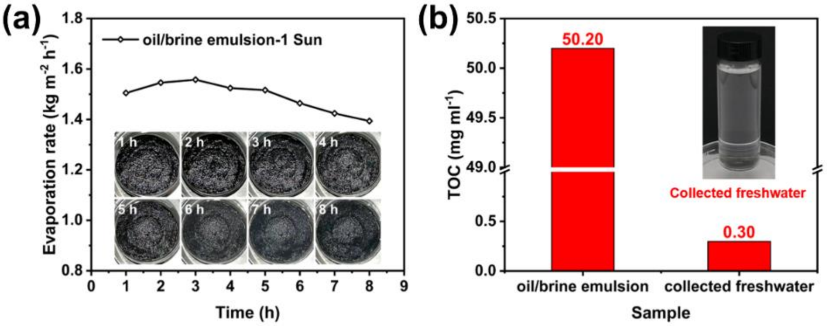

Figure S4.12 (a) Pictures and the corresponding evaporation rates of the MiCAE-12 during the continuous 8-hour solar evaporation of oil/brine emulsion under one-sun irradiation. (b) TOC (Total Organic Carbon) analysis of the oil/brine emulsion and collected freshwater. The inset shows that the freshwater collected from the condensed vapor doesn't contain apparent oil droplets.

Table S4.1 Evaporation rates and efficiencies of various materials and devices for solar powered desalination of seawater from irradiation equivalent to one sun.

Material or device	**Evaporation rate Under one-sun (kg m^{-2} h^{-1})**	**Efficiency (%)**	**References**
Plasmonic wood	1	68.75	[7]
Carbonized longitudinal wood	1.08	74	[8]
CNTs/flexible wood membrane	0.95	65	[9]
Graphite/wood	1.15	80	[10]
Bilayer CNF-CNT aerogel	1.11	76.3	[11]
CNF/CNT hybrid aerogel	1.24	83.3	[12]
CNTs@SiO$_2$ nanofibrous aerogel	1.50	85	[13]
Bilayer MF-PPy foam	1.574	90.4	[14]
Hanging photothermal fabric	1.94	89.9	[15]
Photothermal fabric with 2D/3D structure	1.54	~81.5	[16]
CS/RGO-modified spacer fabric	1.4325	86	[17]
CNT-coupled cotton fabric	1.59	89.6	[18]
Loofahs-based evaporator	~1.42	89.9	[5]
Corn stalk-based evaporator	2.48	68.2	[19]
Carrot-based evaporator	2.04	127.8	[20]
Honeycomb-based evaporator	2.13	85	[3]
Mushroom-based evaporator	1.475	78	[21]
Carbonized sunflower heads	1.51	100.4	[22]
C-PDVB-BF$_4$ILs	1.47	92.4	[23]

3D printing CNT/GO/CNT	1.25	85.6	24
Electrospinning CB/PAN/PVDF	1.20	82	25
3D printing CB/GO/EPS	~1.27	87.5	26
Monolithic integrated Cellulose aerogel-based evaporator	1.903	89.2	**This work**

4.6.3 Supporting references

(1) Ghasemi, H.; Ni, G.; Marconnet, A. M.; Loomis, J.; Yerci, S.; Miljkovic, N.; Chen, G. Solar Steam Generation by Heat Localization. *Nature Communications* **2014,** *5*, 4449.

(2) Liu, Y.; Yu, S.; Feng, R.; Bernard, A.; Liu, Y.; Zhang, Y.; Duan, H.; Shang, W.; Tao, P.; Song, C.; Deng, T. A Bioinspired, Reusable, Paper-Based System for High-Performance Large-Scale Evaporation. *Advanced Materials* **2015,** *27* (17), 2768-2774.

(3) Song, X.; Song, H.; Wang, S.; Liu, J.; Zhou, L.; Xu, J.; Chen, K. Enhancement of Solar Vapor Generation by a 3D Hierarchical Heat Trapping Structure. *Journal of Materials Chemistry A* **2019,** *7* (46), 26496-26503.

(4) Popiel, C.; Wojtkowiak, J. Simple Formulas for Thermophysical Properties of Liquid Water for Heat Transfer Calculations (from 0 °C to 150 °C). *Heat Transfer Engineering* **1998,** *19* (3), 87-101.

(5) Liu, C.; Hong, K.; Sun, X.; Natan, A.; Luan, P.; Yang, Y.; Zhu, H. An ‘Antifouling’ Porous Loofah Sponge with Internal Microchannels as Solar Absorbers and Water Pumpers for Thermal Desalination. *Journal of Materials Chemistry A* **2020,** *8* (25), 12323-12333.

(6) Li, Y.; Gao, T.; Yang, Z.; Chen, C.; Luo, W.; Song, J.; Hitz, E.; Jia, C.; Zhou, Y.; Liu, B.; Yang, B.; Hu, L. 3D-Printed, All-in-One Evaporator for High-Efficiency Solar Steam Generation under 1 Sun Illumination. *Advanced Materials* **2017,** *29* (26), 1700981.

(7) Zhu, M.; Li, Y.; Chen, F.; Zhu, X.; Dai, J.; Li, Y.; Yang, Z.; Yan, X.; Song, J.; Wang, Y.; Hitz, E.; Luo, W.; Lu, M.; Yang, B.; Hu, L. Plasmonic Wood for High-Efficiency Solar Steam Generation. *Advanced Energy Materials* **2018,** *8* (4), 1701028.

(8) Liu, H.; Chen, C.; Chen, G.; Kuang, Y.; Zhao, X.; Song, J.; Jia, C.; Xu, X.; Hitz, E.; Xie, H.; Wang, S.; Jiang, F.; Li, T.; Li, Y.; Gong, A.; Yang, R.; Das, S.; Hu, L. High-Performance Solar Steam Device with Layered Channels: Artificial Tree with a Reversed Design. *Advanced Energy Materials* **2018,** *8* (8), 1701616.

(9) Chen, C.; Li, Y.; Song, J.; Yang, Z.; Kuang, Y.; Hitz, E.; Jia, C.; Gong, A.; Jiang, F.; Zhu, J.; Yang, B.; Xie, J.; Hu, L. Highly Flexible and Efficient Solar Steam Generation Device. *Advanced Materials* **2017,** *29* (30), 1701756.

(10) Li, T.; Liu, H.; Zhao, X.; Chen, G.; Dai, J.; Pastel, G.; Jia, C.; Chen, C.; Hitz, E.; Siddhartha, D.; Yang, R.; Hu, L. Scalable and Highly Efficient Mesoporous Wood-based Solar Steam Generation Device: Localized Heat, Rapid Water Transport. *Advanced Functional Materials* **2018,** *28* (16), 1707134.

(11) Jiang, F.; Liu, H.; Li, Y.; Kuang, Y.; Xu, X.; Chen, C.; Huang, H.; Jia, C.; Zhao, X.; Hitz, E.; Zhou, Y.; Yang, R.; Cui, L.; Hu, L. Lightweight, Mesoporous, and Highly Absorptive All-Nanofiber Aerogel for Efficient Solar Steam Generation. *ACS Applied Materials & Interfaces* **2018,** *10* (1), 1104-1112.

(12) Hu, R.; Zhang, J.; Kuang, Y.; Wang, K.; Cai, X.; Fang, Z.; Huang, W.; Chen, G.; Wang, Z. A Janus Evaporator with Low Tortuosity for Long-Term Solar Desalination. *Journal of Materials Chemistry A* **2019,** *7* (25), 15333-15340.

(13) Dong, X.; Cao, L.; Si, Y.; Ding, B.; Deng, H. Cellular Structured CNTs@SiO_2 Nanofibrous Aerogels with Vertically Aligned Vessels for Salt-Resistant Solar Desalination. *Advanced Materials* **2020,** *32* (34), 1908269.

(14) Li, C.; Jiang, D.; Huo, B.; Ding, M.; Huang, C.; Jia, D.; Li, H.; Liu, C.-Y.; Liu, J. Scalable and Robust Bilayer Polymer Foams for Highly Efficient and Stable Solar Desalination. *Nano Energy* **2019,** *60*, 841-849.

(15) Liu, Z.; Wu, B.; Zhu, B.; Chen, Z.; Zhu, M.; Liu, X. Continuously Producing Watersteam and Concentrated Brine from Seawater by Hanging Photothermal Fabrics under Sunlight. *Advanced Functional Materials* **2019,** *29* (43), 1905485.

(16) Xiao, P.; Gu, J.; Zhang, C.; Ni, F.; Liang, Y.; He, J.; Zhang, L.; Ouyang, J.; Kuo, S.-W.; Chen, T. A Scalable, Low-Cost and Robust Photo-Thermal Fabric with Tunable and Programmable 2D/3D Structures Towards Environmentally Adaptable Liquid/Solid-Medium Water Extraction. *Nano Energy* **2019,** *65*, 104002.

(17) Wang, F.; Wei, D.; Li, Y.; Chen, T.; Mu, P.; Sun, H.; Zhu, Z.; Liang, W.; Li, A. Chitosan/Reduced Graphene Oxide-Modified Spacer Fabric as a Salt-Resistant Solar Absorber for Efficient Solar Steam Generation. *Journal of Materials Chemistry A* **2019,** *7* (31), 18311-18317.

(18) Kou, H.; Liu, Z.; Zhu, B.; Macharia, D. K.; Ahmed, S.; Wu, B.; Zhu, M.; Liu, X.; Chen, Z. Recyclable CNT-Coupled Cotton Fabrics for Low-Cost and Efficient Desalination of Seawater under Sunlight. *Desalination* **2019,** *462*, 29-38.

(19) Sun, Z.; Li, W.; Song, W.; Zhang, L.; Wang, Z. A High-Efficiency Solar Desalination Evaporator Composite of Corn Stalk, Mcnts and TiO_2: Ultra-fast Capillary Water Moisture Transportation and Porous Bio-tissue Multi-layer Filtration. *Journal of Materials Chemistry A* **2020,** *8* (1), 349-357.

(20) Long, Y.; Huang, S.; Yi, H.; Chen, J.; Wu, J.; Liao, Q.; Liang, H.; Cui, H.; Ruan, S.; Zeng, Y.-J. Carrot-Inspired Solar Thermal Evaporator. *Journal of Materials Chemistry A* **2019,** *7* (47), 26911-26916.

(21) Xu, N.; Hu, X.; Xu, W.; Li, X.; Zhou, L.; Zhu, S.; Zhu, J. Mushrooms as Efficient Solar Steam-Generation Devices. *Advanced Materials* **2017,** *29* (28), 1606762.

(22) Sun, P.; Zhang, W.; Zada, I.; Zhang, Y.; Gu, J.; Liu, Q.; Su, H.; Pantelic, D.; Jelenkovic, B.; Zhang, D. 3D-Structured Carbonized Sunflower Heads for Improved Energy Efficiency in Solar Steam Generation. *ACS Applied Materials & Interfaces* **2019,** *12* (2), 2171-2179.

(23) Xiao, C.; Liang, W.; Chen, L.; He, J.; Liu, F.; Sun, H.; Zhu, Z.; Li, A. Janus Poly (Ionic Liquid) Monolithic Photothermal Materials with Superior Salt-Rejection for Efficient Solar Steam Generation. *ACS Applied Energy Materials* **2019,** *2* (12), 8862-8870.

(24) Li, Y.; Gao, T.; Yang, Z.; Chen, C.; Luo, W.; Song, J.; Hitz, E.; Jia, C.; Zhou, Y.; Liu, B.; Yang, B.; Hu, L. 3D-Printed, All-in-one Evaporator for High-Efficiency Solar Steam

Generation under 1 Sun Illumination. *Advanced Materials* **2017,** *29* (26), 1700981.

(25) Gao, T.; Li, Y.; Chen, C.; Yang, Z.; Kuang, Y.; Jia, C.; Song, J.; Hitz, E. M.; Liu, B.; Huang, H.; Yu, J.; Yang, B.; Hu, L. Architecting a Floatable, Durable, and Scalable Steam Generator: Hydrophobic/Hydrophilic Bifunctional Structure for Solar Evaporation Enhancement. *Small Methods* **2019,** *3* (2), 1800176.

(26) Li, Y.; Gao, T.; Yang, Z.; Chen, C.; Kuang, Y.; Song, J.; Jia, C.; Hitz, E. M.; Yang, B.; Hu, L. Graphene Oxide-Based Evaporator with One-Dimensional Water Transport Enabling High-Efficiency Solar Desalination. *Nano Energy* **2017,** *41*, 201-209.

Chapter 5

Mechanically Flexible, Waterproof, Breathable Composite Aerogels as Wearable Heaters for Personal Thermal Management

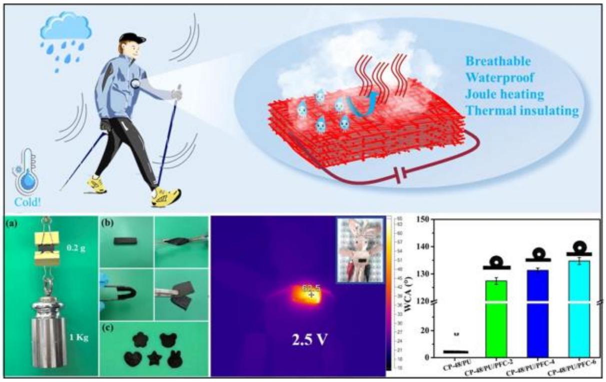

Multifunctional wearable heaters are highly desirable for the growing demand in the field of personal thermal management. In this chapter, we present an efficient and feasible strategy to construct wearable heaters using waterproof and breathable composite aerogels made from cellulose nanofiber (CNF) aerogels, polypyrrole (PPy), fluorinated finishing agent and polyurethane (PU). The named composite aerogels exhibited a lightweight structure (0.14 g cm^{-3}), superior mechanical robustness and outstanding Joule heating performance (up to 173℃ at 4 V in about 70 s). They feature a water contact angle (WCA) up to 135° enabled by the synergistic effect of the fluorinated agents and surface roughness. The aerogels also exhibited high air permeability (186.6 ± 22 L S^{-1} m^{-2}) and satisfiable water vapor transmission (WVT) rate at 5.8 ± 0.8 kg m^{-2} d^{-1}. These favorable features made the composite aerogels highly promising for intelligent garments, wearable devices and personal thermal management systems.

The contents of this chapter have been published as: Yating Wang, Luying Chen, Huan Cheng, Bijia Wang, Xueling Feng, Zhiping Mao, and Xiaofeng Sui. Mechanically flexible, waterproof, breathable cellulose/polypyrrole/polyurethane composite aerogels as wearable heaters for personal thermal management, *Chemical Engineering Journal*, **2020**, *402*, 126222.

5.1 Introduction

Wearable heaters based on the Joule effect *via* converting electrical energy into thermal energy have attracted broad attention due to their wide potential applications including personal thermal management, controlled drug delivery, defogging and defrosting [1-5].

Wearable heaters based on various materials have been developed, such as metal-based [6-10], carbon-based [11-15], conductive polymer-based [16-20] and the ones based on a combination of them [20-22]. Lightweight, flexible and body-conformable wearable heaters have been made possible by incorporating metal nanofibers [23-24], carbon nanotubes [25-26], graphene [27-28], and conductive polymers [16, 29], in papers, films and textiles. For example, Guo et al. [30] prepared foldable graphene papers with micrometer-scale thickness and a saturated Joule heating temperature of 42°C attainable within 130 s at a low supply voltage around 3.2 V. Stretchable thermochromic resistive heaters with a saturated temperature of 95°C at 8 V were prepared by Peng and co-workers using thermochromic silicone elastomer and aligned carbon nanotube sheet[31].

Breathability was also considered key to comfortability of wearable heaters. Hyung et al. [32]fabricated a textile-based wearable and washable heater exhibiting an air permeability of 0.2 g cm^{-2} d^{-1} and a maximum Joule heating temperature of 79°C at 2.1 V attainable in 400 s by spin-coating woven Kevlar with Ag@$Ni_xCo_{1-x}Se$ and polydimethylsiloxane. Using an improved *in situ* polymerization method, Lv et al. [33]prepared high-performance polypyrrole (PPy) coated textile electrodes with low sheet resistance (less than 10 Ω sq^{-1}) suitable for wearable applications, because breathability and comfortability were not compromised by the thin PPy coating.

Multifunctional three-dimensional (3D) wearable heaters based on aerogels showed promising applications in the field of personal thermal management [34]. The desirable 3D networked inner structure of aerogels provide micro channels to allow effective air transmission to the skin. The low thermal conductivity of aerogels owing to their inherent porous structure inhibits loss of thermal energy so as to reduce energy consumption [35]. For example, the multifunctional wearable heaters developed by Zhang et al showed high electrical conductivity (230 S m^{-1}) and excellent hydrophobicity (water contact angle, WCA of up to 137°). These heaters developed based on an aerogel film composed of carbon nanotubes, aramid nanofibers and fluorocarbon resin, could reach 113.5°C within 50 s at a supplied voltage of 10 V [36].

Cellulose aerogels possess a versatile nature and favorable features such as light weight, high surface area, high chemical stability and thermal stability, adjustable porous structure, wide availability, and low cost [37-39]. It is significant to construct multifunctional wearable heaters based on cellulose aerogels. Herein, we report a mechanically flexible, waterproof and breathable composite aerogel derived from a porous cellulose nanofiber (CNF) aerogel, conductive PPy and elastic polyurethane (PU) (**Figure 5.1a**). The conductive CNF/PPy (CP) aerogel was obtained *via in situ* polymerization of PPy on the surface of the CNF aerogel. Benefiting from subsequent coating of PU and fluorinated finishing agent, the resulting CNF/PPy/PU composite aerogel exhibited superior mechanical robustness, good flexibility and easy processing. The composite aerogel also displayed hydrophobicity with a WCA up to 135°, high water vapor transmission (WVT) rate of 5.8±0.8 kg m^{-2} d^{-1} and outstanding Joule heating performance (up to 173°C at 4 V within 70 s). This work demonstrates a promising direction for the fabrication of multifunctional wearable heaters, suitable to be used in extreme environments, such as frigid polar regions, pluvial mountainous areas, and cryogenic workshops.

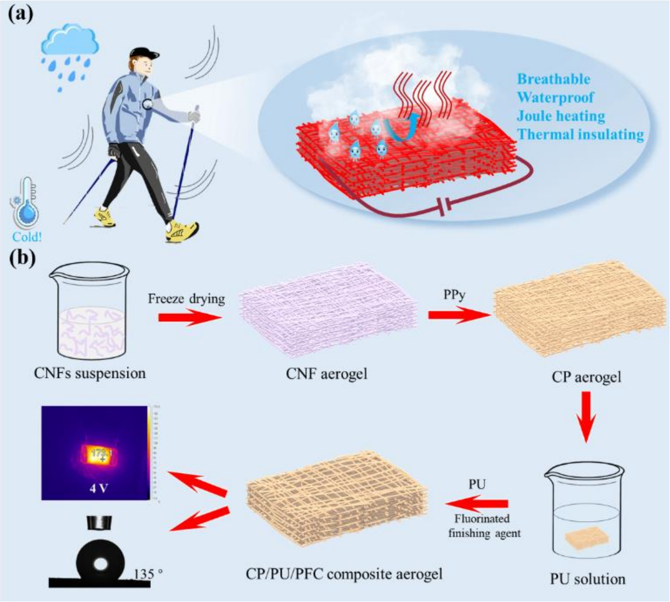

Figure 5.1 (a) Schematic illustration of using the multifunctional CP/PU/PC composite aerogel in personal thermal management. (b) Fabrication process of the CP/PU/PC composite aerogel.

5.2 Results and discussion

5.2.1 Strategy of constructing a multifunctional composite aerogel

We designed the multifunctional composite aerogels based on the following three criteria: (i) CNF aerogels should have reasonable mechanical strength, (ii) the conductive network must be constructed uniformly along the surface of the CNF aerogels, (iii) bonding with the elastic PU and fluorinated finishing agent should have minimum impact on the properties of the CP aerogels. The fabrication process of the CP/PU/PC composite aerogels is briefly illustrated in **Figure 5.1b**. The CNF aerogel obtained *via* freeze-drying features a high surface area and adjustable porous structure providing a stable skeleton for construction of well-insulated wearable heaters [38, 40-41]. Size of the pores could be finely tuned to allow transport of only vapor but not water droplets, which provided excellent water vapor transport capacity for wearable heaters. Subsequently, a thin layer of PPy was introduced to the CNF aerogel by immersion of the aerogel first in an aqueous solution of $FeCl_3$ and NaSSA at room temperature, then in a cyclohexane solution of pyrrole at 4°C. The polymerization of pyrrole occured on the surface of the CNF aerogel. After completion of the oxidative polymerization, the deposited PPy endowed the aerogel with excellent Joule heating performance. Next, PU was chosen as the reinforcement coating to create a robust CP/PU composite aerogel. Finally, the composite aerogel was made hydrophobic by treatment with a fluorinated finishing agent (PHOBOL CP-SLA). Therefore, the resulting thermal insulating, waterproof and breathable performances greatly promoted the comfortability and environmental adaptability of apparels made of the CP/PU/PC composite aerogels in extreme conditions.

5.2.2 Morphology and properties

SEM was used to observe the microstructure of the aerogels. **Figure 5.2a-e** shows the cross-sectional morphologies of the CNF aerogel and CP aerogels at different magnifications. As can be seen from **Figure 5.2a**, the CNF aerogel possessed a highly porous honeycomb structure with cells sized from 30 μm to 100 μm, which was a result of phase separation of water during freeze drying. As shown in **Figure 5.2b-d**, the open-celled honeycomb structure was preserved after the deposition of PPy nanoparticles (inset of **Figure 5.2b-d**) *via in situ* polymerization. It can also be noted in SEM images shown in the insets that the PPy nanoparticles were distributed more tightly and uniformly along the cell wall with increasing PPy loading, which is beneficial to the construction of a highly conductive PPy network. The Raman spectra of the CP aerogel are shown in **Figure S5.1**. The peaks at 934 cm^{-1} and 966 cm^{-1} are attributed to the ring deformation associated with the radical cation of PPy. The double peaks at 1059 cm^{-1}, 1083 cm^{-1} and 1229 cm^{-1} correspond to the in-plane bending of C-Hs. The peaks at 1322 cm^{-1}, 1376 cm^{-1} and 1570 cm^{-1} are C-C, C-N and C=C stretching from PPy, respectively, which were also reported in previous literatures [42-44].

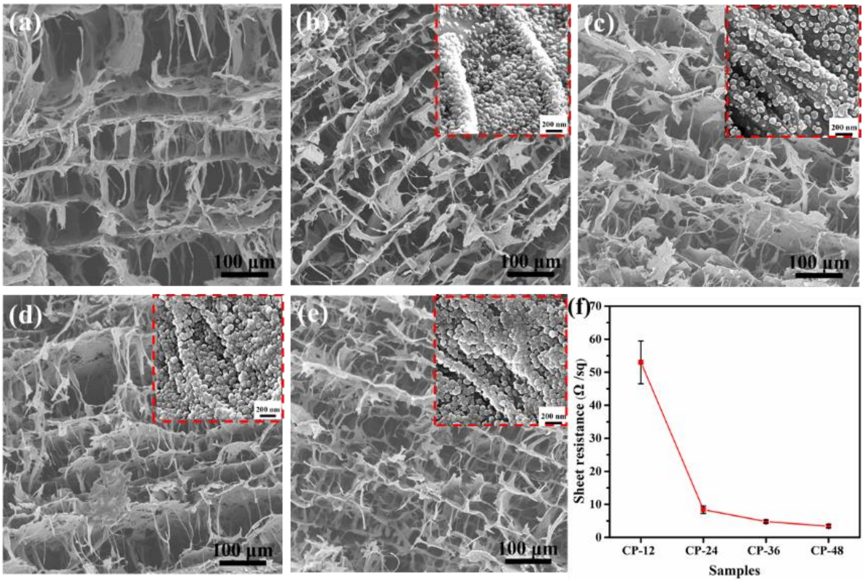

Figure 5.2 SEM and FE-SEM images of (a) CNF aerogel, (b) CP-12, (c) CP-24, (d) CP-36 and (e) CP-48. (f) The sheet resistance of CP aerogel.

Conductivity of CP aerogels is typically evaluated using sheet resistance. The untreated CNF aerogel is electrically insulative. As can be seen from **Figure 5.2f**, the sheet resistance decreased gradually from 53 Ω/sq to 3.4 Ω/sq as more PPy was deposited forming increasingly large junction points and highly conductive networks. It's worth mentioning that low sheet resistance is necessary for the following preparation of conductive composite aerogels.

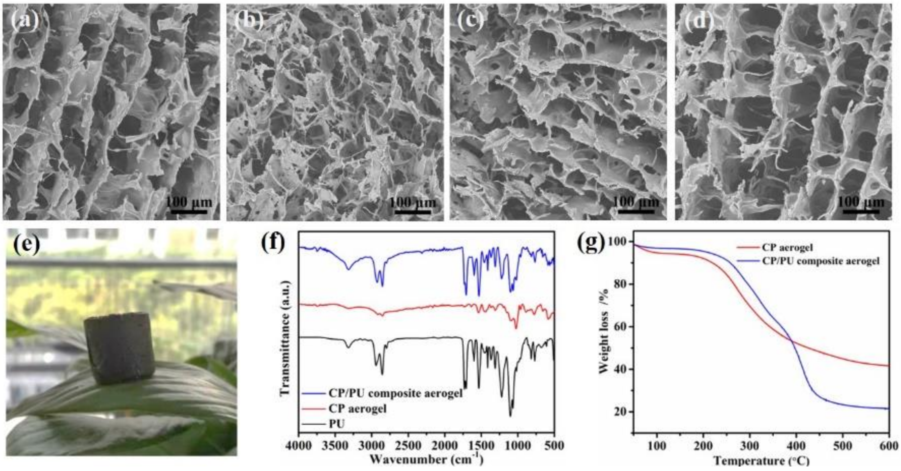

Figure 5.3 SEM images of (a) CP-12/PU, (b) CP-24/PU, (c) CP-36/PU and (d) CP-48/PU. (e) Optical images of CP-48/PU. (f) FTIR spectrum of PU, CP aerogel and CP/PU composite aerogel. (g) TG curves of the CP aerogel and the CP/PU composite aerogel.

SEM images of the CP/PU composite aerogels are shown in **Figure 5.3a-d**. Similar to pristine CP aerogel, the CP/PU composite aerogels still showed a typical 3D networked structure after being coated with PU *via* the wet coagulating method. This indicated that PU was coated uniformly throughout each cell wall of the CP aerogel, which would effectively prevent PPy nanoparticles from falling off the cellulose skeleton. Moreover, PU could endow the aerogels with excellent mechanical strength by dissipating external stress. The CP/PU composite aerogels have super low densities (0.14 g cm^{-3} ~ 0.16 g cm^{-3}), as can be manifested by the fact that it could stand freely on the surface of a leaf of a peace lily plant (**Figure 5.3e**). **Figure 5.3f** shows the FTIR spectrum of the CP aerogel and the CP/PU composite aerogel. The CP/PU composite aerogel showed all characteristic peaks of its components without any new peaks, suggesting there was only physical interactions between PU and the CP aerogel. The TG curves are displayed in **Figure 5.3g**. The PU coating endowed the aerogels with enhanced thermal stability (T_{max} = 412℃ as compared with 275℃ for uncoated CP aerogel), which ensures its safe use during heated processes.

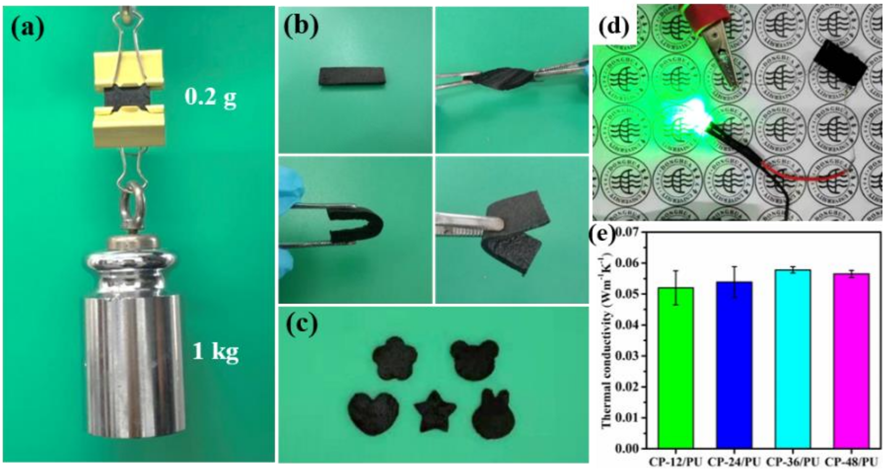

Figure 5.4 (a) A 1 kg loading suspended on a CP-48/PU sheet (thickness = 3 mm, weight = 0.2 g). (b) High flexibility demonstrated by bending and twisting a 3 mm thick CP-48/PU sheet. (c) Processed CP-48/PU of various shapes. (d) Lit LED lamps connected *via* CP-48/PU at a supplied voltage of 3 V. (e) Thermal conductivity of the CP/PU composites.

In dramatic contrast to the brittle CP aerogel, the CP/PU composite aerogel showed significantly improved mechanical properties. As shown in **Figure 5.4a**, a small piece of CP-48/PU sheet (weight=0.2 g, thickness=3 mm) could bear a load of 1 kg, 5000 times its own weight, without breaking. Furthermore, CP-48/PU sheet could quickly restore to its original shape from being bent and twisted (**Figure 5.4b**), showing great potential for practical thermal management applications. **Figure 5.4c** shows that CP-48/PU could be easily tailored into various shapes owning to its structural robustness, which could also greatly expand its field of application.

As shown in **Figure 5.4d**, the electrical conductivity of the prepared composite aerogel was verified by connecting a light-emitting-diode (LED) with a strip of CP-48/PU sheet (1×2 cm^2). The LED lit up instantly and maintained a steady brightness upon being subjected to a working voltage of 3 V, confirming the electrical conductivity of CP-48/PU.

Thermal insulation plays a crucial role in personal thermal management. Compared with most other Joule heating materials, the CP/PU composite aerogels prepared herein also feature low thermal conductivity and therefore effectively inhibit thermal energy loss, highlighting their versatility. As shown in **Figure 5.4e**, thermal conductivity only changed slightly from 0.052 W m^{-1} K^{-1} to 0.056 W m^{-1} K^{-1} as the PPy content was varied from 0.12 mol to 0.48 mol, which means the composite aerogels could be taken as thermal insulation material to restrain loss of body heat as well as deliver heating by electricity to humans.

5.2.3 Electrical and thermal properties

The electrical responses of the CP/PU composite aerogels are shown in **Figure 5.5a**, and the corresponding parameters and equations used in the linear fittings for the curves are listed in **Table S5.1**. All CP/PU composite aerogels displayed a linear correlation between working voltage and currents from 2 V to 6 V (R^2 >0.99), demonstrating their ohmic behavior. The slopes of the fitted curves are negatively correlated with the resistance of composite aerogels, with CP-48/PU exhibiting the lowest resistance of 8.6 Ω. The electrical conductivities of the CP/PU composite aerogels (**Table S5.2**) increased with the increase of PPy content. CP-48/PU exhibited the highest measured value of 88 S m^{-1}, comparable to most of the wearable heaters reported in the literature.

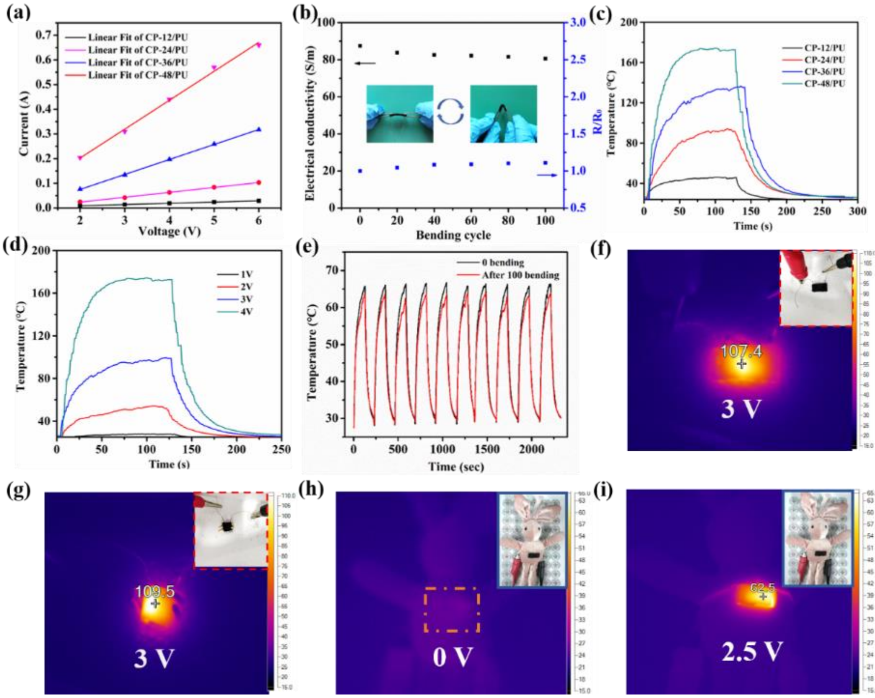

Figure 5.5 (a) The electrical response of the CP/PU composite aerogels. (b) Electrical conductivity and relative resistance of the CP-48/PU upon repeated bending and stretching. (c) Joule heating behaviors of the CP/PU composite aerogels at 4 V. (d) Joule heating behavior of CP-48/PU under various working voltages. (e) Electrical stability and

repeatability of CP-48/PU upon repeated supplied voltages of 2.5 V. IR camera images of CP-48/PU upon (f) stretching and (g) bending at a working voltage of 3 V. (h) and (i) IR thermal images of CP-48/PU in wearable thermotherapy at a working voltage of 0 V and 2.5 V.

Figure 5.5b shows the changes in electrical conductivity of CP-48/PU after being bended and stretched. The electrical conductivity of CP-48/PU remained above 80 S m^{-1} during the 100 bending/stretching cycles, verifying its stable electrical conductivity performance. **Figure 5.5b** also shows the changes of relative resistance (R/R$_0$) of the CP/PU composite aerogel upon repeated bending and stretch (bending angle: about 90°) for 100 times. A stable and constant R/R$_0$ between 1 and 1.1 was observed, the outstanding electromechanical stability of the CP/PU composite aerogels is attributed to the synergistic effect between high electrical conductivity of PPy and mechanical robustness of PU. This also demonstrates that the composite aerogel can be used as a wearable heater endurable of external stress/strain.

The Joule heating performances of the CP/PU composite aerogels were investigated at a constant applied voltage, and the temperature was monitored using an IR camera (**Figure S5.2**). As shown in **Figure 5.5c**, CP-48/PU reached a maximum surface temperature of 173°C within 70 s at a working voltage of 4 V. The fastest heating rate was due to low resistance. The Joule heating behavior of the CP/PU composite aerogels with different resistances was explored, the following equation was established according to the energy balance principle [23, 45]:

$$\frac{U^2}{R} = mc\frac{dT}{dt} + hA(T - T_0) \qquad (1)$$

where U is working voltage, R is the resistance and m is the mass of the electrical heater, c is the specific heat capacity, h stands for convective heat-transfer coefficient and A stands for the area of the electrical heater, T is the surface temperature of the electrical heater and T_0 is the initial ambient temperature. The time-dependent surface temperature could be calculated after integrating eq (1):

$$T = T_0 + \frac{U^2}{RhA}\left(1 - e^{-(hA/mc)}\right)t \qquad (2)$$

According to the above equations, if the applied voltage of the composite aerogels is kept constant, resistance plays a critical role in the Joule heating performance of the aerogels. As revealed in **Figure 5.5c**, the surface temperature of the samples was negatively correlated with resistance. **Figure 5.5d** compared the surface temperature of CP-48/PU under different applied voltages, which demonstrates a positive correlation of surface temperature and working voltage. Moreover, CP-48/PU could attain a high surface temperature at a lower driving voltage, which is convenient and safe for humans to carry around. Electrical stability is a crucial performance for wearable heaters in practical applications. As shown in **Figure 5.5e**, CP-48/PU exhibited a stable cyclic heating performance at a working voltage of 2.5 V. It is noteworthy that the cyclic temperature curves of the 0 and 100th bending/stretching cycle were almost overlapped. In addition, there are no significant changes in *I–V* curves of CP-48/PU when comparing the first and 100th bending/stretching cycle (Figure S3), which indicate the remarkable electrical stability of CP-48/PU.

In consideration of both Joule heating performance and machinal properties, CP-48/PU was chosen for further study. The IR thermal images in **Figure 5.5f-g** clearly show that the surface temperature of CP-48/PU heated at a constant working voltage was invariant upon external stresses from bending (180°) or stretching. **Figure 5.5h-i** shows the application of CP-48/PU as an electrical heater in wearable thermotherapy. The composite aerogel affixed to the chest of the doll was heated using a working voltage of 2.5 V from ambient temperature to 62.5℃, showing the applicability of using it in medical thermotherapy to effectively relieve pain and stiffness within the temperature range of 41℃~77℃ [46]. **Figure S5.4** demonstrates that the composite aerogel could also be used as a wearable heater for personal thermal management under cold conditions.

5.2.4 Waterproof and breathable performance

In this work, the hydrophobic surface of CP-48/PU was constructed by coating with varied amounts of PFC (2 wt.%, 4 wt.% and 6 wt.%). The obtained composite aerogels were denoted as CP-48/PU/PFC-2, CP-48/PU/PFC-6-4 and CP-48/PU/PFC-6 respectively. FTIR spectra of CP-48/PU and CP-48/PU/PFC-4 are shown in **Figure 5.6a**, where the new peaks due to C-F stretching emerge at 1158 cm^{-1} and 1016 cm^{-1}, indicating the successful incorporation of PFC [47].

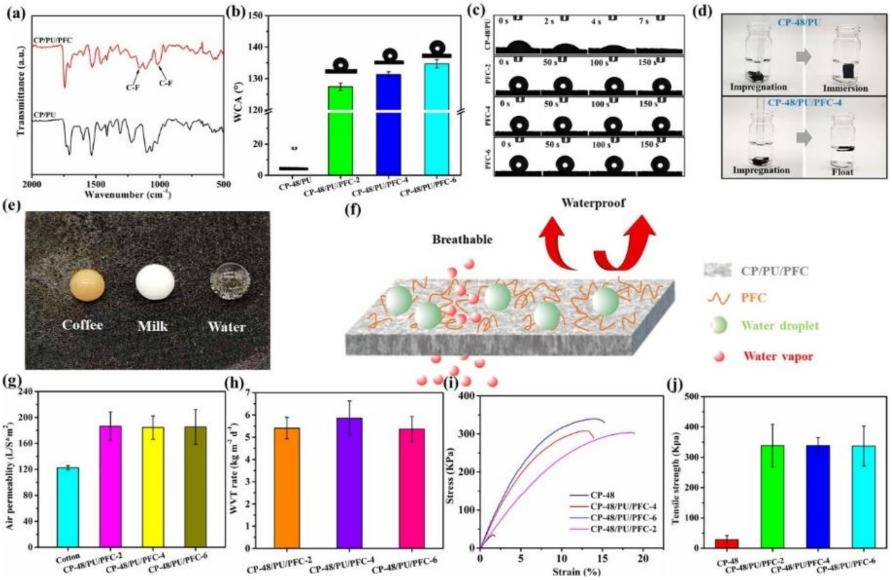

Figure 5.6 (a) FTIR spectra and (b) WCA of CP-48/PU and CP-48/PU/PFC. (c) Comparison of WCA of the aerogels. (d) Different surface behaviors of CP-48/PU and CP-48/PU/PFC-4. (e) The liquids stand on CP-48/PU/PFC-4 with nearly spherical shapes. (f) Breathable waterproof mechanism of CP-48/PU-PFC. (g) Air permeability of the aerogels as compared with cotton, (h) WVT rate, (i) stress–strain curves and (d) tensile strength of the aerogels.

As shown in **Figure 5.6b**, an increase of WCA from 0° to 135° was observed after the treatment with PFC. This highly hydrophobic surface was achieved due to a synergistic effect of the coverage of a coating rich in non-polarizable C-F bonds and an increase in surface roughness (**Figure S5.5**). WCA of CP-48/PU/PFC compares favorably among the reported wearable heaters as shown by the data listed in **Table S5.3**. The retention time of water droplets on CP-48/PU and CP-48/PU/PFC was monitored in **Figure 5.6c**. The droplet was fast absorbed within 7 s through the surface and into the highly porous CP-48/PU, while the surface of CP-48/PU/PFC was able to hold the droplet for over 150 s. Overall, the uniform coating of PU/PFC had converted the hydrophilic surface of the aerogels to hydrophobic with high water contact angle. The hydrophobic coating and rough surface synergistically improved the waterproof performance of the aerogels, allowing the droplet (4 μL) to stand on their surface for a long time. The marked difference in surface behavior of CP-48/PU and CP-48/PU/PFC-4 (behavior imparted by the PFC treatment) is also manifested in **Figure 5.6d**, where CP-48/PU/PFC-4 floated on the water while CP-48/PU completely submerged after impregnation. **Figure 5.6e** showed that coffee and milk dropped to the surface of CP-48/PU/PFC-4 stood on as nearly spherical droplets which could roll off the surface easily, confirming excellent waterproof performance of CP-48/PU/PFC-4. Moreover, CP-48/PU/PFC-4 also demonstrated good resistance to acid and alkaline solutions (**Figure S5.6**).

Breathable performance also needs to be taken into consideration for endowing comfortability to wearable heaters. As shown in **Figure 5.6f**, the pore size of the composite aerogels can be tuned to fall in a range between 30 μm to 100 μm, so as to allow evaporation of water vapor but keep water droplets out.

As shown in **Figure 5.6g**, CP-48/PU/PFC composite aerogels exhibited higher air permeability (184.5±18.0 L S^{-1} m^{-2}~186.6±22 L S^{-1} m^{-2}) than a cotton (122.4±3.3 L S^{-1} m^{-2}) fabric sample of similar thickness (3 mm). As shown in **Figure 5.6h**, The WVT rates of CP-48/PU/PFC composite aerogels were determined to be 5.4±0.5 kg m^{-2} d^{-1} ~ 5.8±0.8 kg m^{-2} d^{-1}, showing that rapid transmission of water vapor was enabled by the 3D networked inner structure of the aerogels. CP-48/PU/PFC composite aerogels coated with various amounts of PFC all exhibited satisfactory tensile strength and elongation at break and outperformed CP-48 in **Figure 5.6i** and **j**, indicating that the incorporation of PFC did not negatively affect the mechanical properties of the aerogels.

5.3 Conclusions

In summary, we presented an effective strategy for fabricating lightweight, robust, stretchable and multifunctional CP/PU/PFC composite aerogels. The microstructures, mechanical strength, thermal insulation properties, Joule heating, waterproof and breathable performances of the resultant composite aerogels were investigated in detail. They exhibited satisfactory Joule heating performance (up to 173℃ at 4 V) with low working voltage and rapid heating rate. Excellent waterproof performance could be achieved with CP-48/PU/PFC-6 which has a large WCA of 135°. Despite having highly waterproof surfaces, the CP/PU/PFC composite aerogels showed prominent breathable performance (the WVT rate of 5.8±0.8 kg m^{-2} d^{-1}) owing to the interconnected porous structure of the aerogels. These results suggest that the mechanically robust and multifunctional CP-48/PU/PFC composite aerogels are highly promising as wearable heaters for applications in harsh environments, such as frigid polar regions, pluvial mountainous areas, and cryogenic workshops.

5.4 Experimental section

5.4.1 Materials

CNFs suspension (1.4 wt.%) was purchased from Tianjin Woodelf biotechnology Co. Ltd. Polyethyleneimine (PEI, with a molecular weight of 600 g/mol) was purchased from Adamas Reagent Co. Ltd. Pyrrole (98%), ferric chloride hexahydrate ($FeCl_3 \cdot 6H_2O$), γ-glycidoxypropyltrimethoxysilane (KH560), sodium 5-sulfosalicylate (NaSSA) and cyclohexane were obtained from Sinopharm Chemical Reagent Co. Ltd. PU solution (solid content 30 wt.%) was supplied from Zhejiang Meisheng New Material Co. Ltd. *N*,*N*-dimethylformamide (DMF) was purchased from Shanghai Chemical Reagent Co. Ltd. PHOBOL CP-SLA (PFC) was obtained from American Du Pont Co. Ltd. All chemicals were used as received without further purification.

5.4.2 Preparation of CP aerogels

The preparation of CNF aerogel was done according to our previously reported procedure [48]. KH560 (1.4 g) was added dropwise into 100 g CNFs suspension (1.4 wt.%), followed by stirring at room temperature for 2 h. Then PEI (1.12 g) was added to the above mixture to afford a uniform suspension (the mass ratio of CNF, KH560 to PEI is 1:1:0.8). The suspension was chilled with liquid nitrogen for 10 min and pumped on a freeze-drier (Labconco FD5-3, USA) for 48 h. At last, the prepared CNF aerogel was kept at 110°C for 30 min to ensure sufficient crosslinking.

The prepared CNF aerogel was subsequently immersed in an aqueous solution containing $FeCl_3 \cdot 6H_2O$ and NaSSA at room temperature for 12 h (the molar ratio of $FeCl_3 \cdot 6H_2O$ to NaSSA is 1:1, and the concentrations are 0.12 mol, 0.24 mol, 0.36 mol and 0.48 mol, respectively). The pyrrole solution was prepared by dissolving pyrrole (0.12 mol, 0.24 mol, 0.36 mol and 0.48 mol) in cyclohexane. The soaked CNF aerogels was transferred and immersed in the above pyrrole solution at 4°C for 30 hours. The molar ratio of the pyrrole monomer, $FeCl_3 \cdot 6H_2O$ to NaSSA was 1:1:1. After polymerization was completed, the composite aerogel was taken out and repeatedly washed with distilled water and ethanol alternately to thoroughly remove the unreacted reagents. Finally, the obtained CP aerogel was dried at 60°C in a vacuum oven for 12 h, and coded as CP-12, CP-24, CP-36 and CP-48 according to the molar mass of pyrrole.

5.4.3 Preparation of CP/PU composite aerogels

The wet coagulating method was employed to fabricate the CP/PU composite aerogels. The prepared CP aerogels were immersed in a PU solution (9 wt.%) for 10 min under reduced pressure (ca. 100 Pa). Subsequently, the above samples were transferred and kept in a DMF/H_2O coagulation bath (15 wt.% DMF and 85 wt.% H_2O) for 10 min at 40°C. Then they were subjected to vacuum drying on a YIHENG vacuum oven (China) for 12 h. The resulting composite aerogels were labeled CP-12/PU, CP-24/PU, CP-36/PU and CP-48/PU. The compositions and densities of CP/PU composite aerogels are shown in **Table 5.1**.

5.4.4 Characterization

General characterization

The chemical structure of the CP/PU composite aerogels was characterized by Fourier transform infrared spectroscopy (FTIR, PerkinElmer Spectrum Two, USA) equipped with an attenuated total reflectance (ATR) accessory at a spectral range of 500 cm^{-1}~4000 cm^{-1}. Raman spectra were recorded using a Renishaw inVia-Reflex Raman micro-spectrometer with a He-Ne 633 nm laser for excitation. The morphologies of CNF aerogels, CP aerogels and CP/PU composite aerogels were observed using a scanning electron microscope (SEM, TM3030, Japan) and field emission scanning electron microscopy (FE-SEM, SU8010, Japan). The electrical conductivity of the CP aerogels was tested with a four-point probe (RTS-8, China). The thermal properties of the CP/PU composites were determined on a thermal gravimetric analyzer (TGA, NETZSCH 209F1, Germany) from room temperature to 600°C under nitrogen atmosphere. The thermal conductivity of the CP/PU composites was measured by a Thermal Constant Analyzer (XIATECH-TC3000E, China) at room temperature. The tensile property of CP/PU composites was tested with a universal testing machine (HY 940F, China). The electrical resistances of the CP/PU composite aerogels were acquired by calculating the slope of curves *I–V*, and the electrical conductivity of the CP/PU composite aerogels can be calculated as follows:

$$k = \frac{IL}{US}$$

where k is the electrical conductivity, I is the current through the sample, L is the length of the current crosses the sample, U is the applied voltage and S is the cross area of current.

Characterization of electric-thermal conversion properties

The electric-thermal conversion experiments were performed at room temperature as follows. Firstly, two copper wires were inserted into the CP aerogel, connected with conductive silver glue to minimize contact resistance. The conductive silver glue was subsequently solidified at 150°C for 30 min in a vacuum oven, immersing in a 9 wt.% PU solution for 10 min to obtain the CP/PU composite aerogel. Next, the CP/PU composite aerogel (the sample size was 1×2 cm^2) was transferred in a foam box to restrain heat dissipation during the whole heating process. An electrochemical workstation (Autolab PGSTAT302N, Switzerland) was employed to provide working voltage by connecting the copper wires embedded in the CP/PU composite aerogel. An infrared camera (IR camera, Fluke TiX450, USA) was used to monitor temperature variations of the sample at different working voltages (2~6 V), from which the temperature-time curves were collected *via* a data collection system (Fluke trend analysis). Simultaneously, the thermal camera images were acquired.

Characterization of hydrophobic and breathable performance

The WCA of CP/PU composite aerogels was tested with a Kino SL200B Contact Angle Analyzer using liquid droplets of 4 μL. The air permeability of CP/PU composite aerogels was measured using a comprehensive filtration performance testing table (LZC-K, China). The WVT rate of the CP/PU composite aerogel was determined on a YG601H moisture permeability equipment (Ningbo Textile Instruments Co., Ltd.) at 38°C, according to the GB/T 12704.1-2009 inverse cup standard. The WVT rate was obtained as follows [47]:

$$\text{WVT rate} = \frac{m-m_0}{A\cdot t}\times 24$$

where m_0 is the mass of the test cup before test, m is the mass of the test cup after test, A is the test area (0.00283 m^2), and t is the testing time. The air permeability and WVT rates were obtained by averaging results from three samples (7 cm in diameter and 0.5 cm in thickness).

Table 5.1 The compositions of CP/PU composite aerogels

Samples	**Cellulose aerogels (wt.%)**	**PPy (wt.%)**	**PU (wt.%)**	**Density (g cm^{-3})**
CP-12/PU	57.8	18.3	23.9	0.14
CP-24/PU	51.7	22.3	26.0	0.15
CP-36/PU	52.2	23.5	24.3	0.15

CP-48/PU	50.3	28.7	21.0	0.16

5.5 References

(1) Jang, N.-S.; Kim, K.-H.; Ha, S.-H.; Jung, S.-H.; Lee, H. M.; Kim, J.-M. Simple approach to high-performance stretchable heaters based on kirigami patterning of conductive paper for wearable thermotherapy applications. *ACS Applied Materials & Interfaces* **2017,** *9* (23), 19612-19621.
(2) Veeramuthu, L.; Chen, B.-Y.; Tsai, C.-Y.; Liang, F.-C.; Venkatesan, M.; Jiang, D.-H.; Chen, C.-W.; Cai, X.; Kuo, C.-C. Novel stretchable thermochromic transparent heaters designed for smart window defroster applications by spray coating silver nanowire. *RSC Advances* **2019,** *9* (61), 35786-35796.
(3) Zhang, L.; Baima, M.; Andrew, T. L. Transforming commercial textiles and threads into sewable and weavable electric heaters. *ACS Applied Materials & Interfaces* **2017,** *9* (37), 32299-32307.
(4) Lee, H.; Song, C.; Hong, Y. S.; Kim, M. S.; Cho, H. R.; Kang, T.; Shin, K.; Choi, S. H.; Hyeon, T.; Kim, D.-H. Wearable/disposable sweat-based glucose monitoring device with multistage transdermal drug delivery module. *Science Advances* **2017,** *3* (3), e1601314.
(5) Lee, T.-W.; Jeong, Y. G. Regenerated cellulose/multiwalled carbon nanotube composite films with efficient electric heating performance. *Carbohydrate Polymers* **2015,** *133*, 456-463.
(6) Jin, H.; Matsuhisa, N.; Lee, S.; Abbas, M.; Yokota, T.; Someya, T. Enhancing the performance of stretchable conductors for e-textiles by controlled ink permeation. *Advanced Materials* **2017,** *29* (21), 1605848.
(7) Liu, M.; Pu, X.; Jiang, C.; Liu, T.; Huang, X.; Chen, L.; Du, C.; Sun, J.; Hu, W.; Wang, Z. L. Large-area all-textile pressure sensors for monitoring human motion and physiological signals. *Advanced Materials* **2017,** *29* (41), 1703700.
(8) Lee, M.-S.; Lee, K.; Kim, S.-Y.; Lee, H.; Park, J.; Choi, K.-H.; Kim, H.-K.; Kim, D.-G.; Lee, D.-Y.; Nam, S.; Park, J.-U. High-performance, transparent, and stretchable electrodes using graphene-metal nanowire hybrid structures. *Nano Letters* **2013,** *13* (6), 2814-2821.
(9) Kim, T.; Kim, Y. W.; Lee, H. S.; Kim, H.; Yang, W. S.; Suh, K. S. Uniformly interconnected silver-nanowire networks for transparent film heaters. *Advanced Functional Materials* **2013,** *23* (10), 1250-1255.
(10) Sorel, S.; Bellet, D.; Coleman, J. N. Relationship between material properties and transparent heater performance for both bulk-like and percolative nanostructured networks. *ACS Nano* **2014,** *8* (5), 4805-4814.
(11) Bae, J. J.; Lim, S. C.; Han, G. H.; Jo, Y. W.; Doung, D. L.; Kim, E. S.; Chae, S. J.; Ta Quang, H.; Nguyen Van, L.; Lee, Y. H. Heat dissipation of transparent graphene defoggers. *Advanced Functional Materials* **2012,** *22* (22), 4819-4826.
(12) Jang, H.-S.; Jeon, S. K.; Nahm, S. H. The manufacture of a transparent film heater by spinning multi-walled carbon nanotubes. *Carbon* **2011,** *49* (1), 111-116.
(13) Sui, D.; Huang, Y.; Huang, L.; Liang, J.; Ma, Y.; Chen, Y. Flexible and transparent electrothermal film heaters based on graphene materials. *Small* **2011,** *7* (22), 3186-3192.

(14) Meng, X.; Chen, T.; Li, Y.; Liu, S.; Pan, H.; Ma, Y.; Chen, Z.; Zhang, Y.; Zhu, S. Assembly of carbon nanodots in graphene-based composite for flexible electro-thermal heater with ultrahigh efficiency. *Nano Research* **2019,** *12* (10), 2498-2508.

(15) Jiang, Z.; Shao, Y.; Zhao, P.; Wang, H. Flexible heteroatom-doped graphitic hollow carbon fibers for ultrasensitive and reusable electric current sensing. *Chemical Communications* **2019,** *55* (85), 12853-12856.

(16) Huang, Y.; Li, H.; Wang, Z.; Zhu, M.; Pei, Z.; Xue, Q.; Huang, Y.; Zhi, C. Nanostructured polypyrrole as a flexible electrode material of supercapacitor. *Nano Energy* **2016,** *22*, 422-438.

(17) Yang, P.; Mai, W. Flexible solid-state electrochemical supercapacitors. *Nano Energy* **2014,** *8*, 274-290.

(18) Ryan, J. D.; Mengistie, D. A.; Gabrielsson, R.; Lund, A.; Mueller, C. Machine-washable pedot:Pss dyed silk yarns for electronic textiles. *ACS Applied Materials & Interfaces* **2017,** *9* (10), 9045-9050.

(19) Sahoo, N. G.; Jung, Y. C.; Goo, N. S.; Cho, J. W. Conducting shape memory polyurethane-polypyrrole composites for an electroactive actuator. *Macromolecular Materials and Engineering* **2005,** *290* (11), 1049-1055.

(20) Luo, M.; Li, M.; Li, Y.; Chang, K.; Liu, K.; Liu, Q.; Wang, Y.; Lu, Z.; Liu, X.; Wang, D. In-situ polymerization of ppy/cellulose composite sponge with high elasticity and conductivity for the application of pressure sensor. *Composites Communications* **2017,** *6*, 68-72.

(21) Shown, I.; Ganguly, A.; Chen, L.-C.; Chen, K.-H. Conducting polymer-based flexible supercapacitor. *Energy Science & Engineering* **2015,** *3* (1), 2-26.

(22) Wang, Q.-W.; Zhang, H.-B.; Liu, J.; Zhao, S.; Xie, X.; Liu, L.; Yang, R.; Koratkar, N.; Yu, Z.-Z. Multifunctional and water-resistant mxene-decorated polyester textiles with outstanding electromagnetic interference shielding and joule heating performances. *Advanced Functional Materials* **2019,** *29* (7), 1806819.

(23) Ma, Z.; Kang, S.; Ma, J.; Shao, L.; Wei, A.; Liang, C.; Gu, J.; Yang, B.; Dong, D.; Wei, L.; Ji, Z. High-performance and rapid-response electrical heaters based on ultraflexible, heat-resistant, and mechanically strong aramid nanofiber/ag nanowire nanocomposite papers. *ACS Nano* **2019,** *13* (7), 7578-7590.

(24) Lee, J.-G.; Lee, J.-H.; An, S.; Kim, D.-Y.; Kim, T.-G.; Al-Deyab, S. S.; Yarin, A. L.; Yoon, S. S. Highly flexible, stretchable, wearable, patternable and transparent heaters on complex 3d surfaces formed from supersonically sprayed silver nanowires. *Journal of Materials Chemistry A* **2017,** *5* (14), 6677-6685.

(25) Yun, S.; Niu, X.; Yu, Z.; Hu, W.; Brochu, P.; Pei, Q. Compliant silver nanowire-polymer composite electrodes for bistable large strain actuation. *Advanced Materials* **2012,** *24* (10), 1321-1327.

(26) Lv, M.; Yang, L.; Wang, X.; Cheng, X.; Song, Y.; Yin, Y.; Liu, H.; Han, Y.; Cao, K.; Ma, W.; Qi, G.; Li, S. Visible-light photocatalytic capability and the mechanism investigation of a novel pani/sn3o4 p-n heterostructure. *RSC Advances* **2019,** *9* (69), 40694-40707.

(27) Zhang, Y.; Liu, H.; Tan, L.; Zhang, Y.; Jeppson, K.; Wei, B.; Liu, J. Properties of undoped few-layer graphene-based transparent heaters. *Materials* **2019,** *13* (1), 104.

(28) Yang, H.; Yilmaz, G.; Han, G.; Eriten, M.; Zhang, Z.; Yu, S.; Shi, M.; Yan, H.; Yang, W.; Xie, P.; Turng, L.-S. A quick response and tribologically durable graphene heater for

rapid heat cycle molding and its applications in injection molding. *Applied Thermal Engineering* **2020,** *167,* 114791.

(29) Lee, S. J.; Yun, C.; Park, C. H. Electrically conductive and superhydrophobic textiles via pyrrole polymerization and surface hydrophobization after alkaline hydrolysis. *Textile Research Journal* **2019,** *89* (8), 1436-1447.

(30) Guo, Y.; Dun, C.; Xu, J.; Mu, J.; Li, P.; Gu, L.; Hou, C.; Hewitt, C. A.; Zhang, Q.; Li, Y.; Carroll, D. L.; Wang, H. Ultrathin, washable, and large-area graphene papers for personal thermal management. *Small* **2017,** *13* (44), 1702645.

(31) Li, Y.; Zhang, Z.; Li, X.; Zhang, J.; Lou, H.; Shi, X.; Cheng, X.; Peng, H. A smart, stretchable resistive heater textile. *Journal of Materials Chemistry C* **2017,** *5* (1), 41-46.

(32) Hazarika, A.; Deka, B. K.; Jeong, C.; Park, Y.-B.; Park, H. W. Biomechanical energy-harvesting wearable textile-based personal thermal management device containing epitaxially grown aligned ag-tipped-nixco1-xse nanowires/reduced graphene oxide. *Advanced Functional Materials* **2019,** *29* (31), 1903144.

(33) Lv, J.; Zhou, P.; Zhang, L.; Zhong, Y.; Sui, X.; Wang, B.; Chen, Z.; Xu, H.; Mao, Z. High-performance textile electrodes for wearable electronics obtained by an improved in situ polymerization method. *Chemical Engineering Journal* **2019,** *361*, 897-907.

(34) He, W.; Li, G.; Zhang, S.; Wei, Y.; Wang, J.; Li, Q.; Zhang, X. Polypyrrole/silver coaxial nanowire aero-sponges for temperature-independent stress sensing and stress-triggered joule heating. *ACS Nano* **2015,** *9* (4), 4244-4251.

(35) Menzel, R.; Barg, S.; Miranda, M.; Anthony, D. B.; Bawaked, S. M.; Mokhtar, M.; Al-Thabaiti, S. A.; Basahel, S. N.; Saiz, E.; Shaffer, M. S. P. Joule heating characteristics of emulsion-templated graphene aerogels. *Advanced Functional Materials* **2015,** *25* (1), 28-35.

(36) Hu, P.; Lyu, J.; Fu, C.; Gong, W.-b.; Liao, J.; Lu, W.; Chen, Y.; Zhang, X. Multifunctional aramid nanofiber/carbon nanotube hybrid aerogel films. *ACS Nano* **2020,** *14* (1), 688-697.

(37) Cheng, H.; Li, C.; Jiang, Y.; Wang, B.; Wang, F.; Mao, Z.; Xu, H.; Wang, L.; Sui, X. Facile preparation of polysaccharide-based sponges and their potential application in wound dressing. *Journal of Materials Chemistry B* **2018,** *6* (4), 634-640.

(38) Li, Y.; Xu, L.; Xu, B.; Mao, Z.; Sui, X. Cellulose sponge supported palladium nanoparticles as recyclable cross-coupling catalysts. *ACS Applied Materials & Interfaces* **2017,** *9* (20), 17155-17162.

(39) Zhang, J.; Cheng, Y.; Tebyetekerwa, M.; Meng, S.; Zhu, M.; Lu, Y. "Stiff-soft" binary synergistic aerogels with superflexibility and high thermal insulation performance. *Advanced Functional Materials* **2019,** *29* (15), 1806407.

(40) Keshipour, S.; Khezerloo, M. Gold nanoparticles supported on cellulose aerogel as a new efficient catalyst for epoxidation of styrene. *Journal of the Iranian Chemical Society* **2017,** *14* (5), 1107-1112.

(41) Cheng, H.; Li, C.; Jiang, Y.; Wang, B.; Sui, X. Facile preparation of polysaccharide-based sponges and its potential application in wound dressing. *Journal of Materials Chemistry B* **2018,** *6* (4), 634-640.

(42) Maráková, N.; Humpolí?ek, P.; Ka?párková, V.; Capáková, Z.; Martinková, L.; Bober, P.; Trchová, M.; Stejskal, J. Antimicrobial activity and cytotoxicity of cotton fabric coated with conducting polymers, polyaniline or polypyrrole, and with deposited silver nanoparticles. *Applied Surface Science*, **2017,** *396*, 169-176..

(43) Gupta, S. Hydrogen bubble-assisted syntheses of polypyrrole micro/nanostructures using electrochemistry: Structural and physical property characterization. **2008,** *39*(10), 1343-1355.
(44) Lima, R. M. A. P.; Alcaraz - Espinoza, J. J.; da Silva Jr., F. A. G.; de Oliveira, H. P. Multifunctional wearable electronic textiles using cotton fibers with polypyrrole and carbon nanotubes. *Acs Appl Mater Interfaces*, **2018**, *10*(16), 13783-13795.
(45) Zhang, M.; Wang, C.; Liang, X.; Yin, Z.; Xia, K.; Wang, H.; Jian, M.; Zhang, Y. Weft-knitted fabric for a highly stretchable and low-voltage wearable heater. *Advanced Electronic Materials* **2017,** *3* (9), 1700193.
(46) Zhou, R.; Li, P.; Fan, Z.; Du, D.; Ouyang, J. Stretchable heaters with composites of an intrinsically conductive polymer, reduced graphene oxide and an elastomer for wearable thermotherapy. *Journal of Materials Chemistry C,* **2017,** *5* (6), 1544-1551.
(47) Dong, Z.; Zhao, J.; Du, J.; Li, C.; Zhao, L. Radiation synthesis of spherical cellulose-based adsorbent for efficient adsorption and detoxification of cr(vi). *Radiation Physics and Chemistry* **2016,** *126*, 68-74.
(48) Cheng, H.; Li, Y.; Wang, B.; Mao, Z.; Xu, H.; Zhang, L.; Zhong, Y.; Sui, X. Chemical crosslinking reinforced flexible cellulose nanofiber-supported cryogel. *Cellulose,* **2018,** *25*(1), 573-582.

5.6 Supporting information

5.6.1 Supporting results and discussion

Table S5.1 Parameters and equations established in the linear fitting for the current-voltage curves of the CP/PU composite aerogel

Samples	Equation of linear fit	R^2
CP-12/PU	Y=-0.0010+0.005X	1.0000
CP-24/PU	Y=-0.0158+0.0198X	0.9983
CP-36/PU	Y=-0.0462+0.0607X	0.9997
CP-48/PU	Y=-0.032+0.1172X	0.9953

Table S5.2 Comparison of electrical conductivity of different wearable heaters

Samples	Electrical conductivity ($S\ m^{-1}$)	Refs.
Reduced graphene oxide aerogels	64	[1]
Aramid nanofibers/carbon nanotubes aerogel films	230	[2]
Conductive paper based on hydroxyapatite nanowires	84	[3]
PEDOT nanofiber	60	[4]
Polyurethane/polypyrrole composites	1	[5]
Graphene aerogel/polydimethylsiloxane composites	100	[6]
Regenerated cellulose/multiwalled carbon nanotube composite films	10	[7]
Epoxy-based composite films	1	[8]
Thermoplastic polyurethane/carbon nanotube composite	142	[9]
CP-12/PU	4	**This work**
CP-24/PU	15	**This work**

CP-36/PU	45	**This work**
CP-48/PU	88	**This work**

Table S5. 3 Comparison of water contact angles of different wearable heaters

Wearable heaters	**WCA (°)**	**Refs.**
Fluorocarbon/Ag/SiNx	100	10
Fluorocarbon/Cu/SiNx	105	11
Aramid nanofibers/CNT aerogel films	137	2
PET/ PPy/MXene textile	126	12
Melamine/Cu sponge	157	13
Nylon/AgNWs/PDMS/fluoroalkylsilanes	131	14
CP-48/PU/PFC-2	127	**This work**
CP-48/PU/PFC-4	132	**This work**
CP-48/PU/PFC-6	135	**This work**

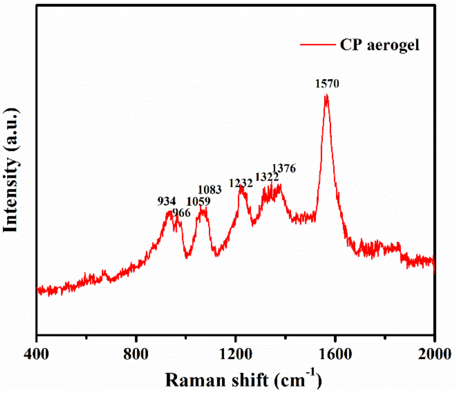

Figure S5.1 Raman spectra of the CP aerogel.

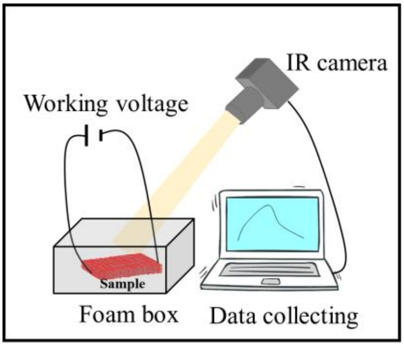

Figure S5.2 Schematic illustration of the electro-to-heat test device.

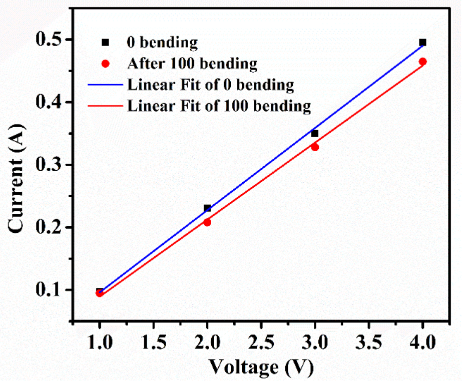

Figure S5.3 The electrical response of CP-48/PU after 0 times bending and 100 times bending.

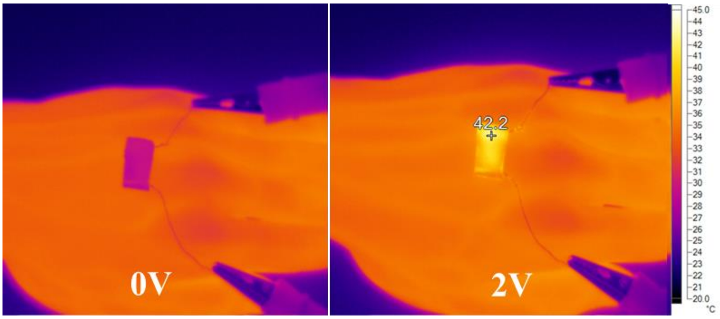

Figure S5.4 IR camera images of CP/PU-48 affixed to human hands.

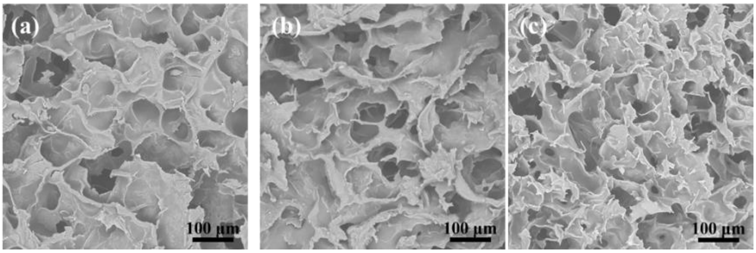

Figure S5.5 SEM images of (a) CP-48/PU/PFC-2, (b) CP-48/PU/PFC-4, (c) CP-48/PU/PFC-6.

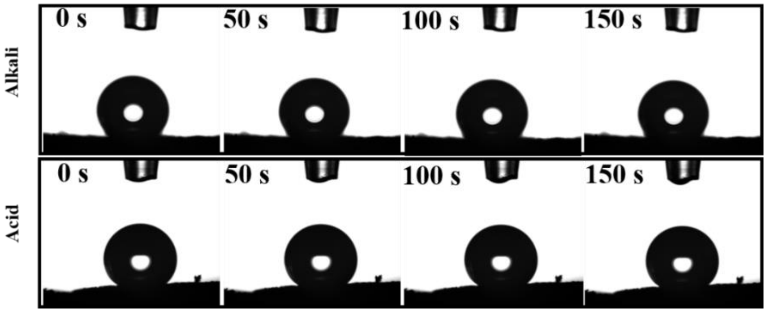

Figure S5.6 Comparison of WCA of CP-48/PU/PFC-4 with different retention times under 1 mol/L alkali and 1 mol/L acid.

5.6.2 Supporting references

(1) Menzel, R.; Barg, S.; Miranda, M.; Anthony, D. B.; Bawaked, S. M.; Mokhtar, M.; Al-Thabaiti, S. A.; Basahel, S. N.; Saiz, E.; Shaffer, M. S. P. Joule heating characteristics of emulsion-templated graphene aerogels. *Advanced Functional Materials* **2015,** *25* (1), 28-35.

(2) Hu, P.; Lyu, J.; Fu, C.; Gong, W. B.; Liao, J.; Lu, W.; Chen, Y.; Zhang, X. Multifunctional aramid nanofiber/carbon nanotube hybrid aerogel films. *ACS Nano* **2020,** *14* (1), 688-697.

(3) Chen, F. F.; Zhu, Y. J.; Xiong, Z. C.; Dong, L. Y.; Chen, F.; Lu, B. Q.; Yang, R. L. Hydroxyapatite nanowire-based all-weather flexible electrically conductive paper with superhydrophobic and flame-retardant properties. *ACS Applied Materials and Interfaces* **2017,** *9* (45), 39534-39548.

(4) Laforgue, A. Electrically controlled colour-changing textiles using the resistive heating properties of pedot nanofibers. *Journal of Materials Chemistry* **2010,** *20* (38), 8233-8235.

(5) Sahoo, N. G.; Jung, Y. C.; Goo, N. S.; Cho, J. W. Conducting shape memory polyurethane-polypyrrole composites for an electroactive actuator. *Macromolecular Materials and Engineering* **2005,** *290* (11), 1049-1055.

(6) Zhang, Q.; Xu, X.; Li, H.; Xiong, G.; Hu, H.; Fisher, T. S. Mechanically robust honeycomb graphene aerogel multifunctional polymer composites. *Carbon* **2015,** *93*, 659-670.

(7) Lee, T. W.; Jeong, Y. G. Regenerated cellulose/multiwalled carbon nanotube composite films with efficient electric heating performance. *Carbohydrate Polymers* **2015,** *133*, 456-463.

(8) Jeong, Y. G.; An, J. E. Effects of mixed carbon filler composition on electric heating behavior of thermally-cured epoxy-based composite films. *Composites Part A: Applied Science and Manufacturing* **2014,** *56*, 1-7.

(9) Sun, W. J.; Xu, L.; Jia, L. C.; Zhou, C. G.; Xiang, Y.; Yin, R. H.; Yan, D. X.; Tang, J. H.; Li, Z. M. Highly conductive and stretchable carbon nanotube/thermoplastic polyurethane composite for wearable heater. *Composites Science and Technology* **2019,**

181, 107695.
(10) Kang, T. W.; Kim, S. H.; Kim, C. H.; Lee, S. M.; Kim, H. K.; Park, J. S.; Lee, J. H.; Yang, Y. S.; Lee, S. J. Flexible polymer/metal/polymer and polymer/metal/inorganic trilayer transparent conducting thin film heaters with highly hydrophobic surface. *ACS Applied Materials and Interfaces* **2017,** *9* (38), 33129-33136.
(11) Kang, T. W.; Kim, S. H.; Kim, M.; Cho, E.; Lee, S. J. Highly flexible, hydrophobic, and large area plasma-polymer-fluorocarbon/Cu/SiNx transparent thin film heater and thermotherapy pad application. *Plasma Processes and Polymers* **2020,** *17*(4), 1900188.
(12) Wang, Q. W.; Zhang, H. B.; Liu, J.; Zhao, S.; Xie, X.; Liu, L.; Yang, R.; Koratkar, N.; Yu, Z. Z. Multifunctional and water-resistant mxene-decorated polyester textiles with outstanding electromagnetic interference shielding and joule heating performances. *Advanced Functional Materials* **2019,** *29* (7), 1806819.
(13) Zhou, H.; Zhang, T.; Yue, X.; Peng, Y.; Qiu, F.; Yang, D. Fabrication of flexible and superhydrophobic melamine sponge with aligned copper nanoparticle coating for self-cleaning and dual thermal management properties. *Industrial and Engineering Chemistry Research* **2019,** *58* (12), 4844-4852.
(14) Guo, Y.; Li, K.; Hou, C.; Li, Y.; Zhang, Q.; Wang, H. Fluoroalkylsilane-modified textile-based personal energy management device for multifunctional wearable applications. *ACS Applied Materials and Interfaces* **2016,** *8* (7), 4676-4683.

Chapter 6

Catalytic Performance of Pd Nanoparticles Obtained by Direct Reduction in Cellulose-Poly(ferrocenylsilane) Hybrid Sponges

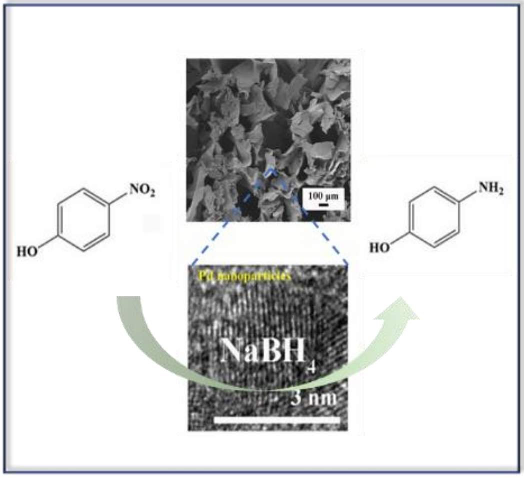

Cellulose - poly(ferrocenylsilane) (PFS) polyionic liquid (PIL) composite sponges were fabricated by co-dissolution of cellulose and PFS-PIL, followed by solvent exchange and freeze-drying. The hybrid sponges were used to *in-situ* produce and immobilize palladium nanoparticles (Pd NPs), leading to Pd NP-decorated porous

supports. The formation of Pd NPs was confirmed by TEM and XPS measurements. The as-prepared cellulose/PFS-PIL@Pd sponges exhibited a high catalytic activity in the reduction of 4-nitrophenol (4-NiP) to 4-aminophenol (4-AmP). As a variety of metal NPs may be immobilized using this method, these sponges constitute a promising new class of catalytic porous supports.

The contents of this chapter have been submitted for publication as: Huan Cheng, Mark Hempenius, Xiaofeng Sui, G. Julius Vancso, Catalytic Performance of Pd Nanoparticles Obtained by Direct Reduction in Cellulose-Poly(ferrocenylsilane) Hybrid Sponges, *submitted*.

6.1 Introduction

Metal nanoparticles (NPs) with unique characteristics such as nanoscale dimensions and high activity are widely used in catalytic applications[1, 2]. However, metal NPs are often unstable due to their high surface energy. This leads to aggregation, limiting their applications at the nanoscale, as well as their catalytic performance[3, 4]. Besides, the separation of metal NPs from the reaction medium is a challenge, and unrecycled metal NPs could cause environmental pollution[5]. Therefore, loading metal NPs onto a matrix is recognized as an effective method to improve their stability, processability, and reusability and to decrease the negative impact on the environment[6, 7].

Numerous studies have been devoted to developing matrices to immobilize metal NPs, such as metal-organic frameworks, microspheres, fibers, films, aerogels, and sponges[2, 8, 9]. Among them, aerogels, or sponges, have received broad attention because they are easily separated and recovered from the reaction media[10, 11]. Focusing on the choice of the materials for preparing aerogels, bio-based polymers (e.g. cellulose) are more appealing than the synthetic polymers due to their inherent "green" properties such as biodegradability, biocompatibility and availability of abundant reserves, as well as low price[12, 13]. Conforming cellulose and metal NPs into porous structures can in principle improve the immobilization and catalytic properties of metal NPs. Importantly, metal NPs can be easily recovered from catalytic reactions when these systems are employed, and the diffusion of reactants through the porous matrix can be enhanced[14-17]. Recently, cellulose aerogels and sponges have been used as supports for metal NPs. For example, bacterial cellulose aerogels were used as the matrix for supporting Cu and Ni NPs and applied in case studies of nitrophenol reduction[18]. In another example, gold NPs were supported on cellulose aerogel as an efficient catalyst for epoxidation of styrene[19].

Commonly, the synthesis of metal NPs on the support requires toxic external reducing agents, such as N_2H_4 and KBH_4, with potentially harmful effects for the environment[10, 20]. Although cellulose with abundant hydroxyl groups can be used as both reducing agent and as stabilizing environment for the synthesis of metal NPs, some additional harsh conditions such as long reaction time, high pressure and temperature are usually needed if cellulose is employed as the sole reducing agent[21]. Therefore, developing a green and simple method to fix a reducing agent into the cellulose sponge matrix, which can reduce and immobilize metal NPs without being released into the environment to cause secondary pollution, is environmentally compelling. For example, *in-situ* reduction of Pd NPs on the surface of cellulose nanofibers was achieved in the presence of polydopamine

(PDA). The catechol moiety in PDA could reduce metal ions without adding any external reducing agent[14]. Thiolated nanocellulose sponge was prepared from hydrolytic silane condensation of cellulose nanofibers and used as support to immobilize copper cations *via in-situ* Cu^{II} to Cu^{I} reduction and complexation[16].

Poly(ferrocenylsilanes) (PFS), which consist of alternating ferrocene and silane units in the main chain, are a promising class of polymers that can be reversibly oxidized and reduced by chemical and electrochemical ways[22]. By post-functionalization of PFS using different substituents, a range of organometallic polymers was received, including PFS-based hydrophilic polyionic liquids[23, 24], and hydrophobic polyionic liquids[25] (PFS-PIL). Our group reported on a metal NP "foundry" based on a platform consisting of redox-active PFS hydrogels[26]. The concept of using a redox-active hydrogel for fabricating noble metal NPs, where the PFS network chains provide confinement and employed as redox agents, i.e. no external reducing agents or ligands are required, is demonstrated to provide an effective platform[27].

Herein, we propose an environmentally benign approach to decorating porous cellulose sponges with metal NPs using PFS-PIL as a fixed reducing agent, which also provides scaffolds for immobilization of NPs. PFS modified with imidazolium groups and ion-exchanged with hydrophobic counterions (dialysis in counterions solution) readily dissolves in ionic liquids and forms homogeneous solutions with cellulose. After solvent exchange and freeze-drying, the as-prepared composite sponges were thoroughly characterized by FTIR, SEM, TEM, XPS, and TGA. To exemplify their catalytic properties, the metal NPs loaded sponges were applied for the reduction of 4-nitrophenol (4-NiP). The results obtained in this study demonstrate that the composite sponges are suitable supports for the generation, immobilization and use of noble metal NPs in catalytic applications.

6.2 Results and discussion

6.2.1. Fabrication of cellulose/PFS-PIL@Pd sponge

The chemical structures of PFS-PIL, cellulose, and ionic liquid used in this study are shown in **Figure 6.1a**. PFS-PIL is a cationic polyelectrolyte composed of a PFS main chain and butylimidazolium bis(trisfluoromethylsulfonyl)-imide side groups (PFS-C_4IM Tf_2N). The counterion in the PIL was exchanged to the Tf_2N^- to make it insoluble in water but soluble in DMF and ionic liquids, following the procedure developed by the Yuan group[28].

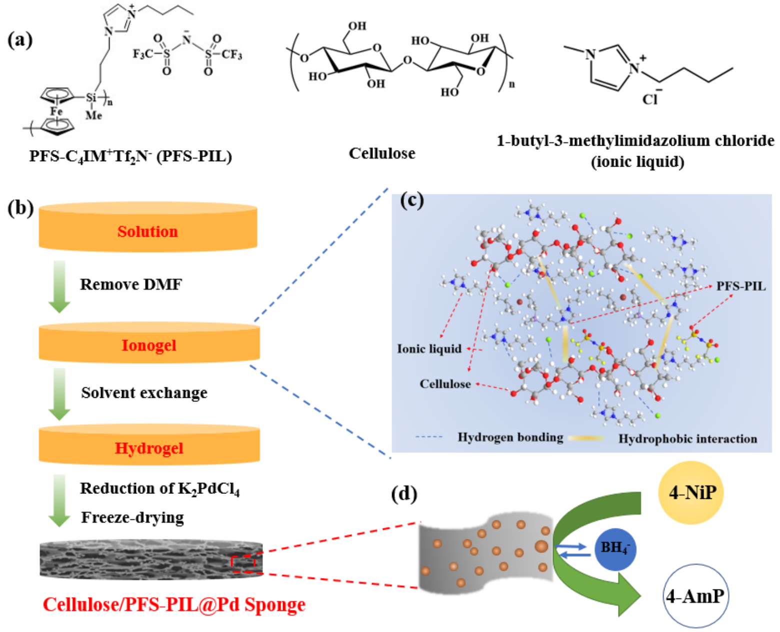

Figure 6.1 Preparation and application of the cellulose/PFS-PIL@Pd sponge. (a) Chemical structure of PFS-PIL, cellulose, and ionic liquid used in this study. (b) Schematic representation illustrating the preparation process of cellulose/PFS-PIL@Pd sponge. (c) Schematic illustration showing the interaction among the components. (d) Reduction of 4-NiP by the Pd NPs on the pore wall.

Figure 6.1b illustrates the fabrication procedure leading to the composite sponge. To satisfy the requirements of an eco-friendly metal NPs support, we designed this composite sponge following three considerations: 1) the composite materials should be assembled into a 3D framework with a well interconnected open porous structure to guarantee the passage of reactant solution; 2) the sponge must be hydrophilic to ensure contact with reactants; 3) metal NPs should be uniformly dispersed and fixed on the pore walls to efficiently catalyze the reaction.

In this work, the ionic liquid (1-butyl-3-methylimidazolium chloride) was used as a solvent to dissolve cellulose. Ionic liquids have been used to replace regular organic solvents in a range of applications due to specific advantages such as excellent dissolution ability and ease of recycling[29, 30]. Polar interactions between hydroxyl groups in cellulose and the anions and cations in ionic liquids favor dissolution. Hydrogen bonding interactions between hydroxyl groups in cellulose and both anions and cations in ionic liquids have been monitored by NMR spectroscopy [31, 32]. The chemical structure of the butylimidazolium groups of PFS-PIL is similar to that of the ionic liquid used in the experiments. Hence, it can be expected that PFS-PIL dissolves in the ionic liquid employed. Indeed, a uniform and homogeneous solution of PFS-PIL and cellulose was obtained (**Figure 6.1c**). After removal of the ionic liquid by solvent exchange and drying, a homogeneously colored PFS-cellulose composite resulted. It therefore seems reasonable to assume that hydrophobic interactions between the hydrophobic PFS main chains and parts of the ionic liquid side groups and cellulose, combined with polar interactions between the ionic liquid side groups of PFS-PIL and the hydroxyl moieties of cellulose, cause the observed uniform distribution of PFS-PIL over the cellulose support.

Functionalization of cellulose/PFS-PIL sponges with Pd NPs was achieved using two different approaches. In the first approach, cellulose/PFS-PIL hydrogels were placed in a 0.1 mM K_2PdCl_4 solution. The PFS chains of the hydrogel reduced this salt to Pd NPs, which caused the hydrogel to turn brown. The porous structure obtained after freeze-drying of the hydrogel was denoted as cellulose/PFS-PIL@Pd sponge.

In a second approach, cellulose/PFS-PIL hydrogels were first freeze-dried and the resulting dry sponge was immersed in 0.1 mM K_2PdCl_4 solution. In this process, the sponge was wetted but it retained its solid-like porous structure. Similar to the hydrogel case, the wetted sponge acquired a brown color as Pd NPs were formed. This porous structure was denoted as cellulose/PFS-PIL@Pd2 sponge. The catalytic performance of these two different sponges is investigated in the subsequent sections.

Unlike external reducing agents, the hydrophobic PFS-PIL remains in the hydrogel. Also, PFS-PIL contributes to the in-situ immobilization of metal NPs. **Figure 6.1d** shows the reduction mechanism of 4-nitrophenol to 4-aminophenol by Pd NPs, which is used to demonstrate catalytic activity as discussed later.

6.2.2 FTIR of sponges

Cellulose sponge, PFS-PIL, and cellulose/PFS-PIL sponge were characterized by FTIR, the results are shown in **Figure 6.2**.

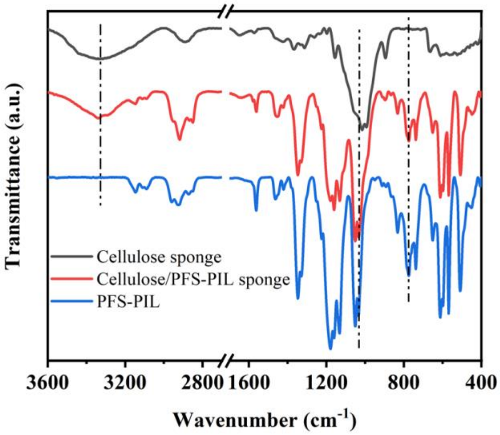

Figure 6.2 FTIR spectra of cellulose sponge, PFS-PIL and cellulose/PFS-PIL sponge.

In the spectrum of cellulose sponge, a strong peak of the stretching vibrations of O-H groups around 3347 cm^{-1} characteristics for cellulose can clearly be seen. Characteristic peaks for PFS around 1037 and 774 cm^{-1} are also clearly present in the spectrum of PFS-PIL. After mixing them in ionic liquid and regenerating in water and freeze-drying, the FTIR spectrum of cellulose/PFS-PIL sponge contains both the characteristics of PFS (1037 and 774 cm^{-1}) and cellulose (3347 cm^{-1}), indicating a successful mixing of cellulose and PFS-PIL.

6.2.3 Morphology of sponges

The morphologies of cellulose, cellulose/PFS-PIL, and cellulose/PFS-PIL@Pd sponges, respectively, were characterized by SEM and the results are shown in **Figure 6.3**.

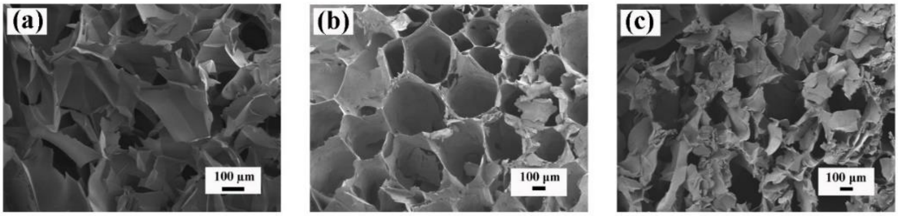

Figure 6.3 Morphology of the sponges. (a) Cellulose sponge, (b) cellulose/PFS-PIL sponge, and (c) cellulose/PFS-PIL@Pd sponge.

All of these three sponges have a porous structure with large pores, and the porous structure did not change after adding PFS-PIL or after the reduction to obtain Pd NPs.

With the growth of ice crystals during the freeze drying process, the gel network composed of cellulose and PFS-PIL gradually arranged itself along the growing crystals, forming the porous structure observed in the SEM images[33].

The pore size of these sponges is around 200 μm, which will allow reactants to pass through smoothly with stirring. In addition, the microporous structure not only provides channels but also provides a large area of contact between solutions and NP catalysts in the sponge, which contributes to the catalytic efficiency of these porous structures.

6.2.4 Characterization of Pd NPs

In order to verify the presence of Pd NPs, the cellulose/PFS-PIL@Pd hydrogel was imaged by TEM.

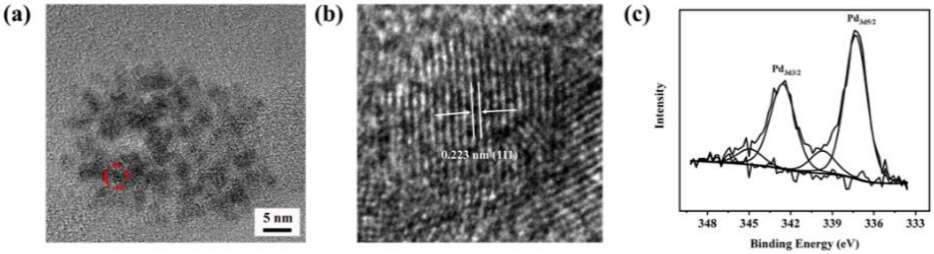

Figure 6.4 Characterization of Pd NPs. XPS spectra of cellulose/PFS-PIL@Pd sponge. (a) TEM image of Pd NPs. (b) HR-TEM image of Pd NPs with many (111) facets with a spacing of lattice fringes of 0.223 nm. (c) Spectrum of Pd $_{3d}$ region of cellulose/PFS-PIL@Pd sponge.

A representative TEM image of NPs formed in-situ is shown in **Figure 6.4a**. The diameter of Pd NPs was in the range of 3–5 nm. A high-resolution TEM image of Pd NPs is shown in **Figure 6.4b**. The image clearly captures that these NPs include single crystals with several [111] facets exposed[34, 35]. The measured interplanar spacing for the lattice fringes is 0.23 nm, corresponding to metallic Pd [111][36].

The XPS spectrum shows double peaks with binding energies of 335.1 eV and 340.5 eV, corresponding to Pd $_{3d5/2}$ and Pd $_{3d3/2}$, respectively (**Figure 6.4c**), which are in good agreement with the standard values for Pd(0)[37]. Combined with the results obtained by TEM, we can confirm that the Pd NPs were successfully obtained.

2.5. Thermal gravimetry analysis (TGA)

In the next section we present thermal characterization data to demonstrate the thermal stability and decomposition features of the sponges discussed.

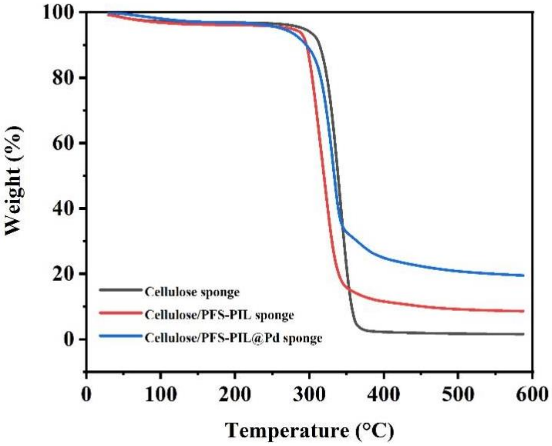

Figure 6.5 TGA results of cellulose sponge, cellulose/PFS-PIL sponge, and cellulose/PFS-PIL@Pd sponge.

Thermal gravimetry analysis (TGA) of a cellulose sponge, a cellulose/PFS-PIL sponge and a cellulose/PFS-PIL@Pd sponge was performed in an N_2 atmosphere. The results obtained are shown in **Figure 6.5**. For the cellulose sponge, substantial weight loss was found with an onset at around 300 °C, and the residual mass approached 2.0%, which is attributed to remaining carbon. For cellulose/PFS-PIL sponge, the residual mass approached 8.8%. This increased residual mass is ascribed to the formation of preceramic Fe-Si oxide (carbide) materials due to the presence of PFS[38]. After the reduction of K_2PdCl_4 to Pd NPs, the residual mass approached 19.5% due to the presence of Pd in the residue. The Pd content calculated from the residual mass is about 12.3%.

6.2.6 Catalytic performance of cellulose/PFS-PIL@Pd sponge

The reduction of 4-NiP to 4-AmP (**Figure 6.6a**) is usually recognized as a model reaction to study the catalytic performance of metal NPs[39, 40]. 4-NiP reduction obeys the classic Langmuir-Hinshelwood mechanism[41, 42]. The BH_4^- ions in the system react with Pd metal particles at their surface and transfer hydrogen to the surface of these particles. Along with the generation of surface-bound hydrogen species, 4-NiP adsorbs onto unoccupied sites of the metal surface. Finally, in a rate-determining step, adsorbed 4-NiP is reduced to 4-AmP which subsequently desorbs[41]. The absorbance peak of 4-NiP shifts from 320 nm to 400 nm as it is turned into a 4-nitrophenolate anion by the hydride ion originating from $NaBH_4$[43].

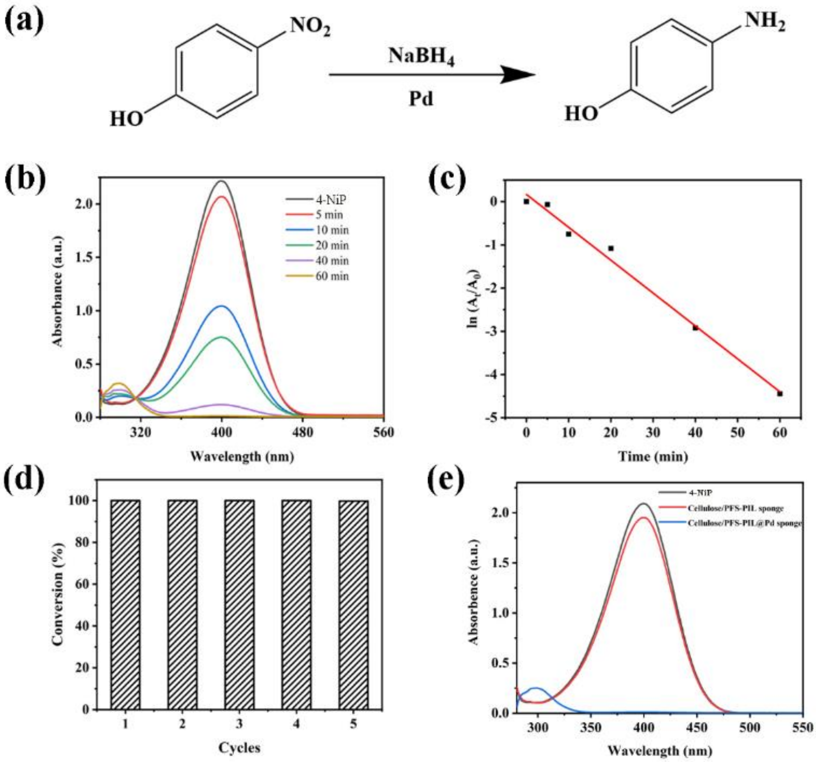

Figure 6.6 The efficiency of the catalytic cellulose/PFS sponge. (a) The chemical reaction of 4-NiP reduction to 4-aminophenol. (b) Time-dependent UV-visible absorption spectra for the reduction of 4-NiP. (c) Plots of ln(A_t/A_0) against reaction time for the catalytic reduction of 4-NiP. (d) Cyclic reduction experiment of 4-NiP by one cellulose/PFS-PIL@Pd sponge. (e) UV-visible absorption spectra for the reduction of 4-NiP with cellulose/PFS-PIL@Pd sponge and cellulose/PFS-PIL sponge.

Due to the excess of $NaBH_4$ used, this reduction is commonly described by a first-order model, and the kinetics can be described by the following equation:

$$\ln (A_t/A_0) = \ln (C_t/C_0) = -kt$$

Where A_t and C_t represent the absorbance and concentration of the 4-NiP at the reaction time t, A_0 and C_0 are the absorbance and concentration values of the initial 4-NiP solution, and t is the residence time[44].

The porous structure and hydrophilic character of this composite sponge are favorable to the adsorption of 4-NiP and the transfer of 4-AmP. The Pd NPs are deposited into the sponge sheets and dispersed in the pores of the sponge material network, maximizing the number of active sites that can participate in the reduction.

Figure 6.6b shows the UV-visible absorption spectra. It took 60 min for cellulose/PFS-PIL@Pd sponge to complete the reduction of 4-NiP to 4-AmP. The reaction medium changed from yellow to colorless (**Figure S6.2**). The relationship between ln (A_t/A_0) and the reaction time are shown in **Figure 6.6c**. After performing a linear fit, the value of the slope is -0.076 min^{-1}, yielding a constant rate value of $k = 0.076$ min^{-1}.

In addition, the same sponge was used for the reusability experiments. The cellulose/PFS-PIL@Pd sponge could be easily recovered from the solution by tweezers. The Pd NPs interact with the sponge sheets and are fixed in the sponge network, which made this NP loaded sponge very stable under the stirring condition. As displayed in **Figure 6.6d**, the sponge could be reused for at least five successive reaction cycles without loss of activity. This confirmed that the cellulose/PFS-PIL@Pd sponge possessed good reusability. The prolonged reaction time for the repeat experiments can be ascribed to the aggregation of NPs during the reuse process[45].

The cellulose/PFS-PIL sponge without NPs was also used to catalyze the reaction. The results obtained are shown in **Figure 6.6e**. It is evident that no reaction occurred within the sponge without NPs. The slight decrease in the peak may be due to adsorption of reactants by the sponge.

6.2.7 Catalytic performance of cellulose/PFS-PIL@Pd2 sponge

We now turn our attention to describing the catalytic performance of the second sponge type, which was freeze-dried prior to reduction of Pd NPs.

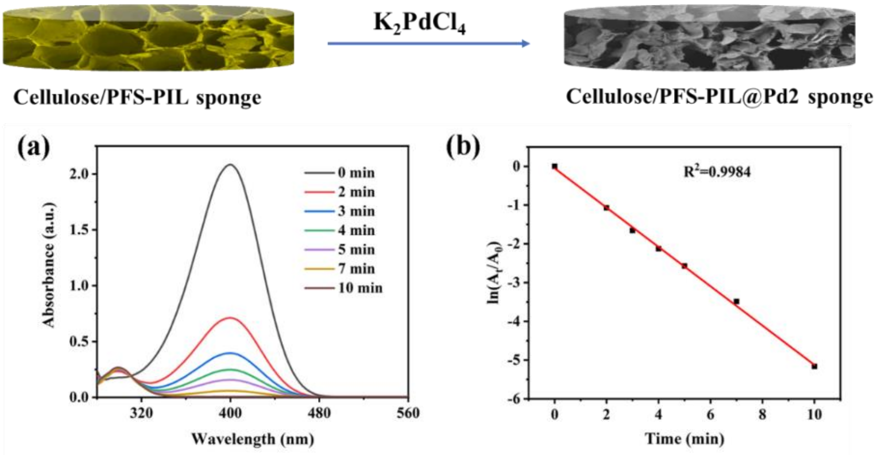

Figure 6.7 The efficiency of the catalytic cellulose/PFS-PIL@Pd2 sponge. (a) Time-dependent UV-visible absorption spectra for the reduction of 4-NiP. (b) Plots of $\ln(A_t/A_0)$ against reaction time for the catalytic reduction of 4-NiP.

The cellulose/PFS-PIL@Pd sponges prepared by in-situ reducing K_2PdCl_4 to Pd NPs, followed by freeze-drying, show a good performance in terms of catalytic activity and cycle stability. However, aggregation of metal NPs during the freeze-drying process and partial covering of metal NPs by the gel layer may limit their catalytic performance to a certain extent. In order to enhance the catalytic performance of cellulose/PFS-PIL@Pd sponges, the protocol for preparing these structures was modified by changing the order of metal loading and freeze-drying. In the adapted approach, cellulose/PFS-PIL hydrogel was first freeze-dried to obtain a cellulose/PFS-PIL dry sponge, followed by in-situ reduction of K_2PdCl_4 to Pd NPs (cellulose/PFS-PIL@Pd2 sponge). Using this approach, it was expected that more NPs are present at the surface of the sponge walls and that aggregation, which might occur during the freeze-drying process, is prevented.

Figure 6.7a records the UV–visible absorption spectra of the reduction of 4-NiP to 4-AmP using a cellulose/PFS-PIL@Pd2 sponge. Only 10 min were required to complete the redox process, which corresponds to a considerable rate enhancement of the reaction. **Figure 6.7b** shows the observed relationship between $\ln(A_t/A_0)$ and the reaction time. After performing a linear fit, the value of the slope shown is $-0.51\ \text{min}^{-1}$, yielding a rate constant value of $k = 0.51\ \text{min}^{-1}$. The catalytic activity of cellulose/PFS-PIL@Pd2 sponges in the reduction of 4-NiP to 4-AmP compares favorably with the activity of a variety of metal NPs in this reaction (**Table 6.1**).

Table 6.1. Rate constants *k* of 4-NiP reduction reactions catalyzed by various metal NPs.

Materials	***k* value ($\mathbf{min^{-1}}$)**	**External reducing agents for metal NPs reduction**	**Refs.**
Cellulosic protic ionic liquids hydrogel with Pd NPs	0.139	$NaBH_4$	46
Pd/Fe_3O_4/polypyrrole hollow capsules	0.122	$NaBH_4$	47
Chitosan/Pd nanocomposites	0.24	$NaBH_4$	48
Au NPs on chitosan-coated iron oxide magnetic nanocarrier	0.072	$NaBH_4$	49
Cu NPs embedded bacterial cellulose aerogels	0.56	$NaBH_4$	18
Cu and Ag NPs @ cellulose acetate nanocomposite	0.34	$NaBH_4$	50
Cellulose films decorated with gold NPs	0.40	Sodium citrate	51
Silver NPs/polydopamine coated polyvinyl alcohol sponge	0.072	$NaBH_4$	52
Pd NPs loaded cellulose-PFS hybrid sponges	0.51	/	**This work**

6.3 Conclusions

In conclusion, palladium nanoparticle-loaded cellulose/PFS-PIL composite sponges were fabricated by co-dissolving cellulose and PFS-PIL, followed by solvent exchange and subsequent freeze-drying. PFS-PIL, possessing butyl imidazolium side groups, could be uniformly mixed with cellulose in an ionic liquid. PFS-PIL reduced and immobilized metal NPs in an in-situ process which required no external reducing agents. The porous cellulose/PFS-PIL sponges were found to be effective supports for Pd NPs. These sponges demonstrated excellent catalytic properties which could be further improved to reach a rate constant value of $k = 0.51\ min^{-1}$ for the reduction of 4-NiP to 4-AmP by a conscientious choice of the NP loading process. The method used to form and immobilize metal NPs on renewable support materials can be applied to create a broad range of metal NPs-decorated porous structures.

6.4 Experimental section

6.4.1 Materials

Poly(ferrocenyl(3-iodopropyl)methylsilane) (PFS-I) (M_n: 2.93×10^5 g mol^{-1}, M_w: 1.27×10^5 g mol^{-1}) was prepared according to an established procedure[53]. Cellulose powder (ultrafine Arbocel UFC-100, JRS GmbH, Rosenberg, Germany), 1-butyl-3-methylimidazolium chloride (ionic liquid, TCI Europe, >98.0%), 1-butylimidazole (Aldrich, 98%), dimethylsulfoxide (DMSO, Biosolve), tetrahydrofuran (THF, Biosolve), sodium chloride (NaCl) (Aldrich, 99.5%), bis(trifluoromethane)sulfonimide lithium salt ($LiTf_2N$, Aldrich), dimethylformamide (DMF, Biosolve), potassium tetrachloropalladate(II) (K_2PdCl_4, Strem chemicals, 99%), 4-NiP (Fluka, ≥99.5%), sodium borohydride (Aldrich, 99%) were used without further purification. Water was purified with a Millipore system.

6.4.2 Characterization methods

Molar mass values were determined by gel permeation chromatography in THF using a calibration curve based on narrow polystyrene standards. ^{1}H NMR spectra were recorded by employing a Bruker Avance III 400 MHz spectrometer and using DMSO-$_{d6}$ as the solvent. FTIR spectra were obtained by an Alpha spectrometer (Bruker). Morphologies of different sponges and Pd NPs were recorded by SEM (JSM-7610FPlus, JEOL) and TEM (CM300, FEI/Philips). XPS was recorded on a PHI Quantera SXM-XPS system. A monochromatic Al Kα radiation source at 1486.6 eV was used with a 100 μm diameter beam and 25 W X-ray gun power. The base pressure of the chamber was 5.4×10^{-10} Torr, and the working pressure was 3.0×10^{-8} Torr (argon). The beam input and detector input angles were 45°. TGA (TGA550, TA Instruments) was used to characterize the relative compositions of three different kinds of sponges. TGA was performed in an N_2 atmosphere from 30 to 600 °C at a rate of 20 °C min^{-1}. The concentration of reactants in the aqueous solutions were monitored using UV-Vis (LAMBDA 850, Perkin Elmer).

6.4.3 Synthesis of PFS-butylimidazolium Tf_2N (PFS-PIL)

PFS-butylimidazolium Tf_2N (PFS-C_4IM Tf_2N, PFS-PIL) was synthesized according to a previously published procedure[54]. 1-Butylimidazole (0.37 g, 3.0 mmol) and DMSO (6 mL) were added to a solution of PFS-I (0.4 g, 1.0 mmol) in THF (12 mL). The mixture was stirred at 60°C for 24 hrs. After removing THF, the mixture was transferred into a Spectra/Por 4 dialysis hose (MWCO 12–14,000 g mol^{-1}) and dialyzed against 0.1 M NaCl (3 × 8L) and MilliQ water (3 × 8L). Concentration of salt-free polyelectrolyte solution by a flow of N_2 produced PFS-C_4IM chloride as orange flakes. The ^{1}H NMR spectrum of PFS-C_4IM chloride is shown in the Supporting Information Figure S1. PFS-C_4IM Tf_2N was prepared by subsequent counterion exchange with Tf_2N^- ions. PFS-C_4IM chloride solution was dropwise added to an aqueous $LiTf_2N$ solution (the molar ratio of PFS-C_4IM chloride and $LiTf_2N$ was 1:3). The resulting precipitate was washed with deionized water three times. PFS-C_4IM Tf_2N was obtained as an orange powder.

6.4.4 Preparation of cellulose/PFS-PIL@Pd sponge

Firstly, the cellulose powder was added to ionic liquid (4 wt.%) and heated to 95°C for 2 hrs to reach dissolution. Meanwhile, PFS-PIL was dissolved in DMF (1 mg mL^{-1}). The PFS-PIL solution was then added to the cellulose/ionic liquid solution at a given PFS-PIL:cellulose weight ratio of 1:4, which resulted in a uniform orange solution. The mixed solution was poured into a small beaker and placed in a vacuum oven at 85°C for 4 hrs to remove DMF to obtain a transparent and viscous solution. After cooling, the viscous solution acquired an ionogel state.

The ionogel was placed in deionized water for solvent exchange, and an orange hydrogel was obtained. Then, the hydrogel was placed in a solution containing 0.1 mM K_2PdCl_4. The PFS chains of the hydrogel reduced this salt to Pd NPs, and the color of the hydrogel became dark brown. Finally, the dark brown hydrogel was placed in a freezer (−28°C) and subsequently dried by freeze drying over 48 hours to obtain a dark brown sponge referred to as cellulose/PFS-PIL@Pd sponge. The orange cellulose/PFS-PIL hydrogel was also frozen at −28°C and dried in a freeze dryer for 48 hrs to obtain an orange sponge referred to as cellulose/PFS-PIL sponge. The colorless cellulose hydrogel was subjected to the same steps, which yielded a white sponge referred to as cellulose sponge.

6.4.5 Preparation of cellulose/PFS-PIL@Pd2 sponge

Immersion of freeze-dried cellulose/PFS-PIL sponge (Section 4.4) in 1 mM K_2PdCl_4 solution led to the in-situ formation and immobilization of Pd nanoparticles in the porous structure, yielding cellulose/PFS-PIL@Pd2 sponges. During this process, the porous structure of the sponge remained intact. After completion of the metal loading step, the sponge was washed three times with deionized water.

6.4.6 Catalysis performance of cellulose/PFS-PIL@Pd sponge

The catalytic performance was evaluated by the reduction of 4-NiP to 4-AmP. First, 250 μL of 4-NiP solution (0.01 M) was added to 25 mL of NaBH4 solution (0.4 mg mL-1) under stirring. Afterwards, a piece of the cellulose/PFS-PIL@Pd sponge (around 10 mg, first wetted by deionized water) was put into the solution. The remaining concentration of 4-NiP (λmax = 400 nm) was determined by UV-Vis absorption spectroscopy at a given time. Finally, the sponges were recovered from the reaction by tweezers, rinsed with deionized water, and then reused in the next cycle.

6.5 References

(1) He, L.; Weniger, F.; Neumann, H.; Beller, M., Synthesis, characterization, and application of metal nanoparticles supported on nitrogen-doped carbon: catalysis beyond electrochemistry. *Angewandte Chemie International Edition* **2016,** *55* (41), 12582-12594.
(2) Astruc, D.; Lu, F.; Aranzaes, J. R., Nanoparticles as recyclable catalysts: the frontier between homogeneous and heterogeneous catalysis. *Angewandte Chemie International Edition* **2005,** *44* (48), 7852-7872.
(3) Pei, X.; Deng, Y.; Duan, B.; Chan, T.-S.; Lee, J.-F.; Lei, A.; Zhang, L., Ultra-small Pd clusters supported by chitin nanowires as highly efficient catalysts. *Nano Research* **2018,** *11* (6), 3145-3153.
(4) Hees, T.; Zhong, F.; Rudolph, T.; Walther, A.; Mülhaupt, R., Nanocellulose aerogels for supporting iron catalysts and in situ formation of polyethylene nanocomposites. *Advanced Functional Materials* **2017,** *27* (11), 1605586.
(5) Xu, P.; Cen, C.; Chen, N.; Lin, H.; Wang, Q.; Xu, N.; Tang, J.; Teng, Z., Facile fabrication of silver nanoparticles deposited cellulose microfiber nanocomposites for catalytic application. *Journal of Colloid and Interface Science* **2018,** *526*, 194-200.
(6) Xiang, Z.; Chen, Y.; Liu, Q.; Lu, F., A highly recyclable dip-catalyst produced from palladium nanoparticle-embedded bacterial cellulose and plant fibers. *Green Chemistry* **2018,** *20* (5), 1085-1094.
(7) Yang, X.; Zhong, H.; Zhu, Y.; Jiang, H.; Shen, J.; Huang, J.; Li, C., Highly efficient reusable catalyst based on silicon nanowire arrays decorated with copper nanoparticles. *Journal of Materials Chemistry A* **2014,** *2* (24), 9040-9047.
(8) Yang, Q.; Xu, Q.; Jiang, H.-L., Metal–organic frameworks meet metal nanoparticles: synergistic effect for enhanced catalysis. *Chemical Society Reviews* **2017,** *46* (15), 4774-4808.
(9) Liu, Y.; Zhang, K.; Li, W.; Ma, J.; Vancso, G. J., Metal nanoparticle loading of gel-brush grafted polymer fibers in membranes for catalysis. *Journal of Materials Chemistry A* **2018,** *6* (17), 7741-7748.
(10) Gu, J.; Hu, C.; Zhang, W.; Dichiara, A. B., Reagentless preparation of shape memory cellulose nanofibril aerogels decorated with Pd nanoparticles and their application in dye discoloration. *Applied Catalysis. B: Environmental* **2018,** *237*, 482-490.
(11) White, R. J.; Luque, R.; Budarin, V. L.; Clark, J. H.; Macquarrie, D. J., Supported metal nanoparticles on porous materials. Methods and applications. *Chemical Society Reviews* **2009,** *38* (2), 481-494.
(12) Klemm, D.; Kramer, F.; Moritz, S.; Lindström, T.; Ankerfors, M.; Gray, D.; Dorris, A., Nanocelluloses: a new family of nature-based materials. *Angewandte Chemie International Edition* **2011,** *50* (24), 5438-5466.
(13) Klemm, D.; Cranston, E. D.; Fischer, D.; Gama, M.; Kedzior, S. A.; Kralisch, D.; Kramer, F.; Kondo, T.; Lindström, T.; Nietzsche, S., Nanocellulose as a natural source for groundbreaking applications in materials science: Today's state. *Mater. Today* **2018,** *21* (7), 720-748.
(14) Li, Y.; Xu, L.; Xu, B.; Mao, Z.; Xu, H.; Zhong, Y.; Zhang, L.; Wang, B.; Sui, X.,

Cellulose sponge supported palladium nanoparticles as recyclable cross-coupling catalysts. *ACS Applied Materials & Interfaces* **2017,** *9* (20), 17155-17162.
(15) Zhang, Q.; Zhang, L.; Wu, W.; Xiao, H., Methods and applications of nanocellulose loaded with inorganic nanomaterials: A review. *Carbohydrate Polymers* **2020,** *229*, 115454.
(16) Zhang, C.; Zhou, M.; Liu, S.; Wang, B.; Mao, Z.; Xu, H.; Zhong, Y.; Zhang, L.; Xu, B.; Sui, X., Copper-loaded nanocellulose sponge as a sustainable catalyst for regioselective hydroboration of alkynes. *Carbohydrate Polymers* **2018,** *191*, 17-24.
(17) Cheng, H.; Li, L.; Wang, B.; Feng, X.; Mao, Z.; Vancso, G. J.; Sui, X., Multifaceted applications of cellulosic porous materials in environment, energy, and health. *Progress in Polymer Science* **2020,** *106*, 101253.
(18) Song, L.; Shu, L.; Wang, Y.; Zhang, X.-F.; Wang, Z.; Feng, Y.; Yao, J., Metal nanoparticle-embedded bacterial cellulose aerogels via swelling-induced adsorption for nitrophenol reduction. *International Journal of Biological Macromolecules* **2020,** *143*, 922-927.
(19) Keshipour, S.; Khezerloo, M., Gold nanoparticles supported on cellulose aerogel as a new efficient catalyst for epoxidation of styrene. *Journal of the Iranian Chemical Society* **2017,** *14* (5), 1107-1112.
(20) Duan, H.; Wang, D.; Li, Y., Green chemistry for nanoparticle synthesis. *Chemical Society Reviews* **2015,** *44* (16), 5778-5792.
(21) Kaushik, M.; Moores, A., Nanocelluloses as versatile supports for metal nanoparticles and their applications in catalysis. *Green Chemistry* **2016,** *18* (3), 622-637.
(22) Hailes, R. L.; Oliver, A. M.; Gwyther, J.; Whittell, G. R.; Manners, I., Polyferrocenylsilanes: synthesis, properties, and applications. *Chemical Society Reviews* **2016,** *45* (19), 5358-5407.
(23) Zhang, K.; Feng, X.; Ye, C.; Hempenius, M. A.; Vancso, G. J., Hydrogels with a memory: dual-responsive, organometallic poly (ionic liquid) s with hysteretic volume-phase transition. *Journal of the American Chemical Society* **2017,** *139* (29), 10029-10035.
(24) Zhang, K.; Zhang, M.; Feng, X.; Hempenius, M. A.; Vancso, G. J., Switching light transmittance by responsive organometallic poly (ionic liquid) s: control by cross talk of thermal and redox stimuli. *Advanced Functional Materials* **2017,** *27* (41), 1702784.
(25) Zhang, K.; Feng, X.; Sui, X.; Hempenius, M. A.; Vancso, G. J., Breathing pores on command: redox-responsive spongy membranes from poly (ferrocenylsilane) s. *Angewandte Chemie International Edition* **2014,** *53* (50), 13789-13793.
(26) Feng, X.; Hempenius, M. A.; Vancso, G. J., Metal nanoparticle foundry with redox responsive hydrogels. *Macromolecular Chemistry and Physics* **2018,** *219* (22), 1800223.
(27) Sui, X.; Feng, X.; Hempenius, M. A.; Vancso, G. J., Redox active gels: synthesis, structures and applications. *Journal of Materials Chemistry B* **2013,** *1* (12), 1658-1672.
(28) Zhao, Q.; Zhang, P.; Antonietti, M.; Yuan, J., Poly (ionic liquid) complex with spontaneous micro-/mesoporosity: template-free synthesis and application as catalyst support. *Journal of the American Chemical Society* **2012,** *134* (29), 11852-11855.
(29) Phillips, D. M.; Drummy, L. F.; Conrady, D. G.; Fox, D. M.; Naik, R. R.; Stone, M. O.; Trulove, P. C.; De Long, H. C.; Mantz, R. A., Dissolution and regeneration of Bombyx mori silk fibroin using ionic liquids. *Journal of the American Chemical Society* **2004,** *126* (44), 14350-14351.
(30) Zhang, H.; Wu, J.; Zhang, J.; He, J., 1-Allyl-3-methylimidazolium chloride room

temperature ionic liquid: a new and powerful nonderivatizing solvent for cellulose. *Macromolecules* **2005,** *38* (20), 8272-8277.

(31) Zhang, J.; Zhang, H.; Wu, J.; Zhang, J.; He, J.; Xiang, J., NMR spectroscopic studies of cellobiose solvation in EmimAc aimed to understand the dissolution mechanism of cellulose in ionic liquids. *Physical Chemistry Chemical Physics* **2010,** *12* (8), 1941-1947.

(32) Zhang, J.; Wu, J.; Yu, J.; Zhang, X.; He, J.; Zhang, J., Application of ionic liquids for dissolving cellulose and fabricating cellulose-based materials: state of the art and future trends. *Materials Chemistry Frontiers* **2017,** *1* (7), 1273-1290.

(33) Si, Y.; Wang, X.; Yan, C.; Yang, L.; Yu, J.; Ding, B., Ultralight biomass-derived carbonaceous nanofibrous aerogels with superelasticity and high pressure-sensitivity. *Advanced Materials* **2016,** *28* (43), 9512-9518.

(34) Zhang, P.; Gong, Y.; Li, H.; Chen, Z.; Wang, Y., Solvent-free aerobic oxidation of hydrocarbons and alcohols with Pd@ N-doped carbon from glucose. *Nature Communications* **2013,** *4* (1), 1-11.

(35) Teranishi, T.; Miyake, M., Size control of palladium nanoparticles and their crystal structures. *Chemistry of Materials* **1998,** *10* (2), 594-600.

(36) Dai, Z.; Bradley, J.; Joswiak, D.; Brownlee, D.; Hill, H.; Genge, M., Possible in situ formation of meteoritic nanodiamonds in the early solar system. *Nature* **2002,** *418* (6894), 157-159.

(37) Yang, S.; Dong, J.; Yao, Z.; Shen, C.; Shi, X.; Tian, Y.; Lin, S.; Zhang, X., One-pot synthesis of graphene-supported monodisperse Pd nanoparticles as catalyst for formic acid electro-oxidation. *Scientific Reports* **2014,** *4* (1), 1-6.

(38) Petersen, R.; Foucher, D. A.; Tang, B.-Z.; Lough, A.; Raju, N. P.; Greedan, J. E.; Manners, I., Pyrolysis of poly (ferrocenylsilanes): synthesis and characterization of ferromagnetic transition-metal-containing ceramics and molecular depolymerization products. *Chemistry of Materials* **1995,** *7* (11), 2045-2053.

(39) Costantini, F.; Benetti, E. M.; Tiggelaar, R. M.; Gardeniers, H. J.; Reinhoudt, D. N.; Huskens, J.; Vancso, G. J.; Verboom, W., A Brush-Gel/Metal-Nanoparticle Hybrid Film as an Efficient Supported Catalyst in Glass Microreactors. *Chemistry-A European Journal* **2010,** *16* (41), 12406-12411.

(40) Strachan, J.; Barnett, C.; Masters, A. F.; Maschmeyer, T., 4-Nitrophenol reduction: probing the putative mechanism of the model reaction. *ACS Catalysis* **2020,** *10* (10), 5516-5521.

(41) Wunder, S.; Lu, Y.; Albrecht, M.; Ballauff, M., Catalytic activity of faceted gold nanoparticles studied by a model reaction: evidence for substrate-induced surface restructuring. *ACS Catalysis* **2011,** *1* (8), 908-916.

(42) Wunder, S.; Polzer, F.; Lu, Y.; Mei, Y.; Ballauff, M., Kinetic analysis of catalytic reduction of 4-nitrophenol by metallic nanoparticles immobilized in spherical polyelectrolyte brushes. *The Journal of Physical Chemistry C* **2010,** *114* (19), 8814-8820.

(43) Lu, W.; Ning, R.; Qin, X.; Zhang, Y.; Chang, G.; Liu, S.; Luo, Y.; Sun, X., Synthesis of Au nanoparticles decorated graphene oxide nanosheets: Noncovalent functionalization by TWEEN 20 in situ reduction of aqueous chloroaurate ions for hydrazine detection and catalytic reduction of 4-nitrophenol. *Journal of Hazardous Materials* **2011,** *197*, 320-326.

(44) Koga, H.; Tokunaga, E.; Hidaka, M.; Umemura, Y.; Saito, T.; Isogai, A.; Kitaoka, T., Topochemical synthesis and catalysis of metal nanoparticles exposed on crystalline cellulose nanofibers. *Chemical Communications* **2010,** *46* (45), 8567-8569.

(45) Han, J.; Li, L.; Guo, R., Novel approach to controllable synthesis of gold nanoparticles supported on polyaniline nanofibers. *Macromolecules* **2010,** *43* (24), 10636-10644.
(46) Li, X.; Dong, F.; Zhang, L.; Xu, Q.; Zhu, X.; Liang, S.; Hu, L.; Xie, H., Cellulosic protic ionic liquids hydrogel: A green and efficient catalyst carrier for Pd nanoparticles in reduction of 4-nitrophenol in water. *Chemical Engineering Journal* **2019,** *372*, 516-525.
(47) Yao, T.; Zuo, Q.; Wang, H.; Wu, J.; Xin, B.; Cui, F.; Cui, T., A simple way to prepare Pd/Fe3O4/polypyrrole hollow capsules and their applications in catalysis. *Journal of Colloid and Interface Science* **2015,** *450*, 366-373.
(48) Dhanavel, S.; Manivannan, N.; Mathivanan, N.; Gupta, V. K.; Narayanan, V.; Stephen, A., Preparation and characterization of cross-linked chitosan/palladium nanocomposites for catalytic and antibacterial activity. *Journal of Molecular Liquids* **2018,** *257*, 32-41.
(49) Chang, Y.-C.; Chen, D.-H., Catalytic reduction of 4-nitrophenol by magnetically recoverable Au nanocatalyst. *Journal of Hazardous Materials* **2009,** *165* (1-3), 664-669.
(50) Khan, F. U.; Khan, S. B.; Kamal, T.; Asiri, A. M.; Khan, I. U.; Akhtar, K., Novel combination of zero-valent Cu and Ag nanoparticles@ cellulose acetate nanocomposite for the reduction of 4-nitro phenol. *International Journal of Biological Macromolecules* **2017,** *102*, 868-877.
(51) Cabreira, C. R.; Camilo, F. F., Evaluation of catalytic activity of cellulose films decorated with gold nanoparticles in the reduction of 4-nitrophenol. *Cellulose* **2020,** *27*, 3919–3929.
(52) Guo, M.; Zhang, Y.; Du, F.; Wu, Y.; Zhang, Q.; Jiang, C., Silver nanoparticles/polydopamine coated polyvinyl alcohol sponge as an effective and recyclable catalyst for reduction of 4-nitrophenol. *Macromolecular Chemistry and Physics* **2019,** *225*, 42-49.
(53) Hempenius, M. A.; Brito, F. F.; Vancso, G. J., Synthesis and characterization of anionic and cationic poly (ferrocenylsilane) polyelectrolytes. *Macromolecules* **2003,** *36* (17), 6683-6688.
(54) Sui, X.; Hempenius, M. A.; Vancso, G. J., Redox-active cross-linkable poly (ionic liquid) s. *Journal of the American Chemical Society* **2012,** *134* (9), 4023-4025.

6.6 Supporting information

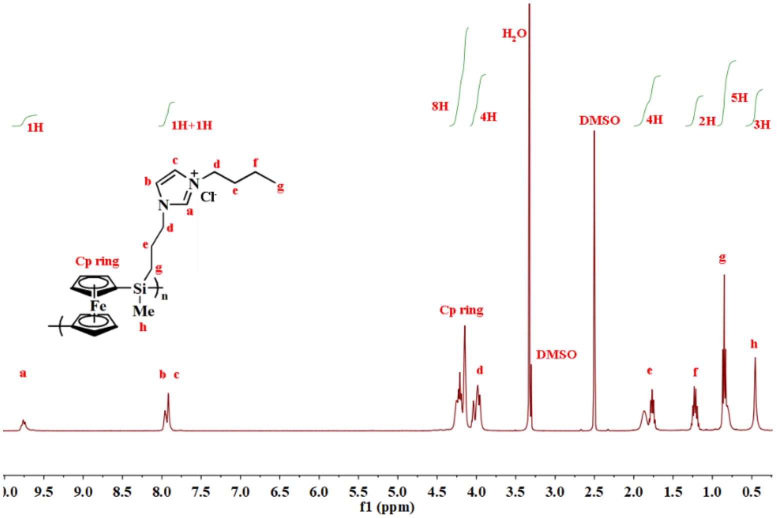

Figure S6.1 ^{1}H NMR spectrum of PFS-C4IM$^+$ Cl$^-$ in DMSO-d_6.

Figure S6.2 Photographs of a cuvette containing an aqueous solution of 4-nitrophenol and $NaBH_4$ before reduction (left), and of the solution after reduction to 4-aminophenol (right).

Chapter 7

New Opportunities for Cellulose-PFS Composites: PFS Based Poly(ionic liquids)

As shown in **Chapter 6**, PFS-based PILs are promising polymers to improve the functionalities of cellulose and their porous derivatives. In this **Outlook** chapter, the fabrication of various new PFS-PILs is proposed and discussed, including methyl imidazolium-PFS, diethyl methylamine-PFS, and PFS-based zwitterionic PILs. We believe that a combination of the unique redox properties of these PFS-PILs with cellulose materials will open new horizons for the creation of advanced stimuli-responsive porous materials.

7.1 PFS based poly(ionic liquids)

PFS-based poly(ionic liquids) have been explored in the MTP group and used in applications such as smart windows, separation membranes, sensors, and actuators [1-3]. In order to explore more PFS-PILs, methylimidazole and diethylmethylamine were reacted with PFS-I according to the method shown in **Chapter 6**. The synthetic routes employed to obtain PFS-methylimidazole chloride and PFS-diethylmethylamine chloride are shown in **Figures 7.1** and **7.3**. The ^{1}H NMR spectra of PFS-methylimidazole chloride and PFS-diethylmethylamine chloride are shown in **Figures 7.2** and **7.4**.

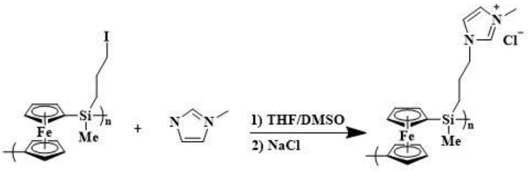

Figure 7.1 Synthesis of PFS-methylimidazolium chloride.

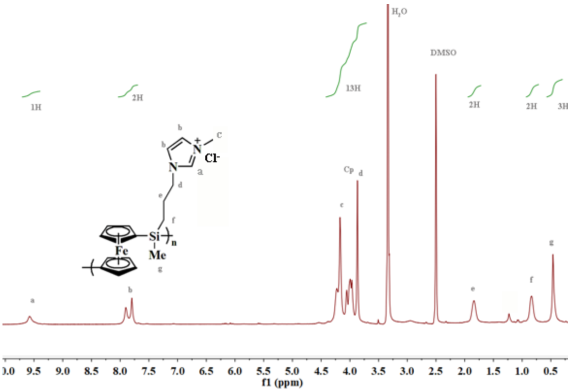

Figure 7.2 ^{1}H NMR spectrum of PFS-methylimidazolium chloride.

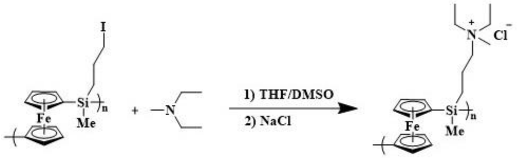

Figure 7.3 Synthesis of PFS-diethylmethylamine chloride.

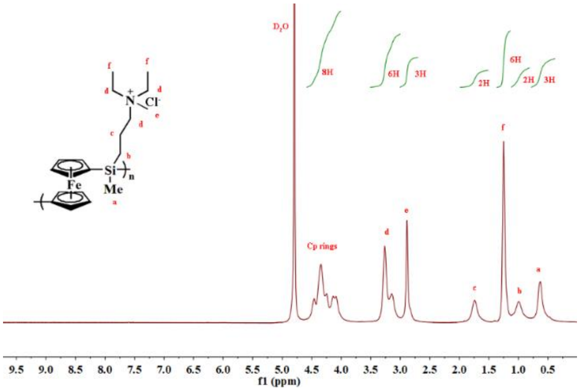

Figure 7.4 ^{1}H NMR spectrum of PFS-diethylmethylamine chloride.

The as-prepared PFS-PILs can easily change their wettability by exchange with different counterions (BF_4^-, Tf_2N^-, $C_5SO_3^-$, etc.). For future experiments, we propose to obtain PFS-PILs with dual responsive properties (redox and thermal responsive) and then combine these with cellulosic porous materials to prepare stimuli-responsive cellulosic porous materials, which could be used in fields of controlled adsorption and separation.

7.2 PFS based zwitterionic poly(ionic liquids)

Zwitterionic polymers consist of macromolecules with positive and negative charges incorporated into their structure. It is a unique class of smart materials with great potential in applications related to energy, environment, and healthcare [4].

Based on previous work on imidazolium modified PFS, we can further design PFS-based zwitterionic poly(ionic liquids) using a zwitterionic 4-(1-imidazolium)butane sulfonate substituent. The synthesis of 4-(1-imidazolium)butane sulfonate is shown in **Figure 7.5**. From the ^{1}H NMR spectrum shown in **Figure 7.6**, the correct product was obtained successfully. However, the yield of this reaction was low, a result which requires further investigation. The next step of modifying PFS with this substituent is shown in **Figure 7.7**. This reaction will be explored in the future.

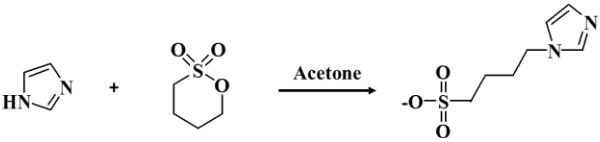

Figure 7.5 Synthesis of 4-(1-imidazolium)butane sulfonate.

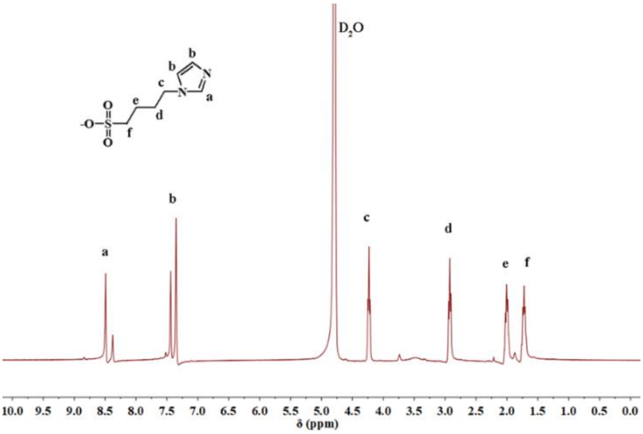

Figure 7.6 ^{1}H NMR spectrum of 4-(1-imidazolium)butane sulfonate.

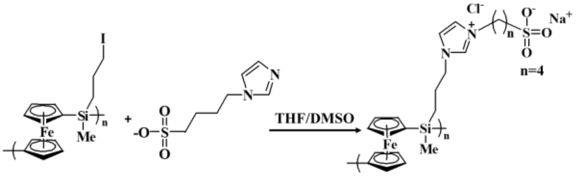

Figure 7.7 Synthesis of PFS-based zwitterionic PILs.

7.3 PFS crosslinked adhesive hydrogel.

Responsive polymeric hydrogels are widely used in applications such as sensors, actuators, drug-delivery systems, etc [5-7]. Promising materials may result when responsive polymeric hydrogels are endowed with adhesive properties. For example, polymeric hydrogel adhesives have been explored for wound management and repair due to their tunable chemical and physical properties. The polymeric hydrogel adhesives can easily adhere or stick to tissues and possess sufficient mechanical strength to stay intact. They can also provide complete wound occlusion and act as a barrier to bacterial infection [8]. These responsive materials can be used as sensors or actuators because they can easily adhere to the surface of most materials [9-11].

Previously, we reported on main-chain redox-active PFS-based hydrogels with redox-controlled collapse and swelling [12]. In the PFS-based hydrogels, the polymer-water interactions could be altered by changing the redox state of the PFS chains. These small interaction changes were further amplified to the macro-scale of the hydrogel and formed the basis of redox-driven mechanical hydrogel actuation [13]. In this work, the zwitterionic monomer [2-(methacryloyloxy)ethyl]dimethyl-(3-sulfopropyl)ammonium hydroxide (SBMA) was introduced to the matrix to provide adhesive properties for hydrogel, which could lead to new prospects for adhesive redox-driven hydrogel actuators.

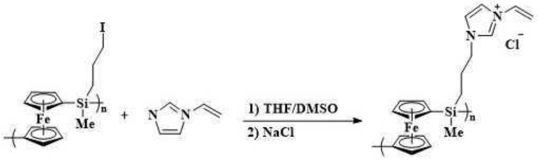

Figure 7.8 Synthesis of PFS-vinylimidazolium chloride.

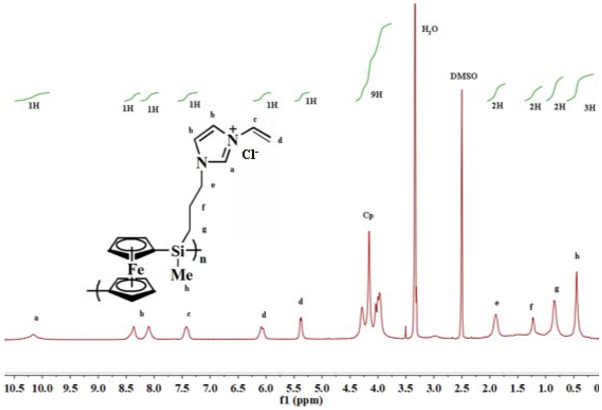

Figure 7.9 ^{1}H NMR spectrum of PFS-vinylimidazolium chloride.

The synthesis and ^{1}H NMR spectrum of PFS-vinylimidazolium chloride are shown in **Figures 7.8** and **7.9**.

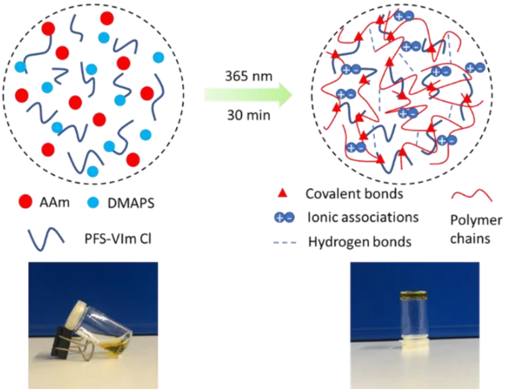

Figure 7.10 Preparation and possible crosslinking of PFS crosslinked adhesive hydrogel.

The preparation and possible crosslinking of the proposed PFS adhesive hydrogel are shown in **Figure 7.10**. In this hydrogel, PFS-Vim chloride not only served as a crosslinking agent but may also provide redox-driven force by applying electrochemical stimuli.

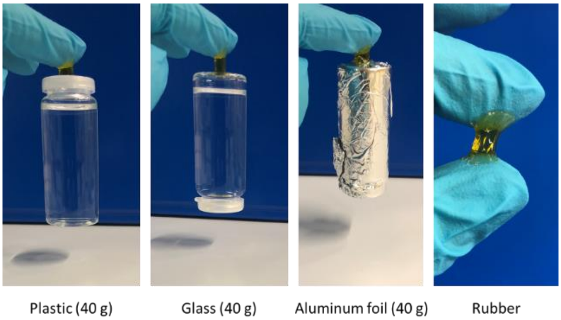

Figure 7.11 Adhesive properties of PFS crosslinked hydrogel.

The adhesive properties of this PFS crosslinked hydrogel are shown in **Figure 7.11**, which illustrates that this hydrogel has superior adhesion properties with different surfaces, including plastic, glass, aluminum foil, and rubber. The sulfonate groups and ammonium cations in SBMA provide strong bonding with different substances. The hydrogels could quickly form hydrogen bonds with the interfaces while the charged groups could interact with other polar groups on the substrate surfaces.

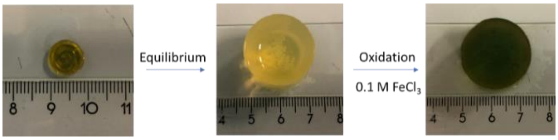

Figure 7.12 Redox responsive behavior of PFS crosslinked hydrogel.

A rapid color change from amber to green occurred when the hydrogel was immersed in 0.01M aqueous $FeCl_3$ solution, demonstrating redox responsivity of the hybrid hydrogel (**Figure 7.12**).

Due to the low concentration of PFS in this hydrogel, size changes induced by oxidation were not noticeable. Therefore, the next step is to explore the composition of the hydrogel and optimize both adhesion and actuation. More importantly, cellulose can be added to adjust the modulus of this hydrogel in a controlled manner [14].

7.4 Experimental section

7.4.1 Materials

Poly(ferrocenyl(3-iodopropyl)methylsilane) (PFS-I) (M_n: 2.93×10^5 g mol^{-1}, M_w: 1.27×10^5 g mol^{-1}) was prepared according to established procedures [15]. 1-Methylimidazole (Aldrich, 99%), *N,N*-diethylmethylamine (Aldrich, 97%), imidazole (Sigma-aldrich, ⩾99.5%), 1,3-butanesulfonate (TCI Europe, >99%), 1-vinylimidazole (Aldrich, ⩾ 99%), [2-(methacryloyloxy)ethyl]dimethyl-(3-sulfopropyl)ammonium hydroxide (SBMA, Merck KGaA), acrylamide (Sigma-aldrich, ⩾98%), acetone (VWR chemicals), dimethylsulfoxide (DMSO, Biosolve), tetrahydrofuran (THF, VWR chemicals) and sodium chloride (NaCl) (Aldrich, 99.5%) were used without further purification. Photo initiator (lithium phenyl-2,4,6-trimethylbenzoylphosphinate, LAP) was prepared according to established procedures [16]. Water was purified with a Millipore system.

7.4.2 Synthesis of methylimidazolium PFS (PFS-C_1IM chloride)

1-Methylimidazole (0.25 g, 3.0 mmol) and DMSO (6 mL) were added to a solution of PFS-I (0.4 g, 1.0 mmol) in THF (12 mL). The mixture was stirred at 60°C for 24 h. After removing THF, the mixture was transferred into a Spectra/Por 4 dialysis hose (MWCO 12-14,000 g mol^{-1}) and dialyzed against 0.1 M NaCl (3×8 L) and Milli Q water (3×8 L). Concentration of the salt-free polyelectrolyte solution by a flow of N_2 produced PFS-C_1IM chloride as orange flakes.

7.4.3 Synthesis of diethylmethylamine-substituted PFS (PFS-DEMA chloride)

N,N-Diethylmethylamine (0.26 g, 3.0 mmol) and DMSO (6 mL) were added to a solution of PFS-I (0.4 g, 1.0 mmol) in THF (12 mL). The mixture was stirred at RT for 24 h. After removing THF, the mixture was transferred into a Spectra/Por 4 dialysis hose (MWCO 12-14,000 g mol^{-1}) and dialyzed against 0.1 M NaCl (3×8L) and Milli Q water (3×8L). Concentration of the salt-free polyelectrolyte solution by a flow of N_2 produced PFS-DEMA chloride as orange flakes.

7.4.4 Synthesis of 4-(1-imidazolium)butane sulfonate

Imidazole (3.0 g, 0.044 mol) was dissolved in 10 mL acetone and then placed in an ice bath with stirring. 1,3-Butanesulfonate (2.0 g 0.015 mol) was dissolved in 10 mL acetone. The 1,3-butanesulfonate solution was then added dropwise to the imidazole solution, which was cooled in an ice bath, while stirring. After this, the solution was warmed to RT. After being stirred overnight, the solution was precipitated in THF and washed with THF three times. Removal of THF by a flow of N_2 produced 4-(1-imidazolium)butane sulfonate as a white powder.

7.4.5 Synthesis of 1-vinylimidazolium PFS (PFS-VIm chloride)

1-Vinylimidazole (0.28 g, 3.0 mmol) and DMSO (6 mL) were added to a solution of PFS-I (0.4 g, 1.0 mmol) in THF (12 mL). The mixture was stirred at 60℃ for 24 h. After removing THF, the mixture was transferred into a Spectra/Por 4 dialysis hose (MWCO 12-14,000 g mol^{-1}) and dialyzed against 0.1 M NaCl (3×8 L) and Milli Q water (3×8 L). Concentration of the salt-free polyelectrolyte solution by a flow of N_2 produced PFS-VIm chloride as orange flakes.

7.4.6 Preparation of hydrogel

PFS-Vim chloride (3 mg), acrylamide (150 mg) and SBMA (150 mg) were dissolved in Milli-Q water (0.3 mL). Photoinitiator (LAP, 2 mg) was added. The solution was purged with N_2 for 30 min before polymerization. The mixture was subsequently transferred to a mold and irradiated in an ultraviolet crosslinker (Analytik Jena US, 365 nm) for 30 min at room temperature.

7.5 References

(1) Zhang, K.; Feng, X.; Sui, X.; Hempenius, M. A.; Vancso, G. J. Breathing pores on command: Redox‐responsive spongy membranes from poly (ferrocenylsilane) s. *Angewandte Chemie International Edition* **2014,** *53* (50), 13789-13793.
(2) Zhang, K.; Feng, X.; Ye, C.; Hempenius, M. A.; Vancso, G. J. Hydrogels with a memory: Dual-responsive, organometallic poly (ionic liquid) s with hysteretic volume-phase transition. *Journal of the American Chemical Society* **2017,** *139* (29), 10029-10035.
(3) Zhang, K.; Zhang, M.; Feng, X.; Hempenius, M. A.; Vancso, G. J. Switching light transmittance by responsive organometallic poly (ionic liquid) s: Control by cross talk of thermal and redox stimuli. *Advanced Functional Materials* **2017,** *27* (41), 1702784.
(4) Blackman, L. D.; Gunatillake, P. A.; Cass, P.; Locock, K. E. An introduction to zwitterionic polymer behavior and applications in solution and at surfaces. *Chemical Society Reviews* **2019,** *48* (3), 757-770.
(5) Kost, J.; Langer, R. Responsive polymeric delivery systems. *Advanced Drug Delivery Reviews* **2012,** *64*, 327-341.
(6) Hu, L.; Zhang, Q.; Li, X.; Serpe, M. J. Stimuli-responsive polymers for sensing and actuation. *Materials Horizons* **2019,** *6* (9), 1774-1793.
(7) Zhang, D.; Ren, B.; Zhang, Y.; Xu, L.; Huang, Q.; He, Y.; Li, X.; Wu, J.; Yang, J.; Chen, Q. From design to applications of stimuli-responsive hydrogel strain sensors. *Journal of Materials Chemistry B* **2020,** *8* (16), 3171-3191.
(8) Ghobril, C.; Grinstaff, M. The chemistry and engineering of polymeric hydrogel adhesives for wound closure: A tutorial. *Chemical Society Reviews* **2015,** *44* (7), 1820-1835.
(9) Zhang, D.; Tang, Y.; Zhang, Y.; Yang, F.; Liu, Y.; Wang, X.; Yang, J.; Gong, X.; Zheng, J. Highly stretchable, self-adhesive, biocompatible, conductive hydrogels as fully polymeric strain sensors. *Journal of Materials Chemistry A* **2020,** *8* (39), 20474-20485.
(10) Wang, L.; Gao, G.; Zhou, Y.; Xu, T.; Chen, J.; Wang, R.; Zhang, R.; Fu, J. Tough, adhesive, self-healable, and transparent ionically conductive zwitterionic nanocomposite hydrogels as skin strain sensors. *ACS Applied Materials & Interfaces* **2018,** *11* (3), 3506-3515.
(11) Xu, J.; Wang, G.; Wu, Y.; Ren, X.; Gao, G. Ultrastretchable wearable strain and pressure sensors based on adhesive, tough, and self-healing hydrogels for human motion monitoring. *ACS Applied Materials & Interfaces* **2019,** *11* (28), 25613-25623.
(12) Hempenius, M. A.; Cirmi, C.; Savio, F. L.; Song, J.; Vancso, G. J. Poly (ferrocenylsilane) gels and hydrogels with redox‐controlled actuation. *Macromolecular Rapid Communications* **2010,** *31* (9‐10), 772-783.
(13) Zhang, K. Metallopolymers as responsive materials: Shifting equilibrium by tuning structure. **2017**.
(14) Yang, B.; Yuan, W. Highly stretchable, adhesive, and mechanical zwitterionic nanocomposite hydrogel biomimetic skin. *ACS Applied Materials & Interfaces* **2019,** *11* (43), 40620-40628.
(15) Hempenius, M. A.; Brito, F. F.; Vancso, G. J. Synthesis and characterization of anionic and cationic poly (ferrocenylsilane) polyelectrolytes. *Macromolecules* **2003,** *36*

(17), 6683-6688.

(16) Fairbanks, B. D.; Schwartz, M. P.; Bowman, C. N.; Anseth, K. S. Photoinitiated polymerization of peg-diacrylate with lithium phenyl-2, 4, 6-trimethylbenzoylphosphinate: Polymerization rate and cytocompatibility. *Biomaterials* **2009,** *30* (35), 6702-6707.

Summary

Structure design and surface modification are promising ways to improve the application performance of functional cellulosic porous materials. This thesis starts with a **general introduction**, including the introduction and problem statements of cellulosic porous materials and presents an outline, which briefly describes the recent advances and the research work performed on structure design and surface modification of cellulosic porous materials.

Chapter 2 provides a literature review on cellulosic porous materials. Based on the current state of the art, novel structures and effective modification methods are considered for improving the application performance of cellulosic porous materials in the fields of environment, energy, and healthcare.

Chapter 3 presents a new hemostatic wound dressing construct sponge obtained by the integration of heterogenous, microporous materials with different wettability. Benefitting from the 3D fibrous cellular network that consists of flexible cellulose nanofibers and organosilanes, the sponges showed Janus characteristics, exhibiting excellent underwater flexibility and shape-memory behavior. The comprehensive advantages of the unique Janus structure with different wettability on both sides, supported by the hemostatic property of chitosan, endowed the sponges with a 49% reduction of blood loss compared with only a hydrophilic control sample and common gauze.

In order to further give full play to the advantages of similar Janus structures, in **chapter 4**, we designed and constructed systems in a cylindrical shape. A robust, nature-inspired and high-performance monolithic integrated cellulose aerogel-based evaporator (MiCAE) for seawater desalination was fabricated from these Janus systems using the facile and scalable heterogeneous mixing and freeze-drying technique. Inspired by woods and mushrooms, the incorporation of the hydrophobic SCA (possessing intrinsic low thermal conductivity) with mushroom-shaped CPA (having vertically aligned channels and porous structures analogous to woods) realized heat localization and effectively suppressed heat dissipation of the system, enhancing the solar-thermal conversion efficiency. The hydrophilic CPA component integrated in the SCA enabled fast water transportation by capillary action and great salt excretion because of the low tortuosity porous structure. By virtue of a synergistic effect of the integrated functional structures, the evaporator can realize the combination of high light absorption, efficient salt-resistance and impressive efficiency. As a result, the MiCAE exhibits a high irradiation absorption of 94%, a great evaporation rate of 1.90 kg m^{-2} h^{-1} and an impressive efficiency of 89% under one-sun irradiation. Moreover, the evaporator demonstrates a stable vapor generation with almost no salt deposition when actual East China Sea water is used, and exhibits an obvious salt-resistance performance in highly concentrated brine (17.5 wt.%) under one-sun irradiation for continuous evaporation of 8 hours.

We describe in **chapter 5** a wearable heater based on the previous work. This chapter presents an effective strategy for fabricating lightweight, robust, stretchable and multifunctional CP/PU/PFC composite aerogels. These materials exhibit satisfactory Joule heating performance (up to 173 °C at 4 V) with low working voltage and rapid heating rate. Excellent waterproof performance could be achieved with CP-48/PU/PFC-6 which has a large WCA of 135°. Despite having highly waterproof surfaces, the CP/PU/PFC composite aerogels showed prominent breathable performance (the WVT rate of 5.8±0.8 kg m^{-2} d^{-1}) owing to their interconnected porous structure. These results suggest that the mechanically robust and multifunctional CP-48/PU/PFC composite aerogels are highly promising as wearable heaters for applications in harsh environments, such as frigid polar regions, pluvial mountainous areas, and cryogenic workshops.

Combining the unique properties of poly(ferrocenylsilanes) (PFS) with those of cellulose, in **chapter 6**, a Pd NPs loaded cellulose/PFS-PIL composite sponge was fabricated by co-dissolving, solvent exchange, and subsequent freeze-drying. The PFS-PILs can reduce and immobilize metal NPs in an in-situ process, which required no external reducing agents. The porous cellulose/PFS-PIL sponges were found to be effective supports for Pd NPs. These sponges demonstrated excellent catalytic properties which could be improved to reach a rate constant value of $k = 0.51$ min^{-1} for the reduction of 4-nitrophenol to 4-aminophenol. The employed method used to form and immobilize metal NPs on renewable support materials can be applied to create a broad range of metal NP-decorated porous structures.

Overall, we presented different structure designs and surface modification methods of cellulosic porous materials which have great potential for application in the areas of environment, energy, and healthcare. Firstly, we designed cellulosic porous materials with a Janus structure. This unique structure with different wettability provides these materials with novel application opportunities. We explored the application of this Janus structure in hemostatic wound dressing and in evaporators for seawater desalination, and obtained superior results compared with some commercial products and results shown in other published work. Second, based on our previous work and the widely researched polymer

PFS, we used a post-modification and physical mixing method to prepare two kinds of porous materials. One is a wearable heater and the other is a catalyst support. In order to further explore the combination of cellulose and PFS, we added some PFS structures in the outlook chapter, hoping to broaden the functionalization options of cellulosic porous materials. Overall, the results presented in this thesis were realized by introducing novel structure and surface modification methods for porous materials with the aim of gaining access to new application areas, and to hopefully give inspiration to researchers in the development of advanced cellulosic porous materials.

Samenvatting

De toepassingsmogelijkheden van poreuze materialen gebaseerd op cellulose kunnen aanzienlijk worden uitgebreid door beïnvloeding van de poreuze structuur en door oppervlaktemodificatie van deze materialen. Dit proefschrift begint met een algemene inleiding, inclusief een inleiding en onderzoeksvragen van poreuze cellulose materialen, en geeft een overzicht van recente ontwikkelingen en onderzoekswerk verricht aan de structuur en oppervlaktemodificatie van poreuze cellulose materialen.

Hoofdstuk 2 geeft een literatuuroverzicht van poreuze cellulose materialen. Op basis van de huidige "state of the art" worden nieuwe structuren en effectieve modificatie methoden onderzocht om de prestaties van poreuze cellulose materialen in toepassingen op het gebied van milieu, energie en gezondheidszorg te verbeteren.

Hoofdstuk 3 beschrijft een nieuwe hemostatische wondbedekkings spons, verkregen door de integratie van heterogene, microporeuze materialen met verschillende bevochtigingskarakteristieken. Gebruikmakend van het 3D vezelachtige cellulaire netwerk dat bestaat uit flexibele cellulose nanovezels en organosilanen, vertoonden de sponzen Janus eigenschappen, uitstekende flexibiliteit onder water, en vormgeheugen gedrag. De voordelen van de unieke Janus structuur met verschillende bevochtigbaarheid aan beide kanten, ondersteund door de hemostatische eigenschappen van chitosan, leidden tot een 49% verlaging van bloedverlies vergeleken met een uitsluitend hydrofiel referentiemateriaal en standaard verband.

Om de voordelen van Janus structuren zo veel mogelijk te benutten ontwierpen en construeerden we in **hoofdstuk 4** cylindervormige systemen. Een robuuste, door de natuur geïnspireerde, monolithische geïntegreerde, op een cellulose aerogel gebaseerde verdamper (MiCAE) voor het ontzouten van zeewater werd gefabriceerd uit deze Janus systemen via de eenvoudig uitvoerbare en opschaalbare heterogene menging en vriesdroogtechniek. Geïnspireerd door hout en paddenstoelen zorgde de inbouw van de hydrofobe SCA (die een intrinsieke lage thermische geleidbaarheid bezit) en de paddenstoelvormige CPA (die verticaal uitgelijnde kanalen en poreuze structuren analoog aan hout bezit) voor warmtelocalisatie en een effectieve onderdrukking van warmtedissipatie door het systeem waardoor de efficiëntie van de omzetting van zonlicht naar warmte werd verhoogd. De hydrofiele CPA component geïntegreerd in de SCA maakte snel transport van water mogelijk door capillaire werking en een hoge zoutafgifte als gevolg van de laag-tortueuze poreuze structuur. Vanwege de synergie tussen de geïntegreerde functionele structuren kon de verdamper een combinatie van hoge lichtabsorptie, efficiënte zoutweerstand en een indrukwekkende efficiëntie realiseren. Hierdoor vertoonde de MiCAE een hoge stralingsabsorptie van 94%, een hoge verdampingssnelheid van 1.90 kg m^{-2} h^{-1} en een indrukwekkende efficiëntie van 89% onder bestraling door het equivalent van één zon. Bovendien vertoont de verdamper een stabiele dampvorming en bijna geen zoutafzetting bij gebruik van zeewater uit de Oost-Chinese zee, en toont een duidelijke weerstand tegen zout in hoog geconcentreerde zoutoplossing (17.5 wt.%) onder "één zon" bestraling in een continu verdampingsproces van 8 uur.

In **hoofdstuk 5** beschrijven we een draagbare verwarmer gebaseerd op eerder werk. Dit hoofdstuk presenteert een effectieve strategie voor de fabricage van lichtgewicht, robuuste, rekbare en multifunctionele CP/PU/PFC composiet aerogels. Deze materialen vertonen een goede Joule verwarming (tot 173 °C bij 4 V) met een laag werkingsvoltage en een hoge opwarmsnelheid. Uitstekende waterwerende prestaties werden bereikt met CP-48/PU/PFC-6 die een hoge water contacthoek heeft van 135°. Ondanks de goede waterafstotende oppervlakken bleken de CP/PU/PFC composiet aerogels ook zeer goed ademend te zijn (WVT snelheid 5.8±0.8 kg m^{-2} d^{-1}) dankzij hun onderling verbonden poreuze structuur. Deze resultaten tonen aan dat de mechanisch robuuste en multifunctionele CP-48/PU/PFC composiet aerogels zeer veelbelovend zijn als draagbare verwarmers voor toepassing onder extreme omstandigheden, zoals de poolgebieden, berggebieden met zware regenval, en cryogene werkplaatsen.

Door het combineren van de unieke eigenschappen van poly(ferrocenylsilanen) (PFS) met die van cellulose kon in **hoofstuk 6** een Pd NP beladen cellulose/PFS-PIL composiet spons worden gefabriceerd door oplossen, oplosmiddel uitwisseling, en daaropvolgend vriesdrogen. De PFS-PILs kunnen metaalzouten reduceren tot metaal nanodeeltjes en deze immobiliseren in een in-situ proces waarin geen externe reducerende reagentia nodig zijn. De poreuze cellulose/PFS-PIL sponzen bleken effectieve dragers voor Pd NPs te zijn. Deze sponzen vertoonden uitstekende katalytische eigenschappen die verder konden worden verbeterd, waardoor waarden voor de snelheidsconstante voor reductie van 4-nitrofenol tot 4-aminofenol van $k = 0.51$ min^{-1} werden bereikt. De gebuikte methode om metaal NPs te vormen en te immobiliseren op duurzame dragermaterialen kan worden toegepast om een breed scala aan metaal NP gefunctionaliseerde poreuze structuren te creëren.

In dit proefschrift presenteerden we verschillende structuurontwerpen en oppervlakte modificatie methoden voor poreuze cellulose materialen die veelbelovende toepassingsmogelijkheden hebben op het gebied van milieu, energie en gezondheidszorg. Ten eerste ontwierpen we poreuze cellulose materialen met een Janus structuur. Deze unieke structuur met verschillende bevochtbaarheid geeft deze materialen nieuwe toepassingsmogelijkheden. We onderzochten de toepassing van deze Janus structuur voor hemostatische wondbedekking en in verdampers voor het ontzouten van zeewater, en behaalden betere resultaten vergeleken met enkele commerciële producten en resultaten uit werk gepubliceerd door anderen. Ten tweede werd, gebaseerd op eerder door ons gepubliceerd werk en het in detail onderzochte polymeer PFS, een post-modificatie en fysische menging methode gebruikt om twee soorten poreuze materialen te fabriceren. Een is een draagbare verwarmer en de andere is een drager voor katalysatoren. Om de combinatie van cellulose en PFS verder te onderzoeken werden enkele PFS structuren in het outlook hoofdstuk beschreven in de hoop om functionaliseringsmogelijkheden van poreuze cellulose materialen te verbreden. Uiteindelijk werden de resultaten gepresenteerd in dit proefschrift gerealiseerd door het introduceren van nieuwe structuur- en oppervlaktemodificatie methoden voor poreuze materialen met als doel om toegang te krijgen tot nieuwe toepassingsgebieden en hopelijk om inspiratie te geven aan onderzoekers bij de ontwikkeling van geavanceerde poreuze cellulose materialen.

Acknowledgements

The two years in Enschede were too fast for me. Although most of the time was in the COVID-19 situation, there are still many good memories. Now, I am sitting in a chair in a quarantined hotel, Shanghai, and I exactly have enough time to recall all the things in the past two years and those who I need to thank and appreciate.

Firstly, I would like to give my best appreciation to my supervisor Prof. Julius Vancso for offering me this opportunity to attend this joint Ph.D project between Donghua University (DHU) and University of Twente (UT). Dear Julius, the first time we met was during you visited DHU in 2016. I remember that it was challenging for me to speak some English with you at that moment. But you always encourage me to express myself. You are a rigorous, and enthusiastic scientist in teaching and scientific research. Whether in the classroom where you teach at DHU or in discussions with you during the scientific research in UT, I have deeply realized this. I hope we can meet again in China soon.

Similarly, I would like to thank my co-supervisor, Prof. Xiaofeng Sui, for offering me this opportunity to attend this joint Ph. D project. Thank you for your trust and help since I enrolled and followed you in the master's degree. You give me ample opportunity to express myself, support me in participating in international conferences, etc., which has benefited me. Too many thanks cannot be described here, but we still have a lot of time to work together in DHU.

I sincerely thank my daily supervisor, Dr. Mark Hempenius. Mark, you are passionate about teaching and experiments and are very responsible. Thank you very much for your time and seriousness in teaching me how to synthesize PFS, encouraging me to try, discussing the results, correcting my manuscript, and translating my summary into Dutch. And thanks for giving me an opportunity to do the lab course, which is helpful for me.

I would also like to thank all the other collaborators in this Thesis: Prof. Zhiping Mao, Prof. Xueling Feng, Dr. Bijia Wang, Prof. Mujun Lu (Renji Hospital), Dr. Dongdong Xiao (Renji hospital), Kuankuan Liu, Yating Wang. Thanks, Prof. Mujun Lu and Dr. Dongdong Xiao, for your help and valuable discussions in cell and animal experiments. Thanks, Prof. Zhiping Mao, Prof. Xueling Feng, and Dr. Bijia Wang, for discussing and revising the manuscripts. Kuankuan, I wish you success in your new position at Qingdao Institute of Bioenergy and Bioprocess Technology. Yating, I hope you enjoy the following year's stay in Enschede and UT.

Grateful acknowledgements to my defense committee members, Prof. Dimitrios Stamatialis, Prof. Wiebe M. de Vos, Prof. Szczepan Zapotoczny, Prof. Corinne Nardin, and Dr. Lixian Xu, for your time to read my thesis and the constructive suggestions. Dear Szczepan, it was nice to meet you at DHU in 2018. I really enjoyed your academic report on ladder-like polymer brushes at DHU. This is a very interesting work about macromolecular engineering on surfaces, which is inspired me significantly. We also had a nice trip to the highest building (Shanghai center) in Shanghai. Dr. Xu, I also benefited a lot from your report on the commercialization of nanocellulose. Thanks for being my committee member.

Truly appreciate our technicians and secretaries, Clemens, Romon, Marion, Nicole, and Izabel, for your help before I arrived in the Netherlands, when I was in the Netherlands, and after I left the Netherlands. You are always there when I need help, whether dealing with various tedious TGS processes or providing support for testing. Clemens, hope to see you in China and have an incredible journey soon.

In particular, I am highly thankful to Yan and Sida, for sharing their expertise and valuable guidance with me in my earlier life and research work. I wish you and your loved ones all the best. Roland and Giorgos, I enjoyed working and the rich discussion with you, from academic discussions to all kinds of novel and interesting things. Thank you for organizing the Wednesday pizza lunch, chicken wings are delicious. Wish you success with your Ph. D and all the best. I also hope to see you in China and have fun soon.

Thanks to my Chinese friends, Jinmeng, Yunchong, Lijie, Min, Wenxing, for the delicious food and hot pot we enjoyed together, for the route we ridden together, and for the happy games we played together. Jinmeng and Min, you almost finish your Ph. D. Wish you good luck in the following steps and have a good job. Lijie, enjoy your next three years in UT, and good luck with your natural biopolymer membrane proposal. Wenxing, wish you success with your postdoc position in Singapore. And Yunchong, we participated in the same joint Ph. D project and started and ended our UT study together. It is a great honor to solve various difficulties with you and work and study together. I also wish you success in your defense.

Thanks to my past and present officemates, Matthijs, Oliver, Olga, and Sishi. It was enjoyable to stay and talk with you. Importantly, I would like to thank all the past MTP and present SPC members, Prof. Frederik Wurm, Joost, Sissi, Hubert, Macro, Michel, Paloma, Amrutha, Anna, Chris, Loann, Ezgi, Adele, Diego, Maria, Timo, Lars, Guido, for your help and the excellent time we together. Thanks for being great colleagues. SPC is an active and enthusiastic research group. I believe that your research can make the world better and more sustainable. Also, thanks to all the research group members in DHU, I look forward to working together with you.

Finally, I would like to express my deepest gratitude to my family members who always support me, my parents (成普华，孟凡翠), my elder brother (成东标), my sister-in-law (王静), my nephew (成林越), and my niece (成梦琪). The video time with you every week is my happiest time. After the quarantine is over, I will run to you immediately.

成欢
Huan Cheng
Enschede and Shanghai, 2021

List of Publications

➢ *Journal articles:*

1. **Cheng, H.**, Li, L., Wang, B., Feng, X., Mao, Z., Vancso, G.J.*, and Sui, X.*, Multifaceted applications of cellulosic porous materials in environment, energy, and health. ***Progress in Polymer Science***, 2020, 106, 101253.
2. **Cheng, H.#**, Xiao, D.#, Tang, Y., Wang, B., Feng, X., Lu, M., Vancso, G.J.*, and Sui, X.*, Sponges with Janus character from nanocellulose: Preparation and applications in the treatment of hemorrhagic wounds. ***Advanced Healthcare Materials***, 2020, 9(17), 1901796. (Inside Front Cover)
3. Liu, K., Zhang, W., **Cheng, H.**, Luo, L., Wang, B., Mao, Z., Sui X., and Feng, X.*, A nature-inspired monolithic integrated cellulose aerogel-based evaporator for efficient solar desalination. ***ACS Applied Materials & Interfaces***, 2021, 13(8), 10612–10622.
4. Wang, Y., Chen, L., **Cheng, H.**, Wang, B., Feng, X., Mao, Z., and Sui, X.*, Mechanically flexible, waterproof, breathable cellulose/polypyrrole/polyurethane composite aerogels as wearable heaters for personal thermal management. ***Chemical Engineering Journal***, 2020, 402, 126222.
5. Wang, Y., Li, X., **Cheng, H.**, Wang, B., Feng, X., Mao, Z., and Sui, X.*, Facile fabrication of robust and stretchable cellulose nanofibers/polyurethane hybrid aerogels. ***ACS Sustainable Chemistry & Engineering***, 2020, 8(24), 8977-8985.
6. Yang, G., Wang, B.*, **Cheng, H.**, Mao, Z., Xu, H., Zhong, Y., Feng, X., Yu, J.*, and Sui, X.*, Cellulosic scaffolds doped with boron nitride nanosheets for shape-stabilized phase change composites with enhanced thermal conductivity. ***International Journal of Biological Macromolecules***, 2020, 148, 627-634.

➢ *Book chapter:*

1. Zhang, Y., **Cheng, H.**, Li, X., Wang, B., Feng, X., Mao, Z., Vancso, G.J.*, and Sui, X.*, Pickering emulsions as designer platforms for polymer-based hybrid materials: Routes to controlled structures, ***Macromolecular Engineering***, John Wiley & Sons

Ltd, *in production*

➢ *Manuscripts:*

1. **Cheng, H.**, Hempenius, M.A. Sui, X., and Vancso, G.J., Catalytic performance of Pd nanoparticles obtained by direct reduction in cellulose-poly(ferrocenylsilane) hybrid sponges, *submitted*.
2. **Cheng, H.**, Vancso, G.J., and Sui, X., Cellulose sponges with integrated thermal insulation and heat storage for personal thermal management, *in preparation*.

➢ *Other publications and patent:*

1. **Cheng, H.#**, Li, C.#, Jiang, Y., Wang, B., Wang, F., Mao, Z., Xu, H., Wang, L.*, and Sui, X.*, Facile preparation of polysaccharide-based sponges and its potential application in wound dressing, ***Journal of Materials Chemistry B***, 2018, 6, 634-640.
2. **Cheng, H.,** Du, Y., Wang, B., Mao, Z., Xu, H., Zhang, L., Zhong, Y., Jiang, W., Wang, L.*, and Sui, X.*, Flexible cellulose-based thermoelectric sponge towards wearable pressure sensor and energy harvesting, ***Chemical Engineering Journal***, 2018, 338, 1-7.
3. **Cheng, H.,** Li, Y., Wang, B., Mao, Z., Xu, H., Zhang, L., Zhong, Y., and Sui, X.*, Chemical crosslinking reinforced flexible cellulose nanofiber-supported cryogel, ***Cellulose***, 2018, 25, 573-582. (Cover Art)
4. Du, Y., **Cheng, H.**, Li, Y., Wang, B., Mao, Z., Xu, H., Zhang L., Zhong Y., Yan X. and Sui, X.*, Temperature-responsive cellulose sponge with switchable pore size: Application as a water flow manipulator. ***Materials Letters***, 2018, 210, 337-340.
5. Agaba, A., **Cheng, H.**, Zhao, J., Zhang, C., Tebyetekerwa, M., Rong, L., Sui X.* and Wang, B.*, Precipitated silica agglomerates reinforced with cellulose nanofibrils as adsorbents for heavy metals. ***RSC Advances***, 2018, 8(25), 33129-33137.
6. Sui, X., **Cheng, H.**, Li, Y., Mao, Z., Xu, H., Zhong, Y., and Zhang, L., Preparation of multi-chemical crosslinked cellulose aerogel, ZL201610835308.7

Curriculum Vitae

Huan Cheng was born on December 26th, 1992 in Shandong, China. He obtained his B.Sc. degree for Qingdao University with the *"Outstanding Graduates of Shandong Province"* in June 2015. In the same year, he entered Donghua University, College of Chemistry, Chemical Engineering and Biotechnology and started his master research in Textile Chemistry and Dyeing & Finishing Engineering under supervision of Prof. Xiaofeng Sui. His project focused on preparation and applications of functional cellulosic porous materials. He successfully defended his M.Sc. degree in March, 2018 and obtained the *"Outstanding thesis of Donghua University"* on his master thesis. Following that he continued as a joint Ph. D candidate of University of Twente and Donghua University from September 2018 under the supervision of Prof. G. Julius Vancso and Prof. Xiaofeng Sui. His project as described in this thesis focused on the cellulosic porous materials, discussing the preparation *via* structure design and surface engineering, and the multifaced applications.

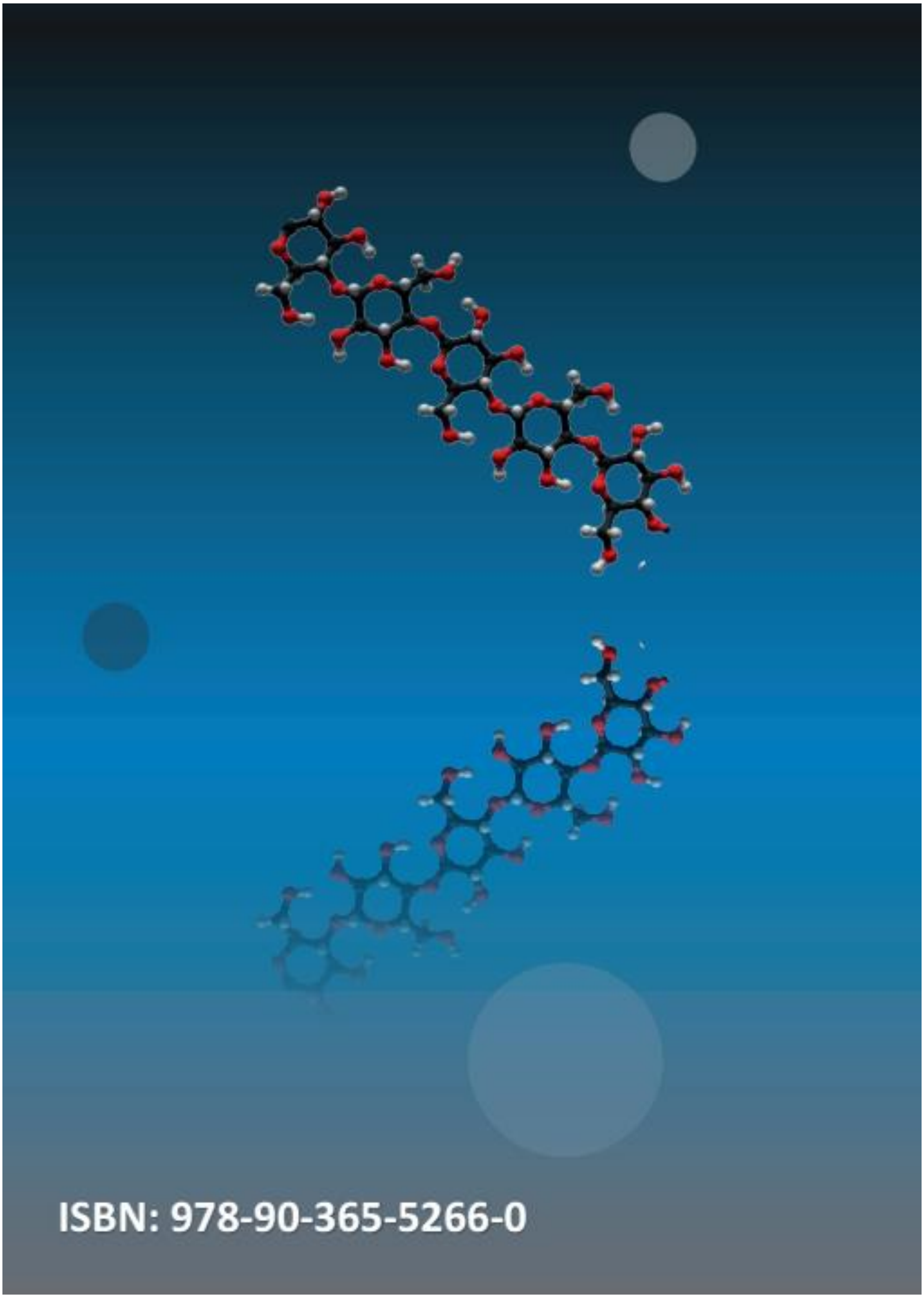

ISBN: 978-90-365-5266-0